ENGINEERING HYSTERESIS AND NON-DIFFUSIVE PHASE TRANSFORMATIONS IN MAGNETOCALORIC $(MN,FE)_2(P,SI)$ ALLOYS FOR MAGNETIC REFRIGERATION APPLICATIONS

A Dissertation

by

TIMOTHY DAVID BROWN

Submitted to the Office of Graduate and Professional Studies of
Texas A&M University
in partial fulfillment of the requirements for the degree of

DOCTOR OF PHILOSOPHY

Chair of Committee,	Patrick J. Shamberger
Committee Members,	Ibrahim Karaman
	Karl T. Hartwig
	Raymundo Arróyave
	Joseph H. Ross, Jr.
Head of Department,	Ibrahim Karaman

August 2019

Major Subject: Materials Science and Engineering

ABSTRACT

Magneto-structural transformations are non-diffusive phase transformations manifesting coupled magnetothermal properties that can enable useful applications like sensing, thermomagnetic generation, and especially, efficient solid-state refrigeration. However, implementation of magnetocaloric materials within these technologies requires a complex optimization over their underlying transformations' critical temperatures, enthalpies, and hysteresis, with hysteresis losses a critical limiting factor. Successful engineering of transformations within this application space requires deeper understanding of (1) the trade-offs between transformation properties and their effects on macroscopic system efficiencies and (2) the underlying microscale mechanisms that control the transformation and its hysteresis.

In this study, phase transformations in caloric hexagonal $(Mn,Fe)_2(P,Si)$ alloys are investigated using a combination of modeling and experimental techniques. First, alloys' macroscopic magnetothermal properties are coupled with a thermodynamic model incorporating hysteretic path-dependent evolution to simulate refrigeration efficiencies and cooling for relevant cycle classes. Results demonstrate extreme decreases in thermodynamic efficiencies of 10 % per 1 K thermal hysteresis, and the importance of First Law refrigeration work terms in governing cycle performance, both aspects rarely appreciated in the literature. Second, quantitative compositional analysis and calorimetry experiments are used to demonstrate mechanisms controlling the transformation, like heat-treatment induced multi-step behavior and oxygen-mediated

shifts in transformation properties due to phase segregation. Finally, force microscopy techniques are employed to directly image reversible movement of the phase boundary, suggesting growth-dominated behavior from pockets of retained martensite. Together, these results both create rational efficiency-based benchmarks for engineering phase transformations in $(Mn,Fe)_2(P,Si)$ alloys and point towards processing techniques for achieving them.

DEDICATION

This dissertation and the body of work it represents is dedicated:

First to my family and friends: my father, John Brown, who always supported my interest in science; my mother, Natalie Brown, whose artistry has always inspired me; and my sister, Elia Brown, who pushes me to be the best version of myself. To my grandparents, for countless phone calls and encouragement, and to my aunts and uncles and cousins, for their constant love and support. To my dear friends, Jack Welch, Prof. Charlie Walter, Patrick Creedon, and Luke Thompson, whose weekend visits and adventures created such good memories.

Second, to the MSEN department and to the staff that keep it up and running, most especially Jules Henry and Murat Kaynak, Andrea Raines, Amanda Sanders, Erin Bandza, who have done so much of the day-to-day work to help get me through this program. I am grateful to Prof. Ibraham Karaman, Prof. Miladin Radovic, and Jan Gerston for investing so much in my education.

Last and most important, to all the teachers and mentors who have helped put me on my career path: to my advisor, Prof. Patrick Shamberger, who always encouraged me to do my very best and who has taught me so much. To my college professors, especially Prof. Alexei Grigoriev and Prof. George Miller, Prof. Christi Patton-Luks, Prof. Ben Peters, and Prof. Ron Jepperson, To my high school teachers Joe Hutchinson, Beth McKee-Rohrig, Stan Reimer, and Melinda Sears. Finally, *in memoriam* for my middle school English teacher, Wendy Donaldson, who first taught me how to write.

ACKNOWLEDGEMENTS

So many people contributed in large and small ways to this work:

My committee, Prof. Patrick Shamberger, Prof. Ibrahim Karaman, Prof. Karl T. Hartwig, Prof. Joseph H. Ross, Jr., and Prof. Raymundo Arróyave, who pushed me to the limit to think critically about my data and also took time to help me untangle some of the more subtle aspects of the experiments.

My friends, colleagues, and collaborators, especially Dr. Heidi A. Clarke, Dominic Gehring, Prof. Nick M. Bruno, Erick Braham, Ruben Villarreal, Diane Sellers, Emily Emmons, Olga Eliseeva, Evan Prehn, Dr. Luke Johnson, Yijia Zhang, Hande Ozcan, Dr. Jing-Han Chen, Dr. Nick Barta, Dr. Brian E. Franco, Dr. Daniel Salas-Mula, Dr. Robert Niemann, and Herr. Prof. Ekkes Brück, and so many more who were always willing to share a fragment of their knowledge to point me in the right direction.

The excellent staff and staff scientists who are the lifeblood of the department, especially Michael Elverud, who has patiently cut, milled, and assembled shims, sample stages, and various small apparatus that have had such a large impact on this work; Dr. Andrew Mott, with whom I've logged so many EPMA hours; Dr. Anup Bandyopadhyay whose DSC and XRD trainings first enabled my experimental work; Dr. Nattamai Bhuvanesh who has kindly given his time to help us with single crystal diffraction experiments.

Finally, I want to acknowledge the small army of undergraduate researchers it has been my pleasure to work with: Daniel Galvan, who has been writing code and

helping synthesize alloys since the early days of this project; Julia Billman, whose enormous dedication and curiosity has helped us overcome enormous challenges; Tyler Buffington, Jonathan Van Buskirk, Gaby Lammoglia and Haley Jones, who all made critical contributions to this work. I am grateful to have been able to partner with so many talented students and hope that this work can contribute in some small way to their long and fruitful careers.

CONTRIBUTORS AND FUNDING SOURCES

Contributors

This work was supervised by a dissertation committee chaired by Professor Patrick Shamberger of the Department of Materials Science and Engineering, and consisting also of Professor Ibrahim Karaman, Professor Karl T. Hartwig, and Professor Arróyave of the Department of Materials Science and Engineering, and Professor Joseph H. Ross, Jr. of the Department of Astronomy and Physics.

Some of the data used to fit models in Chapters I-V were provided by Professor Ibrahim Karaman, and by Professor Vitalij Pecharsky of the Department of Materials Science and Engineering at Iowa State University. The isothermal magnetization data and temperature-dependent diffraction data in Chapter VI were taken by Dr. Jing-Han Chen of the Department of Physics at Louisiana State University, and Erick Braham of the Department of Chemistry at Texas A&M University, respectively. Undergraduate researchers Daniel Galvan, Julia Billman, and Jonathan Van Buskirk all contributed code, synthesis, or characterizations under the supervision of the doctoral candidate.

All other work conducted for the dissertation was completed by the student independently.

Funding Sources

Graduate study was supported in part by the Merit Fellowship from Texas A&M University.

This work was also made possible by a Graduate Research Fellowship Program fellowship from the United States National Science Foundation (NSF-GRFP), Award No. DGE-1252521, and through the Division of Civil, Mechanical and Manufacturing Innovation (NSF-CMMI), through Grant No. 1636105. The data collection provided by Dr. Chen was supported in part by the United States Department of Energy, Office of Basic Energy Sciences through Award No. DE-FG02-13ER46946, and the data collection provided by Mr. Braham was supported in part by a fellowship through an NSF-sponsored Integrative Graduate Education and Research Traineeship (NSF-IGERT) entitled the Data-Enabled Discovery and Design of Energy Materials (D3EM) program, under grant DGE-154540. Work by undergraduate researchers Daniel Galvan and Johnathan Van Buskirk was also supported under the NSF-sponsored Research Experience for Undergraduates (NSF-REU) under Award Numbers 1005178 and 1461202, respectively, and work by Julia Billman was also supported under the Clare Booth Luce Scholars program.

TABLE OF CONTENTS

Page

Page

Page

LIST OF FIGURES

Page

Page

Page

LIST OF TABLES

Page

CHAPTER I

INTRODUCTION AND RESEARCH OBJECTIVES

I.1 Magnetocaloric Materials and Hysteresis Effects

Materials display magnetocaloric effect (MCE), the effective coupling between magnetic and thermal degrees of freedom [1] that enables control of magnetic properties through external temperature control [2]; or more commonly for applications, control of thermal properties through an external applied magnetic field [3]. Depending on the manner in which the magnetic field B is applied, the magnetocaloric coupling can manifest as either an observed change in the material's entropy under isothermal conditions (ΔS_{m}), or in its temperature under adiabatic conditions (ΔT_{ad}) [4]. The magnitudes of the magnetocaloric effect metrics at some temperature T_0 are in turn primarily governed by the sensitivity of the magnetization surface $M(T,B)$ to temperature T [5], as in:

$$\Delta S_{\mathrm{m}}(T_0, B_0 \to B_1) = \int_{B_0}^{B_1} \left(\frac{\partial M}{\partial T}\right) dB\,, \qquad (I.1)$$

$$\Delta T_{\mathrm{ad}}(T_0, B_0 \to B_1) \approx \langle \frac{T}{c_p} \rangle \Delta S_{\mathrm{m}}(T_0, B_0 \to B_1). \qquad (I.2)$$

For most magnetic materials at room temperature, the magnetization-temperature sensitivity and magnetocaloric metrics Eq. I.1-I.2 are small; however, both can be larger around the second-order Curie transition from ferro- to para-magnetic ordering in strong, soft ferromagnetic materials [6]. This Curie-derived MCE is substantial enough to serve as a basis for efficient, greenhouse gas-free room temperature magnetic refrigeration

(MR) applications, as shown by Brown and Papell's proof-of-concept magnetic refrigerator using MCE in Gd [7]. However, despite the large change in magnetization of Gd across the Curie transition (~275 Am2/kg along {0001} axis) and its desirable Curie temperature near room temperature, the temperature range of the Curie transition is typically large (~100 K) [8], resulting in small cooling performance. Hence, although the Gd refrigerator demonstrated satisfactory performance for future research investment, continually pumping 38 W/kg-Gd of heat from a reservoir at 253 K to one at 258 K, it did so at the expense of a large 0.9 kg mass of critical rare-earth working material, and by using large magnetic fields on the order of 7 T only attainable through the use of cryogenic superconductors. Despite subsequent work to improve MR system design through improved regeneration techniques [9,10], external magnet apparatus [5,11,12], and heat transfer between the reservoirs and refrigeration bed [13,14], magnetic refrigerators remained largely Gd-based and so limited by the materials problem of its intrinsically small Curie-derived MCE.

Research interest was renewed with the discovery of a "giant" MCE (GMCE) in $Gd_5(Si_2Ge_2)$ (12 J/kg K for 0 T → 2T) [15]. This GMCE was shown to result from a first-order magneto-structural phase transformation where crystallographic structure, magnetic ordering, and specific entropy were all observed to change discontinuously at a critical temperature [16]. Furthermore, the change in crystal structure from monoclinic to orthorhombic in this system was shown to be consistent with the kind of non-diffusive, purely displacive atomic movements characteristic of martensitic transformation [17], and this structural transformation was found to contribute its own share of the magnetic

entropy change separate from the "conventional" Curie-derived effect [18]. Subsequently, GMCE was discovered in a range of other alloy systems, notably the $Ni_2(Mn,X)_2$ (X=In, Sb, Sn) magnetic shape memory alloys [19-22], the Fe_2P based hexagonal ferromagnet $(Mn,Fe)_2X$ (X = P, Ge, Si, As, Sb) alloy systems [23-28], and the $La(Fe,X)_{13}$ (X=Si, Al) alloy system [29-33]. However, despite the much larger GMCE metrics in these materials potentially enabling better MR system performance at smaller applied fields, actual studies of the GMCE materials in functioning MR systems remain exceedingly rare [34].

The major hurdle to implementation of optimized GMCE materials into improved MR systems is the hysteresis associated with the first-order magneto-structural phase transformation, whereby the forward and reverse phase transformations are both induced by over-driving thermal or magnetic forces. Experimentally, the material's phase is observed to evolve out-of-equilibrium; the state path deviates substantially when reversing the driving force (even infinitesimally), and hysteresis loops result [35]. Practically, the hysteretic behavior of the first-order GMCE transformation adversely impacts MR multiple times over: with hysteresis, the transformation requires larger switching magnetic fields [36], an important problem since maximum fields are feasibly limited to ~1T; excess driving force is required for the same phase switching capability, so refrigeration efficiency is decreased; excess energy from the over-driving force is dissipated in irreversible processes like defect generation, thus increasing fatigue and reducing lifetime [37]; entropy generation during out-of-equilibrium phase evolution reduces the transformation's capability to absorb heat from the cold reservoir (Q_c) and requires excess heat to be expelled at the hot reservoir (Q_h), as:

$$Q_{\mathrm{c}} = \int T_{\mathrm{c}}(dS - \delta S_{\mathrm{irr}}) < \int T_{\mathrm{c}} dS\,, \qquad (I.3)$$

$$|Q_{\mathrm{h}}| = \int T_{\mathrm{h}}(|dS| + \delta S_{\mathrm{irr}}) > \int T_{\mathrm{h}}|dS|\,, \qquad (I.4)$$

thus requiring more input energy for less cooling (Eqn. I.3) and more required heat extraction (Eqn. I.4). Although direct observations of these hysteretic effects in MR systems are somewhat rare due to the limited implementation of GMCE materials into completed MR systems, indirect experimental evidence is provided by, for example, the substantial discrepancy between direct observations and theoretical predictions of ΔT_{ad} in Fe_2P hexagonal systems [27,38] and poor cycle lifetimes before substantial GMCE decay correlated with hysteresis in $La(Fe_{11.6}Si_{2.4})$ [39].

Once understood, the impact of hysteresis loss on effective GMCE metrics provided the impetus for targeted research campaigns aimed at minimizing hysteresis in the GMCE candidate materials. For example, in the $La(Fe,Si)_{13}$ alloy system, introducing porosity reduces hysteresis by ~5x , but also reduces the GMCE metrics by 20-30% [32,40]. Reduced hysteresis with mostly constant GMCE metrics have also been reported by interstitial doping with H [41] and C [42]. Compositional tuning of hysteresis has also been used in $(Mn,Fe)_2(P,Ge)$ alloys, enabling reductions from 6 K to 2 K hysteresis at larger Mn and Ge contents [43]. In $(Mn,Fe)_2(P,Si)$ as well compositional tuning with lower hysteresis at increased Mn and Si content is reported, with the underlying cause being related to a “mixed magnetism” effect with alternating layers of high and low average magnetic moments [44]. Finally, in the NiMn-based Heusler alloys,

hysteresis has been reduced with special secondary annealing heat treatments which either relieve internal stresses [36], or promote B_2 disorder over L_{21} ordering [45]. These techniques have proven to be effective, reducing thermal hysteresis from 10-60 K to 0-5 K in these systems. However, there have only been a handful of cases where thermal hysteresis has been made so low as to be virtually eliminated, and even this usually comes at some cost to the GMCE metrics.

I.2 Scope of Dissertation

The main research objectives addressed by this dissertation are motivated by the observations that, first, optimizing GMCE materials for MR applications requires the ability to eliminate the hysteresis of the phase transformation while retaining all of its other aspects (large ΔS_{m} and ΔT_{ad}; transformation near room temperature; actuated by small applied fields); second, that developing a general capability for optimizing GMCE transformation properties for MR applications while reducing hysteresis has so far proven slow and difficult. Two complementary approaches have here been developed to work within these constraints, one modeling-based approach focusing on bridging the gap between MR system design and transformation properties of GMCE materials; the second an experimental investigation into understanding the deeper material factors controlling the GMCE properties, particularly the nature of the transformation energy barriers that control the magnitude of the hysteresis effects.

The primary research questions that guide this dissertation are:

1. How can we **quantify the effects of macroscopic transformation properties and hysteresis losses** on the heat / work transfers developed in viable refrigeration cycles?
2. **What are the transformation mechanisms** controlling the energy landscape and barriers driving and opposing non-diffusive transformation in a candidate GMCE material system, $(Mn,Fe)_2(P,Si)$ alloys?

I.2.1 Modeling Hysteresis Impacts: Summary of Approach

The first modeling-based approach can be viewed as a kind of feasibility analysis for MR using the state-of-the-art GMCE materials currently available. Given the observed complicated interdependence of transformation properties, particularly, the GMCE metrics ΔS_{m} and ΔT_{ad}, the entropy and magnetization changes across the magneto-structural transformation, the critical temperature, and not least, the magnitude of hysteresis as measured by thermal hysteresis loops, it is very difficult to eliminate hysteresis effects while still retaining all other beneficial properties of the GMCE transformation. Furthermore, because MR system design is intrinsically multi-objective (the system should maximize cooling power while minimizing energy input; its absolute cooling power should be on a par with currently available vapor compression systems; it should pump heat from a specified refrigerated temperature up to near room temperature; it should be able to operate using small fields <1 T capable of generation by permanent magnets; not to mention "secondary" concerns like cost, safety, lifetime, reliability), it is more than likely that design compromises will force the optimized

GMCE working material to have some extent of non-zero hysteresis losses. In this case, it is useful from a design perspective to take some level of hysteresis for granted and develop a materials-focused analysis that explicitly incorporates the effects of hysteresis and materials properties on the efficacy of potential MR cycles using GMCE materials as refrigerants.

This analysis has here been developed into a modeling framework enabling direct simulation of the magnetization and entropy state paths traversed by GMCE refrigerants with non-zero hysteresis as they undergo MR cycles, with the models parameterized by experimental magnetization, entropy, and hysteresis data taken from the literature. In this way, we have been able to extend understanding of how materials behave under non-equilibrium conditions while also pursuing an investigation into the impacts of hysteresis losses on MR system performance measured by cooling power, work input, and efficiency. Thus, we have been able to quantify what level of hysteresis is acceptable to obtain some benchmark level in some meaningful performance metric, for example, a Brayton cycle operating between 0 and 1 T with efficiency at least 80% of the Carnot limit. By further generalizing this methodology to treat all candidate GMCE materials and potential refrigeration cycles on an equal basis, the interacting effects of cycle design parameters and materials design parameters on potential MR system performance can be investigated. Thus insight can be gained into the materials properties / performance trade-offs relevant to actual MR system design, for example, if an optimized material can be designed with twice as large ΔS_{m} but at the cost of a 3 K

increase in thermal hysteresis, does this ultimately help or hinder MR system performance.

I.2.2 Investigation of Hysteresis Mechanisms: Summary of Approach

Whereas the first modeling approach focuses on developing specifications for maximum allowable hysteresis to enable some desired MR application, the second experimental approach is a controlled study to develop materials design principles to enable meeting those hysteresis specifications. In this respect, developing a mechanistic understanding for how the magneto-structural transformation nucleates and grows, and what are the obstacles that oppose it and what are their effects, is key. From a design standpoint, each of the relevant mechanisms is associated with an energy barrier, and control of the energy barriers opposing the transformation translates directly to control of the transformation hysteresis. Also, at a basic science level, many questions remain about how non-diffusive solid-solid first-order phase transformations propagate, for example: whether the energy barriers associated with martensitic atomic displacements primarily affect nucleation or growth regimes of the transformation; what are the mechanisms by which the transformation proceeds and their corresponding energy barriers, *e.g.* "lattice friction" as the phase boundary moves across free surfaces or grows into the daughter phase; or how the magnitude of these barriers can be affected by defects, *e.g.* preferential heterogeneous nucleation off of, or growth pinning by, grain boundaries. Some of these questions about solid-solid phase transformation have been investigated in similar martensitic transformations, typically in shape memory alloy systems, and powerful explanatory theories have emerged, most notably the lattice

matching theory of Ball and James that relates hysteresis to martensite / austenite lattice compatibility at the interface between austenite and martensite twins [46-50]. Although indirect evidence and inference has played a valuable role in supporting these theories, some of the most compelling evidence has come from direct observations of the martensitic transformation, where phase boundary motion [51] and orientation relationships [52], are imaged directly. Similar observations in GMCE transformations would be valuable for elucidating these aspects of magneto-structural transformations.

In the second experimental thrust we develop such an experimental program to study mechanisms of transformation in the (MnxFe2-x)(P1-y,Siy) alloy system. In addition to being strong candidates for GMCE refrigerants, these alloys show an extremely strong sensitivity of hysteresis and critical temperature to composition, varying from 2 K to 22 K and 260 K to 350 K, respectively, for about 6.5 at. % change in composition, making them amenable to a study of the factors controlling hysteresis that underlie this composition dependence. Through powder metallurgy synthesis of ~40 alloys throughout the composition space, we have fabricated a suite of materials with varying hysteresis and critical temperature, all processed under the same conditions, working towards the eventual goal of making *in-situ* observations of the magneto-structural transformation, for several members of the varied hysteresis set. In this way, we hope to gain insight into the way in which the observed phase transformation progresses, and how this progression might be different for samples that manifest small / large hysteresis.

I.3 Summary of Research Objectives

The main research objectives comprising the modeling-based investigations into the impact of hysteresis on potential magnetic refrigeration cycle performance are:

To develop a self-contained modeling framework for hysteretic magnetic cycle simulations, addressed in Chapter II of the dissertation, which explains in detail the mathematics underpinning the parameterization of material and hysteresis models from experimental data, and the use of such models for simulating out-of-equilibrium material response for arbitrary explicit $T - B$ refrigeration cycles.

To investigate dependence of cycle performance metrics on hysteresis, addressed in Chapter III of the dissertation, which introduces the cycle performance metrics of cooling power, work input, efficiency, and effective temperature span, and systematically investigates how these depend upon hysteresis of the magneto-structural transformation in a $(Ni,Co)_2(Mn,Sn)_2$ alloy undergoing Ericsson refrigeration cycles.

To explore the dependence of hysteresis interactions on cycle class, addressed in Chapter IV of the dissertation, which extends the methodology to simulate performance metrics for Brayton cycles with implicitly-defined non-equilibrium adiabatic state paths, thus enabling comparisons between hysteresis impacts on performance for Ericsson and Brayton refrigeration cycles across a range of cycle conditions.

To elucidate how cycle-hysteresis interactions are impacted by material properties, addressed in Chapter V of the dissertation, which using the same methodology, generates material and hysteresis models for members of each of the leading NiMn-based Heusler, Fe_2P-based hexagonal ferromagnet, and $La(Fe,Si)_{13}$ GMCE materials

classes, as well as a Gd benchmark, and compares their performance directly through simulation in Brayton cycles. Direct comparisons between materials with as-modeled and idealized transformation hysteresis under various cycle conditions allows the interacting effects of maximum field constraint, hysteresis, and magnetothermal properties reported in the literature to be decoupled and their individual effects on potential cycle performance to be thoroughly investigated.

The main research objectives of the experimental investigations into the transformation mechanisms belying hysteresis in (Mn,Fe)2(P,Si) alloys are:

To investigate the effect of heat treatments on transformations and hysteresis in the alloy system, addressed in Chapter VI of the dissertation, which investigates the role of a thermally-activated dynamic re-equilibration process in driving the relaxation of single-step magneto-structural transformations into multi-step transformations, or of subsequent recovery back into single-step transformations.

To explore the compositional dependence of hysteresis in the alloy system and its modulation by phase segregation mechanisms, addressed in Chapter VII of the dissertation, which uses calorimetry and compositional analyses to map out how transformation properties depend on alloy composition, and develops an oxygen-mediated mechanism for how these underlying relationships are systematically obscured by segregation of impurity phases.

To directly observe the phase transformation and determine nucleation vs. growth limited behavior, addressed in Chapter IX of the dissertation, which focuses on direct imaging of phase boundary movement during heating and cooling through the magneto-

structural transformation through *in-situ* magnetic force microscopy, thereby establishing both sudden single-step transformation behavior in individual grains, as well as reversible thermoelastic growth behavior enabled by sites of martensite retention at high-stress triple junction defects.

I.4 References

[1] E. Brück, Journal of Physics D: Applied Physics **38,** R381 (2005).

[2] K. A. Gschneidner and V. K. Pecharsky, Materials Science and Engineering a-Structural Materials Properties Microstructure and Processing **287,** 301 (2000).

[3] A. Smith, C. R. H. Bahl, R. Bjork, K. Engelbrecht, K. K. Nielsen, and N. Pryds, Advanced Energy Materials **2,** 1288 (2012).

[4] R. P. Santana, N. A. de Oliveira, and P. J. von Ranke, Journal of Alloys and Compounds **509,** 6346 (2011).

[5] V. Franco, J. S. Blázquez, B. Ingale, and A. Conde, Annual Review of Materials Research **42,** 305 (2012).

[6] V. Pecharsky, K. Gschneidner, A. Pecharsky, and A. Tishin, Physical Review B **64** (2001).

[7] G. V. Brown, Journal of Applied Physics **47,** 3673 (1976).

[8] S. Y. Dan'kov, A. M. Tishin, V. K. Pecharsky, and K. A. Gschneidner, Physical Review B **57,** 3478 (1998).

[9] C. Zimm, A. Jastrab, A. Sternberg, V. Pecharsky, K. Gschneidner, M. Osborne, and I. Anderson, in *Advances in Cryogenic Engineering, Vol 43 Pts a and B*; *Vol.*

43, edited by P. Kittel (Plenum Press Div Plenum Publishing Corp, New York, 1998), p. 1759.

[10] A. M. Rowe and J. A. Barclay, **613,** 995 (2002).

[11] K. A. Gschneidner and V. K. Pecharsky, International Journal of Refrigeration **31,** 945 (2008).

[12] C. Aprea, A. Greco, A. Maiorino, R. Mastrullo, and A. Tura, International Journal of Refrigeration **43,** 111 (2014).

[13] K. L. Engelbrecht, G. F. Nellis, and S. A. Klein, HVAC&R Research **12,** 1077 (2006).

[14] F. Shir, C. Mavriplis, L. H. Bennett, and E. D. Torre, International Journal of Refrigeration **28,** 616 (2005).

[15] V. K. Pecharsky and J. K. A. Gschneidner, Physical Review Letters **78,** 4494 (1997).

[16] V. K. Pecharsky, A. P. Holm, K. A. Gschneidner, Jr., and R. Rink, Phys Rev Lett **91,** 197204 (2003).

[17] V. K. Pecharsky and K. A. Gschneidner, Advanced Materials **13,** 683 (2001).

[18] K. A. Gschneidner, Y. Mudryk, and V. K. Pecharsky, Scripta Materialia **67,** 572 (2012).

[19] J. Liu, T. Gottschall, K. P. Skokov, J. D. Moore, and O. Gutfleisch, Nat Mater **11,** 620 (2012).

[20] M. Khan, N. Ali, and S. Stadler, Journal of Applied Physics **101** (2007).

[21] V. Srivastava, X. Chen, and R. D. James, Applied Physics Letters **97** (2010).

[22] T. Krenke, E. Duman, M. Acet, E. F. Wassermann, X. Moya, L. Manosa, and A. Planes, Nat Mater **4,** 450 (2005).

[23] H. Wada and Y. Tanabe, Applied Physics Letters **79,** 3302 (2001).

[24] O. Tegus, B. Fuquan, W. Dagula, L. Zhang, E. Brück, P. Z. Si, F. R. de Boer, and K. H. J. Buschow, Journal of Alloys and Compounds **396,** 6 (2005).

[25] W. Dagula, O. Tegus, B. Fuquan, L. Zhang, P. Z. Si, M. Zhang, W. S. Zhang, E. Bruck, F. R. de Boer, and K. H. J. Buschow, IEEE Transactions on Magnetics **41,** 2778 (2005).

[26] E. Brück, O. Tegus, D. T. Cam Thanh, N. T. Trung, and K. H. J. Buschow, International Journal of Refrigeration **31,** 763 (2008).

[27] F. Guillou, H. Yibole, G. Porcari, L. Zhang, N. H. van Dijk, and E. Brück, Journal of Applied Physics **116** (2014).

[28] D. T. Cam Thanh, E. Brück, O. Tegus, J. C. P. Klaasse, T. J. Gortenmulder, and K. H. J. Buschow, Journal of Applied Physics **99** (2006).

[29] A. Fujita, S. Fujieda, Y. Hasegawa, and K. Fukamichi, Physical Review B **67,** 104416 (2003).

[30] S. Fujieda, A. Fujita, and K. Fukamichi, Science and Technology of Advanced Materials **4,** 339 (2016).

[31] S. M. Podgornykh and Y. V. Shcherbakova, Physical Review B **73,** 184421 (2006).

[32] J. Lyubina, O. Gutfleisch, M. D. Kuz'min, and M. Richter, Journal of Magnetism and Magnetic Materials **321,** 3571 (2009).

[33] B.-G. Shen, F.-X. Hu, Q.-Y. Dong, and J.-R. Sun, Chinese Physics B **22** (2013).

[34] K. Navickaitė, H. N. Bez, T. Lei, A. Barcza, H. Vieyra, C. R. H. Bahl, and K. Engelbrecht, International Journal of Refrigeration **86,** 322 (2018).

[35] I. Mayergoyz, IEEE Transactions on Magnetics **22,** 603 (1986).

[36] J. Liu, T. G. Woodcock, N. Scheerbaum, and O. Gutfleisch, Acta Materialia **57,** 4911 (2009).

[37] K. C. Atli, B. E. Franco, I. Karaman, D. Gaydosh, and R. D. Noebe, Materials Science and Engineering: A **574,** 9 (2013).

[38] H. Yibole, F. Guillou, L. Zhang, N. H. van Dijk, and E. Brück, Journal of Physics D: Applied Physics **47** (2014).

[39] K. P. Skokov, K. H. Müller, J. D. Moore, J. Liu, A. Y. Karpenkov, M. Krautz, and O. Gutfleisch, Journal of Alloys and Compounds **552,** 310 (2013).

[40] J. Lyubina, Journal of Applied Physics **109** (2011).

[41] J. C. Debnath, R. Zeng, J. H. Kim, P. Shamba, and S. X. Dou, Applied Physics A **106,** 245 (2011).

[42] B. G. Shen, J. R. Sun, F. X. Hu, H. W. Zhang, and Z. H. Cheng, Advanced Materials **21,** 4545 (2009).

[43] N. T. Trung, Z. Q. Ou, T. J. Gortenmulder, O. Tegus, K. H. J. Buschow, and E. Brück, Applied Physics Letters **94** (2009).

[44] N. H. Dung, Z. Q. Ou, L. Caron, L. Zhang, D. T. C. Thanh, G. A. de Wijs, R. A. de Groot, K. H. J. Buschow, and E. Brück, Advanced Energy Materials **1,** 1215 (2011).

[45] N. M. Bruno, C. Yegin, I. Karaman, J.-H. Chen, J. H. Ross, J. Liu, and J. Li, Acta Materialia **74,** 66 (2014).

[46] J. M. B. a. R. D. James, **338,** 389 (1992).

[47] J. Cui, Y. S. Chu, O. O. Famodu, Y. Furuya, J. Hattrick-Simpers, R. D. James, A. Ludwig, S. Thienhaus, M. Wuttig, Z. Zhang, and I. Takeuchi, Nat Mater **5,** 286 (2006).

[48] R. Zarnetta, R. Takahashi, M. L. Young, A. Savan, Y. Furuya, S. Thienhaus, B. Maaß, M. Rahim, J. Frenzel, H. Brunken, Y. S. Chu, V. Srivastava, R. D. James, I. Takeuchi, G. Eggeler, and A. Ludwig, Advanced Functional Materials **20,** 1917 (2010).

[49] Z. Zhang, R. D. James, and S. Müller, Acta Materialia **57,** 4332 (2009).

[50] K. Bhattacharya, S. Conti, G. Zanzotto, and J. Zimmer, Nature **428,** 55 (2004).

[51] Y. Song, X. Chen, V. Dabade, T. W. Shield, and R. D. James, Nature **502,** 85 (2013).

[52] R. Delville, D. Schryvers, Z. Zhang, and R. James, Scripta Materialia **60,** 293 (2009).

CHAPTER II

A PREISACH-BASED NONEQUILIBRIUM METHODOLOGY FOR SIMULATING PERFORMANCE OF HYSTERETIC MAGNETIC REFRIGERATION CYCLES*

II.1 Introduction

The need to improve upon the efficiency and environmental impact of vapor compression refrigeration has led to the development of materials for novel refrigeration cycles [1-2]. Magnetic refrigeration cycles via the magnetocaloric effect (MCE) are possible in materials with strongly coupled thermal and magnetic properties [3,4]. In materials manifesting MCE, application of an external magnetic field H induces an entropy change, ΔS_{m}, under isothermal conditions, or a corresponding temperature change, ΔT_{ad}, under adiabatic temperature conditions [5–7]. These parameters are indirectly related to potential heat transfers occurring in a material as it undergoes a refrigeration cycle, and they have been used as figures of merit to quantify materials' refrigeration potential.

For temperatures above 1 K [8], ΔS_{m} and ΔT_{ad} are conventionally largest near magnetic order–disorder transitions, [9,10] where the magnetic order is sensitive to H; For example, near the Curie temperature, T_{C}, in ferromagnetic Gd, changing the applied field

---

*Reprinted with permission from "A Preisach-Based Nonequilibrium Methodology for Simulating Performance of Hysteretic Magnetic Refrigeration Cycles," T. D. Brown, N. M. Bruno, J. Chen, I. Karaman, J. H. Ross, Jr., P. J. Shamberger, 2015. *The Journal of The Minerals, Metals & Materials Society (TMS)*, vol. 67, pg. 2123-2132, Copyright [2015] by The Minerals, Metals & Materials Society. © Springer Publishing. Reproduced with permission. All rights reserved. DOI 10.1007/s11837-015-1519-0.

from 0 T to 2 T yields a ΔS_{m} and ΔT_{ad} of 5 J kg^{-1}K^{-1} and 6 K [11,12], respectively. Cycles based on this larger MCE have been shown to potentially achieve temperature spans (~50 K) comparable to those obtained using vapor compression [13–15]; however, the large fields required (~7 T), make these cycles commercially unviable.

The prospect of near-room-temperature magnetic refrigeration was greatly advanced by the discovery of the giant magnetocaloric effect (GMCE) in $Gd_5(Ge,Si)_4$ [11,16] ($\Delta S_{\mathrm{m}} = 27$ J kg^{-1}K^{-1}; $\Delta T_{\mathrm{ad}} = 7$ K under 2 T) associated with a magneto-structural first-order phase transition (FOPT) [12]. Following this, many GMCE materials were discovered, most notably (values quoted for 0 to 2 T field change): $La(Fe,Si)_{13}$ and its hydrides (15 J kg^{-1}K^{-1} to 25 J kg^{-1}K^{-1}; 4 K to 8 K) [17–19], $(Mn,Fe)_2(P,Si,Ge)$ compounds (12 J kg^{-1}K^{-1} to 25 J kg^{-1}K^{-1}; 1.8 K) [20–22], and several Ni-Mn-based off-stoichiometric Heusler alloys (6 J kg^{-1}K^{-1} to 15 J kg^{-1}K^{-1}; 2K to 6 K) [23–25].

In these classes of materials, the system transforms between two phases with different crystal structures and magnetizations, M. During the FOPT, the sudden structural change also creates an abrupt change in the system's entropy, ΔS, due to the latent heat of transformation, which contributes greatly to the GMCE [12]. The field H stabilizes the higher-M phase by reducing the free energy via the Zeeman energy $\mu_0 H \cdot M$, thus coupling the transition temperature and GMCE to an applied magnetic field. Hence, the GMCE can serve as a vehicle for $T-H$ refrigeration cycles.

Despite the magnitude of the GMCE, its implementation in real cycles remains critically limited by a variety of factors including hysteresis loss from cycling the magnetostructural FOPT, eddy-current loss, low cycle frequencies imposed by poor

thermal conductivities, and FOPT instability where the GMCE may decrease after many cycles [26–29]. Of these, hysteresis loss has been observed to reduce the actual extent of the FOPT so that only about 5% of the potential ΔS_{m} or ΔT_{ad} is actually accessible with field cycling [26]. Furthermore, unlike thermal conductivities and eddy-current loss, which may be effectively controlled through design of the refrigerant's geometry, hysteresis loss is difficult to reduce purely at the system level. Therefore, materials-based analysis of hysteresis losses is critical to improve the state of GMCE-based magnetic refrigeration [6,26,30]

Phenomenologically, hysteresis is the path-dependent branching of a material response at input extrema [31], and in GMCE systems can manifest as loops in $M(T)$ profiles under fixed H; generally, thermal hysteresis widths ΔT_{hyst} are used to quantify the magnitude of this effect macroscopically. Microscopically, these loops arise from thermodynamic irreversibility in the material mechanisms driving the FOPT. Knowledge of these mechanisms has allowed the design of systems with reduced ΔT_{hyst}; For example, introducing porosity and/or hydrogen interstitials into $La(Fe,Si)_{13}$ [32–34], tuning lattice parameters to introduce mixed magnetism in $(Mn,Fe)_2(P,Si,Ge)$ [35–37], and reducing the martensite–austenite coherency strain in shape-memory alloys [29,38,39] have all been explored to reduce ΔT_{hyst} to within the ranges of 0.4 K to 3 K, 1 K to 5 K, and 2 K to 5 K, respectively.

Despite these advances, fundamental questions about the practical utilization of cycles based on hysteretic GMCE materials remain largely unanswered. Of particular interest are four classes of questions defining the materials science aspect of GMCE

refrigeration: What is the effect on the refrigeration work and cycle efficiency of (1) the hysteretic character of the FOPT for a given GMCE and $T-H$ path, (2) the thermomagnetic GMCE material properties for a given cycle and hysteresis, and (3) the chosen $T-H$ path for a given hysteresis and thermomagnetic properties? Finally, (4) accounting for hysteresis, how do cycles based on GMCE materials perform when compared against each other or against those based on standards such as conventional MCE or vapor compression?

Experimentally exploring solutions to the above questions requires resources to characterize and analyze a large number of GMCE materials under an impractically wide range of conceivable $T-H$ paths. A preferable approach is to use existing limited datasets to construct simplified models for a given material's magnetothermal and hysteresis properties from a few independent materials parameters, and then to subject them to rigorous, thermodynamically validated simulations across a range of cycle conditions. Previous work utilized microscopic hysteresis models defined by mostly phenomenological parameters to predict the general behavior of systems undergoing special cases of $T-H$ paths (e.g., Carnot or Brayton cycles) [40–42] or validation of models by comparison with experimental hysteresis loops. In contrast, the method proposed herein aims to quantify refrigeration ability through overall work and efficiency terms for an arbitrary thermodynamic cycle and, further, to relate these to macroscopic material properties and to loss terms due to hysteresis. Through exploration of the relationship between refrigeration cycle, hysteresis, and material properties, this methodology can serve as an essential tool for GMCE materials design.

In this paper we describe a system-independent, materials-centered approach to evaluate an irreversible cycle based on the hysteretic GMCE. We then demonstrate its utility by considering a particular instance of question (1) above, by first fixing magnetothermal material parameters according to experimental data from $Ni_{45}Co_5Mn_{36.6}In_{13.4}$ at. % single crystals, and then using a simple but observationally consistent two-parameter Preisach model to simulate the transition under a particular $T-H$ cycle. We report on the thermodynamic effect of each Preisach parameter on refrigeration figures of merit and interpret the results within the context of materials design principles.

II.2 Hysteresis and Thermomagnetic Modeling

During a magnetic refrigeration cycle, the net magnetic work W_{in} done on the system is quantified as below:

$$W_{\text{in}} = \oint \mu_0 H \, \mathrm{d}M \geq 0, \qquad (II.1)$$

where μ_0 is the magnetic permeability of vacuum, with magnitude 1.26×10^{-6} kg m s^{-2}A^{-2}, and the integrand of the cyclic integral, $H(M)$, describes the material's magnetic response throughout a $T-H$ cycle. This W_{in} is employed to lift a quantity of heat Q_{c} from a cold reservoir and to pump another heat Q_{h} into the ambient hot reservoir, as in Fig. II.1. The refrigeration work is defined as $W_{\text{ref}} = Q_{\text{h}} - Q_{\text{c}}$, and is the portion of W_{in} creating the desired net heat transports against the temperature gradient. For an

idealized, thermodynamically reversible system, W_{ref} and W_{in} are equal. The situation is very different in the GMCE materials under consideration, as the mechanisms responsible for hysteresis produce an unwanted irreversible entropy contribution, ΔS_{prod}. As the FOPT progresses infinitesimally, a differential entropy element $\delta S > 0$ is produced. Additionally, a small element of heat δQ may be expelled. Then, the second law of thermodynamics gives the small change in the system entropy, S, as $dS = -\frac{\delta Q}{T} + \delta S_{\mathrm{prod}}$. When these small contributions are summed over the $T-H$ cycle, and with some manipulation, the net heat expelled is found to be $Q_{\mathrm{net}} = -\oint TdS + I$, where the integrand of the cyclic integral $T(S)$ describes the material's thermal response to the $T-H$ cycle. The last term, $I = \oint TdS_{\mathrm{prod}} \geq 0$, quantifies the lost work due to entropy produced by irreversibilities. The first law of thermodynamics requires that $Q_{\mathrm{net}} = W_{\mathrm{in}}$, therefore W_{ref} is given as below by:

$$W_{\mathrm{ref}} = -\oint TdS = W_{\mathrm{in}} - W_{\mathrm{ref}}, \qquad (II.2)$$

and the energy flows are related as in Fig. II.1.

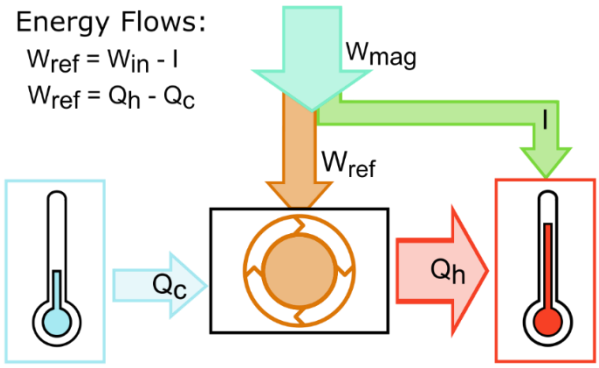

Figure II.1 Energy flows in an arbitrary refrigeration cycle. Hysteresis loss generates irreversible lost work I which decreases the potential refrigeration work W_{ref} for a given cycle. Reprinted with permission from [43]. © Springer Publishing 2015. DOI 10.1007/s11837-015-1519-0.

Therefore, in every refrigeration cycle actuating irreversible processes in a material, a quantity I of potential refrigeration work is lost to entropy production. This general result is based only on a thermodynamic analysis of irreversibility, and its effect on W_{ref} motivates our investigation into the limits that macroscopic hysteresis places on GMCE-based refrigeration. To better quantify the effect of hysteresis on cycle performance, an efficiency figure of merit can be defined as, below:

$$\eta = \frac{W_{\mathrm{ref}}}{W_{\mathrm{in}}} = 1 - \frac{I}{W_{\mathrm{in}}}, \qquad (II.3)$$

with $0 \leq \eta \leq 1$. This η is the fraction of the total work that must be done by external means which actually generates useful refrigeration work. Note that for $\eta \simeq 1$, the potential input work of the cycle has been most effectively utilized; i.e., the lost work due to hysteresis is minimized.

Here it is important to note that W_{ref}, I, and η are all purely materials parameters; they are defined without reference to the details (e.g., refrigerant flow rates, cycle frequencies) of any particular refrigeration system design. Within this framework, the performance of GMCE refrigeration cycles may be quantified by computing W_{ref}, I, and η for various cycles of interest. According to Eqs. 1–3, this requires determination of the system's magnetization $M(T,H)$ and entropy $S(T,H)$ at each point of the cycle, a task which is generally complicated by the interaction between the H-induced transition shift and the hysteretic path dependence.

To apply the preceding methodology, calculations are broken down into four parts, as in Fig. II.2. First a particular $T-H$ path is selected, and models for a material's single-phase magneto-thermal and hysteresis properties are created. Then the phase fraction at each point of the cycle is generated from a nonequilibrium Preisach hysteresis model. Next, the total system magnetization $M(T,H)$ and entropy $S(T,H)$ along each leg of the cycle are computed from the rule of mixtures. Finally, W_{ref}, I, and η are determined from Eqs. 1–3. Thus, beginning from only the fundamental laws of thermodynamics and a small set of material parameters, the relevant energy flows in an arbitrary GMCE-based refrigeration cycle can be computed and, for different material/cycle combinations, compared.

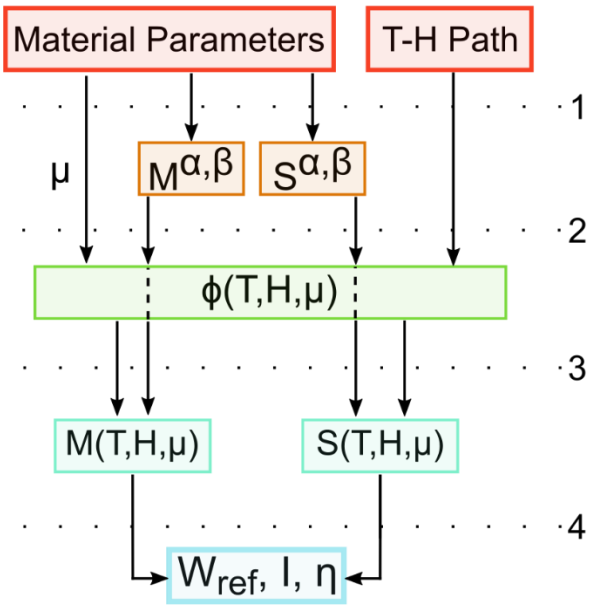

Figure II.2 Methodology flow diagram. (1) Material model parameterized in terms of hysteresis parameters, l, and single-phase properties, $M^{\alpha,\beta}$ and $S^{\alpha,\beta}$, which are combined with the $T-H$ path using (2) a nonequilibrium Preisach model to yield the phase fraction, ϕ. (3) Total system properties, M and S, are calculated with the rule of mixtures, allowing (4) figures of merit, W_{ref}, I, and η, to be calculated. Reprinted with permission from [43]. © Springer Publishing 2015. DOI 10.1007/s11837-015-1519-0.

II.2.1 Nonequilibrium Thermodynamic Analysis

For systems exhibiting ideal rate-independent hysteresis, the relaxation kinetics are infinitesimally fast; such systems can remain in nonequilibrium states for an arbitrarily long time. Since the system is not at equilibrium, the specification of the external conditions does not uniquely specify the system state [44]; i.e., the thermodynamic properties are no longer state variables. However, this may be resolved by introducing an additional set of variables which, together with the thermodynamic properties, reestablish the state of the system. Such variables do not appear explicitly in the equilibrium thermodynamic potentials and are hence called internal variables [45].

We model the GMCE system as a two-phase system consisting of an α (β) phase stabilized under a given field at a low (high) temperature. Although within Heusler alloys the FOPT is generally martensitic, we have deliberately avoided naming the phases ‘‘martensite’’ or ‘‘austenite,’’ as the development introduced here generalizes beyond just martensitic transitions. Given this notation, the phase fraction ϕ, defined as the mass fraction of β, is the appropriate internal variable [40] referred to above. In the two-phase region of the $T-H$ space, one has $0 \leq \phi \leq 1$, with some complicated path dependence on T and H.

II.2.2 Equi-Driving Force Diagrams

To simplify the determination of $\phi(T, H)$, we use an observation from studies of polycrystalline GMCE materials [26,46] suggesting that (1) when converted to free energy changes, variations in either T or H drive the transition equivalently, since (2) when variations in T and H are converted into free energy changes, identical internal and envelope hysteresis loops are obtained regardless of whether H is cycled at constant T or T is cycled at constant H. For these materials, the extent of phase transformation (including hysteresis losses) induced by T or H can be equivalently converted into that of a single generalized driving force D, defined as the difference in free energies of the two component phases, i.e., $D = G^{\beta} - G^{\alpha}$. This construction is shown in Fig. II.3a.

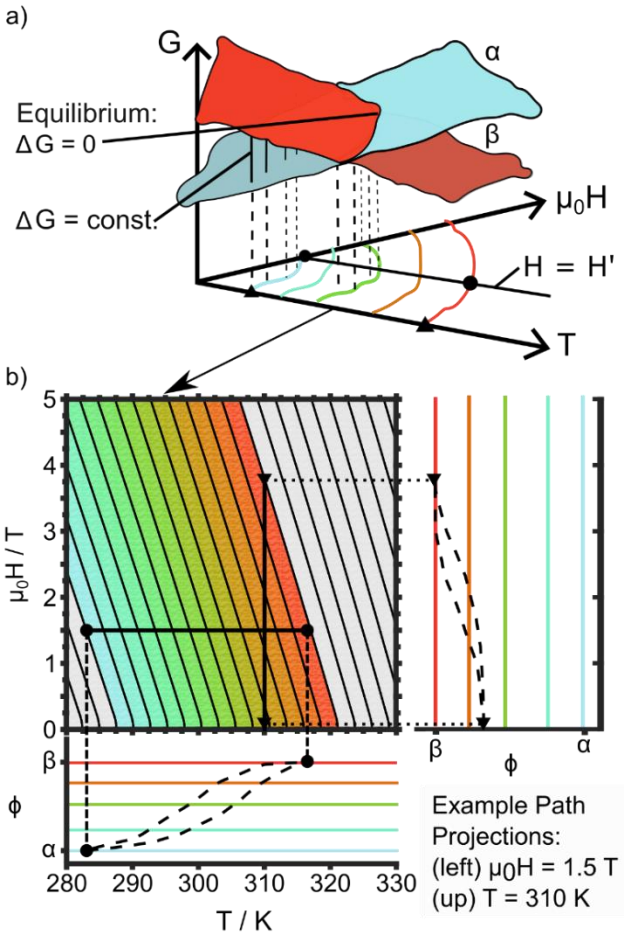

Figure II.3 Equi-driving force contour construction. (a) Curves of constant $D = G^{\beta} - G^{\alpha}$. For every pair of transformation-finish temperatures $T_0^{\alpha f}$ and $T_0^{\beta f}$ (triangles) under zero field, there are corresponding temperatures $T_{H'}^{\alpha f}$ and $T_{H'}^{\beta f}$ (circles) under nonzero field. (b) Different $T-H$ paths between the same equi-driving force contours induce the same extent of phase transformation. Reprinted with permission from [43]. © Springer Publishing 2015. DOI 10.1007/s11837-015-1519-0.

Now, the determination of $\phi(T, H)$ is reduced to determining $\phi(D)$. The preceding assumptions imply that, whatever ϕ's path-dependent relation to D, when plotted in $T-H$ space, contours of equal D and of equal ϕ coincide. These equi-driving force contours are calculated from a generalization of the Clausius–Clapeyron relation. Along such a contour, the driving force is some constant D', so $G^{\beta} = G^{\alpha} + D'$. If T or H

is changed, to remain on the D' contour, variations in the free energy must be balanced as $dG^{\alpha} = dG^{\beta}$ with $dG = -SdT - M\mu_0 dH$ for each phase. This yields the equation,

$$\frac{\mu_0 dH}{dT}|_{D'} = -\frac{S^{\beta}(T,H) - S^{\alpha}(T,H)}{M^{\beta}(T,H) - M^{\alpha}(T,H)}, \qquad (II.4)$$

where $\mu_0\, dH/dT\,|_{D'}$ is the slope in $T - H$ space of the D' equidriving force contour, and $S^{\alpha,\beta}$ and $M^{\alpha,\beta}$ are the entropies and magnetizations, respectively, of the component α and β phases along that contour. This formalism is equivalent to the assertion that the equilibrium ($D' = 0$) magnetic Clausius–Clapeyron relationship also holds for the iso-D and iso-ϕ contours in irreversible phase transitions.

Eqn. 4 is a set of differential equations, one for each D', with the magnetic field-temperature slope for each specified by the single-phase properties $S^{\alpha,\beta}$ and $M^{\alpha,\beta}$. The iso-D contours have a useful interpretation, as shown in Fig. II.3a. At zero applied field (e.g., the $H = 0$ axis), the material finishes its transition to β on warming at a temperature $T_0^{\beta f}$; similarly, it finishes its transition to a on cooling at $T_0^{\alpha f}$. At some nonzero applied field ($H = H'$), the corresponding transition-finish temperatures are $T_{H'}^{\beta f}$ and $T_{H'}^{\alpha f}$. These pairs of corresponding zero-field and nonzero-field transition-finish temperatures are by definition linked by a pair of specific iso-D contours, as illustrated in Fig. II.3a and Fig. II.3b, bottom. Similar contours also link $T_0^{\alpha,\beta s}$, the transition start temperatures at zero field, with the corresponding $T_{H'}^{\alpha,\beta s}$ at some higher field.

Alternatively, the contours may be viewed as linking corresponding transition-finish fields $H_T^{\alpha f}$ and $H_T^{\beta f}$ at each constant T, as in Fig. II.3b, right.

Equi-driving force contours allow the conversion of a given iso-T variation in H into a ‘‘transformation-equivalent’’ iso-H variation in T: along each, there is an equivalent evolution of ϕ. In general, an arbitrary $T-H$ path may be decomposed into legs along which either T or H is constant. Then, using the equi-driving force contours, each leg may be converted into a transformation-equivalent path at zero field. Therefore, any arbitrary $T-H$ path can be converted into a series of T variations at $H = 0$, which defines a pseudo-temperature T' axis; For example, in Fig. II.3b, both the horizontal and vertical lines correspond with 305 K $\leq T' \leq$321.8 K.

II.2.3 Hysteresis and the Preisach Model

The above treatment considerably simplifies the problem, as the complicated relationship between ϕ and the $T-H$ path under consideration simplifies to an equivalent relation between ϕ and T'. However, because of path dependence, T' does not uniquely determine ϕ in the two-phase region, and the relationship is not that of a function, but of some operator. The Preisach hysteresis operator, $\hat{P}$ [31,47], has proved especially robust in hysteresis modeling. Although significant work has been done to interpret the Preisach model’s parameters within the context of energy landscapes [48,49] and entropy production [41,50,51], it remains essentially phenomenological. Despite this, experimental hysteresis loops approximately demonstrate the necessary conditions of the model: (1) larger input variations erase memory of smaller input variations (wiping out property),

and (2) no matter the previous history, equivalent input variations create output loops that differ at most by a constant (congruency property) [31].

The basic unit of the model is the Preisach hysteron $\hat{h}$, a discrete on/off operator which contains all of the model's essential nonlinearity and path dependence [31]. We assume that this hysteron represents some phenomenological unit which contributes an element of ϕ_1 to ϕ, depending on T'. As T' increases from large negative values, the element is entirely α and $\phi_1 = 0$ until $T' > T_\beta{}'$, at which point it transforms completely to β and $\phi_1 = 1$. As T' is decreased back through $T_\beta{}'$ the unit remains completely β until $' < T_\alpha{}' < T_\beta{}'$, at which point it transforms completely to α again, as shown in Fig. II.4a, inset.

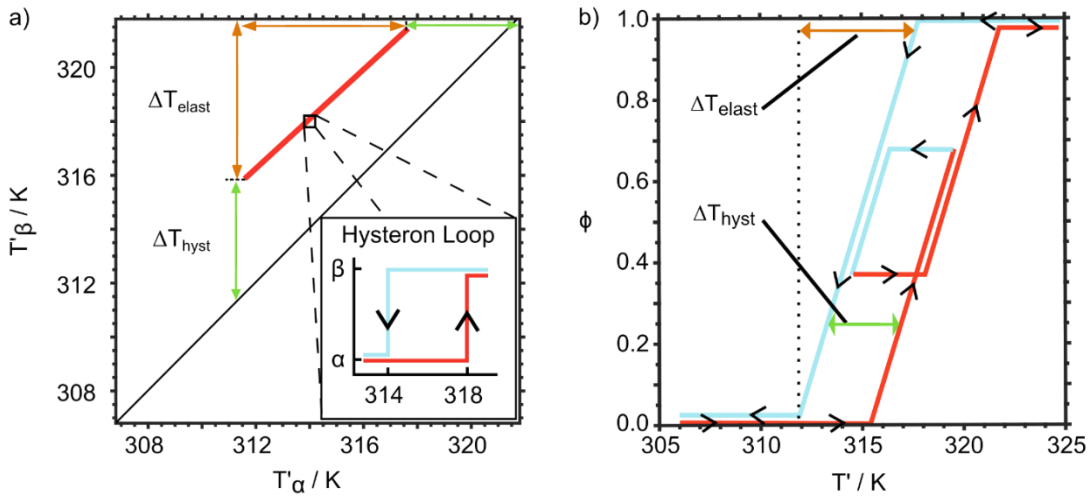

Figure II.4 Representations of hysteresis properties. (a) The Preisach plane. (Inset) Unit hysteron output corresponding with each point in the Preisach plane. Outputs are weighted by Preisach density and summed to obtain total response (Full). A special two-parameter Preisach density (bold red line) has been selected for this manuscript. (b) Envelope and interior hysteresis loops resulting from density in (a). Reprinted with permission from [43]. © Springer Publishing 2015. DOI 10.1007/s11837-015-1519-0.

To obtain the full operator $\hat{P}$, we imagine a distribution of hysterons with unique pairs of switching inputs $\{\widehat{h_\iota}(T_\alpha{}', T_\beta{}')\}$, whose contributions $\{\phi_i\}$ are weighted by some corresponding distribution $\{\mu_i\}$, then summed in parallel. Then, as the hysteron density grows infinitely dense, the Preisach model for ϕ with input T' is given as below by:

$$\phi = \hat{P}[T] = \iint \mu(\alpha, \beta)\hat{h}_{\alpha\beta}\,[T']\,\mathrm{d}\alpha\,\mathrm{d}\beta, \qquad (II.5)$$

where we have renamed our indexing from $(T_\alpha{}', T_\beta{}')$ to (α, β) for notational simplicity.

The Preisach operator has a convenient geometrical interpretation when the switching inputs are plotted on Cartesian axes $(x, y) \rightarrow (\alpha, \beta)$, defining the Preisach plane [31] (Fig. II.4a, full). Then, the so-called Preisach density μ is some surface (here, the surface is nonzero only over the thick red region) over the Preisach plane. As T' increases, contributions to ϕ can be visualized as filling up under μ along the β axis; similarly, as T' decreases, ϕ empties out along the $-\alpha$ axis. Hysteresis is accommodated as the path dependence of the ‘‘state line’’ composed of alternating fill-up/empty-out segments.

Once μ is specified, the path-dependent response of ϕ to any arbitrary T' path is uniquely determined (Fig. II.4b), and hence the surface $\mu(\alpha, \beta)$ completely and uniquely characterizes the hysteretic character of the FOPT. The reverse problem of determining $\mu(\alpha, \beta)$ for a given hysteresis is uniquely determined by the system’s internal and envelope hysteresis loops [31].

Here, a two-parameter $(\Delta T_{\mathrm{hyst}}, \Delta T_{\mathrm{elast}})$ Preisach density is used to describe hysteresis, as in Fig. II.4a. This parameterization is motivated by experimental observations of constant-H hysteresis loops in $\phi(T)$for thermoelastic martensites [52]. In these loops, the one-way transitions extend over some temperature range $(\Delta T_{\mathrm{elast}})$ and the forward and reverse transformations are also displaced relative to each other by another temperature difference $(\Delta T_{\mathrm{hyst}})$, as shown schematically in Fig. II.4b. The former is thought to arise from reversible storage of elastic strain energy due to coherency effects, whereas the latter is a manifestation of hysteresis. This choice of parameterization captures some of the essential behavior of general hysteresis observed experimentally in these systems [26,52], while reducing it to a space of parameters with an intuitive interpretation.

II.2.4 Magnetothermal Modeling

The description of a self-consistent model for a GMCE system's single-phase thermomagnetic properties $M^{\alpha,\beta}$ and $S^{\alpha,\beta}$ follows below. These models have been parameterized using data from a $Ni_{45}Co_5Mn_{36.6}In_{13.4}$ magnetic shape-memory alloy with $M^{\beta} > M^{\alpha}$ so that the material manifests what is commonly referred to as inverse GMCE. It is important to note that the general approach outlined in the previous two sections is equally valid for purely empirical fits to experimental data as for more sophisticated models derived from fundamental physical relationships. For this manuscript a compromise between purely empirical and first-principles approaches has been reached, in order to balance model fidelity with physically meaningful parameters.

II.2.5 Magnetization

The β phase is assumed to be ferromagnetically ordered with high saturation magnetization M_s. Determining the α ordering is difficult due to its small saturation magnetization, but in NiMnIn systems there is evidence that the α (martensite) phase exhibits frustrated anti-ferromagnetism. In either case, a Brillouin model has been used to describe the magnetization contours $M(T)$ at some saturation field H', which assumes that the strong individual exchange interactions can be replaced with an internal mean field that greatly exceeds the applied field. We choose a $j = 1/2$ model, since it provides a reasonably good fit to the M^β contours, and $M^\alpha \ll M^\beta$ so that a 10% variation in M^α perturbs the W_{ref} and η calculations by less than 1.5%. These assumptions result in a determinate implicit equation relating M and T as below:

$$\frac{M}{M_s} = B_j(x), \qquad (II.6)$$

with $B_j(x)$ being the jth Brillouin function defined in terms of $x = \frac{M}{M_s}\frac{T_C}{T}$.

The magnetization contours $M(H)$ at constant T are guided phenomenologically to match experimental observations. The β phase is approximated as a soft ferromagnet with some small saturating field $H_s{}'$ at each T, above which $M_\beta(H)$ saturates and below which $M_\beta(H)$ increases linearly. For α, the experimental data suggest a response typical of a weakly magnetic material, demonstrating a linear $M(H)$ relationship and no saturating field. In sum, this particular model is defined by five material parameters: two

Curie temperatures $T_{\mathrm{C}}^{\alpha,\beta}$ (for the model considered here, they are 298.0 K and 421.6 K, respectively), two saturation magnetizations $M_{\mathrm{s}}^{\alpha,\beta}$, (9.3Am^{-2}kg^{-1} and 125.4 A m^{-2}kg^{-1}, respectively), and the maximum β-saturating field H_{s} (0.25 T).

II.2.6 Entropy

The GMCE system is partitioned into α and β phases. The total entropy for each phase consists generally of electronic, lattice, and magnetic contributions, $S_{\mathrm{tot}} = S_{\mathrm{elec}} + S_{\mathrm{lat}} + S_{\mathrm{mag}}$, with the first term assumed negligible. The total entropy can also be divided into zero-field and applied-field terms as $S(T,H) = S(T,0) + \Delta S(T,H)$, with possible lattice and magnetic contributions to each. Debye's method is used to approximate the lattice as an isotropic gas of noninteracting and nonmagnetic phonons; then S_{lat} is field independent and contributes only to $S(T,0)$. For simplicity, the magnetic interaction between α and β is assumed negligible, so that $S_{\mathrm{mag}} = 0$ at zero field and only contributes to $\Delta S(T,H)$. Hence, for the single-phase entropies we have the equation:

$$S_{\mathrm{tot}} = S_{\mathrm{lat}}(T) + \Delta S_{\mathrm{mag}}(T,H). \qquad (II.7)$$

The first term $S_{\mathrm{lat}}(T)$ is calculated from the Debye model, which yields the lattice heat capacity as below:

$$C_{\mathrm{lat}}(T) = 9R\left(\frac{T}{T_{\mathrm{D}}}\right)^3 \int_0^{T_{\mathrm{D}}} \frac{x^4 \exp x}{(\exp x - 1)^2}\, \mathrm{d}x\,, \qquad (II.8)$$

where R is the ideal gas constant (8.314 J mol^{-1}K^{-1}) and T_{D} is the Debye temperature, above which essentially all phonon modes are excited. The zero field entropies are then computed as below:

$$S_{\mathrm{lat}}(T) = \int_0^T \frac{C_{\mathrm{lat}}(T')}{T'}\,\mathrm{d}T', \qquad (II.9)$$

with $S_{\mathrm{lat}}(0) = 0$ consistent with the third law of thermodynamics.

The second term $\Delta S_{\mathrm{mag}}(T, H)$ is computed from Maxwell's relation applied to the single phases, derived as follows: The free energy in each phase is analytic and path independent. This requires equality of the free energy cross derivatives, expressed as:

$$\frac{1}{\mu_0}\left(\frac{\partial S_{\mathrm{mag}}}{\partial H}\right)|_T = \left(\frac{\partial M}{\partial T}\right)|_H. \qquad (II.10)$$

Integrating and using the independence of T and H yields the equation,

$$\Delta S_{\mathrm{mag}}(T, H) = \frac{\mathrm{d}}{\mathrm{d}T'}\left(\int_0^H M(T, H')\,\mu_0\,\mathrm{d}H\right)|_T. \qquad (II.11)$$

Thus, $\Delta S_{\mathrm{mag}}(T, H)$ is calculated directly from the magnetization model, and introduces no extra parameters. The final entropy model adds just two additional materials parameters: the Debye temperatures $T_{\mathrm{D}}^{\alpha,\beta}$ (340 K and 306 K, respectively) of α

and β phases.

II.2.7 Total System Properties and Figures of Merit

Combining this and the previous subsections, ϕ, $M^{\alpha,\beta}$, and $S^{\alpha,\beta}$ can be determined throughout the whole $T-H$ space. The properties of the system $X = \{S, M, G, ...\}$ are assumed to be simply related to ϕ and single-phase properties $X^{\alpha,\beta}$ through the rule of mixtures, expressed as:

$$X = (1-\phi)X^{\alpha} + \phi X^{\beta}. \qquad (II.12)$$

This procedure assumes that the contribution to the β properties X from the coupling between the separate phases, e.g., at interfaces, is negligible compared with that from the bulk single phases. While X generally depends on the size, shape, and distribution of the phases in the two-phase region, this assumption can be expected to hold when all phases are magnetically saturated, as in the high-field regime.

The treatment of Sects. 1 and 2 yields the total system M and S along any conceivable cycle in the $T-H$ space. By parameterizing a particular cycle, e.g., by its minimum and maximum temperatures and fields, the magnetothermal response, $M(T,H)$ and $S(T,H)$, can be determined. Hence, W_{ref} , I, and η for this cycle can be determined by a handful of intuitively interpreted parameters. Comparison between different sets of parameters allows comprehensive investigation of the effect of each parameter on the GMCE cycle performance.

II.3 Results

Interactions between a specific $T-H$ path and hysteresis have been modeled by fitting experimental data from a $Ni_{45}Co_5Mn_{36.6}In_{13.4}$ single crystal to the parameterized models described in the previous section. The response of this model has been investigated for a rectangular $T-H$ path composed of four segments: (1) iso-field cooling from $T_{\max} = 325$ K to $T_{\min} = 310$ K at 0 T, (2) isothermal field increase at $T_{\min}$ from 0 T to 5 T, (3) iso-field warming at 5 T from $T_{\min}$ to $T_{\max}$, and (4) isothermal field decrease at $T_{\max}$ from 5 T to 0 T. The temperature $T_{\max}$ is about 30 K above room temperature, but has been chosen to emphasize the effects of the transition characteristics of this particular alloy, for which $T_0^{\beta f}$ is 321.8 K. The maximum field of 5 T represents a reasonable field obtainable with a large-bore superconducting magnet system, and compares to the apparatus usually used to measure ΔS_{m} and ΔT_{ad}. Although for this investigation a rectangular $T-H$ path is used, more complicated and realistic $T-H$ paths, such as those with adiabatic/isentropic or isenthalpic legs, are easily considered following this methodology.

The effects of phase transformation behavior on refrigeration capability were investigated by varying $\Delta T_{\mathrm{elast}}$ from 0 K to 14 K and ΔT_{hyst} from 0 K to 10 K and calculating W_{ref} , I, and η for each pair of values. The results are summarized in Fig. II.5. To facilitate interpretation of the W_{ref} , I, and η surfaces, the contour plots have been divided into three distinct regions with different behaviors. Region 1 is defined approximately by $\Delta T_{\mathrm{hyst}} > 8$ K and $\Delta T_{\mathrm{elast}} > 4$ K. Within this region, hysteresis losses are so large that $I \geq W_{\mathrm{in}}$, so that both W_{ref} and $\eta \leq 0$; no useful refrigeration work may

be performed. For none of the plots in Fig. II.5 do the contours suffer a discontinuity at the boundary between regions 1 and 2; this confirms that W_{ref} decreases smoothly to zero at the boundary between regions 1 and 2.

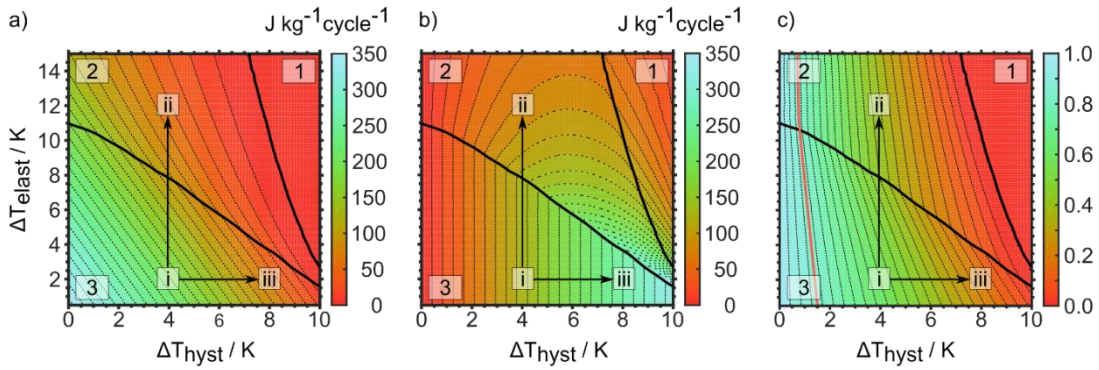

Figure II.5 Refrigeration metric contour maps. Contours of (a) W_{ref}, (b) I, and (c) η as functions of elastic ($\Delta T_{\mathrm{elast}}$) and hysteresis ($\Delta T_{\mathrm{hyst}}$) widths for a material undergoing a 0 T to 5 T rectangular $T-H$ cycle. Regions labeled 1, 2, and 3 are discussed in the text. Points labeled (i), (ii), and (iii) correspond with Fig. II.7 as described in text. The 90% efficiency limit is marked on (c) in red. Reprinted with permission from [43]. © Springer Publishing 2015. DOI 10.1007/s11837-015-1519-0.

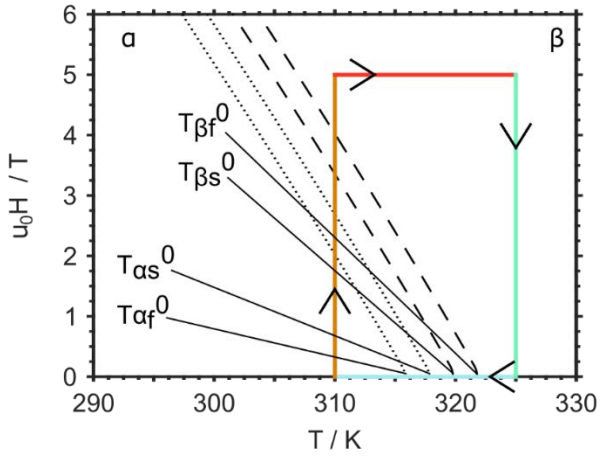

Figure II.6 Cycle-hysteresis interaction. Interaction of representative $T-H$ cycle with two-parameter hysteresis discussed in text. Dashed and dotted lines are equi-driving force contours for the point marked (i) on Fig. II.5, i.e. $\Delta T_{\mathrm{hyst}} = 4$ K, $\Delta T_{\mathrm{elast}} = 2$ K. Reprinted with permission from [43]. © Springer Publishing 2015. DOI 10.1007/s11837-015-1519-0.

This behavior stands in contrast to the interface between regions 2 and 3, where the contours of constant I and η both suffer slope discontinuities. In region 3, I is independent of $\Delta T_{\mathrm{elast}}$ and increases linearly with ΔT_{hyst}, whereas in region 2, I increases with $\Delta T_{\mathrm{elast}}$, with this dependence becoming stronger as ΔT_{hyst} also increases. For η, this behavior is reversed.

The system's behavior within each of these regions may be understood by referencing Fig. II.6 and Fig. II.7, where several ϕ versus T graphs are shown for particular combinations of ΔT_{hyst} and $\Delta T_{\mathrm{elast}}$. First consider the relation of these ϕ versus T plots to the underlying $T-H$ cycle, in Fig. II.6, where the equi-driving force contours passing through the transition finish (dashed contours) and transition start (dotted contours) are plotted along with the $T-H$ cycle. Note that $\Delta T_{\mathrm{hyst}} = T_0^{\beta \mathrm{f}} - T_0^{\alpha \mathrm{s}} = T_0^{\beta \mathrm{s}} - T_0^{\alpha \mathrm{f}}$ and $\Delta T_{\mathrm{elast}} = T_0^{\beta \mathrm{f}} - T_0^{\beta \mathrm{s}} = T_0^{\alpha \mathrm{f}} - T_0^{\alpha \mathrm{s}}$.

Along the zero-field cooling leg of the cycle, the system crosses the α transition-start contour at $T = 317.8$ K and begins to transform to α from β; this transition finishes at 315.8 K, when the system crosses the α transition-finish contour. Along the increasing field leg, even though the temperature does not change, the magnetic driving force induces the $\alpha \rightarrow \beta$ transition to occur; this begins on crossing the β transition-start contour at $\mu_0 H = 3.5$ T and completes at 4.0 T. Although T and H both vary along the two remaining legs of the cycle, note that $\phi = 1$ until the zero-field cooling leg repeats. The net result is the ϕ versus T graph plotted in Fig. II.7a.

Figure 7a and b show ϕ versus T plots for two sets of hysteresis parameters lying within regions 3 and 2, respectively, of Fig. II.5. These specific values have been chosen so that $\Delta T_{\mathrm{hyst}} = 4$ K is the same for both, but $\Delta T_{\mathrm{elast}}$ varies significantly between them, being 4 K for the former and 12 K for the latter. Comparison of Figs. 6 and 7a shows that the difference in behavior between regions 2 and 3 arises because, in region 2, $T_0^{\alpha \mathrm{f}} < T_{\mathrm{min}}$ and the full transition is not obtained, whereas for region 3, $T_0^{\alpha \mathrm{f}} > T_{\mathrm{min}}$. Stated explicitly in terms of hysteresis parameters, points within region 2 satisfy:

$$T_0^{\beta \mathrm{f}} - \Delta T_{\mathrm{elast}} - \Delta T_{\mathrm{hyst}} < T_{\mathrm{min}}. \qquad (II.13)$$

In contrast, Fig. II.7a and Fig. II.7c show ϕ versus T plots for $\Delta T_{\mathrm{elast}} = 2$ K and $\Delta T_{\mathrm{hyst}} = 4$ K and 8 K, respectively; however, both of these lie within region 3, since they do not satisfy Eq. II.13. Within region 3, the total phase transition is accessible, and the lost work I is given approximately by the equation:

$$I \approx \Delta T_{\mathrm{hyst}} \times \Delta S_{\mathrm{tr}}, \qquad (II.14)$$

where ΔS_{tr} is the approximately field- and temperature-independent entropy of transformation. From Eq. II.9, I increases linearly with ΔT_{hyst}, as confirmed by Fig. II.5b.

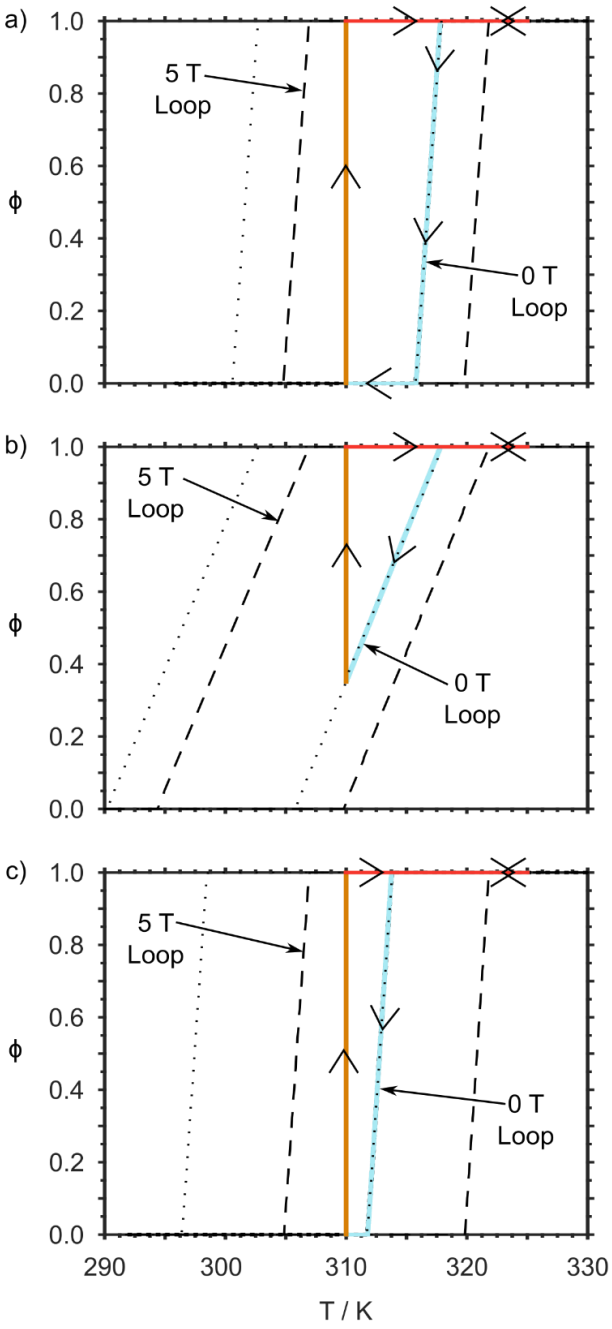

Figure II.7 Corresponding phase fraction paths. Phase fraction along $T-H$ path defined in Fig. II.6 for three representative sets of hysteresis parameters marked (i), (ii), and (iii) in Fig. II.5: (a) $\Delta T_{\mathrm{hyst}} = 4$ K, $\Delta T_{\mathrm{elast}} = 2$ K, (b) $\Delta T_{\mathrm{hyst}} = 4$ K, $\Delta T_{\mathrm{elast}} = 12$ K, and (c) $\Delta T_{\mathrm{hyst}} = 8$ K, $\Delta T_{\mathrm{elast}} = 2$ K. Reprinted with permission from [43]. DOI 10.1007/s11837-015-1519-0.

II.4 Implications for Materials Design

The calculated dependence of W_{ref} , I, and η on ΔT_{hyst} and $\Delta T_{\mathrm{elast}}$ has important implications for materials design principles. First, note that the $\eta = 0.90$ contour lies within the region $\Delta T_{\mathrm{hyst}} < 1$ K, so that if high-efficiency refrigeration is defined as that for which W_{ref} is at least 90% of W_{in}, this requires small ΔT_{hyst} on the order of 1 K. Importantly, this evaluation ignores any system-level inefficiencies; practically, one would have to design the hysteresis properties of the GMCE somewhat above this contour to obtain real 90% efficiency for the total system. Due to the cycle-dependent nature of η, these results vary quantitatively with varying cycles and material characteristics; however, the same qualitative behavior is expected, providing motivation for the important work on the reduction of ΔT_{hyst} in GMCE material systems summarized in the ‘‘Introduction.’’

Second, regions 2 and 3 have been emphasized, where two distinct behaviors in I are observed. In region 2, decreasing $\Delta T_{\mathrm{elast}}$ at constant ΔT_{hyst} causes I to decrease monotonically so that the GMCE based cycle becomes more efficient. Thus, if a material is initially within region 2 and further decreases in ΔT_{hyst} are impossible, η can still be increased by decreasing $\Delta T_{\mathrm{elast}}$ instead. There has recently been some experimental work exploring how to achieve these $\Delta T_{\mathrm{elast}}$ with heat treatments [52]. On the other hand, in region 3, decreasing $\Delta T_{\mathrm{elast}}$ at constant ΔT_{hyst} has no effect on I (and reduced effect on η). Thus, if a material is initially within region 3, decreasing $\Delta T_{\mathrm{elast}}$ will be ineffective, and further improvement of cycle efficiency requires decreasing ΔT_{hyst}.

Finally, this manuscript has focused on the interactions between hysteresis and the $T-H$ cycle for one particular material system. However, the methodology described here can easily be reconfigured to investigations of interactions between, e.g., material properties and cycle parameters, or material properties and hysteresis. Then one could conceive that the methodology could be used to generate materials property-focused design principles, such as a minimum saturation magnetization for a given cycle and hysteresis parameters in order to achieve 90% efficiency.

II.5 Conclusion

We have presented a methodology for quantifying the effects of irreversible FOPTs on refrigeration cycles based on GMCE materials, and for relating these effects to parameterizations of refrigeration cycles, hysteresis properties, and material properties. We have used this approach to confirm the importance of accounting for hysteresis in analyses of these materials, as the presence of region 1 in Fig. II.5 clearly shows that hysteresis losses can reduce the refrigeration entirely to zero. Under these conditions, no heat is transported from the cold to hot reservoir, and even worse, some heat may actually flow backwards, from the hot to cold reservoir. This result alone demonstrates the importance of considering the effect of hysteresis losses, and of the interplay between the $T-H$ cycle and losses, on GMCE-based refrigeration. Our results imply that, for future studies, cycle-dependent figures of merit must be calculated, as the relevant figures of merit for refrigerants ($W_{\mathrm{ref}}, I, \eta$) cannot be separated from the cycle being considered. This opens the possibility of optimizing refrigeration performance for a GMCE material by carefully choosing the $T-H$ cycle.

For the specific investigation reviewed in this manuscript, we have demonstrated the efficacy of a new approach to analyzing hysteretic materials by combining an extension of classical equilibrium phase diagrams with Preisach hysteresis models. Although utilizing less sophisticated magnetization and entropy models, the methodology we have chosen here allows the interpretation of our cycle figures of merit in terms of fundamental materials properties (Curie temperatures, Debye temperatures, saturation magnetizations), while retaining realistic temperature- and field-dependent behavior. These parameters have a clear material interpretation, and so one may hope that further exploration of the relationship between figures of merit and materials parameters could guide material design without as much reliance on experimental trial and error.

Finally, we find that, due to the interaction between the chosen $T-H$ cycle and hysteresis effects on the equi-driving force contours, for some cases (i.e., hysteresis in region 2), η can be increased by decreasing $\Delta T_{\mathrm{elast}}$, the width of the one-way transition. We see that the interactions between material properties, hysteresis, and cycle constitute a large and complex parameter space, but one for which our improved understanding is essential. The methodology presented here provides a means to begin accomplishing this goal.

II.6 References

1. V. Pecharsky and K. Gschneidner, Int. J. Refrig. 29, 1239 (2006).

2. E. Bruck and E. Bru¨ ck, J. Phys. D. Appl. Phys. 38, R381 (2005).

3. S. Russek and C. Zimm, Int. J. Refrig. 29, 1366 (2006).

4. K. Engelbrecht, G. Nellis, and S. Klein, HVACR Res. 12, 1077 (2006).

5. V. Pecharsky, K. Gschneider, A. Pecharsky, A. Tishin, and K. Gschneidner, Phys. Rev. B Condens. Matter Mater. Phys., 64 (2001).

6. A. Smith, R. Bjork, K. Engelbrecht, K. Nielsen, R. Bjørk, and N. Pryds, Adv. Energy Mater. 2, 1288 (2012).

7. H. Ucar, J. Ipus, V. Franco, M.E. McHenry, and D.E. Laughlin, JOM 64, 782 (2012).

8. W. Giauque and D. MacDougall, Phys. Rev. 43, 768 (1933).

9. K.A. Gschneidner and V.K. Pecharsky, Annu. Rev. Mater. Sci. 30, 387 (2000).

10. K. Gschneidner and V. Pecharsky, Mater. Sci. Eng. A 287, 301 (2000).

11. V.K. Pecharsky, Phys. Rev. Lett. 78, 4494 (1997).

12. K.A. Gschneidner, Y. Mudryk, and V.K. Pecharsky, Scr. Mater. 67, 572 (2012).

13. G.V. Brown, J. Appl. Phys. 47, 3673 (1976).

14. C. Zimm, A. Jastrab, A. Sternberg, V. Pecharsky, and K. Gschneidner, Adv. Cryog. Eng. 43, 1759 (1998).

15. K.A. Gschneidner and V.K. Pecharsky, Int. J. Refrig. 31, 945 (2008).

16. A. Pecharsky, K.A. Gschneidener Jr., and V.K. Pecharsky, J. Appl. Phys. 93, 4722 (2003).

17. F.-X. Hu, B.-G. Shen, J.-R. Sun, Z.-H. Cheng, G.-H. Rao, and X.-X. Zhang, Appl. Phys. Lett. 78, 3675 (2001).

18. S. Fujieda, A. Fujita, and K. Fukamichi, Sci. Technol. Adv. Mater. 4, 339 (2003).

19. B.G. Shen, J.R. Sun, F.X. Hu, H.W. Zhang, and Z.H. Cheng, Adv. Mater. 21, 4545 (2009).

20. D. Thanh, E. Bruck, O. Tegus, J. Klaasse, D.T. Cam-Thanh, E. Brück, and T.J.Gortenmulder, J. Appl. Phys. 99, 08Q107 (2006).

21. W. Dagula, O. Tegus, B. Fuquan, L. Zhang, P.Z. Si, M. Zhang, W.S. Zhang, E. Bruck, and F.R. de Boer, IEEE Trans. Magn. 41, 2778 (2005).

22. H. Yibole, F. Guillou, L. Zhang, N.H. van Dijk, E. Bruck, N.H. van Dijk, and E. Bru¨ ck, J. Phys. D. Appl. Phys. 47, 075002 (2014).

23. R. Kainuma, Y. Imano, W. Ito, Y. Sutou, H. Morito, S. Okamoto, O. Kitakami, K. Oikawa, A. Fujita, T. Kanomata, and K. Ishida, Nature 439, 957 (2006).

24. T. Krenke, E. Duman, M. Acet, E.F. Wassermann, X. Moya, L. Mañosa, and A. Planes, Nat. Mater. 4, 450 (2005).

25. J. Liu, T. Gottschall, K.P. Skokov, J.D. Moore, and O. Gutfleisch, Nat. Mater. 11, 620 (2012).

26. P.J. Shamberger and F.S. Ohuchi, Phys. Rev. B Condens. Matter Mater. Phys., 79 (2009).

27. V. Franco, J.S. Blazquez, B. Ingale, A. Conde, and J.S. Blàzquez, Annu. Rev. Mater. Res. 42, 305 (2012).

28. J. Lyubina, J. Appl. Phys. 109, 07A902 (2011).

29. Y. Song, X. Chen, V. Dabade, T. Shield, and R. James, Nature 502, 85 (2013).

30. C. Sasso, M. Kuepferling, L. Giudici, V. Basso, and M. Pasquale, J. Appl. Phys. 103, 07B306 (2008).

31. I.D. Mayergoyz, IEEE Trans. Magn. 22, 603 (1986).

[32] J. Lyubina, R. Schaefer, N. Martin, L. Schultz, O. Gutfleisch, and R. Schäfer, Adv. Mater. 22, 3735 (2010).

[33] J. Lyubina, O. Gutfleisch, M. Richter, and M. Kuzmin, J. Magn. Magn. Mater. 321, 3571 (2009).

[34] J.C. Debnath, R. Zeng, J.H. Kim, P. Shamba, and S.X. Dou, Appl. Phys. A. Mater. Sci. Process. 106, 245 (2012).

[35] N. Dung, Z. Ou, L. Caron, L. Zhang, G. de Wijs, R. de Groot, and E. Brück, Adv. Energy Mater. 1, 1215 (2011).

[36] N.H. Dung, L. Zhang, Z.Q. Ou, E. and E. Brück, Appl. Phys. Lett. 99, 092511 (2011).

[37] N.T. Trung, Z.Q. Ou, T.J. Gortenmulder, O. Tegus, and E. Bru¨ ck, Appl. Phys. Lett. 94, 102513 (2009).

[38] J. Cui, Y. Chu, O. Famodu, Y. Furuya, J. Hattrick Simpers, R. James, A. Ludwig, S. Thienhaus, M. Wuttig, Z. Zhang, and I. Takeuchi, Nat. Mater. 5, 286 (2006).

[39] J.M. Ball and R.D. James, Arch. Ration. Mech. Anal. 100, 13 (1987).

[40] V. Basso, M. Kupferling, C. Sasso, M. LoBue, and M. Kuepferling, IEEE Trans. Magn. 44, 3177 (2008).

[41] V. Basso, C. Sasso, G. Bertotti, and M. LoBue, Int. J. Refrig. 29, 1358 (2006).

[42] V. Basso, J. Phys. Condens. Matter 23, 226004 (2011).

[43] T.D. Brown, N.M. Bruno, J.H. Chen, I. Karaman, J.H. Ross, Jr., and P.J. Shamberger, JOM 67 2123 (2015).

[44] B. Coleman and M. Gurtin, J. Chem. Phys. 47, 597 (1967).

45. V. Basso, G. Bertotti, M. LoBue, C. Sasso, V. Basso, G. Basso, M. Bertotti, and C.P. LoBue, J. Magn. Magn. Mater. 290, 654 (2005).

46. V. Basso, C. Sasso, K. Skokov, O. Gutfleisch, and V. Khovaylo, Phys. Rev. B Condens. Matter Mater. Phys., 85 (2012).

47. F. Preisach, Eur. Phys. J. A 94, 277 (1935).

48. G. Bertotti and V. Basso, J. Appl. Phys. 73, 5827 (1993).

49. V. Basso, C.P. Sasso, and M. LoBue, J. Magn. Magn. Mater. 316, 262 (2007).

50. I.D. Mayergoyz, J. Appl. Phys. 61, 3910 (1987).

51. I.D. Mayergoyz, J. Appl. Phys. 69, 4602 (1991).

52. N.M. Bruno, C. Yegin, I. Karaman, J.-H. Chen, J.H. Ross Jr, J. Liu, and J. Li, Acta Mater. 74, 66 (2005).

CHAPTER III

IMPACT OF CYCLE-HYSTERESIS INTERACTIONS ON THE PERFORMANCE OF GIANT MAGNETOCALORIC EFFECT REFRIGERANTS*

III.1 Introduction

Existing vapor-compression (VC) refrigeration and heat pump technology consumes approximately six hundred billion kWh of electricity in the US each year, roughly 25% of total yearly US electricity consumption [1, 2]. However, more than half of that energy is dissipated during thermodynamically irreversible throttling and compression of the working vapor [3], leading to typical operating efficiencies of 10%–40% of the Carnot limit [4, 5]. Furthermore, VC systems pose real environmental risk, since the vapor refrigerants used have high global warming potential [6], with vapor leak rates reported at an average of 10% yr^{-1}, and exceeding 20% yr^{-1} in some cases [7]. A developing competitor is magnetic refrigeration [8–10], which uses magneto-thermal coupling in solid-state refrigerants to pump heat without need for mechanical compressors [11]; therefore it could greatly improve operating efficiencies while also eliminating the need for harmful vapor refrigerants [12]. However, systems based on spin-lattice coupling in 'conventional' magnetic materials are not currently viable due to their relatively small magnetocaloric effect (MCE), measured as the isothermal magnetic

*Reprinted from "Impact of cycle-hysteresis interactions on the performance of giant magnetocaloric effect refrigerants" by T. D. Brown, I. Karaman, and P. J. Shamberger, 2016. *Materials Research Express*, vol. 3, pg. 1-18, Copyright [2016] by IOP publishing. © IOP Publishing Ltd. Reproduced with permission from publisher. All rights reserved. DOI 10.1088/2053-1591/3/7/074001.

entropy change, ΔS_{m}, and adiabatic temperature change, ΔT_{ad}, resulting from a change in applied magnetic field, B [13]. Pecharsky and Gschneidner first reported a giant magnetocaloric effect (GMCE) in $Gd_5(Si_xGe_{1-x})_4$ (1.5–2× larger than MCE in Gd) [14], resulting from the underlying first-order diffusion-less magneto-structural phase transition (MST) [15, 16]. Since then, researchers have investigated GMCE in several other families of materials [17], notably, MnFe-based compounds [18–20], $La(Fe_xSi_{1-x})13$and its hydrides [21–23], and NiMn-based magnetic shape memory alloys [24–28], with the expectation that the larger magnitude of GMCE could provide a viable material basis for magnetic refrigeration systems.

Despite this advantage, the solid–solid MST that drives GMCE requires additional driving force to overcome energy barriers generated as the new phase begins to form and grow [29]. This extra driving force tends to be dissipated by thermodynamically irreversible mechanisms like dislocation formation and motion, so that some portion of the input energy is lost in compensating the additional entropy generated by those processes [30].Hence, the nature of the MST imposes an intrinsic, material-level reduction in refrigeration efficiency even before compounding system-level losses like those from friction and finite heat transfer. Meaningful performance comparisons between VC and GMCE-based systems, and between competing magnetic refrigerant materials must quantitatively account for these inefficiencies [31, 32]. However, this accounting is difficult, since thermodynamically irreversible systems manifest hysteresis, meaning that their current state depends not only on the present external conditions, but also on the entire past history of states [33]. Complete experimental

characterization of such systems requires infeasibly large data sets, and although the few modeling efforts proposed that do incorporate path-dependence [34–37] have demonstrated predictive power in describing the evolution of hysteretic GMCE materials, they have had limited application towards answering the general question of how hysteresis limits the performance of a given GMCE material in refrigeration cycles.

We have recently developed a new approach that explicitly addresses path dependence through a Preisach model of rate-independent hysteresis [33] and calculates the evolution of a GMCE material's state properties along a given path in temperature–magnetic field ($T - B$) space [31]. From these path-dependent properties it is possible to calculate cyclic energy flows and various energy-conversion figures of merit, such as the fractional Carnot efficiency. Because the method couples independent parameter sets for $T - B$ cycles, phase transition hysteresis, and magnetization and entropy properties of the constituent phases, the effect of each material property on the conversion efficiency can be explored. In particular, it is now within reach to investigate previously unanswered, yet critical questions about GMCE refrigerant cycle-based performance, such as (1) which $T - B$ cycle achieves the largest temperature span and efficiency for a particular GMCE material with known hysteresis properties; (2) how large of a thermal hysteresis can be allowed for a material undergoing its optimal $T - B$ cycle, while still meeting some target metric, e.g., efficiency; (3) for a given cycle, what material properties optimize the efficiency of that cycle; and finally (4) how does the refrigeration performance of various GMCE materials compare, as simulated in physically feasible cycles that incorporate hysteresis effects? Thus, for the first time, we propose a method

to evaluate cycle-dependent GMCE material performance metrics, accounting for dissipative losses associated with first-order phase transformations.

In this manuscript, we explore the general effects of hysteresis and cycle on refrigeration performance by answering questions (1)–(3) for a model material ($Ni_{45}Co_5Mn_{36.6}In_{13.4}$ inverse-GMCE [38, 39] magnetic shape memory alloy) and a particular class of $T-B$ cycle (Ericsson) consisting of alternating iso-T and iso-B legs (Fig. III.1a).

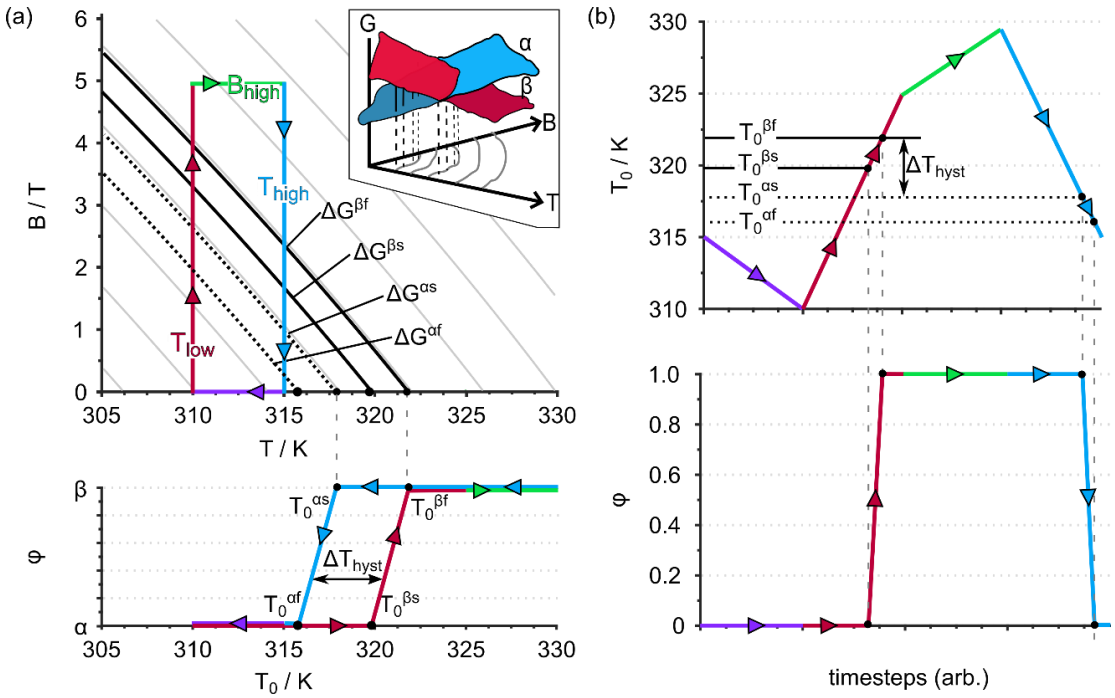

Figure III.1 Calculating path-dependent phase fraction for a specified $T-B$ path. (a) Free energy surfaces for α and β phases (inset) and corresponding constant ΔG contours (gray) plotted with Ericsson cycle (colored rectangle) in T-B space (top). Threshold contours, $\Delta G^{\alpha s,\alpha f,\beta s,\beta f}$, defining two-parameter Preisach model are also emphasized, then projected onto the $B=0$ axis to visualize the thermal hysteresis loop (bottom); (b) Corresponding evolution of T_0 (top) and ϕ (bottom) throughout the $T-B$ cycle. Reprinted with permission from [40]. © IOP Publishing Ltd 2015. DOI 10.1088/2053-1591/3/7/074001.

These cycles are of practical interest, as they are easily implemented in refrigeration systems, and resemble the conditions experienced by an infinitesimal volume of refrigerant in an active magnetic regenerator refrigeration cycle. For these cycles, we investigate the effect of a two-parameter Preisach hysteresis operator on cycle performance for a variety of conditions: First, for a fixed cycle operating between 0 and 5 T magnetic field, we determine the effect of hysteresis parameters on cycle performance, identifying three regimes of behavior depending on how the MST is induced. Next, we show that for each set of hysteresis parameters, there is a unique cycle determined by the transformation temperatures that maximizes the fractional Carnot efficiency. By comparing performance across these efficiency-optimized cycles, we demonstrate both the mechanism and extent by which hysteresis adversely affects cycle performance through a combination of decreased cooling power, increased work input, and decreased temperature span. Furthermore, by performing this analysis for cycles constrained to 5 and 1.5 T maximum field, we determine quantitative relationships between thermal hysteresis width and Carnot efficiency for each of these maximum magnetic field constraints. Finally, we conclude with some general GMCE materials design principles for mitigating performance-limiting hysteresis effects, like increasing the single-phase magnetic ordering temperatures and maximizing the difference in the single-phase saturated magnetizations.

III.2 Methods

III.2.1 Quantifying Performance

Meaningful performance and efficiency metrics are a prerequisite for developing comparisons between candidate refrigeration systems. The most commonly reported metrics for (G)MCE materials remain the magnitudes of the isothermal entropy change, ΔS_{m}, and adiabatic temperature change, ΔT_{ad}, when an applied external magnetic field is varied. Each metric completely characterizes an independent material response under some different prescribed process conditions (constant temperature, zero heat flow). However, ΔS_{m} and ΔT_{ad} are less useful for characterizing the cycle as a whole, since they do not account for the constraint imposed by cyclic conditions, that the constituent processes must return the system to its initial state. In general, the isothermal and adiabatic legs corresponding to ΔS_{m} and ΔT_{ad} have to be combined with at least one other leg in order to satisfy this cycle constraint, but additional heating and cooling can occur along these other cycle legs; ΔS_{m} and ΔT_{ad} contain no information about the material responses along these other necessary cycle legs. Other metrics, such as the refrigerant capacity (RC) [41], and refrigerant coefficients of performance (RCP_S and RCP_T [11]), have been proposed to address this issue, with each defined as a product of either ΔS_{m} or ΔT_{ad} together with a temperature range representing a potential cycle over which that metric is 'large.' However, none of these metrics account for thermodynamic irreversibility or energy dissipation (there is no explicit dependence on the hysteresis properties of the MST), so they cannot account for these phenomena in GMCE materials.

Our previous work [31] developed a framework addressing both the need to consider cycle interactions and to account for energy dissipation. There, the first and second laws of thermodynamics were used to partition the total magnetic work input to the system, $W_{\mathrm{in}} = \oint B \, \mathrm{d}M$ into two terms, $W_{\mathrm{ref}} = -\oint T \, \mathrm{d}S$ and $I = \oint T \, \mathrm{d}S_{\mathrm{irr}}$, where M is the material's total magnetization, S is its total entropy, S_{irr} is the irreversible entropy generation, and all integrals are line integrals evaluated along the closed path defining the cycle. The term W_{ref} is the portion of W_{in} which is available to lift heat between two temperature reservoirs; whereas I is work that is unavailable, due to irreversible entropy generation. The ratio, $\eta = W_{\mathrm{ref}}/W_{\mathrm{in}}$, indicates the fraction of how much energy input to the system actually generates the desired heat transfer, and is termed a 'thermodynamic efficiency.' The analysis makes no assumptions beyond that the system is returned to its initial state at the end of the $T - B$ cycle.

For this paper, we adopt metrics that are closely related to η, W_{ref}, and W_{in}, but more directly related to energy fluxes and temperature ranges, and more commonly encountered when describing refrigeration performance. These are (1) the temperature span of the cycle, $[T_{\mathrm{c}}, T_{\mathrm{h}}]$; (2) the heat absorbed from the cold reservoir per cycle, Q_{c}; (3) the required input work per cycle, W_{in}; and (4) the fractional Carnot efficiency, χ.

We define the temperature span so that T_{c}, the temperature of the cold reservoir associated with the cycle, is just slightly greater than the temperature at which the forward $\alpha \rightarrow \beta$ MST completes; similarly, the hot reservoir is at T_{h}, just slightly less than the temperature at which the reverse MST completes. This ensures, not only that the cycle transfers heat from T_{c} to T_{h} as required in refrigeration, but also that all of the

forward and reverse transformation latent heats contribute to the heat fluxes to and from the external temperature reservoirs.

This corresponds to a kind of convention where one can arrange the cycle according to the refrigerant's transformation properties, so that a greater cooling power, $Q_{\mathrm{c}} = \int_{T}^{T_{\mathrm{c}}} T \, \mathrm{d}S$, is absorbed, even at the expense of reduced $\Delta T_{\mathrm{span}} = T_{\mathrm{h}} - T_{\mathrm{c}}$.

The fractional Carnot efficiency, χ, is defined as below:

$$\chi = \frac{Q_{\mathrm{c}}}{W_{\mathrm{in}}} \left(\frac{T_{\mathrm{c}}}{T_{\mathrm{h}} - T_{\mathrm{c}}} \right)^{-1}, \qquad (III.1)$$

and quantifies how nearly the coefficient of performance of the real cycle, $\mathrm{COP} = Q_{\mathrm{c}}/W_{\mathrm{in}}$, approaches the theoretical limit of a thermodynamically reversible Carnot cycle operating over the same temperature range. As the entropy generated in the cycle increases, χ decreases from unity to zero, yielding a performance metric that rationally accounts for irreversibility.

III.2.2 Thermodynamic Modeling

The assumptions and methodology of the modeling framework used in this work are again detailed elsewhere [31], but we briefly review the main points here. All of the above metrics are calculated from the bulk magnetization, M, and entropy, S, of the refrigerant along a given $T - B$ path; determining the state of these internal properties is the main objective of the framework. Mathematically, path-dependence transforms M and S from functions into hysteresis operators, $\widehat{M}$ and $\hat{S}$, that depend recursively on their

previous values, as well as on the current (T, B) point. Furthermore, the hysteresis properties of these operators themselves generally vary throughout $T - B$ space.

Enormous simplification results from assuming (1) the state of a GMCE system at any point is a mixture of a low-temperature α phase and a high-temperature β phase, with mass fractions $1 - \phi$, and ϕ, respectively; (2) thermodynamic irreversibility and energy dissipation occurs only within the two-phase region, $0 < \phi < 1$; and (3) the details of irreversibility as characterized by hysteresis operators depends only on the MST itself and on the underlying energy barriers, but not on which external potential, T or B, is varied to overcome those barriers. Together, these assumptions imply that the complex hysteresis operators $\widehat{M}(T, B)$ and $\hat{S}(T, B)$may be reduced to a more fundamental $\hat{\phi}(\Delta G)$ hysteresis, where $\Delta G = G^{\beta} - G^{\alpha}$ is the difference in free energy, $G = U - TS - MB$, between the phases (Fig. III.1a, inset). This critical prediction is borne out by experimental observations on thermal and magnetic field hysteresis loops in bulk poly-crystalline $Ni_2(Mn,X)_2$ alloys [32, 42], which show that isothermal field variations and iso-field temperature variations corresponding to the same ΔG path each generate identical ϕ evolutions. A similar relationship is also expected for T and B hysteresis loops in oriented or single-crystal samples, so long as characterization methods account for magnetic anisotropy.

Within the framework, ΔG is calculated by creating models (developed in the following section) for the single-phase properties, M^{α}, M^{β}, S^{α}, $S^{\beta}(T, B)$ then using them to integrate Eq, 2.2 below:

$$d(\Delta G) = -\left(S^{\beta} - S^{\alpha}\right)\mathrm{d}T - \left(M^{\beta} - M^{\alpha}\right)\mathrm{d}B. \qquad (III.2)$$

This calculation is usefully visualized in Fig. III.1a, which plots the contours of constant ΔG for $Ni_{45}Co_5Mn_{36.6}In_{13.4}$ throughout the $T - B$ space, obtained as below:

$$\frac{\mathrm{d}B}{\mathrm{d}T} = -\frac{S^{\beta} - S^{\alpha}}{M^{\beta} - M^{\alpha}}, \qquad (III.3)$$

which is an extension of the magnetic Clausius–Clapeyron equation. Such contours connect $T - B$ points that correspond to the same ΔG.

The operator $\hat{\phi}(\Delta G)$ is modeled with the Preisach formalism. Preisach operators are capable of describing complex rate-independent hysteresis, but here a simpler model with fewer free parameters is used. It is assumed there are four critical ΔG contours associated with the characteristic transformation points of a diffusion-less transformation: $\Delta G^{\alpha s}$, $\Delta G^{\alpha f}$, $\Delta G^{\beta s}$, and $\Delta G^{\beta f}$ .When ΔG increases above $\Delta G^{\alpha s}$, the $\beta \rightarrow \alpha$ transition starts, and when ΔG then increases above $\Delta G^{\alpha f}$, the $\beta \rightarrow \alpha$ transition finishes (Fig. III.1a, top). Analogous evolution for the $\alpha \rightarrow \beta$ transition occurs as ΔG decreases below $\Delta G^{\beta s}$ and then $\Delta G^{\beta f}$. Furthermore, within the two-phase regions $\Delta G^{\beta f} \leq \Delta G \leq \Delta G^{\beta s}$ and $\Delta G^{\alpha s} \leq \Delta G \leq \Delta G^{\alpha f}$, ϕ increases linearly with ΔG (Fig. III.1a, bottom). This is the simplest model which accounts for the experimental observations, that (1) the MST occurs incrementally over a range of ΔG values and (2) hysteresis loops occur because the $\alpha \rightarrow \beta$ and $\beta \rightarrow \alpha$ transitions occur over distinct ranges of ΔG.

It is convenient to associate with each ΔG contour the temperature at which it intersects the $B = 0$ T axis, which defines the T_0 axis. The transition ΔG contours, $\Delta G^{\alpha,\beta;\mathrm{s,f}}$, are re-indexed in terms of this axis as $T_0^{\alpha,\beta;\mathrm{s,f}}$, which reveals the nature of the resulting hysteresis loops (Fig. III.1a, bottom). This notation is inspired by a traditional nomenclature used for thermoelastic martensites; there α may be a low-temperature Martensite and β a high-temperature Austenite, and the corresponding transition start and finish temperatures are known as M_s, M_f, A_s, and A_f. A 'magnitude of hysteresis' can be defined as $\Delta T_{\mathrm{hyst}} = T_0^{\beta\mathrm{s}} - T_0^{\alpha\mathrm{f}} = T_0^{\beta\mathrm{f}} - T_0^{\alpha\mathrm{s}}$,which is the width of the MST hysteresis loop at zero applied field (Fig. III.1a, bottom). Similarly, a 'one-way transition width' may be defined as $\Delta T_{\mathrm{elast}} = T_0^{\beta\mathrm{f}} - T_0^{\beta\mathrm{s}} = T_0^{\alpha\mathrm{f}} - T_0^{\alpha\mathrm{s}}$. As T and B vary along the cycle, various ΔG contours are crossed and T_0 evolves correspondingly (Fig. III.1b, top). The values T_0 takes on the cycle (Fig. III.1b, top) combined with the Preisach operator (Fig. III.1a, bottom) determines ϕ (Fig. III.1b, bottom). By translating the T_0 values obtained in the cycle back into their corresponding $T - B$ values, the cyclic and path-dependent evolution of ϕ throughout the $T - B$ cycle is recovered.

The system properties are computed from the rule of mixtures, assumed to hold for the overall entropy of the two-phase mixture, as well as its magnetization above saturation magnetization, yielding the equations:

$$M = (1 - \phi)M^{\alpha} + \phi M^{\beta}, \qquad (III.4)$$

$$S = (1 - \phi)S^{\alpha} + \phi S^{\beta}. \qquad (III.5)$$

III.2.3 Material Model Parameterization

Models for the single-phase material properties are required for the calculations in (2.2), (2.3), and (2.4). In this paper, mean-field models for $M^{\alpha,\beta}(T,B)$ and $S^{\alpha,\beta}(T,B)$ are parameterized using fitting procedures to the experimental data from the $Ni_{45}Co_5Mn_{36.6}In_{13.4}$ alloy (see appendix A).

The single-phase magnetization is modeled with Curie–Weiss molecular field theory, which approximates the effect of a neighborhood of exchange-coupled magnetic moments on an individual moment using a Weiss mean field. The relevant model parameters are the saturated magnetization, M_s, Curie ordering temperature, T_C, and total angular momentum per moment, j, of each phase. Defining the normalized magnetization $\widetilde{M}$ and temperature $\tilde{T}$ by dividing M and T by M_s and T_C, respectively, the Curie–Weiss model is obtained by solving the below nonlinear system of equations:

$$\widetilde{M}(T,B;x) = \bar{B}_j(x), \tag{III.6}$$

$$\widetilde{M}(T,B;x) = \left(\frac{j+1}{3j}\tilde{T}\right)x - \left(\frac{\mu_\mathrm{B} g(j+1)}{3k_\mathrm{B}T_\mathrm{C}}\right)B, \tag{III.7}$$

where μ_B is the Bohr magneton, k_B is the Boltzmann constant, and g is a constant very nearly equal to two; $\bar{B}_j(x)$ is the jth Brillouin function. For the $(Ni,Co)_2(Mn,In)_2$ alloy model used here, $M_\mathrm{s}^\alpha = 12$ A m^{2}kg^{-1} , $M_\mathrm{s}^\beta = 155$ A m^{2}kg^{-1}, $T_\mathrm{C}^\alpha = 70$ K, $T_\mathrm{C}^\beta = 388$ K, $j^\alpha = 18.5$, and $j^\beta = 2.5$.

The single-phase entropy at zero field is modeled with Debye theory, which approximates the heat-carrying phonons in the material as a gas of vibrations in an isotropic lattice of harmonic potentials. Electronic contributions to the heat capacity are assumed negligible. The relevant model parameters are just the Debye temperatures, T_{D}, of each phase. Defining an inverse normalized temperature parameter $\tilde{T}$ by dividing T_{D} by T, the Debye model yields the zero-field entropy, $S(T,0)$, as below:

$$S(T,0) = \frac{9R}{T_{\mathrm{D}}} \int_0^{\tilde{T}} \left(\tilde{T}''\right)^2 \int_0^{\tilde{T}''} \frac{\left(\widetilde{T'}\right)^4 \exp \widetilde{T'}}{\left(\exp \widetilde{T'} - 1\right)^2} \, \mathrm{d}\tilde{T}' \, \mathrm{d}\tilde{T}'' , \qquad (III.8)$$

where R is the ideal gas constant. At non-zero fields, the total entropy for each phase is taken to be $S(T,B) = S(T,0) + \Delta S(T,B)$, i.e., the sum of the Debye entropy and an independent magnetic entropy term given by the Maxwell relation as below:

$$\Delta S(T,B) = \frac{\mathrm{d}}{\mathrm{d}T} \int_0^B M(T',B') \, \mathrm{d}B' . \qquad (III.9)$$

For the NiCoMnIn alloy, $T_{\mathrm{D}}^{\alpha} = 336$ K and $T_{\mathrm{D}}^{\alpha} = 309$ K.

Finally, the experimental magnetization data has been used to estimate the forward zero-field MST temperature as $T_0^{\beta} = 321.8$ K. All of these parameters describing $M^{\alpha,\beta}$ and $S^{\alpha,\beta}(T,B)$ are fixed for the remainder of this paper. In contrast, we vary those parameters describing the hysteretic phase transition behavior

$(\Delta T_{\mathrm{hyst}}, \Delta T_{\mathrm{elast}})$ and the refrigeration cycle $\left(T_{\mathrm{low}}, T_{\mathrm{high}}, B_{\mathrm{low}}, B_{\mathrm{high}}\right)$ on the material behavior within the cycle, and on the resulting cycle performance metrics.

III.3 Results

The modeling method described in the previous section has been used to investigate (1) how the degree and form of transformation hysteresis (described by ΔT_{hyst}, $\Delta T_{\mathrm{elast}}$) interactwith a particular cycle to affect refrigerant performance (measured by $[T_{\mathrm{c}}, T_{\mathrm{h}}]$, Q_{c}, W_{in}, χ); (2) to what extent these effects are mediated by varying the absolute minimum and maximum T and B of the cycle $\left(T_{\mathrm{low}}, T_{\mathrm{high}}, B_{\mathrm{low}}, B_{\mathrm{high}}\right)$; and (3) the implications of these factors for the maximum efficiency, χ, attainable with hysteretic GMCE materials.

III.3.1 Effects of Hysteresis on a Fixed Cycle

To begin understanding the effects of hysteresis on the performance of the Ericsson cycle class, we select an arbitrary fixed cycle operating between $B_{\mathrm{low}} = 0$ T and $B_{\mathrm{high}} = 5$ T, and between $T_{\mathrm{low}} = 310$ K and $T_{\mathrm{high}} = 315$ K (Fig. III.2, colored rectangle), and then examine how the system evolution and performance metrics vary with hysteresis magnitude, 0 K $\leq \Delta T_{\mathrm{hyst}} \leq$ 10 K. These chosen parameters reflect that (1) fields of 5 T are readily attainable in small volumes of superconducting apparatus routinely used to characterize GMCE materials; (2) for room temperature refrigeration, the cycle temperature range should be near 300 K and near the MST transformation temperatures; and (3) the hysteresis values cover the range from an ideal anhysteretic system (0 K hysteresis) to the order of those obtained in similar material systems that

have undergone treatments specifically to reduce solid–solid phase transition hysteresis (10 K hysteresis) [43–46].

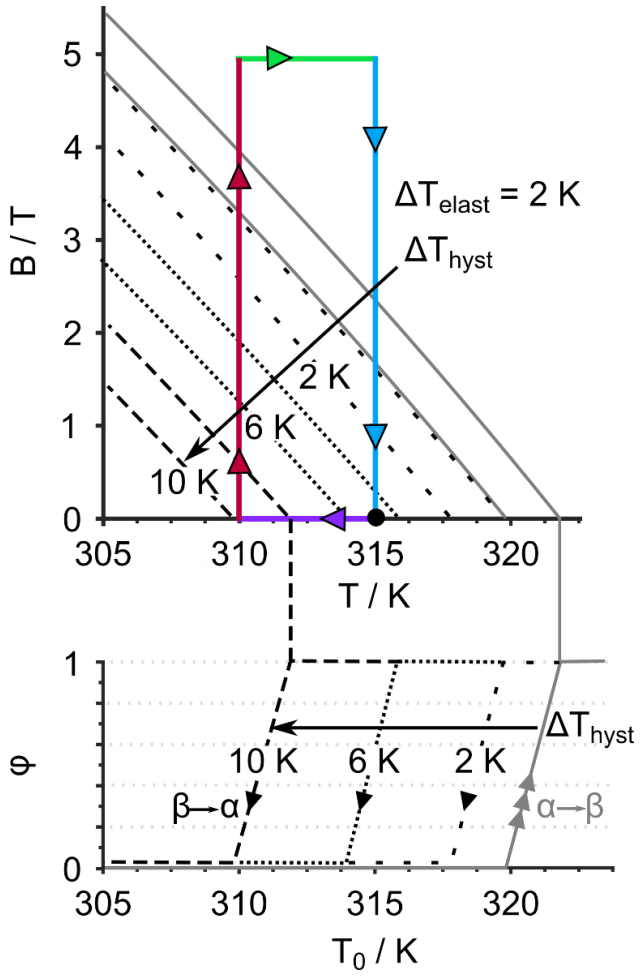

Figure III.2 Visualization of increasing hysteresis within a fixed Ericsson cycle. Fixed $\Delta T_{\mathrm{elast}}$ = 2 K and ΔT_{hyst} = {2 K, 6 K, 10 K}. As hysteresis increases, the difference in free energy between the α→β transition (gray) and the β→α transition (black) increases. Reprinted with permission from [40]. © IOP Publishing Ltd 2015. DOI 10.1088/2053-1591/3/7/074001.

First consider the case for the one-way transition width fixed at $\Delta T_{\mathrm{elast}} = 2$ K, as the magnitude of hysteresis, ΔT_{hyst}, increases from 0 to 10 K.

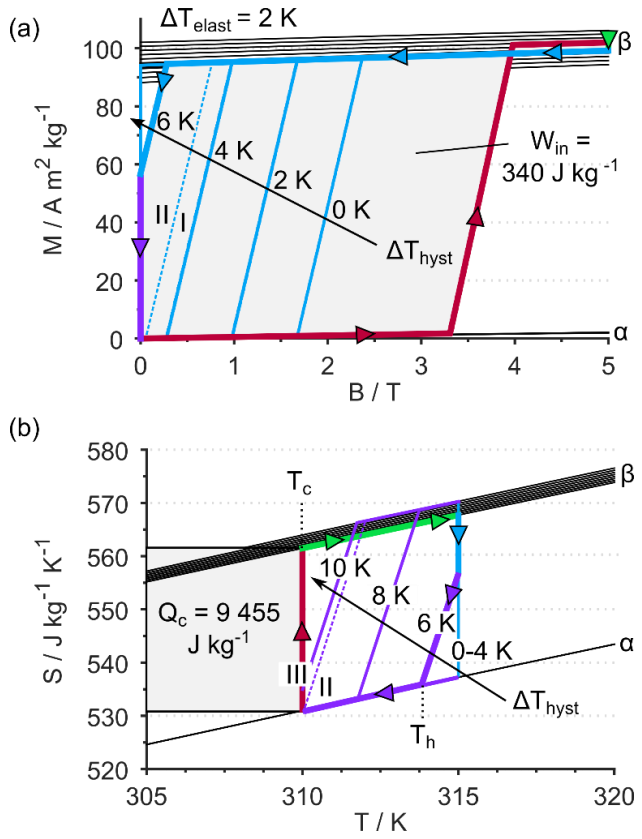

Figure III.3 Effects of ΔT_{hyst} on cyclic magnetothermal properties. (a) $M(B)$ and (b) $S(T)$ evolution for $\Delta T_{\mathrm{elast}}$ =22 K in a given cycle. Colored cycle legs correspond with those in figures 1 and 2.Calculation of the performance parameters, Q_{c}, W_{in}, $[T_{\mathrm{c}}, T_{\mathrm{h}}]$ are shown by shading for ΔT_{hyst} = 6 K. Thin dashed lines demarcate the boundaries between regimes I/II and II/III described in the text. Reprinted with permission from [40]. © IOP Publishing Ltd 2015. DOI 10.1088/2053-1591/3/7/074001.

As hysteresis increases, the $\beta \rightarrow \alpha$ transition is shifted to higher T / B driving force (lower T_0) relative to the $\alpha \rightarrow \beta$ transition, so that there is increased separation between the corresponding ΔG contours in $T - B$ space (figure 2, top) and T_0 space (bottom). This in turn changes the resulting phase evolution, $\phi(T, B)$, leading to evident differences in the evolution of $M(B)$ and $S(T)$ (Fig. III.3a and Fig. III.b, respectively), and in the corresponding performance metrics as well, as a function of hysteresis. For clarity, we show graphically with shading in figure 3 how performance metrics, Q_{c}, W_{in},

$[T_c, T_h]$ are calculated for $\Delta T_{hyst} = 6$ K, with the corresponding value marked by black diamonds in Fig. III.4.

Interestingly, there are three regimes of behavior when considering how the $M(B)$ and $S(T)$ evolution changes as ΔT_{hyst} increases (Fig. III.3). In regime I, hysteresis is relatively small, 0 K $\leq \Delta T_{hyst} \leq$ 4.7 K, and has the effect of stabilizing the β phase, so that a greater B field removal is required to induce the $\beta \rightarrow \alpha$ transition. This increases the area enclosed by the $M(B)$ curve, and so the net input magnetic work increases. At the same time, there are no effects on the $S(T)$ evolution, and $T_c = 310$ K, $T_h = 315$ K, and $Q_c = 9.445$ kJ kg^{-1} are all constant. Thus in regime I, hysteresis increases the cost in net magnetic work required by the cycle for a given cooling power and temperature span.

In regime II, 4.7 K $\leq \Delta T_{hyst} \leq$ 9.8 K, the driving force cost to overcome the stabilization of β becomes so large that the $\beta \rightarrow \alpha$ transition cannot be completed by the B removal from 5 to 0 T alone. In this case, additional driving force is required to complete the transition in the form of additional cooling, thus decreasing T_h relative to $T_c$and hence decreasing the temperature span. At the same time, the $M(B)$ curve encloses nearly all the area between M^{α} and M^{β} from 0 to 5 T, and the input work saturates at about 340 J kg^{-1} (Fig. 3a). Hence in regime II, hysteresis decreases the temperature span of the cycle for a given input work cost and cooling power. However, the hysteretic driving force cost is still low enough that the combination of B removal and T cooling is able to induce the full $\beta \rightarrow \alpha$ transition. The material still undergoes its

full transformation range, $0 \leq \phi \leq 1$, within each cycle, and its full latent heat is able to contribute to the potential cooling power.

In regime III, $\Delta T_{\mathrm{hyst}} > 9.8$ K, the hysteretic driving force cost is so large that even with the full B removal and maximum T cooling to the cycle minimum, 310 K (Fig. 3b), there is not enough driving force to complete the $\beta \rightarrow \alpha$ transition. In this case, only a partial transition can be induced and only a fraction of its latent heat is accessible to the cycle, so the cycle cooling power drops off rapidly. At the same time, the input work remains saturated, and the temperature span is constant at 0 K. Hence within regime III, the effect of hysteresis is to decrease the cooling power for a given input work cost and (zero) temperature span. Because zero temperature span implies that the refrigerator interior is as warm as the exterior environment, this regime is of little practical use. All of these trends and the three regimes of behavior can be confirmed in Fig. III.4, which directly plots the performance metrics as a function of ΔT_{hyst}. By examining the cycles in $T - B$ space (Fig. III.2) as a function of ΔT_{hyst}, we have determined that the boundaries between regimes I and II, and regimes II and III, occur at $\Delta T_{\mathrm{hyst}} = 4.7$ K and $\Delta T_{\mathrm{hyst}} = 9.8$ K, respectively. These values correspond precisely to the conditions where the MST changes from completely B-induced to at least partially T-induced ($T_0^{\alpha \mathrm{f}} = T_{\mathrm{high}}$), and where the MST changes from a complete to partial phase transition ($T_0^{\alpha \mathrm{f}} = T_{\mathrm{low}}$), as expected.

Having considered how performance metrics vary with ΔT_{hyst} for $\Delta T_{\mathrm{elast}} = 2$ K, we repeat the analysis for 0 K $\leq \Delta T_{\mathrm{elast}} \leq 8$ K.

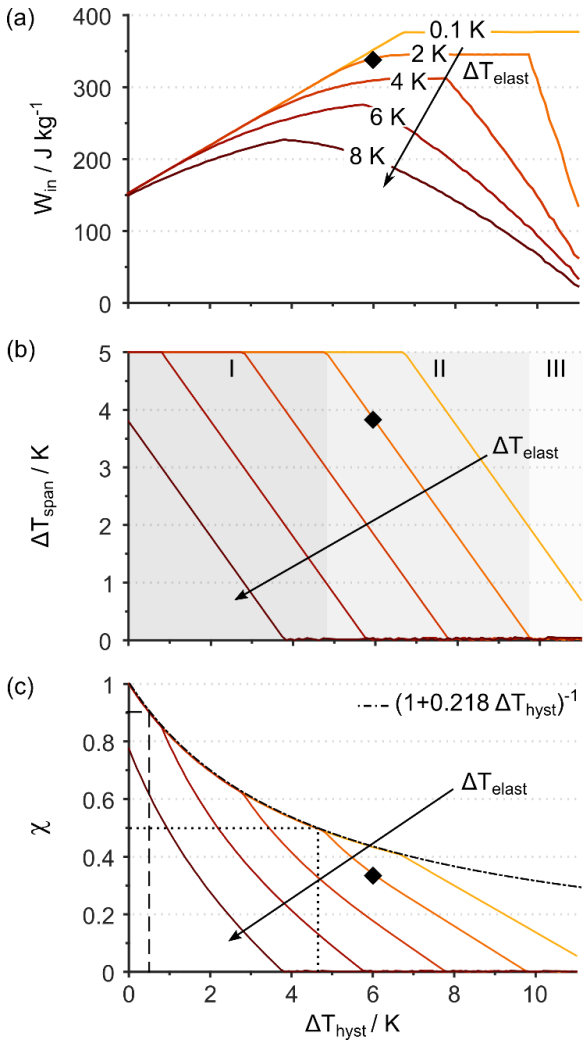

Figure III.4 Effects of hysteresis parameter on refrigeration metrics. Impact of ΔT_{hyst} and ΔT_{elast} on (a)W_{in}, (b) ΔT_{span}, and (c)χ for a fixed Ericsson cycle. Black diamonds mark performance metric values for the $\Delta T_{elast} = 2$ K, $\Delta T_{hyst} = 6$ K cycle emphasized by shading in Fig. III.3. Regimes of behavior for $\Delta T_{elast} = 2$ K are also emphasized in (b). Reprinted with permission from [40]. © IOP Publishing Ltd 2015. DOI 10.1088/2053-1591/3/7/074001.

The qualitative dependence is very similar for all values of ΔT_{elast}, with the three regimes of behavior in which either W_{in} increases, ΔT_{span} decreases, or Q_c decreases as hysteresis increases (Fig. III.4). As a result, χ decreases monotonically with ΔT_{hyst} for all values of ΔT_{elast}. Again, these regimes of behavior are separated according to

whether the full MST is accessible to the cycle, and if so, whether it may be entirely induced by isothermally removing B. The qualitative trends in $\chi(\Delta T_{\mathrm{hyst}})$ within each regime can be determined by considering the behavior of the other performance metrics in each regime. By factoring the constant $a = Q_{\mathrm{c}}/T_{\mathrm{c}}$ out from (2.1),we obtain:

$$\chi = a\left(\frac{T_{\mathrm{h}} - T_{\mathrm{c}}}{W_{\mathrm{in}}}\right). \qquad (III.10)$$

In regime I, W_{in} increases approximately linearly with ΔT_{hyst}, and χ is of the form $(1 + c\Delta T_{\mathrm{hyst}})^{-1}$. In regime II, T_{h} decreases linearly with ΔT_{hyst}, while for small $\Delta T_{\mathrm{elast}}$, W_{in} is relatively constant, so the decrease in χ with increasing ΔT_{hyst} is approximately linear. For larger $\Delta T_{\mathrm{elast}}$, W_{in} actually increases significantly with ΔT_{hyst} in regime II, and so $\chi(\Delta T_{\mathrm{hyst}})$ is more complicated, but still tends towards decreasing linearly. In regime III, the temperature span is uniformly zero, and so is the fractional Carnot efficiency (Fig. III.4c).

Although qualitatively similar, the trends in performance metrics as a function of ΔT_{hyst} for different values of transition sharpness, $\Delta T_{\mathrm{elast}}$, are quantitatively different. For a given hysteresis magnitude, ΔT_{hyst}, as $\Delta T_{\mathrm{elast}}$ increases, the cycle input work decreases and competes with a simultaneous decrease in the temperature span (Fig. III.4a and Fig. III.4b). This arises from two competing effects, (1) the broader $\alpha \rightarrow \beta$ transition begins at a smaller B field, so both the $M(B)$ enclosed area and W_{in} decrease, and (2) within regime II, the broader $\beta \rightarrow \alpha$ transition requires more T cooling to

complete, decreasing both T_{h} and ΔT_{span}. However, the adverse decrease in temperature span dominates the decrease in input work (e.g., at 6.7 K hysteresis, an increase in $\Delta T_{\mathrm{elast}}$ from 0.1 to 2 K decreases ΔT_{span} by 40%; whereas W_{in} only decreases by 7%), so $\chi(\Delta T_{\mathrm{elast}})$ also decreases monotonically for all hysteresis widths.

In summary, as hysteresis increases, it always increases the driving force cost required to cyclically induce the forward and reverse phase transitions. For a fixed cycle, the effect of this increasing hysteretic driving force cost on the performance metrics differs, according to regimes of behavior determined by the interaction of the cycle with the hysteretic MST: whether the complete MST may be induced by B alone, and whether the complete or only a partial MST is accessible. However, in every regime, either the work input, W_{in}, or the cooling power, Q_{c}, or the temperature span, ΔT_{span}, increases or decreases adversely, and the fractional Carnot efficiency, χ, decreases in every regime. Also, χ decreases rapidly with both ΔT_{hyst} and $\Delta T_{\mathrm{elast}}$, due to them decreasing ΔT_{span}, which dominates the behavior.

III.3.2 Optimized Ericsson Cycles for NiCoMnIn

We have shown there is a complex interplay between a GMCE material's hysteretic behavior and specific cycle parameters, which determines the effect of hysteresis on the cycle performance metrics. Therefore it is of interest to investigate whether cycles that optimize refrigerant performance for a given hysteresis behavior exist, and what their properties are.

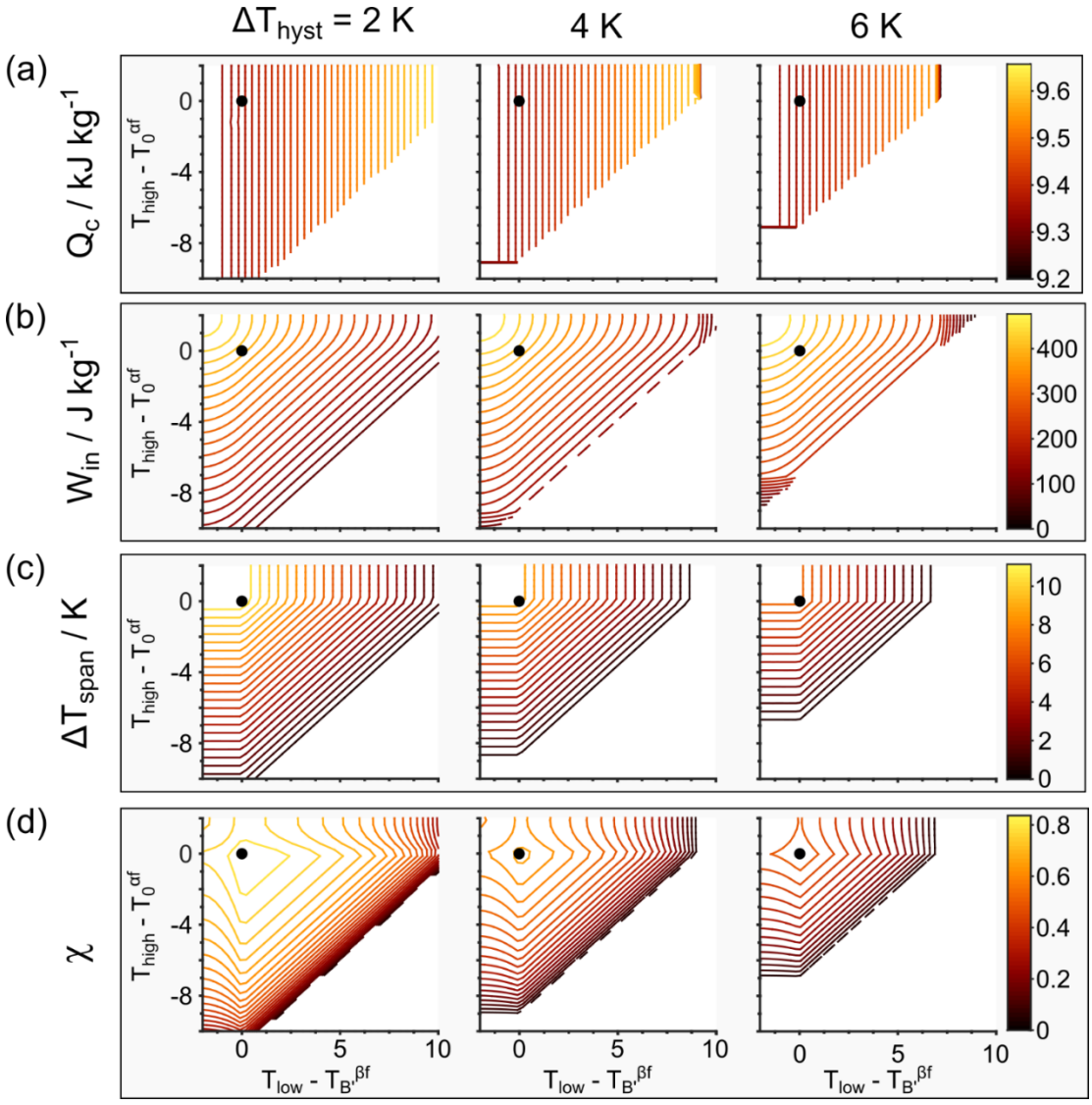

Figure III.5 Contour plots of cycle performance parameters. (a) Q_c, (b)W_{in}, (c) ΔT_{span}, and (d) χ, plotted in contour plots as functions of T_{low} and T_{high}, for constant $\Delta T_{elast} = 2$ K. ΔT_{hyst} increases along rows from left to right. Black dots mark the performance metrics evaluated at the unique cycle optimizing χ, which are plotted in Fig. III.7. Reprinted with permission from [40]. © IOP Publishing Ltd 2015. DOI 10.1088/2053-1591/3/7/074001.

To explore this possibility, and to partially decouple the combined effects of hysteresis and cycle choice on cycle performance, we have fixed the hysteresis parameters (ΔT_{hyst}, ΔT_{elast}), and explored the variation of the cooling power, input

work, temperature span, and efficiency with the cycle parameters (T_{low}, T_{high}) for cycles operating between 0 and 5 T. This analysis has been repeated for many different combinations of hysteresis parameters; a subset of these data are shown in the matrix of contour plots in Fig. III.5, for $\Delta T_{\mathrm{elast}} = 2$ K and ΔT_{hyst} ={2 K, 4 K, 6 K}(columns, left to right). Additionally, in analogy to $T_0^{\beta \mathrm{f}}$, we define the parameter, $T_{B'}^{\beta \mathrm{f}}$: where the former is the temperature of intersection of the $\Delta G^{\beta \mathrm{f}}$ contour with $B = 0$, the latter is its intersection with $B = B_{\mathrm{high}}$ (Fig. III.6). Then the contour plot axes in Fig. III.5 have been normalized to ($T_{\mathrm{low}} - T_{B'}^{\beta \mathrm{f}}, T_{\mathrm{high}} - T_0^{\alpha \mathrm{f}}$); this shifts our consideration from the absolute positions of T_{low} and T_{high}, to their positions relative to the MST transformation finish temperatures, which allows a more ready comparison between contour plots with different hysteresis parameters. The white space in the Fig. III.5 plots represents undefined cycle parameters, corresponding to cases where $T_{\mathrm{low}} \geq T_{\mathrm{high}}$. Cycles for which only the conventional MCEplays a role, and the alloy is trapped in either its pure α phase ($T_{\mathrm{high}} \leq T_{B'}^{\beta \mathrm{s}}$) or its pure β phase ($T_{\mathrm{low}} \geq T_0^{\alpha \mathrm{s}}$) are similarly excluded from the computation domain.

The cooling power, Q_{c}, increases linearly with T_{low}, but is independent of T_{high}; this is true even as the hysteresis magnitude increases (Fig. III.5a). This makes sense, as in our calculations, Q_{c} is approximated by $T_{\mathrm{low}}\, \Delta S_{\mathrm{m}}$ (independent of T_{high}), and for GMCE materials, ΔS_{m} is nearly independent of temperature.

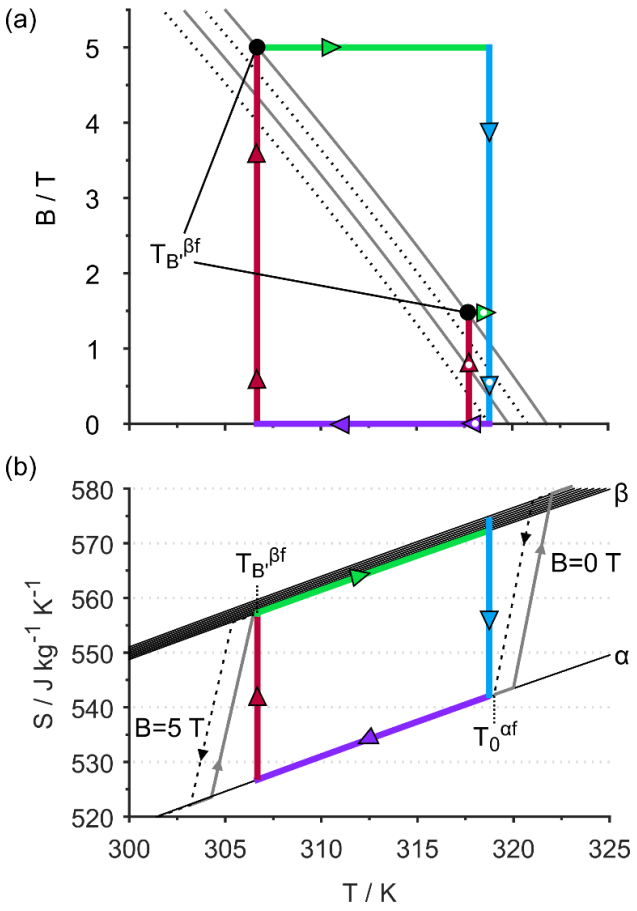

Figure III.6 Efficiency-optimized cycles. Unique Ericsson cycles that maximize χ for $\Delta T_{elast} = 2$ K and $\Delta T_{hyst} = 1$ K. χ-optimized cycle for 5 T maximum magnetic field is shown in (a) $T - B$ space (colored triangles) along with (b) the corresponding S(T) evolution. For comparison, the χ-optimized cycle for 1.5 T is also shown in (a) (triangles with white dots). Reprinted with permission from [40]. © IOP Publishing Ltd 2015. DOI 10.1088/2053-1591/3/7/074001.

However, at some point, T_{low} increases to the point that only a partial MST is possible (i.e., regime III behavior), and the cooling power drops rapidly to zero. At larger hysteresis magnitudes, this drop-off occurs at smaller T_{low}, and the area of the plot with non-zero Q_c representing feasible GMCE refrigeration cycles is smaller. On the other hand, the work input, W_{in}, increases as either T_{low}, is decreased or T_{high}, is increased, so that their difference is larger (Fig. 5b). This is consistent with the fact that

there is a work cost associated with generating the temperature difference, $T_{\mathrm{high}} - T_{\mathrm{low}}$, as well as for generating the cooling power, Q_{c}, which is consistent with Wood and Potter's association of RC $= \Delta S \Delta T$ with refrigeration work [41]. At larger hysteresis magnitudes, the required work input is slightly larger, varying at most by about 4%from 2 to 6 K hysteresis width, for corresponding points in the plots. The effective temperature span of the cycle, ΔT_{span}, increases as either T_{low} decreases or as T_{high} increases (Fig. 5c); this is unsurprising, as there is a correspondence between the temperature extremes experienced by the refrigerant, $[T_{\mathrm{low}}, T_{\mathrm{high}}]$, and the potential range of temperatures for the cold and hot reservoirs between which heat is effectively transported, $[T_c, T_{\mathrm{h}}]$.However, as stated previously, we assume that the temperatures associated with the MST also control the potential range of $[T_{\mathrm{c}}, T_{\mathrm{h}}]$due to them determining the temperatures at which the latent heat of the forward and reverse MSTs may be absorbed or expelled. This implies the below equations:

$$T_{\mathrm{c}} = \max\left(T_{\mathrm{low}}, T_{B'}^{\beta \mathrm{f}}\right), \qquad (III.11)$$

$$T_{\mathrm{h}} = \max\left(T_{\mathrm{high}}, T_{0}^{\alpha \mathrm{f}}\right). \qquad (III.12)$$

As hysteresis increases, the temperature span decreases rapidly, at most by 33% from 2 K to 6 K hysteresis.

Trends in Q_c, W_{in}, and ΔT_{span} interact, resulting in a unique Ericsson refrigeration cycle between 0 and 5 T that maximizes the fractional Carnot efficiency, χ (Fig. 5d). This occurs for the below conditions:

$$T_{low} = T_c = T_{B'}^{\beta f}, \qquad (III.13)$$

$$T_{high} = T_h = T_0^{\alpha f}. \qquad (III.14)$$

The unique cycle satisfying this condition is shown for $\Delta T_{elast} = 2$ K and $\Delta T_{hyst} = 1$ K in Fig. III.6. In general, the separate parameters Q_c, W_{in}, and ΔT_{span} will have their optima for different cycles. However, when considered together, the variation in Q_c and W_{in} with (T_{low}, T_{high}) is much smaller than for ΔT_{span}; hence, the effect of temperature span dominates and $\chi(T_{low}, T_{high})$ has its maximum at a cycle with maximum ΔT_{span}. Seen in another light, the cycle defined by (3.3) is such that the temperature span of the cycle, $T_h - T_c$, is the largest possible consistent with the forward and reverse MSTs being completely field induced. This is the same condition defining the boundary between regime I and regime II behavior, for which the detrimental undercooling effects that reduce ΔT_{span} and χ are avoided. Again, as the hysteresis magnitude increases, the efficiency decreases rapidly, at most by 55% from 2 to 6 K hysteresis.

Returning to the question posed at this section's beginning, it is clear that for every value of hysteresis magnitude, ΔT_{hyst}, there is a unique Ericsson cycle between 0 and 5 T that maximizes refrigeration performance, as measured by the fractional Carnot efficiency, χ. Furthermore, analysis of additional data (see appendix B) demonstrates that this is true for every combination of hysteresis parameters (ΔT_{hyst}, ΔT_{elast}) and for

other maximum field constraints as well; in each case there is a cycle that optimizes χ, and it is described simply by (3.3) (Fig. III.6, white dotted triangles). Furthermore, the analysis has shown how refrigerator performance may be improved by varying the cycle parameters, with important implications for GMCE refrigeration system design. For example, the fixed cycle considered in section 3.1 ($T_{\mathrm{low}} = 310$ K, $T_{\mathrm{high}} = 315$ K), with $\Delta T_{\mathrm{hyst}} = 2$ K and $\Delta T_{\mathrm{elast}} = 2$ K, had a temperature span of $\Delta T_{\mathrm{span}} = 5$ K and an efficiency of $\chi = 0.75$; whereas by using the same material in a cycle with $T_{\mathrm{low}} = 306.7$ K and $T_{\mathrm{high}} = 317.8$ K, $\Delta T_{\mathrm{span}} = 11.1$ K and $\chi = 0.82$ are significantly improved.

III.3.3 Target Hysteresis for Optimized Ericsson Cycles

The previous section decoupled the effects of cycle choice and transformation hysteresis on the performance of potential GMCE refrigeration cycles, establishing (1) the partial dependence of performance metrics on cycle parameters, for fixed hysteresis parameters, and (2) the conditions (3.3) that describe, for each combination of hysteresis parameters (ΔT_{hyst}, $\Delta T_{\mathrm{elast}}$) and each maximum field constraint, B_{high}, the unique Ericsson cycle which optimizes the fractional Carnot efficiency, χ. By comparing the performance metrics for these χ-optimized cycles, the hysteresis effects themselves are isolated, enabling a meaningful specification of, e.g., target hysteresis parameters for a given GMCE material under the best-case scenario, for which it undergoes its optimal Ericsson cycle.

To this end, Fig. III.7 plots the performance metrics, W_{in}, ΔT_{span}, and χ as functions of the hysteresis parameters (ΔT_{hyst}, $\Delta T_{\mathrm{elast}}$), for only those χ-optimized

Ericsson cycles between 0 and 5 T (Fig. III.5, black circles). Throughout the range of hysteresis parameters considered, $Q_c = 9.63$ kJ kg^{-1} and $T_c = 306.7$ K are constant. As hysteresis increases, the input work cost increases slightly (8% over the total range), and the resulting temperature span rapidly decreases by 1 K per each 1 K increase in ΔT_{hyst}.

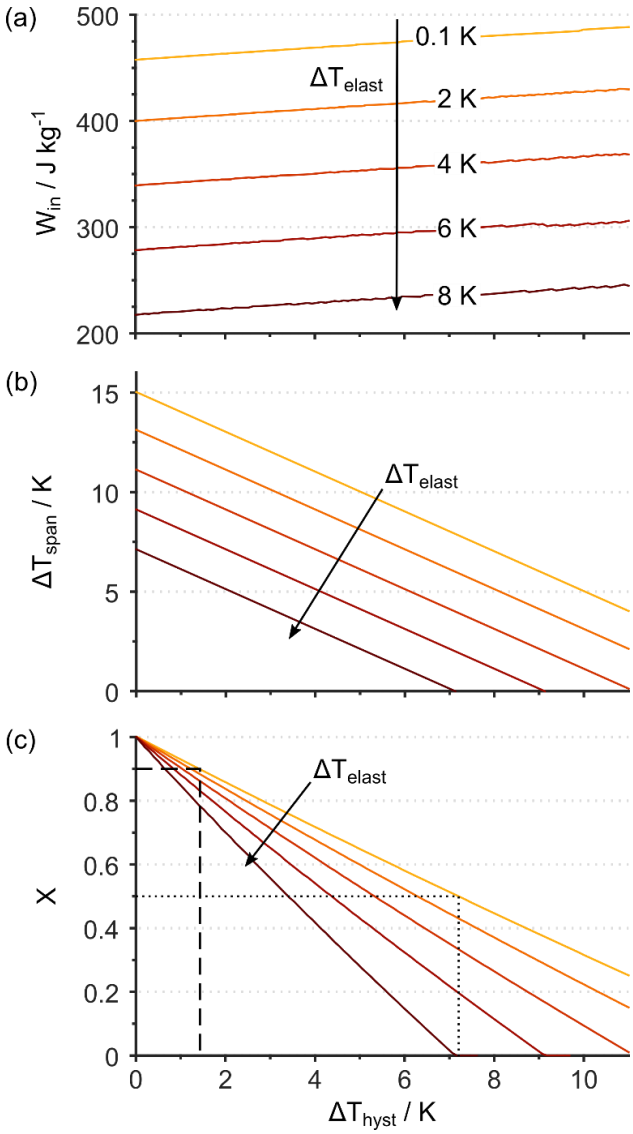

Figure III.7 Effect of hysteresis on refrigeration metrics in 5 T optimized cycles. Effects of hysteresis parameters ΔT_{hyst} and ΔT_{elast} on (a) W_{in}, (b) ΔT_{span}, and (c) χ for χ-optimized Ericsson cycles between 0 and 5 T fields. Reprinted with permission from [40]. © IOP Publishing Ltd 2015. DOI 10.1088/2053-1591/3/7/074001.

As the one-way transition width increases, the input work cost decreases significantly, but the temperature span also rapidly decreases, again decreasing 1 K per each 1 K increase in $\Delta T_{\mathrm{elast}}$. In either case, the variation in ΔT_{span} with the hysteresis parameters dominates the variation in Q_{c} or W_{in}, so that the fractional Carnot efficiency decreases monotonically as $\chi\left(\Delta T_{\mathrm{hyst}}\right) = -m\Delta T_{\mathrm{hyst}}$,with the slope of decrease, $\mid m \mid$, being greater for larger one-way transition widths, $\Delta T_{\mathrm{elast}}$. Therefore, even when controlling for cycle effects through comparing only cycles with maximum efficiency, the effect of hysteresis is to always adversely affect the performance of the cycle as measured by cooling power, work input, temperature span, and efficiency. The effect of a non-zero one-way transition width is to exacerbate the hysteresis effects, so that the hysteresis effects are magnified for larger one-way transition widths. In order to obtain the best refrigeration performance from the model GMCE material in Ericsson cycles, the MST hysteresis should be small, and the MST itself should be sharp. Using 50% (dotted line) and 90% (dashed line) fractional Carnot efficiencies as reasonable benchmarks for GMCE performance, we see that for 5 T maximum field constraint and $\Delta T_{\mathrm{elast}} = 0$ K, the hysteresis of the model alloy can be at most 7.2 K or 1.4 K, respectively. In general, the one-way transition widths are much greater than zero, in which case the target hysteresis values are even lower. For example, for $\Delta T_{\mathrm{elast}} \leq 8$ K and just 2 K hysteresis, the maximum possible fractional Carnot efficiencies are limited to $0.75 \leq \chi \leq 0.88$.

Finally, this same optimized-cycle analysis may be performed for Ericsson cycles constrained between 0 and 1.5 T, representing the current upper limit for fields produced by ceramic permanent magnets (Fig. III.8).

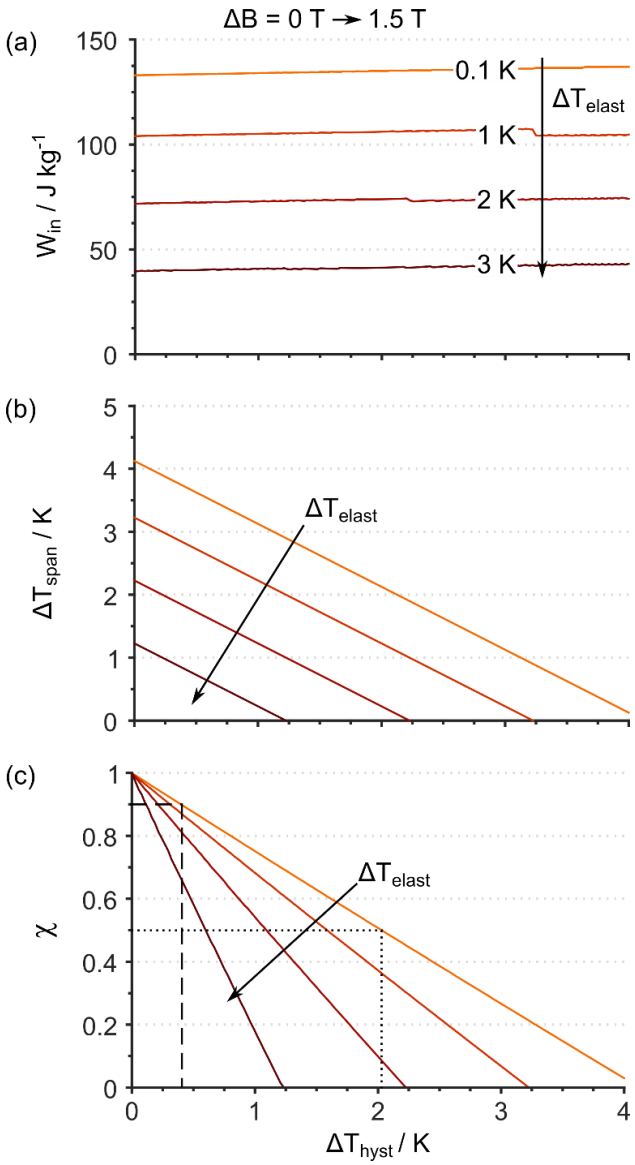

Figure III.8 Effect of hysteresis on refrigeration metrics in 1.5 T optimized cycles. Effects of hysteresis parameters ΔT_{hyst} and ΔT_{elast} on (a) W_{in}, (b) ΔT_{span}, and (c) χ for χ-optimized Ericsson cycles between 0 and 1.5 T fields. Reprinted with permission from [40]. © IOP Publishing Ltd 2015. DOI 10.1088/2053-1591/3/7/074001.

The same trends hold true for the 1.5 T maximum-field case as for the 5 T case: the cooling power is approximately constant across the range, the work input increases slightly with ΔT_{hyst} and decreases with $\Delta T_{\mathrm{elast}}$, and the temperature span decreases by 1 K for every 1 K increase in either ΔT_{hyst} or $\Delta T_{\mathrm{elast}}$. Again, the combined effects on χ are that the fractional Carnot efficiency decreases rapidly with increased hysteresis, with the slope of decrease being significantly greater for larger one-way transition widths. Furthermore, the rates of decrease in χ with the hysteresis parameters are significantly larger for the cycles operating between 0 and 1.5 T than for those between 0 and 5 T. Once again using the 50% and 90% efficiency benchmarks, the target hysteresis values for these cycles can be estimated as not more than 2.03 K or 0.40 K respectively. For $\Delta T_{\mathrm{elast}} \leq 3$ K and just 2 K hysteresis, the maximum obtainable fractional Carnot efficiencies are $0.0 \leq \chi \leq 0.5$.

This increased sensitivity of performance metrics to hysteresis parameters at lower ΔB is not surprising, since although the maximum temperature span scales down with B as $(\Delta M/\Delta S)\Delta B$, the hysteresis penalties do not scale with B. Because χ-optimized cycles operate in the region for which the complete $\alpha \rightarrow \beta$ MST is induced by applying magnetic field at $T_{\mathrm{c}} = T_{B'}^{\beta \mathrm{f}}$, and W_{in} is saturated at its maximum value, the values of all the performance metrics for χ-optimized Ericsson cycles may be written approximately as below:

$$Q_{\mathrm{c}} \approx T_{B'}^{\beta \mathrm{f}} \, \Delta S, \qquad (III.15)$$

$$W_{\text{in}} \approx \Delta M \Delta B - \Delta S \Delta T_{\text{elast}}, \qquad (III.16)$$

$$\Delta T_{\text{span}} \approx \left(\frac{\Delta M}{\Delta S}\right) \Delta B - \left(\Delta T_{\text{hyst}} + \Delta T_{\text{elast}}\right), \qquad (III.17)$$

$$\chi \approx \left[1 - \frac{\Delta S\left(\Delta T_{\text{hyst}} + \Delta T_{\text{elast}}\right)}{\Delta M \Delta B}\right]\left(1 - \frac{\Delta S \Delta T_{\text{elast}}}{\Delta M \Delta B}\right)^{-1} . \qquad (III.18)$$

These approximations hold insofar as the Clausius–Clapeyron slopes, $\Delta M/\Delta S$, are essentially unvarying throughout the relevant region of $T - B$ space; in other words, the ΔG contours are assumed to very nearly be parallel, straight lines. Note that for zero hysteresis width, the phase transition is reversible and $\chi \to 1$; furthermore $| m | = | \partial\chi/\partial\Delta T_{\text{hyst}} |$ is larger for larger ΔT_{elast}, as expected from Fig. III.7 and Fig. III.8. It is clear that (1) the reduction in Ericsson temperature span and efficiency is due to the thermal hysteresis of the MST (ΔT_{hyst}) and becomes worse as it becomes less abrupt (ΔT_{elast}), (2) these effects become significantly more pronounced as the maximum magnetic field constraint (ΔB) is reduced, and (3) these effects are mitigated for larger $\Delta M/\Delta S$.

III.4 Conclusions and Materials Design Implications

This investigation has, for the first time, quantitatively explored the interacting effects of hysteresis properties and choice of refrigeration cycle on the potential performance of a GMCE refrigerant in magnetic refrigeration cycles. By studying the $Ni_{45}Co_5Mn_{36.6}In_{13.4}$ model alloy with simplified hysteresis parameters in χ-optimized Ericsson cycles, it has been found that hysteresis presents a critical limitation to refrigeration performance, by greatly reducing the effective temperature span while slightly increasing the input work cost of the cycle for a given cooling power. Hysteresis

effects are exacerbated as the one-way transition width deviates from ideal discontinuity ($\Delta T_{\text{elast}} \neq 0$). Furthermore, these results hold regardless of the particular $T - B$ cycle chosen: for every fixed cycle, increases in hysteresis and one-way transition width adversely affect the cycle's performance.

The investigation has yielded important results regarding the interaction between cycle parameters and GMCE refrigerant hysteresis properties in determining the potential performance of the material in magnetic refrigeration cycles. For every combination of hysteresis parameters and magnetic field constraint there is a unique Ericsson cycle which maximizes the fractional Carnot efficiency. Even when comparing these optimal cycles, we find that the presence of hysteresis drastically limits the potential performance of the refrigerant. The sensitivity of performance metrics on hysteresis becomes increasingly pronounced for lower magnetic fields, since the scaling-down of temperature span with magnetic field is not compensated by similar scaling in the hysteresis effects. Together these effects imply that the maximum efficiency, χ, of a cycle using a given refrigerant is critically limited by the hysteresis properties of its phase transition; e.g., the best-case efficiency for this model alloy with 2 K one-way transition width and 1 K thermal hysteresis undergoing a 0 to 1.5 T field change is just 0.55. The investigation also reveals which material properties are important for optimizing the performance of hysteretic GMCE refrigeration cycles. From (3.4), increases in the refrigerator temperature span and efficiency for a fixed hysteresis can be obtained by maximizing $\Delta M/\Delta S$ that is, the magnitude of the change in magnetization of

the refrigerant, relative to its entropy, at the MST. Given that ΔS at the MST is also closely related to Q_c, optimal refrigerants are obtained by maximizing ΔM.

These results have critical implications for materials design. First, (3.3) essentially shows how the MST transition temperatures of an inverse-GMCE refrigerant control the temperature span of the Ericsson cycle it is used in, so that by controlling phase stability, for example, through compositional modifications and heat treatments, engineers may directly optimize refrigerants for desired refrigeration specifications. Second, the drastic decrease in refrigeration performance with increased hysteresis and one-way transition width provides new impetus to the search for novel techniques to decrease hysteresis and make the MST more abrupt. Significant steps have been made in this direction, especially in exploiting lattice compatibility [46–48], or through microstructure design via heat treatment procedures [43], to reduce thermal hysteresis in thermoelastic martensites. However, these advances have not yet led to GMCE Heusler alloys with $\Delta T_{\mathrm{hyst}} < 1$ K, necessary here to achieve $\chi > 0.9$ with 1.5 T maximum field constraints. Future studies may attempt to adapt these techniques to GMCE martensites and other GMCE materials, but in general it is challenging to decrease hysteresis without also adversely affecting the magnitude of the GMCE, and more work is needed here. Finally, (3.4) shows that Ericsson temperature spans decrease rapidly with decreased maximum applied field, and this compounds the hysteresis reduction in cycle efficiencies. In order to counteract this, ΔM at the phase transition should be increased, perhaps by increasing the magnetic ordering temperature, T_C of the β phase, or by increasing the difference between the single phase saturated magnetizations. Both of

these could be modified with compositional treatments, by substituting elements which have either stronger exchange coupling or larger magnetic moments in the β phase.

In conclusion, we have formulated a new thermodynamic framework for investigating the performance of GMCE magnetic refrigeration cycles, incorporating reductions due to hysteresis from the outset. For the class of Ericsson-type cycles and a particular GMCE magnetic shape memory alloy, we show that both the hysteresis properties and the cycle constraints critically determine the cycle's performance, as measured by the suggested metrics, but that reductions in performance can be offset by appropriately designing the thermo-magnetic properties of the refrigerant. We anticipate this methodology to be broadly applicable to other GMCE material systems, so that they may be compared and selected for a given application, based off of rational efficiency considerations.

III.5 References

1. Energy Information Administration 2013 Residential Energy Consumption Survey 2009 Table CE4.1 Tech. Rep. U.S. Dept. of Energy (www.eia.gov/consumption/residential/data/2009)
2. Energy Information Administration 2008 Commercial Buildings Energy Consumption Survey 2003 Table E5A Tech. Rep. U.S. Dept. of Energy (www.eia.gov/consumption/commercial/data/2003)
3. Engelbrecht K L, Nellis G F and Klein SA 2006HVAC&R Res. 12 1077–95
4. Yu B F, Gao Q, Zhang B, Meng XZ and Chen Z 2003 Int. J. Refrig. 26 622–36

5. Franco V, Blázquez J S, Ingale B and Conde A2012 Annu. Rev. Mater. Res. 42 305–42

6. Yu B, Liu M, Egolf PWand Kitanovski A 2010 Int. J. Refrig. 33 1029–60

7. Goetzler W, GuernseyMand Young J 2015 Research and Development Opportunities for Joining Technologies inHVAC&R Tech. rep. Navigant Consulting, Inc. (http://energy.gov/eere/buildings/downloads/research-development-opportunities-joiningtechnologies-hvacr)

8. Brown G V 1976 J. Appl. Phys. 47 3673–80

9. Zimm C, Jastrab A, Sternberg A, Pecharsky V, Gschneidner KJr, OsborneMand Anderson I 1998 Adv. Cryog. Eng. 43 1759–66

10. Gschneidner K A Jr and PecharskyVK2008 Int. J. Refrig. 31 945–61

11. Gschneidner K A Jr and PecharskyVK2000 Annu. Rev. Mater. Sci. 30 387–429

12. Brück E 2005 J. Phys. D: Appl. Phys. 38 R381–91

13. Pecharsky V K, Gschneider K A Jr, Pecharsky A O and Tishin AM2001 Phys. Rev. B 64 144406

14. Pecharsky V K, and Gschneidner KA Jr 1997 Phys. Rev. Lett. 78 4494–7

15. Pecharsky V K, Holm A P, Gschneidner KA Jr and Rink R 2003 Phys. Rev. Lett. 91 197204

16. Gschneidner K A Jr, Mudryk Y and PecharskyVK2012 Scr. Mater. 67 572–7

17. Gschneidner K A Jr, Pecharsky VKand TsokolAO2005 Rep. Prog. Phys. 68 1479–539

18. Dagula W, Tegus O, Fuquan B, Zhang L, Si P Z, Zhang M, Zhang W S, Brück E, de Boer F R and Buschow K H J 2005 IEEE Trans. Magn. 41 2778–80

19. Tegus O, Fuquan B, Dagula W, Zhang L, Brück E, Si P, de Boer F and Buschow K H J 2005 J. Alloys Compd. 396 6–9

20. Yibole H, Guillou F, Zhang L, van Dijk N H and Brück E 2014 J. Phys.D47 075002

21. Fujita A, Fujieda S, Hasegawa Y and FukamichiK2003 Phys. Rev. B 67 104416

22. Shen BG, Sun J R,Hu F X, ZhangHWand Cheng ZH2009 Adv. Mater. 21 4545–64

23. Lyubina J, Schäfer R, Martin N, Schultz L and GutfleischO2010 Adv. Mater. 22 3735–9

24. Karaca H E, Karaman I, Basaran B, Ren Y, Chumlyakov Y I and Maier H J 2009 Adv. Funct. Mater. 19 983–98

25. Moya X, Mañosa L, Planes A, Aksoy S, Acet M, Wassermann E F and Krenke T 2007 Phys. Rev. B 75 184412

26. Liu J, Gottschall T, Skokov KP, Moore J D and GutfleischO2012 Nat. Mater. 11 620–6

27. Niemann R, Heczko O, Schlultz L and Fähler S 2010 Appl. Phys. Lett. 97 222507

28. Diestel A, Niemann R, Schleicher B, Schwabe S, Schultz L and Fähler S 2015 J. Appl. Phys. 118 023908

29. Smith A, Bahl C R H, Bjørk R, Engelbrecht K, Nielsen K K and Pryds N 2012 Adv. Energy Mater. 2 1288–318

30. Mayergoyz I D 1987 J. Appl. Phys. 61 3910–2

[31] Brown T D, Bruno N M, Chen J H, Karaman I, Ross J H Jr and Shamberger P J 2015 JOM 67 2123–32

[32] Shamberger P J and Ohuchi F S 2009 Phys. Rev. B 79 144407

[33] Mayergoyz IsaakD1986 IEEE Trans. Magn. 22 603–8

[34] Basso V, Kuepferling M, Sasso C P and LoBueM2008 IEEE Trans. Magn. 44 3177–80

[35] Basso V, Sasso C P, Bertotti G and LoBueM2006 Int. J. Refrig. 29 1358–65

[36] Basso V, Bertotti G, LoBue M and Sasso C P 2005 J. Magn. Magn. Mater. 290 654–7

[37] Basso V, Sasso C P and LoBue M 2007 J. Magn. Magn. Mater. 316 262–8

[38] Krenke T, Duman E, Acet M, Wasserman E F, Moya X, Manosa L and Planes A 2005 Nat. Mater. 4 450–4

[39] Khan M, Ali N and Stadler S 2007 J. Appl. Phys. 101 053919

[40] Brown TD, Karaman I, and Shamberger PJ 2016 Mater. Res. Express. 7 074001

[41] Wood M E and Potter W H 1985 Cryogenics 25 667–83

[42] Basso V and Sasso C P 2012 Phys. Rev. B 85 014430

[43] Bruno N M, Yegin C, Karaman I, Chen JH, Ross J H Jr, Liu J and Li J 2005 Acta Mater. 74 66–84

[44] Trung N T, Ou Z Q, Gortenmulder T J, Tegus O, Tegus O and Bruck E 2009 Appl. Phys. Lett. 94 102513

[45] Lyubina J, Gutfleisch O, Richter Mand KuzminM2009 J. Magn. Magn. Mater. 321 3571–7

46. Song Y, Chen X, Dabade V, Shield T and James R 2013 Nature 502 85–8

47. Cui J et al 2006 Nat. Mater. 5 286–90

48. Chen X, Srivastava V, Dabade V, and James R 2013 J. Mech. Phys. Solids 61 2566–87

CHAPTER IV

EFFECTS OF HYSTERESIS AND BRAYTON CYCLE CONSTRAINTS ON MAGNETOCALORIC REFRIGERANT PERFORMANCE*

IV.1 Introduction

Magnetic refrigeration (MR) is an emerging solid-state cooling technology with potential environmental and energy use benefits [1-2] over current vapor compression systems. MR harnesses the magnetocaloric effect (MCE) coupling in magnetic refrigerant materials using cyclic magnetic field variations to control the refrigerant's temperature or entropy, thereby transferring heat from a cold to hot reservoir [3]. The most promising refrigerants are alloys undergoing a first-order non-diffusive magneto-structural transformation (MST) between distinct crystal phases, leading to an abrupt, "giant" MCE (GMCE) [4-5] over a narrow temperature window. The larger-magnitude coupling in GMCE materials is advantageous for commercial applications, potentially enabling MR systems based on GMCE refrigerants using permanent magnets with field strengths of 1.5-2.0 T. Despite this advantage, high-efficiency MR systems based on GMCE refrigerants have not yet been developed. This is due in part to an incomplete understanding of how systems-level refrigeration performance depends simultaneously

on the refrigerant material properties and the thermodynamic cycle governing the system's operation acting together.

One major factor in this interplay between material and governing cycle is the partial dissipation of input thermal and magnetic energy by the refrigerants' MST as hysteresis losses [6-7]. These losses result directly from the magnetothermal driving force having to overcome energy barriers associated with the non-diffusive atomic displacements induced by the MST, with the additional driving force ultimately providing energy for irreversible generation and activation of defects like dislocations [8-9]. As a typical MR system repeatedly cycles back and forth through the MST, this microscale dissipation translates into reduced efficiency and performance of the overall MR system. Although in certain specialized materials [10-11] energy barriers have been greatly reduced while retaining many of the properties of the first-order MST, typically GMCE materials manifest significant hysteresis losses, which in many cases are large enough to negate the advantage of the GMCE. However, with few exceptions [12-14] typical thermodynamic analyses neglect these impacts due to hysteresis, yielding overly-optimistic predictions for system performance.

Another important factor is how refrigeration metrics (heat lifted, work input, efficiency) and trade-offs between them depend on the system's temperature and magnetic field constraints. For example, in their seminal refrigerator based on MCE in Gd, Brown and Papell [15] used an isothermal magnetic field change from 0 to 7 T to lift 38 W/kg-Gd of heat between 253 K and 258 K; for a cycle from 243 K to 284 K the same system then lifted a reduced 7 W/kg-Gd. MR performance also depends on how

temperature and magnetic field change together during the cycle, *i.e.* the class of cycle used. For the Brown Gd refrigerator, the system exhibited approximately cyclic behavior composed of alternating isothermal / constant-field legs, which in analogy with isothermal / isobaric gas systems are said to comprise magnetic Ericsson cycles. In contrast, Brayton cycles simultaneously vary temperature with magnetic field by maintaining adiabatic (zero-heat transfer) conditions throughout magnetization. These adiabatic cycle legs are much faster than the corresponding Ericsson isothermal legs, yielding higher cycle frequencies, but reduced heat lifted per cycle.

As a final example, performance metrics (especially temperature span) can be favorably impacted by introducing more complex cycles, such as those in Active Magnetic Regenerator Refrigerator (AMRR) designs. In these systems, a regenerative temperature gradient is maintained within the refrigerant bed, resulting in a much larger cooling power for a given total temperature span, for example 200 W/kg-Gd for a 10 K span and 33 W/kg-Gd for a 23 K span in an AMRR system operating between 0 T and 5 T [16]. Analyzing these systems is even more difficult, since the refrigerant bed is never all at one temperature-entropy state and can't be simply represented in a corresponding $T - S$ diagram. However, at some critical resolution, the bed can be viewed as a system of volume elements coupled by mutual heat fluxes within the bed, each undergoing some simple cycle representable as a definite path in $T - S$ space. In general, the magnetic field application in each of these elemental cycles will be accompanied by a combination of both non-zero heat transfer and temperature change (and therefore is not well-described by an adiabat nor an isotherm). However, under certain conditions, such as

weak heat coupling along the refrigeration bed, or appropriate applied magnetic field profiles [17] even these elemental cycles may approximate members of the Ericsson or Brayton classes to a desired precision. Otherwise, the "infinitely fast" Brayton adiabats and "infinitely slow" Ericsson isotherms may be viewed as appropriate limiting cases constraining all cycles with constant-field legs, including those in AMRR volume elements. In this way, a detailed study of simpler Brayton and Ericsson MR cycles can illuminate the behavior of more complex AMRR systems.

The dependence of MR performance metrics jointly on the GMCE and hysteresis of candidate refrigerant materials, in combination with the classes and properties of the governing cycles, constitutes a large and complicated design space. If we are to realize commercial MR systems soon, the joint dependencies governing this space must be better understood. Along these lines, we have developed an irreversible thermodynamics framework based on Preisach hysteresis operators [18-19] that incorporates hysteresis while simulating the path-dependent magnetothermal properties of a given GMCE alloy as it undergoes a specified temperature-magnetic field ($T - B$) path. From these simulations the relevant work and heat transfers are computed, yielding cycle- and hysteresis-dependent refrigeration performance metrics that can be compared directly between different cycles and material classes. Previously, this methodology was applied to a $Ni_{45}Co_5Mn_{36.6}In_{13.4}$ GMCE alloy [20-22] undergoing Ericsson-type cycles over a range of temperatures for field changes between 0 and 1.5 T, and 0 and 5 T, allowing specification of optimal-efficiency cycles, as well as their dependence on the hysteresis properties of the alloy's MST.

Here we extend previous work on simulations of hysteretic Ericsson cycles to Brayton cycles. By making reasonable simplifications relating entropy generation in out-of-equilibrium processes to phase transition hysteresis loops, we develop formulae for temperature as a function of magnetic field $T(B)$ along adiabatic paths in the presence of entropy generation, *i.e.*, under non-equilibrium conditions. By simulating the magnetization and entropy of a $Ni_{45}Co_5Mn_{36.6}In_{13.4}$ GMCE alloy within magnetic Brayton cycles operating between 0 T and 5 T, and 0 T and 1.5 T, we: (1) compute refrigeration performance metrics (cooling power, work input, temperature span, 2nd law efficiency) throughout the space of feasible temperature reservoirs and for a variety of MST hysteresis properties; (2) determine relationships to quantify the adverse effect of refrigerant hysteresis on each of the performance metrics; and using these relationships, we (3) develop simple heuristics for choosing cycle temperature reservoirs to obtain maximum 2nd law efficiency. Finally, Ericsson and Brayton cycles are themselves compared by analyzing corresponding Pareto fronts of refrigeration cooling power and temperature span. Discussion shows that (1) hysteresis in refrigerants remains a critical materials-level limitation to GMCE refrigeration using permanent magnets with strength ≤ 2 T, and (2) Brayton cycles lift less heat per cycle than Ericsson cycles for a given temperature span, although this difference can be made negligible by decreasing the heat capacity of the parent and daughter phases while the latent heat of transformation remains high.

IV.2. Methods

IV.2.1 Modeling Overview

The previous work [18] described a general methodology for computing the heat transfers evolved within out-of-equilibrium magnetic refrigeration cycles, by utilizing and interpreting Preisach hysteresis operators within the context of non-equilibrium thermodynamics. Quantitative relationships describing the dependence of energy dissipated in Ericsson cycles on the hysteresis of the MST are then elucidated by simulating the path-dependent evolution of a candidate refrigerant's bulk properties (phase fraction by mass φ, entropy S, magnetization M) throughout the cycle and calculating the resultant heat and magnetic work transfers.

At the core of the modeling framework are the experimentally-motivated simplifications that (1) MST hysteresis contributions dominate energy dissipation, so that energy dissipation occurs ($\delta E_{\mathrm{diss}} > 0$) only when the phase fraction evolves ($d\varphi \neq 0$) and is zero otherwise; and (2) the hysteretic phase evolution depends only on the underlying energy barriers, but not on which of the thermodynamic driving forces, temperature *T* or magnetic field *B*, actually drives the system over the energy barriers. This simplification is expected to hold for saturated soft magnetic materials with minimal magnetic hysteresis and for polycrystalline materials where the system can be considered macroscopically isotropic, as is typical for the refrigerant materials typically studied. The second assumption implies that the phase fraction has a simplified dependence on the $T - B$ state path through the generalized thermodynamic driving force function ΔG, described as below:

$$\varphi = \hat{P}\{T,B\} = \hat{P}\{\Delta G(T,B)\}, \qquad (IV.1)$$

where ΔG is the difference in free energy driving the system from its low-temperature phase α to its high-temperature phase β. The hysteretic path-dependence is contained entirely within a specified Preisach hysteresis operator $\hat{P}\{x\}$ [23], which is essentially a weighted sum over a distribution of hysteresis units with specified threshold values. The form of this Preisach distribution then completely and uniquely defines the hysteretic dependence of the phase fraction φ on the generalized driving force ΔG (Fig. IV.1a-1b).

The Preisach model is chosen as a simple parameterized physics-free model that manifests non-local memory properties, and thus can capture the hysteretic phase fraction for ΔG paths of interest, including paths with incomplete phase transformation (Appendix A.1). The differential of the driving force ΔG is expressed as:

$$d(\Delta G) = d\left(G^{\beta} - G^{\alpha}\right) = -\left(S^{\beta} - S^{\alpha}\right)dT - \left(M^{\beta} - M^{\alpha}\right)dB, \qquad (IV.2)$$

with the entropy $S(T,B)$ and magnetization $M(T,B)$ of each pure phase $\{\alpha,\beta\}$ evaluated by fitting physical models to experimental heat capacity and magnetization data, then using them to extrapolate across the two-phase region. Afterwards, Eq. IV.2 is integrated along the $T-B$ path under consideration, giving the driving force $\Delta G(T,B)$ and through Eqn. IV.1, the path-dependent phase fraction φ. Finally, the total properties $X = \{S,M\}$ of the refrigerant are approximated with the rule of mixtures, $X = (1-\varphi)X^{\alpha} + \varphi X^{\beta}$, expected to hold for soft ferromagnetic phases above magnetic saturation and low-

entropy hetero-phase interfaces, as in the highly-ordered martensite twin walls and austenite-martensite habit planes that mediate the MST in GMCE refrigerants.

An immediate consequence of Eq. IV.1 is that however different a given pair of $T - B$ paths acting on a material may be, if they correspond to the same ΔG path, then they will develop identical φ hysteresis behavior. This is consistent with investigations in NiMnX (X ={Co,Sn,Ga}) Heusler alloys manifesting GMCE comparing hysteresis loops obtained from isothermal and constant-field processes [24-25]. Given this interpretation, any $T - B$ path may be projected onto the $B = 0$ axis, yielding a zero-field heating and cooling operation with the same ΔG as the original path, and therefore the same hysteretic phase transformation behavior. Now designating the temperature of this projected zero-field path as θ, the hysteresis loops generated by $\hat{\phi}\{\theta\}$ through the Preisach model generate a convenient representation of a given MST's basic hysteresis characteristic (Fig. IV.1b) that is seen to be independent of any $T - B$ path operating on the system (Fig. IV.1c). Although the actual hysteresis character $\hat{\phi}\{\theta\}$ may be determined along with the functions $M(T, B)$ and $S(T, B)$ from experimental data, here a simplified Preisach model with two variable parameters is used in order to study the interacting effects of cycle parameters and hysteresis properties on the refrigerant's Brayton cycle performance. The two-parameter model used here captures the salient features of observed GMCE refrigerant hysteresis, that (1) the phase transition proceeding in each direction has some finite width (ΔT_{elast}); and (2) there is always some lag (ΔT_{hyst}) between the completion of the forward $\alpha \rightarrow \beta$ and the onset of the reverse $\beta \rightarrow \alpha$ transition, and vice-versa.

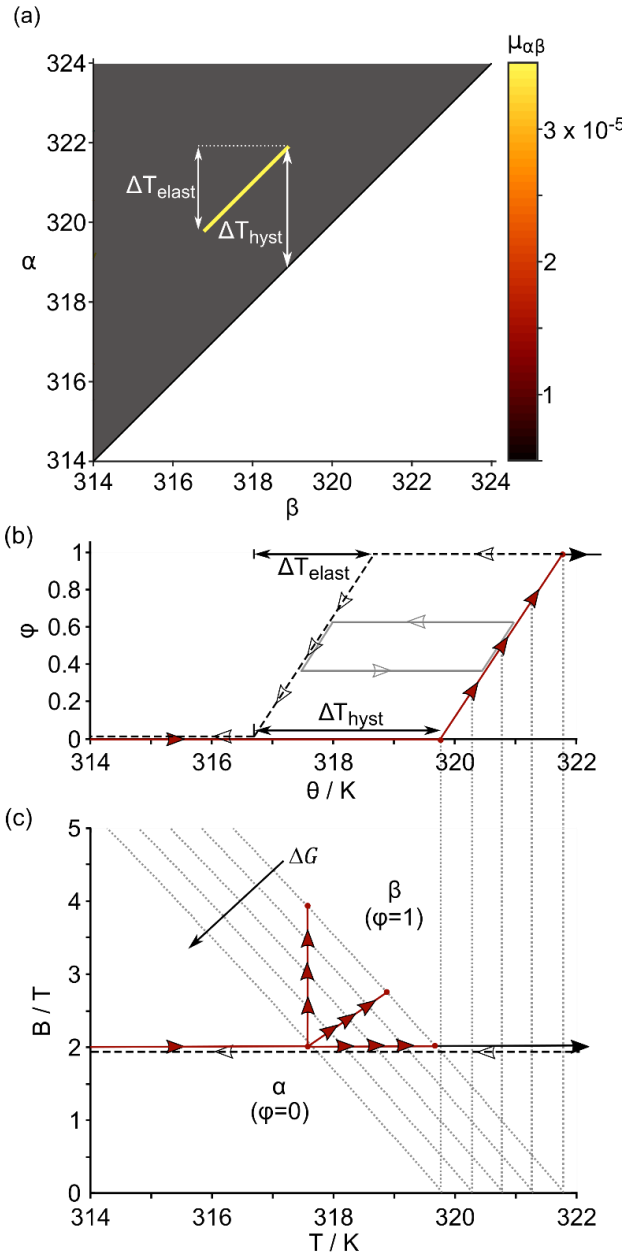

Figure IV.1 Representations of two-parameter Preisach hysteresis model (a) the Preisach distribution function $\mu_{\alpha\beta}$ and (b) corresponding envelope and partial hysteresis loops $\varphi\{\Delta G\}$. The three red-arrow $T-B$ paths in (c) all correspond to the same red ΔG path in (b), and therefore by Eqn. IV.1, develop the same hysteretic phase fraction evolution. Reprinted with permission from [26]. © AIP Publishing LLC 2018. DOI 10.1063/1.5022467.

IV.2.2 Treating Hysteresis in Brayton Cycles

In the prior work, Ericsson cycles were studied, with alternating iso-thermal and constant-magnetic field legs specified explicitly by isothermal and iso-field constraints ($dT = 0; dB = 0$). For adiabatic legs in Brayton cycles the situation is more complicated, as the corresponding path constraint ($\delta Q = 0$) specifies the state path $T(B)$ only implicitly. Analyses of adiabatic processes begin from the second law of thermodynamics, expressed as:

$$dS = \frac{\delta Q}{T} + \delta S_{\text{irr}}, \qquad (IV.3)$$

where the first term on the right represents the increase in entropy due to heat transfer δQ across the system boundary at temperature T, and the second term subsumes the entropy generated within the system, for example internal thermal gradients or defect generation and motion. Typical treatments assume the adiabatic path is also isentropic ($dS = 0;\ S(T,B) = S(T_0, B_0)$): a second implicit condition that easily can be solved using the known function $S(T,B)$. However, this simplification only follows for cases where the material evolves in equilibrium and for which there is no internal entropy generation ($\delta S_{\text{irr}} = 0$). Systems that manifest hysteresis always evolve to some degree out-of-equilibrium [27], in which case $\delta S_{\text{irr}} \neq 0$, and a means must be found to estimate the magnitude of generated entropy. Along these lines, first consider the well-accepted equation for energy dissipated within a hard-magnet's magnetic hysteresis loop:

$$E_{\text{diss}} = \oint B dM\,. \qquad (IV.4)$$

That is, the dissipated energy is equal to the area with dimension of energy enclosed by a hysteresis loop. This dissipative formula has also been generalized from its origins in hard magnet domain wall pinning to apply to the hysteresis in GMCE MST transitions [24, 28, 29]. Given the assumption that energy barriers leading to hysteresis and irreversible entropy generation are independent of the acting thermodynamic field, the energy dissipated by the MST energy barriers can be written equivalently as:

$$E_{\text{diss}} = \oint T\delta S_{\text{irr}} = \oint \Delta G d\varphi\,. \qquad (IV.5)$$

Energy is not only dissipated at the conclusion of the hysteresis loop, but also at every point throughout. A natural assignment of the energy dissipated, $\delta E_{\text{diss}} = T\delta S_{\text{irr}}$, during some small phase evolution, $\delta\varphi$, is then given by:

$$T\delta S_{\text{irr}} = ||\Delta G(\varphi)|\,\delta\varphi|, \qquad (IV.6)$$

with absolute values ensuring that dissipation is always positive, regardless of which phase is stable or in which direction the MST proceeds.

Eqn. IV.6 simply postulates that the energy dissipated in some small phase evolution $\delta\varphi$ is proportional to how far out-of-equilibrium the system is during the

evolution. This interpretation is self-consistent with the rest of the methodology and its acceptance leads to several sensible consequences. First, there is no dissipation if the phase fraction is unable to evolve ($\delta\varphi = 0 \rightarrow \delta E_{\text{diss}} = 0$); this is consistent with the previous assumption that it is the hysteresis losses during the phase evolution that dominate energy dissipation. Second, if the phase fraction evolves while at all times very nearly in equilibrium, there is still essentially no dissipation ($\Delta G \approx 0 \rightarrow \delta E_{\text{diss}} \approx 0$); this is the situation usually understood within the thermodynamics of quasi-static processes. In this study, it is imposed that the piece-wise hysteresis characteristics all have equal ΔG across the phase transition, so Eqn. IV.4 simplifies to a direct proportionality: $\int_{\varphi_1}^{\varphi_1+\Delta\varphi} T\delta S_{\text{irr}} = |\Delta G|\Delta\varphi$.

Substituting Eqn. IV.6 into Eqn. IV.3 makes solving the implicit governing equation ($\delta Q = 0$) again tractable, so that the adiabatic magnetization paths of the Brayton cycle may be computed without the invalid simplification of zero energy dissipation. This theory forms the basis for the method used throughout the remainder of this work.

IV.2.3 Material Model and Example Brayton Cycle

The magnetic refrigerant under investigation in this paper is a $Ni_{45}Co_5Mn_{36.6}In_{13.4}$ alloy manifesting inverse GMCE, where "inverse" denotes that increasing the magnetic field adiabatically and inducing the $\alpha \rightarrow \beta$ transition lowers the material's temperature (the opposite effect from direct GMCE materials [30-31]). The single-phase properties $M^{\alpha,\beta}(T,B)$ and $S^{\alpha,\beta}(T,B)$ in Eqn. IV.2 are given by least-squares regression fitting of Brillouin and Debye-Sommerfeld physical models, respectively, to experimental data. In

this way, the magneto-thermal properties of each individual phase are specified by six physical parameters (Appendix A), all of which, *e.g.* the Curie Temperature $T_{\mathrm{C}}^{\alpha,\beta}$, have clear physical interpretations, and can be meaningfully compared between candidate refrigerants. When estimated from the data, the hysteresis model parameters for the $Ni_{45}Co_5Mn_{36.6}In_{13.4}$ refrigerant are about $\Delta T_{\mathrm{hyst}} = 10$ K and $\Delta T_{\mathrm{elast}} = 10$ K; however, here the parameters are methodically varied between $0 \leq \Delta T_{\mathrm{hyst}} \leq 12$ K and $0 \leq \Delta T_{\mathrm{elast}} \leq 8$ K so as to explore the interacting effects of hysteresis properties of the phase transition and cycle parameters on the overall performance metrics.

Having fully specified the material model in terms of its MST hysteresis characteristic and its single-phase magnetothermal properties, the simulation of a Brayton cycle (Fig. IV.2) proceeds in stages.

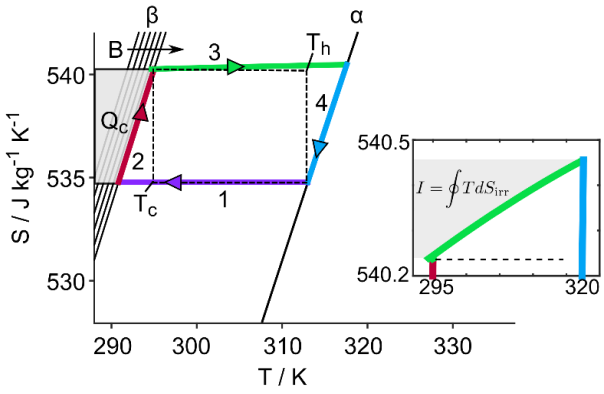

Figure IV.2 Example Brayton cycle in $S - T$ space. ΔB from 0 to 8 T and $(T_c, T_h) = (295\ K, 314\ K)$. The four constituent processes are [1] adiabatic magnetization beginning at T_h; [2] Iso-field heat absorption from the cold reservoir at T_c; [3] adiabatic demagnetization beginning at T_c; [4] Iso-field heat rejection to the hot reservoir at T_h. Entropy is generated throughout adiabatic demagnetization [inset] as discussed in text. Actual Brayton cycle may deviate significantly from reference Carnot cycle between T_c and T_h (dashed black line). Reprinted with permission from [26]. © AIP Publishing LLC 2018. DOI 10.1063/1.5022467.

First, the Brayton cycle parameters are specified as a pair of field magnitudes ($B_{\min}$, $B_{\max}$) and temperatures (T_{c} , T_{h}), with the former specifying the starting and ending magnetic fields for the adiabatic legs; the second pair specifies the temperatures of the reservoirs from which the refrigerant absorbs and expels heat, respectively. Next, beginning from $T = T_{\mathrm{h}}$ and $B = B_{\min}$ (0 T) the field B is increased adiabatically according to Eqn. IV.4, causing this refrigerant to cool several degrees below T_{c}. After the field increase has been exhausted, the refrigerant is gradually warmed at constant field to T_{c}, absorbing heat indirectly from the refrigerated volume. The heat absorbed in this stage is the heat lifted per cycle per unit mass of refrigerant, which we call cooling power, expressed as:

$$Q_{\mathrm{c}} = \int T(dS - \delta S_{\mathrm{irr}}). \qquad (IV.7)$$

After reaching $T = T_{\mathrm{c}}$, the field is adiabatically removed, decreasing from $B_{\max}$ to $B_{\min}$, and the refrigerant warms several degrees above T_{h}. Finally, the refrigerant is cooled to T_{h}, expelling heat to the ambient heat sink, and resetting the system state for the next cycle. At all times, the only source of entropy generation is assumed to be the hysteresis losses specified within Eqn. IV.6. In particular, system losses from pressure drops of the external heat transfer fluid or from heat transfer across a finite temperature difference from the heat transfer fluid to the magnetocaloric volume are neglected to ensure a material focused, system agnostic analysis.

The corresponding net input magnetic work per cycle per mass is given by:

$$W = \oint BdM\,, \qquad (IV.8)$$

which together with the cooling power Q_{c} and the temperature span $(T_{\mathrm{c}}\,, T_{\mathrm{h}})$ of the cycle enable a 2nd law efficiency metric to be defined as the ratio of the actual system coefficient of performance (c.o.p. $\equiv Q_c/W$) to that of an ideal reversible Carnot cycle (Fig. IV.2) operating across the same temperature span, expressed as:

$$\chi = \left(\frac{Q_{\mathrm{c}}}{W}\right) / \left(\frac{T_{\mathrm{c}}}{T_{\mathrm{h}} - T_{\mathrm{c}}}\right). \qquad (IV.9)$$

Together, the cooling power Q_{c}, required work W, temperature span $\Delta T_{\mathrm{span}} \equiv T_{\mathrm{h}} - T_{\mathrm{c}}$, and percent Carnot efficiency χ are taken to characterize the performance of the refrigerant in a given cycle, allowing direct comparisons between different cycles and MST hysteresis properties.

IV.3 Results

IV.3.1 Cycle-Hysteresis Effects on Brayton Performance

By fixing the MST hysteresis parameters at $\Delta T_{\mathrm{hyst}} = \{2\ \mathrm{K}, 4\ \mathrm{K}, 6\ \mathrm{K}\}$ and $\Delta T_{\mathrm{elast}} = 2\ \mathrm{K}$, and methodically varying $(T_{\mathrm{c}}\,, T_{\mathrm{h}})$, the cycle performance metrics $\{Q_{\mathrm{c}}, W, \Delta T_{\mathrm{span}}, \chi\}$ have been computed across the range of combinations of cycle parameters $(T_{\mathrm{c}}\,, T_{\mathrm{h}})$ for cycles operating between 0 and 5 T, and 0 and 1.5 T.

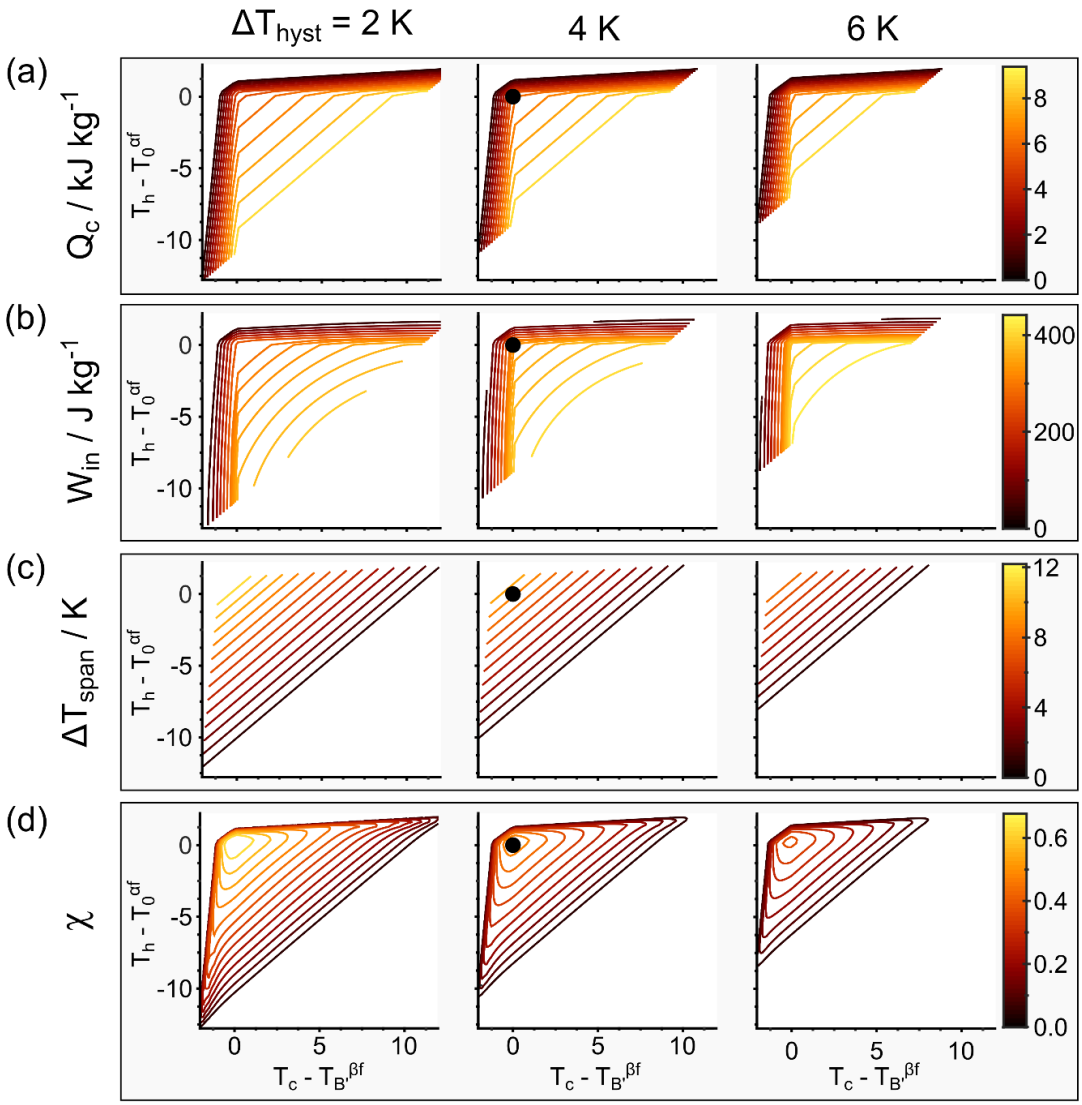

Figure IV.3 Contours of refrigeration metrics for 5 T cycles. Refrigeration performance metrics (Q_c, W, $\Delta T_{span}, \chi$) for ΔB =5.0 T field-constrained cycles as a function of T_c and T_h relative to $T_{B'}^{\beta f}$ and $T_0^{\alpha f}$, respectively. Columns separate performance metrics evaluated at three different hysteresis widths: 2 K, 4 K, and 6 K with the elastic width held constant at 2 K. Black circles correspond to cycle metrics for the unique cycle with maximum χ for 4 K hysteresis width expanded in Fig. IV.5. Reprinted with permission from [26]. © AIP Publishing LLC 2018. DOI 10.1063/1.5022467.

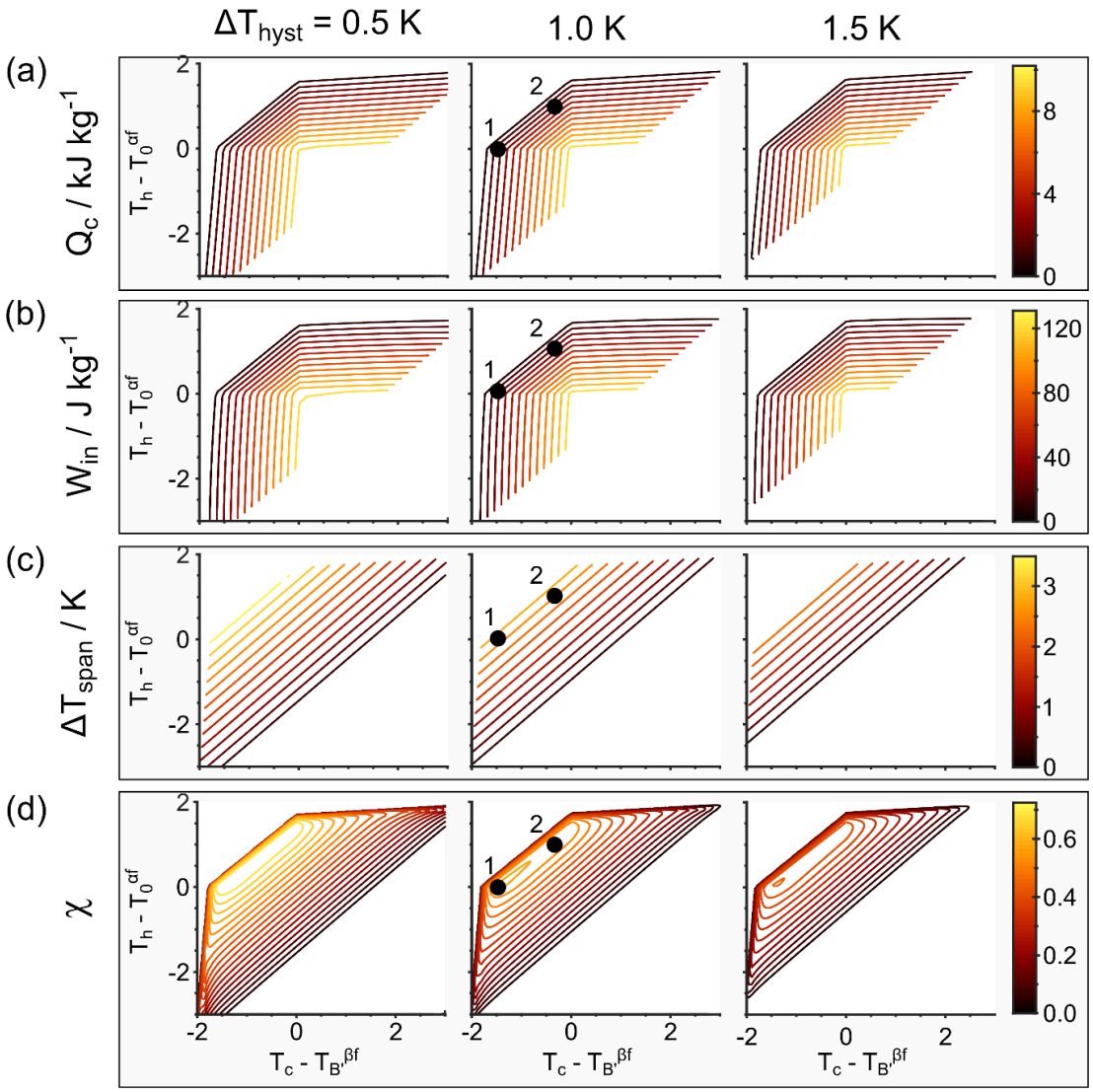

Figure IV.4 Contours of refrigeration metrics for 1.5 T cycles. Refrigeration performance metrics (Q_c, W, $\Delta T_{span}, \chi$) for ΔB =1.5 T field-constrained cycles as a function of T_c and T_h relative to $T_{B'}^{\beta f}$ and $T_0^{\alpha f}$, respectively. Columns separate performance metrics evaluated at three different hysteresis widths: 0.5 K, 1.0 K, and 1.5 K with the elastic width held constant at 2 K. Numbered black circles correspond to cycle metrics for the cycles with nearly-equal maximum χ for 1 K hysteresis width shown in Fig. IV.6. Reprinted with permission from [26]. © AIP Publishing LLC 2018. DOI 10.1063/1.5022467.

These magnetic field extremes have been chosen as representative of the conditions studied in magnetocaloric characterization experiments and of the maximum fields currently produced by the best permanent magnets, respectively. The results of

these simulations for 5 T and 1.5 T maximum field strength are summarized in the contour plot arrays in Fig. IV.3 and Fig. IV.4, respectively. The axes in each plot are the reservoir temperatures $(T_{\mathrm{c}}, T_{\mathrm{h}})$, normalized by subtracting the two transformation temperatures $T_B^{\beta \mathrm{f}}$ and $T_0^{\alpha \mathrm{f}}$, the temperatures at which the $\alpha \rightarrow \underline{\beta}$ transition finishes at $B_{\max}$, and the temperature where the $\beta \rightarrow \underline{\alpha}$ transition finishes at 0 T, respectively. This normalization accounts for the shift in transformation temperatures that occurs as ΔT_{hyst} varies, thus allowing meaningful comparison of the columns in Fig. IV.3-4. Finally, there are regions in the plots for which the metrics are undefined. These correspond to one of three cases: (1) the cycle specification is itself unphysical ($T_{\mathrm{c}} > T_{\mathrm{h}}$); (2) the refrigerant remains at all times in either the pure α or β phase (so neither GMCE nor hysteresis has any effect whatever on the cycle); or (3) the cycle is impossible in principle due to the finite temperature change afforded by GMCE. In this final case, the cycle is such that the refrigerant temperature after adiabatic magnetization is still warmer than T_{c}, or the temperature after demagnetization is cooler than T_{h}; in either case, absorbing heat from T_{c} or expelling heat to T_{h} violates the 2nd law of thermodynamics. Within these restrictions, the contour plots summarize the dependence of the refrigeration performance metrics $\{Q_{\mathrm{c}}, W, \Delta T_{\mathrm{span}}, \chi\}$ on the cycle temperature reservoirs $(T_{\mathrm{c}}, T_{\mathrm{h}})$ as the hysteresis ΔT_{hyst} increases from 2 K to 6 K.

Under all hysteresis and maximum field constraints considered, the cycle cooling power Q_{c} increases as either T_{c} increases or as T_{h} decreases (towards the bottom-right in the plots) since both create a larger undercooling of the refrigerant below T_{c} after

adiabatic magnetization. This larger temperature difference enables more heat transfer ($Q_{\mathrm{c}} \sim \int T dS$) before the refrigerant equilibrates with T_{c}, so the cooling power is larger. However, it is clear that the same conditions also decrease the temperature span ΔT_{span}, so that for a given ambient temperature T_{h} the refrigerated volume temperature T_{c} cannot be as cool; this is an example of a general trade-off between Q_{c} and ΔT_{span} resulting from the 1st law of thermodynamics and also seen in the real refrigeration systems reviewed previously. The advantage of increased cooling power as T_{c} increases and T_{h} decreases is further offset by a simultaneous increase in the magnetic work input $W = \oint B dM$ due to there being a greater magnetization difference between the α and β phases in this regime. This is again supported by the 1st law of thermodynamics: creating a larger cooling heat transfer requires more input energy. The trade-offs between the temperature and heat transfer metrics are combined in calculating the % Carnot efficiency metric χ, leading to an optimum in its surface towards the top-left of the plots. Although increased hysteresis ΔT_{hyst} does not impact the general trends in the performance metrics described above, it does result in several adverse effects on Brayton cycle performance (Fig. IV.3-4). First, increasing hysteresis constrains the design space of $(T_{\mathrm{c}}, T_{\mathrm{h}})$ yielding feasible refrigeration cycles, so that refrigeration systems with larger ΔT_{span} become physically impossible beyond some critical MST hysteresis. The increased under and over-cooling required to induce the MST when hysteresis increases results in ever larger regions of 2nd-law violating cycles. Second, comparing corresponding points in the contour plots shows that ΔT_{span} decreases by 1 K for each 1

K increase in the hysteresis width ΔT_{hyst}. Because these cycles have approximately equal cooling power Q_{c} and require the same magnetic work W, this result is again an illustration of a dissipative 1st law of thermodynamics: dissipation causes the available refrigeration work $W_{\mathrm{ref}} \approx \Delta S \Delta T_{\mathrm{span}}$ to be considerably decreased from the input magnetic work W. With Q_{c} and therefore ΔS constant between corresponding cycles, it follows that increased MST hysteresis and dissipation causes ΔT_{span} to decrease. Finally, by visually shifting the contour plots so that corresponding cycles have constant ΔT_{span}, it is clear that increased hysteresis also decreases the cooling power Q_{c}, a result also consistent with the 1st law interpretation. Hence, the primary impact of MST hysteresis on cycle performance is to indirectly affect the intrinsic trade-offs between Q_{c} and ΔT_{span} by reducing the amount of work available for heat transfer or temperature control.

These trade-offs between the performance metrics and their dependence on hysteresis are essentially the same for maximum field constraints of 1.5 T or 5.0 T. In either case it is still true that ΔT_{span} decreases for corresponding cycles by 1 K for each 1 K increase in ΔT_{hyst}; however, this same 1 K decrease has a much larger effect on the smaller magnitude of the GMCE at 1.5 T compared to 5.0 T. For this reason, the refrigerator temperature span is much smaller across the entire feasible range in the 1.5 T contour plots (maximum $\Delta T_{\mathrm{span}} = 3$ K) than for the 5.0 T plots (maximum $\Delta T_{\mathrm{span}} = 12$ K), and the regions of feasibility are correspondingly smaller (note the different axis scales and ΔT_{hyst} column values between Fig. IV.3-4). For this alloy at least, extending

the reduced 1.5 T temperature span likely presents additional design challenges. On the other hand, the range of cooling powers Q_c throughout the design space are comparable for both maximum field constraints, since there exist cycles in both cases that obtain the maximum possible entropy change across the complete phase transition $\Delta S \sim S^{\beta} - S^{\alpha}$, although for 1.5 T field, these cycles require near-zero temperature span. The required work input W for 1.5 T cycles is decreased compared to 5.0 T cycles, as expected from Eqn. IV.8. The decreased temperature span for 1.5 T field constraint is more than enough to compensate the slight decrease in work input, so that for comparable ΔT_{hyst} the % Carnot efficiency χ is much less for 1.5 T than for 5.0 T maximum field constraint, and the latter already decreases from 65% for 2 K hysteresis to 40% for 6 K hysteresis. This means that when confined to realistic 1.5 T fields generated by permanent magnets, obtaining equal operating efficiency requires much smaller GMCE hysteresis, with 1.5 T cycles yielding 65% efficiency only at $\Delta T_{hyst} \leq$0.5 K, a significant challenge in this alloy system.

IV.3.2 Maximum Efficiency Cycles and Dependence on Hysteresis

To further elucidate the joint effects of the choice of cycle reservoirs (T_c, T_h) and hysteresis parameters (ΔT_{hyst}, ΔT_{elast}) on the MR system performance metrics, it is useful to condense the parametric materials performance information (Fig. IV.3-4) to focus on the cycles that maximize the % Carnot efficiency χ. These χ-optimized cycles present a natural comparison point since (1) presumably, most practical interest is in operating MR systems at or near their maximum efficiency point, and (2) as will be shown, these cycles have particularly simple characteristics making them amenable to

simulate for a variety of hysteresis characteristics without first mapping out the performance metrics throughout the (T_c, T_h) design space.

First, consider χ-optimal cycles for 5.0 T maximum field. For all hysteresis characteristics considered (ΔT_{hyst}, ΔT_{elast} =2K), the χ-optimal cycle occurs at $(T_c, T_h) = (T_B^{\beta f}, T_0^{\alpha f})$. In other words, the temperature reservoirs are matched exactly to the transformation temperatures at the minimum and maximum magnetic field. The projection of the χ-optimal cycle for ($\Delta T_{hyst} = 4$ K, $\Delta T_{elast} = 2$ K) in $TB - \varphi$ (Fig. IV. 5a) $T - B$ (Fig. IV.5b) and $S - T$ (Fig. IV.5c) space helps to clarify this point: beginning from the completion of the $\beta \rightarrow \alpha$ MST, the refrigerant is adiabatically magnetized, "crossing over" in Fig. IV.4b from the 0 T hysteresis loop to the 5 T loop. From there, the refrigerant entropy follows along the $\alpha \rightarrow \beta$ MST path as it absorbs heat from the reservoir at $T_c = T_B^{\beta f}$. It is also clear why T_c must be exactly equal to $T_B^{\beta f}$ to maximize efficiency: any lower, and the $\alpha \rightarrow \beta$ transition is incomplete and the cycle neglects some of the cooling power Q_c it could otherwise access; any higher, and ΔT_{span} is decreased without any significant compensation by increased Q_c, since the $\alpha \rightarrow \beta$ transition has already proceeded to completion. In this sense, the χ-optimized cycles can be said to leverage the latent heat of the MST most effectively, by accessing nearly all of the potential cooling power of the MST while also maintaining large temperature span.

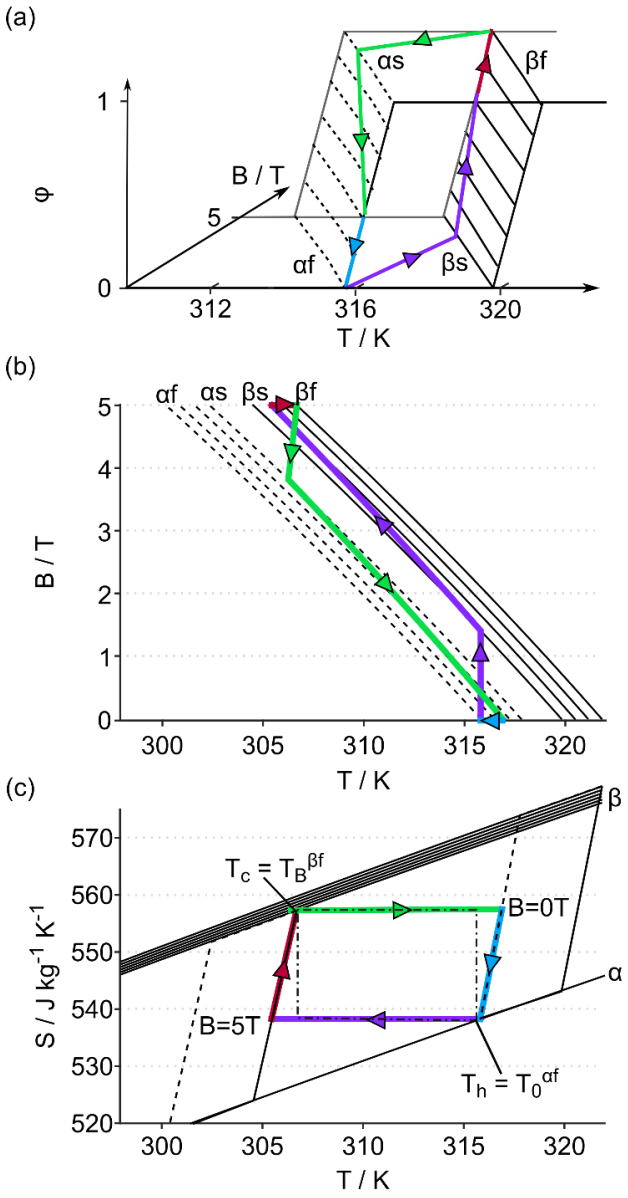

Figure IV.5 An efficiency optimized 5 T cycle. The unique χ-optimized cycle for $\Delta B = 0$ T to 5 T, $\Delta T_{hyst} = 4$ K, and $\Delta T_{elast} = 2$ K represented as (a) phase fraction φ along the optimized $T - B$ path and its projections on (b) $T - B$ and (c) $S - T$ space. For this cycle, adiabatic magnetization begins exactly at $T_h = T_0{}^{\alpha f}$ and iso-field heat absorption concludes at $T_c = T_B^{\beta f}$. Reference Carnot cycle from T_c to T_h also shown (dot-dash line). Reprinted with permission from [26]. © AIP Publishing LLC 2018. DOI 10.1063/1.5022467.

For 1.5 T maximum field cycles, Fig. IV.4 suggests that for each hysteresis characteristic there is a family of χ-optimal cycles with approximately equal maximum

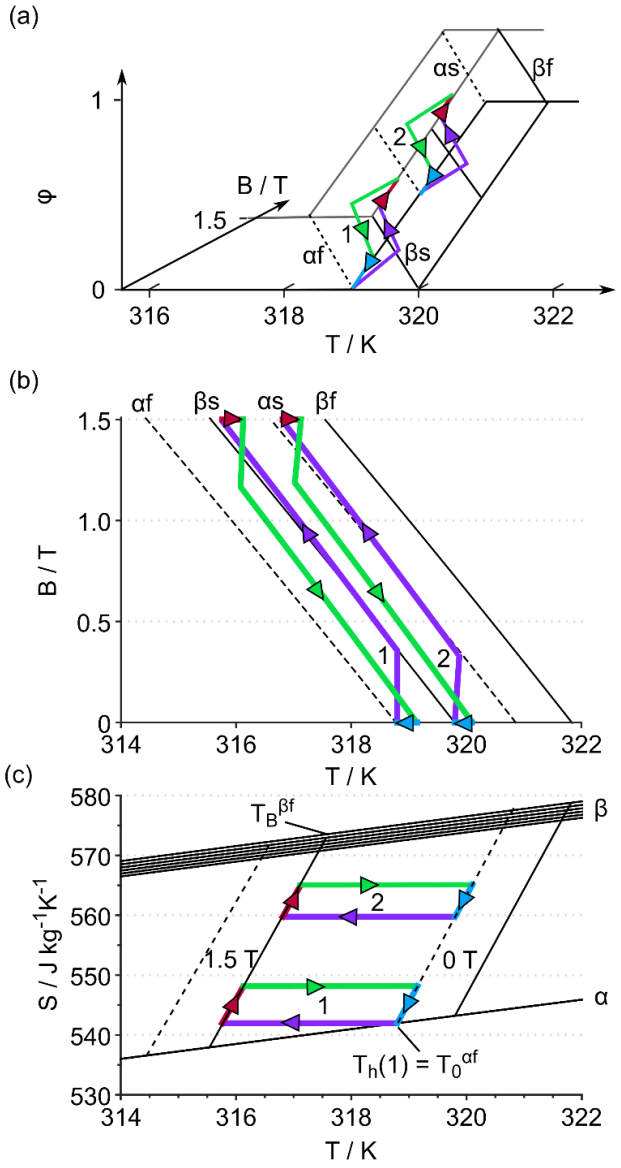

Figure IV.6 Efficiency optimized 1.5 T cycles. Two examples of χ-optimized cycles for $\Delta B = 0$ T to 1.5 T, $\Delta T_{hyst} = 1$ K, and $\Delta T_{elast} = 2$ K represented (a) phase fraction φ along the optimized $T - B$ path and its projections on (b) $T - B$ and (c) $S - T$ space. For these cycles, adiabatic magnetization begins somewhere in the two-phase region at exactly at $B = 0$ T (not necessarily $T_h = T_0{}^{\alpha f}$) and iso-field heat absorption also concludes within the two-phase region at at $B = 1.5$ T (not necessarily $T_c = T_B^{\beta f}$). Reprinted with permission from [26]. © AIP Publishing LLC 2018. DOI 10.1063/1.5022467.

efficiency. Evidently all cycles in the family have equal temperature span, and their temperature reservoirs extend from $(T_c, T_h) = (T_B^{\beta f} - \epsilon, T_0^{\alpha f})$ to $(T_B^{\beta f}, T_0^{\alpha f} + \epsilon)$. This

result is better understood by again referencing the projections of the cycles on the relevant potentials (Fig. IV.6).

Just as in the 5.0 T case, the χ-optimal cycles for 1.5 T constraint are also those where the magnetization and demagnetization legs "cross over" from the $\beta \rightarrow \alpha$ MST at 0 T to touch the $\alpha \rightarrow \beta$ MST at maximum field; in either case, the cycle is designed so that heat absorption from T_{c} occurs only within the two-phase region where the GMCE is active. The main difference between cycles with 5.0 T and 1.5 T maximum field is that in the former case the full MST is accessible (ϕ: $0 \rightarrow 1 \rightarrow 0$ ...); however, in the latter case the smaller magnetic field generates insufficient magnetic work for the MST to proceed to completion ($W < 2|\Delta G_{\alpha\beta}|$) and the refrigerant passes through only a fraction of the MST in each cycle (ϕ: $\phi_0 \rightarrow \phi_0 + \delta \rightarrow \phi_0$ ...). Hence there are no χ-optimal cycles at 1.5 T that operate between both $T_{\mathrm{c}} = T_B^{\beta\mathrm{f}}$ and $T_{\mathrm{h}} = T_0^{\alpha\mathrm{f}}$, and the cooling power is correspondingly less. Finally, it should be noted that the cycle with $(T_{\mathrm{c}}, T_{\mathrm{h}}) = (T_B^{\beta\mathrm{f}} - \epsilon, T_0^{\alpha\mathrm{f}})$ has a very slightly (<1%) greater efficiency than the other cycles in the 1.5 T χ-optimal family. This is a consequence of the definition of χ, which may be alternately written as $\chi = (Q_{\mathrm{c}}/T_{\mathrm{c}})(\Delta T_{\mathrm{span}}/W)$, showing that with all else equal it is the cycle with lowest T_{c} that has the true maximum efficiency.

IV.4. Discussion

IV.4.1 Effect of Hysteresis on Brayton Performance Metrics

Having discovered simple heuristics to specify the required temperature reservoirs for χ-optimal cycles, it is possible to simulate these cycles for a variety of

hysteresis characteristics (ΔT_{hyst}, $\Delta T_{\mathrm{elast}}$). For each simulation, the performance metrics $\{Q_c, W, \Delta T_{\mathrm{span}}, \chi\}$ are calculated and their dependence on (ΔT_{hyst}, $\Delta T_{\mathrm{elast}}$) is plotted for $B_{\max} = 5.0$ T (Fig. IV.7a) and $B_{\max} = 1.5$ T (Fig. IV.7b).

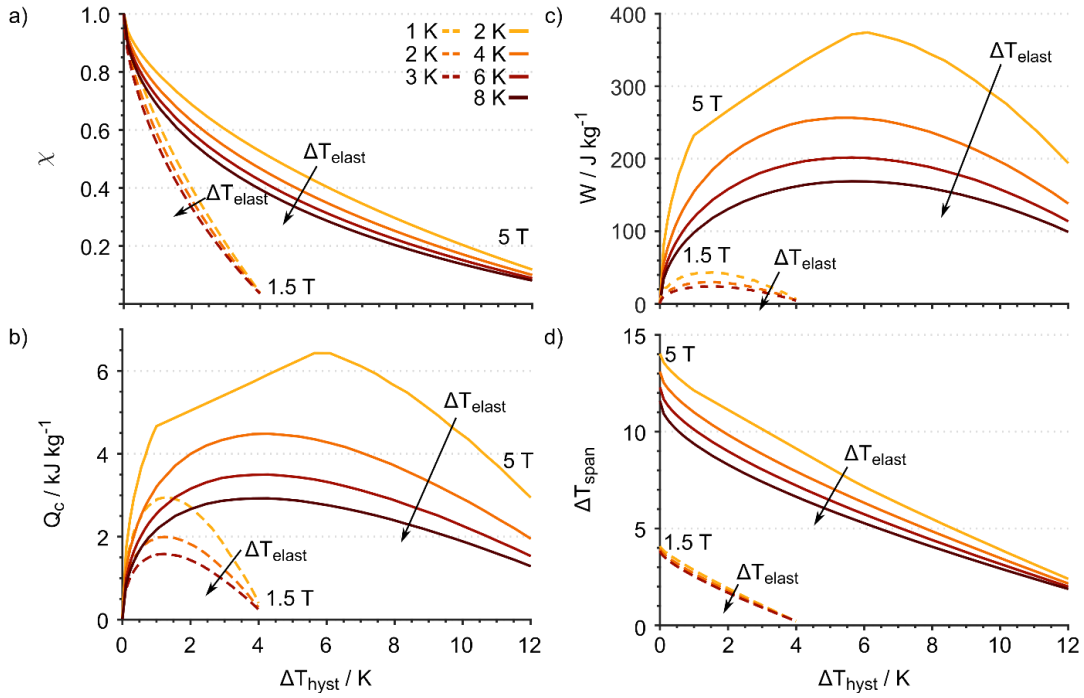

Figure IV.7 Effect of hysteresis on refrigeration metrics for optimized cycles. Dependence of refrigeration performance metrics (a) 2nd law thermodynamic efficiency, χ; (b) specific heat lifted per cycle, Q_c; (c) specific required magnetic work per cycle, W; (d) temperature span, ΔT_{span} on hysteresis model parameters for χ-optimized cycles for field changes from 0 to 1.5 T and to 5.0 T. Reprinted with permission from [26]. © AIP Publishing LLC 2018. DOI 10.1063/1.5022467.

For both maximum magnetic field strengths and for all $\Delta T_{\mathrm{elast}}$, the % Carnot efficiency χ approaches 1.0 as the hysteresis magnitude ΔT_{hyst} decreases towards zero, consistent with the model's complete focus on entropy generation associated with hysteresis losses embodied by Eq. IV.6. As the hysteresis width ΔT_{hyst} increases for 5 T cycles, both the temperature span ΔT_{span} and % Carnot efficiency χ decrease

monotonically, at rates of about -1 K and -7 %, respectively, for each 1 K increase in ΔT_{hyst}. For 1.5 T field constraints, the drop-off in efficiency is even more precipitous, decreasing at a rate of -22 %/K, and the temperature span again decreases at a rate of -1 K/K. In either case, the interaction effect with the sharpness of the transition $\Delta T_{\mathrm{elast}}$ is less significant, although as the transition becomes less sharp, both temperature span and efficiency decrease. On the other hand, the cooling power Q_c and work input W both exhibit inflected behavior, increasing from zero to a maximum at mid-range ΔT_{hyst}, then decreasing again towards zero. Although at first it seems counterintuitive that increasing hysteresis initially increases the cooling power, this is a consequence of limiting focus here to χ-optimized cycles, and the interplay between hysteresis, cooling power, and the horizontal adiabatic legs. Because these legs cut straight across from the 0 T hysteresis loops to the 5 T or 1.5 T loops (Fig. IV.5-6), and because of the finite heat capacity of the phases, the line always ends at high field at some $\varphi > 0$. Thus $\Delta\phi < 1$ and only the remaining $1 - \phi$ fraction of the MST contributes its latent heat to Q_c. As hysteresis increases, the loops grow closer together, so the post-magnetization φ decreases and $\Delta\phi$ approaches unity again; hence the observed initial increase in Q_c as ΔT_{hyst} increases from zero. As ΔT_{hyst} continues to increase, there is so much dissipation and $W_{\mathrm{ref}} = \Delta S \Delta T_{\mathrm{span}}$ becomes so much less than the work input W, that ΔS and Q_c again decrease. A similar trade-off between work produced W or heat absorbed Q versus efficiency has also been investigated for reversible heat engine cycles with adiabats [32] and appears to hold quite generally for these types of cycles. When ΔT_{span} is held constant, increasing hysteresis increases the work input and decreases the cooling power (Fig. IV.3-4).

Using χ-optimized cycles also provides a summary of magnetocaloric refrigerant performance that is useful for comparing candidate materials or specifying benchmarks for future materials design. Taking 80% of Carnot efficiency as a standard for magnetocaloric performance in MR systems (system losses will always decrease net efficiency below this), and assuming extremely sharp transitions with limited regions of co-existence, the NiMnCoIn alloy used here would require a hysteresis of about 1.75 K or less to operate under 5 T magnetic field change, and could be expected to lift 5 kJ/kg of heat in each Brayton cycle over a 12 K temperature span. Under 1.5 T field constraint the performance is even more limited, with an 80% Carnot efficiency cycle requiring less than 0.5 K hysteresis and lifting 2.5 kJ/kg/cycle over 3.5 K. Although this last condition is certainly restrictive, a continually improving ability to control and reduce hysteresis in similar structural phase transitions through lattice matching [33-34] and secondary heat treatments in NiMn compounds [35], specialized magnetic ordering [36] in Fe_2P-structured ferromagnets, and hydrogen doping in $La(Fe,Si)_{13}$ magnetocalorics [37-38] puts this goal within reach [39-40]. Finally, the potential improvement in efficiency of low-hysteresis MR systems over current systems is significant, and has even greater implications for consumers when considering the near-complete replacement of compression work accompanied by significant frictional losses, with magnetic work.

IV.4.2 Comparison of Brayton and Ericsson cycles

With the dependence of MR performance metrics on cycle parameters and hysteresis properties sufficiently characterized for Ericsson (in [18]) and now for Brayton cycle classes, the benefits and drawbacks of each class may be compared. The analysis

based on χ-optimal cycles is necessarily incomplete, so it is useful to visualize the Ericsson and Brayton cycle metrics in a third way using Pareto fronts. Taking the cooling power Q_c and temperature span ΔT_{span} as primary metrics of interest for most cooling systems, the cycles represented throughout Fig. IV.3-4 can be plotted within a $(\Delta T_{span}, Q_c)$ coordinate space (Fig. IV.8, inset) to create a filled region representing feasible cycles for given field constraint and hysteresis.

Most of the cycles in the region are dominated, in the sense that there is at least one other cycle with equal ΔT_{span} and higher Q_c (or equal Q_c, higher ΔT_{span}); however, on the boundary, further increase in Q_c or ΔT_{span} necessarily requires a decrease in the other. For each cycle class, field constraint, and hysteresis width, the Pareto boundary represents the set of optimal cycles that can be obtained when trying to maximize both cooling power and temperature span. As discussed previously, hysteresis critically impacts the $Q_c - \Delta T_{span}$ trade-off, tending to primarily shift the Pareto fronts towards cycles with reduced temperature span; the maximum ΔT_{span} decreases by 1 K for every 1 K addition to ΔT_{hyst}. Although this reduction is somewhat manageable assuming access to 5 T maximum fields, for feasible commercial magnetic refrigeration system operating up to 1.5 T maximum field, even minor hysteresis forces ΔT_{span} reductions from 4 K (7.2 °F) to 2 K (1.8 °F) —and even these rather small temperature spans correspond to infeasible zero-heat load conditions.

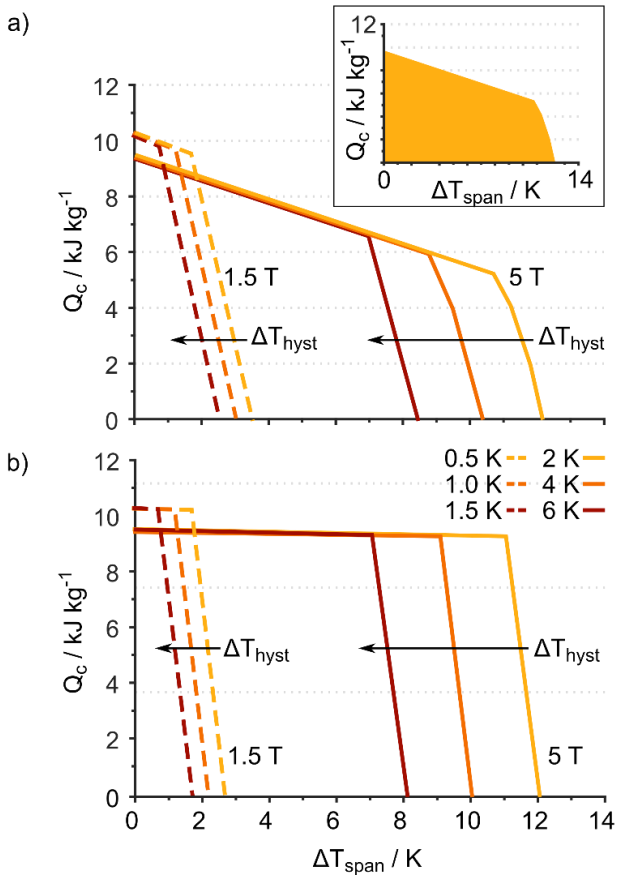

Figure IV.8 Pareto fronts of Brayton and Ericsson cycles. Comparison of a) Brayton and b) Ericsson (data from [18]) cycle performance in terms of Pareto fronts of cooling power Q_c and temperature span ΔT_{span} achieved by the model alloy under 1.5 T and 5.0 T maximum field constraints. As hysteresis ΔT_{hyst} increases, the Pareto fronts are constrained to cycles with reduced Q_c and ΔT_{hyst}. Reprinted with permission from [26]. © AIP Publishing LLC 2018. DOI 10.1063/1.5022467.

The main difference between Brayton and Ericsson cycle classes is in the tradeoffs between Q_c and ΔT_{span}. For a given field change, both Brayton (Fig. IV.8a) and Ericsson (Fig. IV.8b) cycles are able to access cycles with similar ΔT_{span}, with the zero-heat load temperature span for 5 T constraint and 2 K hysteresis for both at about 12 K. Similarly, the zero-span cooling power for both cycle classes is about equal, at 9 kJ/kg for 5.0 T cycles and 10 kJ/kg for 1.5 T cycles. But for Ericsson cycles, the penalty

in cooling power for increased temperature span is nearly negligible across the range, up to the point where only partial phase transformation is possible (the "knee" on the Pareto curves). For Brayton cycles, on the other hand, there is a significant trade-off between the cooling power and temperature span, with Q_c decreasing by about -2 kJ/kg for each 1 K increase in ΔT_{span}. This is the same effect discussed earlier due to the finite heat capacities of the pure phases, where the positively-sloped $S(T)$ curves intersect the horizontal adiabats at a higher ending phase fraction φ than they otherwise would. For Ericsson cycles, the horizontal adiabats are replaced with constant-field legs that more nearly follow along the $S(T)$ curves and the penalty in Q_c incurred for increased ΔT_{span} is far smaller. It is evident that the Brayton $Q_c - \Delta T_{span}$ trade-off would also be minimized if the specific sensible heat capacities of the pure phases of the refrigerant were significantly reduced. In this limit, the Brayton cycle performance would essentially approach that of a corresponding Ericsson cycle, but while retaining its relative advantage of greater cycle frequencies and thus, heat lifted per unit time.

IV.5 Conclusion and Implications

The investigation of the effects of hysteresis and Brayton cycle constraints on resultant refrigeration performance has clear implications for designers at both the materials and systems levels. Cyclic heat lifted, required work, temperature span, and efficiency all depend strongly on the transformation behavior of the magnetocaloric refrigerant, regardless of cycle class or field constraint. The transformation properties are in turn determined by the temperatures at which the martensitic phase transition occurs at given field, as well as the hysteresis and sharpness manifested by the transition. The

strong dependence of performance metrics on transformation temperatures, especially at lower fields, defines an application space with narrow tolerance; for example, at 1.5 T and minimal hysteresis, the model alloy requires temperature reservoirs at about 310 K ± 1 K to maintain efficiency > 50%. Therefore, materials engineers should design for specific applications (*e.g.*, refrigeration from 4.5 C to 30 C vs. air conditioning from 25 C to 35 C); similarly, systems engineers should be advised that realizing magnetic refrigeration will likely require more complicated systems built on cascading or regeneration.

At the same time, refrigerant hysteresis presents a critical obstacle to MR systems, and although the analyses are expected to be somewhat different for competing refrigerant alloy systems, the requirement of hysteresis < 1 K in order to obtain reasonably high efficiency performance at 1.5 T appears to be a good benchmark, with the model alloy requiring 45 J/kg work to obtain 2.75 J/g heat lifted, 4 K temperature span, and 75% Carnot efficiency under these conditions. The methodology developed here explicitly considers internal hysteresis losses as the only source of cycle inefficiencies in order to create a system agnostic, material focused analysis. In all practical systems, external losses like fluid friction and finite temperature difference between the magnetocaloric bed and the external heat transfer fluid will also be significant, compounding the adverse effects of internal hysteresis losses even further. Finally, the finding that Brayton cycles are on par with Ericsson cycles in terms of efficiency means that high-efficiency MR systems may be built on adiabatic processes with faster cycle times— provided the improvement in frequency is great enough to

offset Brayton cycles' reduced heat lifted per cycle. The convergence of Brayton and Ericsson cycles as the refrigerant's specific sensible heat capacities decrease suggests reducing sensible heat capacity could be a path forward to design refrigerants for high-performance Brayton cycles; however, given the convergence of all solid-state molar heat capacities to $3R$ around room temperature, this is probably not actionable beyond simply increasing the mass density of refrigerant materials.

IV.6 References

1. O. Gutfleisch, M. A. Willard, E. Bruck, C. H. Chen, S. G. Sankar, and J. P. Liu, Adv. Mater. **23**, 821-842 (2011).
2. S. L. Russek and C. B. Zimm, Int. J. Refrig. **29**, 1366-1373 (2006).
3. V. Franco, J. S. Blazquez, B. Ingale, and A. Conde, Annu. Rev. Mater. Res. **42**, 305-342 (2012).
4. V. K. Pecharsky and K. A. Gschneidner, Jr., Phys. Rev. Lett. **78**, 4494-4497 (1997).
5. K. A. Gschneidner, Jr., Y. Mudryk, and V. K. Pecharsky, Scripta Mater. **67**, 572-577 (2012).
6. Z. Zhang, R. D. James, and S. Muller, Acta Mater. **57**, 4332-4352 (2009).
7. V. Basso, M. Kuepferling, C. P. Sasso, and M. LoBue, IEEE Trans. Magn. **44**, 3177-3180 (2008).
8. A. Kosogor, N. J. Matsishin, and V. A. L'vov, Phase Trans. **86**, 796-810 (2013).
9. C. K. Atli, B. E. Franco, I. Karaman, D. Gaydosh, and R. D. Noebe, Mater. Sci. Eng. A **574**, 9-16 (2013).

10. E. Brück, N. T. Trung, Z. Q. Ou, and K. H. J. Buschow, Scripta Mater. **67**, 590-593 (2012)

11. F. Guillou, G. Porcari, H. Yibole, N. van Dijk, and E. Brück, Adv. Mater. **26**, 2671-2675 (2014)

12. V. Basso, C. P. Sasso, and M. LoBue, J. Mag. Mag. Mater. **316**, 262-268 (2007).

13. V. Basso, C. P. Sasso, G. Bertotti, and M. LoBue, Int. J. Refrig. **29**, 1358-1365 (2006).

14. W. Brey, G. Nellis, and S. Klein, Int. J. Refrig. **47**, 85-97 (2014).

15. G. V. Brown and S. S. Papell, "Regeneration tests of a room temperature magnetic refrigerator and heat pump" (1978). Unpublished manuscript.

16. C. Zimm, A. Jastrab, A. Sternberg, V. Pecharsky, K. Gschneidner, Jr., M. Osborne, and I. Anderson, Adv. Cryog. Eng. **43**, 1759-1766 (1998).

17. G. V. Brown, J. Appl. Phys. **47**, 3673-3680 (1976).

18. T. D. Brown, N. M. Bruno, J. Chen, I. Karaman, J. H. Ross, Jr., and P. J. Shamberger, JOM **67**, 2123-2132 (2015).

19. T. D. Brown, I. Karaman, and P. J. Shamberger, MRX **3**, 1-18 (2016).

20. N. M. Bruno, I. Karaman, J. H. Ross, Jr., and Y. I. Chumlyakov, Rev. Sci. Instrum. **86**, 113902 (2015).

21. J. A. Monroe, I. Karaman, B. Basaran, W. Ito, R. Y. Umetsu, R. Kainuma, K. Koyama, and Y. I. Chumlyakov, Acta Mater. **60**, 6883–91 (2012).

22. J. H. Chen, N. M. Bruno, I. Karaman, Y. Huang, J. Li, and J. H. Ross, Jr., Acta Mater. **105**, 176–81 (2016).

[23] I. D. Mayergoyz, IEEE Trans. Magn. **5**, 603-608 (1986).

[24] P. J. Shamberger and F. S. Ohuchi, Phys. Rev. B **79**, 144407 (2009).

[25] V. Basso, C. P. Sasso, K. P. Skokov, O. Gutfleisch, Phys. Rev. B **85**, 014430 (2012).

[26] T. D. Brown, T. Buffington, P. J. Shamberger, J. Appl. Phys. **123**, 185101 (2018).

[27] G. Bertotti, Phys. Rev. Lett. **76**, 1739-1742 (1996).

[28] C. P. Sasso, V. Basso, M. LoBue, G. Bertotti, Physica B **372**, 9-12 (2006)

[29] I. D. Mayergoyz and G. Friedman, J. Appl. Phys. **61**, 3910-3912 (1987).

[30] H. Wada and Y. Tanabe, Appl. Phys. Lett. **79**, 3302-3304 (2001).

[31] A. Fujita, S. Fujieda, Y. Hasegawa, and K. Fukamichi, Phys. Rev. B **67**, 104416 (2003).

[32] P. T. Landsberg and H. S. Leff, J. Phys. A Math. Gen. **22**, 4019-4026 (1989).

[33] R. Zarnetta, R. Takahashi, M. L. Young, A. Savan, Y. Furuya, S. Theinhaus, B. Maafs, M. Rahim, J. Frenzel, H. Brunken, Y. S. Chu, V. Srivastava, R. D. James, I. Takeuchi, G. Eggeler, and A. Ludwig, Adv. Funct. Mater. **20**, 1917-1923 (2010).

[34] Y. Song, X. Chen, V. Dabade, T. Shield, and R. James, Nature **502**, 85–8 (2013).

[35] N. M. Bruno, C. Yegin, I. Karaman, J. Chen, J. H. Ross, Jr., J. Liu, and J. Li, Acta Mater. **74**, 66-84 (2014).

36. N. H. Dung, Z. Q. Ou, L. Caron, L. Zhang, D. T. Cam Thanh, G. A. de Wijs, R. A. de Groot, K. H. Jurgen Buschow, and E. Bruck, Adv. Energy Mater. **1**, 1215-1219 (2011).

37. J. Lyubina, O. Gutfleisch, M. D. Kuz'min, M. Richter, J. Mag. Magn. Mater. **321**, 3571-3577 (2009).

38. J. Lyubina, R. Schäfer, N. Martin, L. Schultz, O. Gutfleisch, Adv. Mater. **22**, 3735-3739 (2010).

39. S. Jacobs, J. Auringer, A. Boeder, J. Chell, L. Komorowski, J. Leonard, S. Russek, C. Zimm, Int. J. Refrig. **37**, 84-91 (2014).

40. K. Navickaite, H. N. Bez, T. Lei, A. Barcza, H. Vieyra, C. R. H. Bahl, K. Engelbrecht, Int. J. Refrig. **86**, 322-330 (2018).

CHAPTER V

EFFECT OF MAGNETOCALORIC PROPERTIES AND HYSTERESIS ON POTENTIAL EFFICACY OF MAGNETIC REFRIGERATION CYCLES

V.1 Introduction

Coupled first-order magneto-structural transformations in alloy systems like Ni-Mn-X magnetic shape memory alloys (MSMAs) [1], La-Fe-Si and its hydrides [2], and Fe_2P based transition metal pnictides [3] give rise to a giant magnetocaloric effect (GMCE) [4], in which discontinuous entropy changes on the order of 15-30 J/kg K are accessible by applying external magnetic fields. Such an effect would provide an effective material basis for solid-state magnetic refrigeration (MR) [5-7], in which repeated magnetization and demagnetization of a GMCE refrigerant pumps heat from a refrigerated volume to the ambient reservoir, in much the same way as conventional systems provide cooling through repeated compression and expansion of liquid-vapor refrigerant. The main advantages of MR relative to vapor cooling are (1) the replacement of complex compressors operating at hazardous pressures and their attendant frictional losses, by single-unit magnet arrays operating at ambient pressure with a minimum of moving parts; (2) the replacement of harmful gaseous refrigerants that when leaked pose long-term extreme environmental hazards, by stable generally non-toxic solid regenerator beds with low vapor pressure; (3) the replacement of low-efficiency thermodynamic cycles requiring highly irreversible Joule-Thomson expansion steps, by

naturally regenerative cycles that can approach optimal efficiency at 80 % - 90 % of the Carnot limit [8].

From a systems design standpoint, there are four critical challenges limiting implementation of these GMCE-based MR systems: (1) the cost of the GMCE material, although this continually reduces in proportion with reduced rare-earth content; (2) the cost of the magnetic field required to actuate the magneto-structural transformation, although again, cost reductions are possible through clever arrangement of permanent magnets [9] to obtain uniform ~2 T fields; (3) the necessarily slow cycle frequencies due to slow transformation kinetics, which translates directly to slow cycle frequencies and low cooling powers; (4) the smaller transformation entropy for solid-solid transformations as compared to liquid-vapor transformations (~20-30 J/kg-K vs. ~1000 J/kg-K in R-134a [10]), which means that the same amount of entropy generation will cause a correspondingly greater proportional decrease in the *accessible* entropy of transformation that enables heat absorption, as below:

$$dS_{\text{trans}} = \delta S_{\text{acces}} + \delta S_{\text{gen}}, \qquad \delta S_{\text{gen}} \geq 0. \tag{V.1}$$

Unfortunately, the same discontinuous changes in crystal structure that enable the first order phase transformations underlying GMCE in the first place also induce interfacial and elastic energy barriers as the daughter phase forms and grows in the parent [11,12]. When these barriers are substantial, the transformation in either direction cannot proceed until the barriers are overcome by an over-driving force, leading to

hysteretic energy dissipation. This hysteresis becomes a further limiting factor in the above challenges, since hysteresis increases the driving force, and therefore the magnetic field required to induce and complete the transformation, often to the point of infeasibility; hysteresis often manifests rate-dependent effects, so that required over-driving forces are larger at faster rates; hysteretic processes are by definition irreversible, and therefore, associated with entropy generation that decreases the amount of accessible transformation entropy.

Although by far the most important consideration for determining MR efficiency, transformation hysteresis is just one of several transformation properties that must be simultaneously optimized over for a given application: the transformation critical temperatures at specified magnetic fields should be well matched to the temperature reservoirs of the problem at hand [13,14], and the transformation's enthalpy should be as large as possible. Although effective materials design principles for minimizing hysteresis in each of the major GMCE systems have been developed [15-23], the three transformation properties are often coupled in complex ways, and it is only in rare instances that hysteresis minimization can be achieved without also adversely affecting the other transformation properties that make MR viable. It is more than likely that practical GMCE materials optimization will be Pareto-optimal, retaining some non-zero hysteresis in order to better satisfy other constraints on critical temperatures and hysteresis. Thus understanding of the dependence of system-level heat flows and efficiencies on GMCE properties must move beyond the heuristic of *always seek minimum hysteresis* to instead *what degree of hysteresis is allowable for the particular*

design problem and what trade-offs are there with the other transformation properties? From a materials design standpoint, an MR systems analysis framework that incorporates hysteresis effects is crucial.

At the same time, the cyclic nature of MR systems is essential and must be appreciated, *i.e.*, optimization of GMCE transformation properties must account for the behavior of the GMCE state properties along particular and heavily constrained paths in $T - B$ space. Such an analysis may lead to counter-intuitive results, for example, it has long been a guiding design principle that optimized GMCE materials should have large magnetic entropy change ΔS_{m} and adiabatic temperature change ΔT_{ad} over the largest possible temperatures, so that quantities such as $\int \Delta S_{\mathrm{m}} \mathrm{d}T$ and $\int \Delta T_{\mathrm{ad}} \mathrm{d}T$ are maximized [24]. However, these heuristics ignore fundamental tradeoffs occurring during cyclic conditions: for example, because ΔS_{m} and ΔT_{ad} refer to different thermodynamic paths through the GMCE transformation (isothermal and adiabatic field application, respectively), it is impossible for a single $T - B$ cycle to traverse both paths required to obtain its maximum ΔS_{m} and ΔT_{ad}. For a given work input (constrained by the maximum available magnetic field), if the cycle pumps heat across a maximum temperature span its carried heat load must decrease, and vice-versa. Recent simulation work along these lines has suggested that for Brayton cycles constrained to 1.5 T maximum field, only about ~25% of the total ΔS_{m} is actually accessible in cycles obtaining their maximum temperature span [13]. Furthermore, the presence of hysteresis appears to primarily affect the effective temperature span, subtracting 1 K from the effective span for each 1 K increase in thermal hysteresis; with ΔT_{ad} at 1.5 T already

starting out at 1-8 K, the resultant restrictions on maximum allowable hysteresis then become very strict [14]. For Brayton cycle applications at least, it appears that materials design tradeoffs that decrease ΔS_{m} and ΔT_{hyst} together while increasing ΔT_{ad} could still ultimately be in favor of increasing potential MR performance.

In this work we further investigate these tradeoffs between GMCE properties, transformation hysteresis, and potential cycle performance, using a previously developed modeling framework to directly simulate the hysteretic magnetization and entropy response of candidate GMCE materials under magnetic Brayton cycles of interest. Using experimental data from the literature, we parameterize material models for members of each of the leading GMCE materials classes, $(Ni,Co)_2(Mn,In)_2$, $(Mn,Fe)_2(P,Si)$, and $La(Fe,Si)_{13}$, (Table V.1) and compare their potential performance in cycles with 1.5 T and 5 T maximum field using Pareto fronts of cooling power and temperature span. Models are also created for comparison against Gd, a non-GMCE benchmark refrigerant that has been used successfully in several proof-of-concept MR systems [25-27]. Finally, in order to decouple the effect of transformation hysteresis on performance we compare performance for "actual" materials with hysteresis taken from data, with "ideal" material models where the hysteresis model is uniformly reduced to 0.1 K hysteresis and 0.1 K phase coexistence (with all other magnetothermal model parameters set constant). Together, these explorations both demonstrate the feasibility of GMCE based refrigeration for commercial applications, and begin to explore the interacting effects of transformation and GMCE properties on potential MR performance metrics.

ID	Composition	$M(T,B)$ Ref.	$S(T,B)$ Ref.	Notes
NiMnX	$(Ni_{0.9}\,In_{0.1})(Mn_{0.732}\,In_{0.268})$	[28]	[29]	Combined with unpublished PPMS data
Fe2P-1	$(Mn_{1.25}\,Fe_{0.70})(P_{0.49}\,Si_{0.51})$	[30]	[31]	Combined Mn and Fe rich data
Fe2P-2	$(Mn_{0.66}\,Fe_{1.29})(P_{0.63\&0.67}\,Si_{0.37\&0.33})$	[31]	[31]	Combined two P/Si ratios
LaFeSi	$La(Fe_{0.88}\,Si_{0.12})_{13}$	[32]	[32]	
Gd	Gd	[33]	[33]	Along $[10\bar{1}0]$ axis

Table V.1 Summary of data sources. Experimental data from named sources are used to parametrize material models, thereby coupling the analysis framework to real observations of GMCE material properties.

V.2 Methods

Our method for simulating potential and Brayton and Ericsson magnetic refrigeration cycles is described in detail elsewhere [8,13,14], but the main points are (1) incorporation of experimental hysteretic magnetization and entropy data, and their partition into models for the pure-phase magnetization and entropy (Curie-Weiss and Debye-Sommerfeld models) and transformation hysteresis characteristic (Preisach models [34]), extrapolated across the entire temperature-magnetic field $T-B$ space; (2) use of the single phase and hysteresis models to reduce a specified cycle represented as a path in *T*-*B* space to an equivalent one in free energy space along which the phase fraction evolution ϕ is easily evaluated; (3) computation of bulk magnetization $M(T,B)$ and entropy $S(T,B)$ properties *along the specified cycle* through mass-averaged rule-of-mixtures formulae. We note this partition and recombination of single-phase volumetric properties under the rule of mixtures should hold for the GMCE materials modeled here, given that magnetic domain hysteresis is excluded due to their ferromagnetic phases being magnetically soft, and due to the relatively low interfacial entropy contained in

ordered twin walls and habit planes relative to the bulk entropy terms. Finally, the analysis concludes with (4) calculation of the cycle-specific MR performance metrics: the cooling power Q_c, the required work input W, the effective temperature span ΔT_{span}, and the 2nd Law thermodynamic efficiency χ (Eqn. V.2-V.5):

$$Q_c = \oint T(dS - dS_{gen}), \tag{V.2}$$

$$W = \oint B\, dM = -\oint M\, dB, \tag{V.3}$$

$$\Delta T_{span} = T_h - T_c, \tag{V.4}$$

$$\chi = \frac{Q_c}{W}\left(\frac{T_c}{T_h - T_c}\right)^{-1}. \tag{V.5}$$

$M(T,B)$: α / β					
Alloy	**Phase**	**T_C / K**	**M_s / Am^{2}kg^{-1}**	**J**	**R^2**
NiMnX	α	90 ± 2	10.2 ± 0.1	20.7 ± 0.4	0.54
	β	387 ± 1	157 ± 0.5	2.5 ± 0.1	0.99
Fe2P-1	α	340 ± 50	166 ± 95	2 ± 24	0.92
	β	291 ± 1	200 ± 30	2.0 ± 0.5	0.91
Fe2P-2	α	470 ± 40	178 ± 35	3 ± 18	0.92
	β	334 ± 1	183 ± 11	3.5 ± 0.2	0.98
LaFeSi	α	270 ± 440	170 ± 140	4 ± 80	0.78
	β	197 ± 1	122 ± 13	2.6 ± 1.0	0.59
Gd	N/A	309	261	3.8	

Table V.2 Summary of magnetization model parameters.Table of model parameters for Brillouin functions used to model pure-phase magnetization **M**(**T**, **B**) for low temperature (**α**) and high-temperature (**β**) phases.

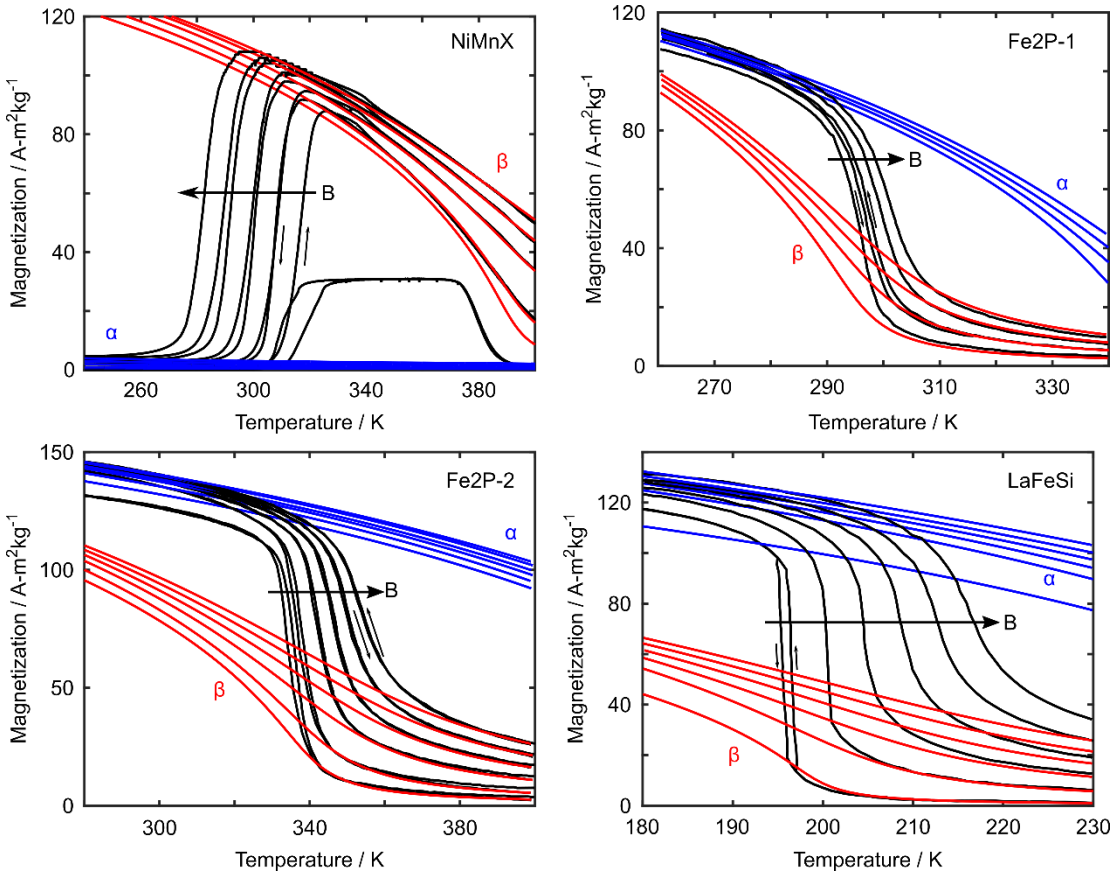

Figure V.1 Magnetization data and models.Comparison of experimental magnetization data and partition into single-phase Brillouin models $\mathbf{M}(\mathbf{T},\mathbf{B})$ for low temperature ($\boldsymbol{\alpha}$) and high-temperature ($\boldsymbol{\beta}$) phases.

In every case, the models describing the thermomagnetic properties $S^{\alpha,\beta}(T,B)$ and $M^{\alpha,\beta}(T,B)$ of the single phases are purely material models, in the sense that they are parameterized by constants that depend only on the alloy under consideration, and are independent of (T,B). These parameters are also intended to have some real physical meaning behind them, consisting of the saturation magnetization M_S, Curie temperature T_C, and average net angular momentum j for the magnetization models (Fig. V.1, Table V.2), and the Debye temperature T_D and Sommerfeld coefficient γ for the entropy models (Fig. V.2, Table V.3).

$S(T,B)$: α / β				
Alloy	**Phase**	T_D / K	γ / J (kg K^2)$^{-1}$	R^2
NiMnX	α	341 ± 4	0.14 ± 0.01	1.00
	β	400 ± 6	0.41 ± 0.01	0.98
Fe2P-1	α	803 ± 87	0.32 ± 0.08	0.95
	β	601 ± 2	0.06 ± 0.01	0.79
Fe2P-2	α	803 ± 87	0.32 ± 0.08	0.95
	β	601 ± 2	0.06 ± 0.01	0.79
LaFeSi	α	100 ± 570	0.40 ± 0.40	0.99
	β	87.1 ± 0.4	0.26 ± 0.01	0.79
Gd	N/A	152.5	0.37	

Table V.3 Summary of entropy model parameters.Table of model parameters for Debye-Sommerfeld functions used to model pure-phase entropy **S**(**T**, **B**) for low temperature (**α**) and high-temperature (**β**) phases.

Similarly, after reducing measured thermal or magnetic hysteresis to the fundamental phase fraction-free energy hysteresis characteristic $\varphi\{\Delta G\}$, the hysteretic properties for each modeled alloy are represented solely by a single set of materials parameters; in this case they are the means $\vec{\boldsymbol{\mu}}$, variance $\vec{\boldsymbol{\sigma}}$, and weighting λ of a pseudo-Voight (mixed Gaussian-Lorentzian) fit to the two-dimensional Preisach distribution μ, which in turn describe the hysteresis and coexistence of the observed phase transformation (Fig. V.3, Table V.4):

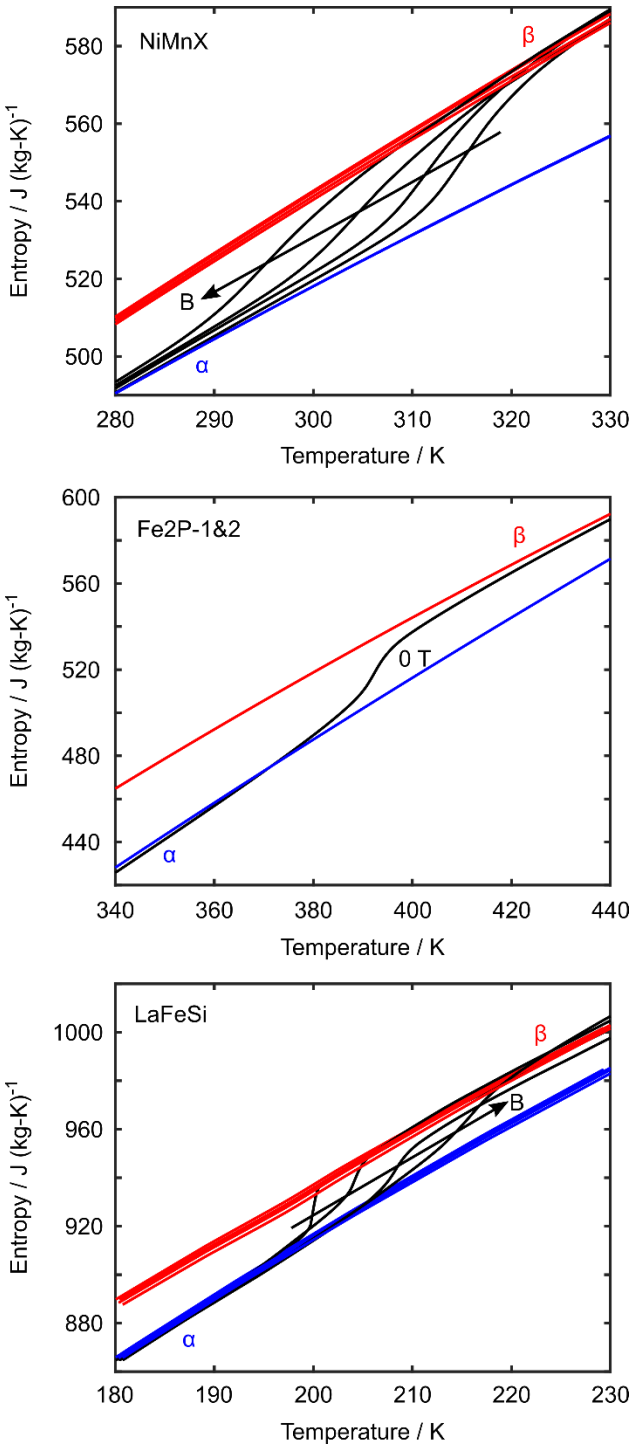

Figure V.2 Entropy data and models.Comparison of experimental entropy data and partition into single-phase Debye-Sommerfeld models **S**(**T**, **B**) for low temperature (**α**) and high-temperature (**β**) phases.

The equations governing the pseudo-Voight Preisach model are as below:

$$\mu(x_1, x_2;\ \boldsymbol{\mu}, \boldsymbol{\sigma}, \lambda) = \lambda\, G(\hat{x}_1, \hat{x}_2;\ \boldsymbol{\mu}, \boldsymbol{\sigma}) + (1-\lambda)\, L(\hat{x}_1, \hat{x}_2;\ \boldsymbol{\mu}, \boldsymbol{\sigma}), \qquad (V.6)$$

$$\hat{\boldsymbol{x}} = \boldsymbol{\mu} + \boldsymbol{R}(+45°)(\boldsymbol{x} - \boldsymbol{\mu}), \qquad (V.7)$$

$$G(\hat{x}_1, \hat{x}_2;\ \boldsymbol{\mu}, \boldsymbol{\sigma}) = 2\pi^{-1}({\sigma_1}^2 + {\sigma_2}^2)^{\frac{1}{2}} \exp\left(-\left(\frac{(\hat{x}_1 - \mu_1)^2}{2{\sigma_1}^2} + \frac{(\hat{x}_2 - \mu_2)^2}{2{\sigma_2}^2}\right)\right), \qquad (V.8)$$

$$L(\hat{x}_1, \hat{x}_2;\ \boldsymbol{\mu}, \boldsymbol{\sigma}) = 2\pi^{-1}(\sigma_1\sigma_2)^{-1}\left(\frac{(\hat{x}_1 - \mu_1)^2}{{\sigma_1}^2} + \frac{(\hat{x}_2 - \mu_2)^2}{{\sigma_2}^2} + \frac{1}{4}\right)^{-1}. \qquad (V.9)$$

$\phi\{\Delta G\}$: Pseudo-Voight Preisach parameters					
Alloy	**Range / K**	$\boldsymbol{\lambda}$	$(\boldsymbol{\mu_1}, \boldsymbol{\mu_2})$ / K	$(\boldsymbol{\sigma_1}, \boldsymbol{\sigma_2})$ / K	$\mathbf{R^2}$
NiMnX	[292.9, 334.2]	0.98 ± 0.34	(319.0, 312.3) ± (0.1, 0.1)	(4.4, 0.001) ± (0.4, 0.02)	0.99
Fe2P-1	[269.2, 307.6]	0.99 ± 0.02	(293.1, 296.4) ± (0.7, 0.7)	(3.6, 0.68) ± (0.2, 0.1)	0.99
Fe2P-2	[307.4, 362.2]	0.77 ± 0.28	(336.8, 336.0) ± (0.06, 0.06)	(4.0, 0.02) ± (1.4, 0.1)	0.98
LaFeSi	[180.5, 212.1]	0.99 ± 0.01	(195.7, 194.7) ± (0.1, 0.1)	(0.53, 0.02) ± (0.11, 0.03)	0.95

Table V.4 Summary of Preisach model parameters.Table of model parameters for pseudo-Voight Preisach hysteresis operators used to model the free energy-phase hysteresis loops, $\boldsymbol{\phi}\{\boldsymbol{\Delta G}\}$.

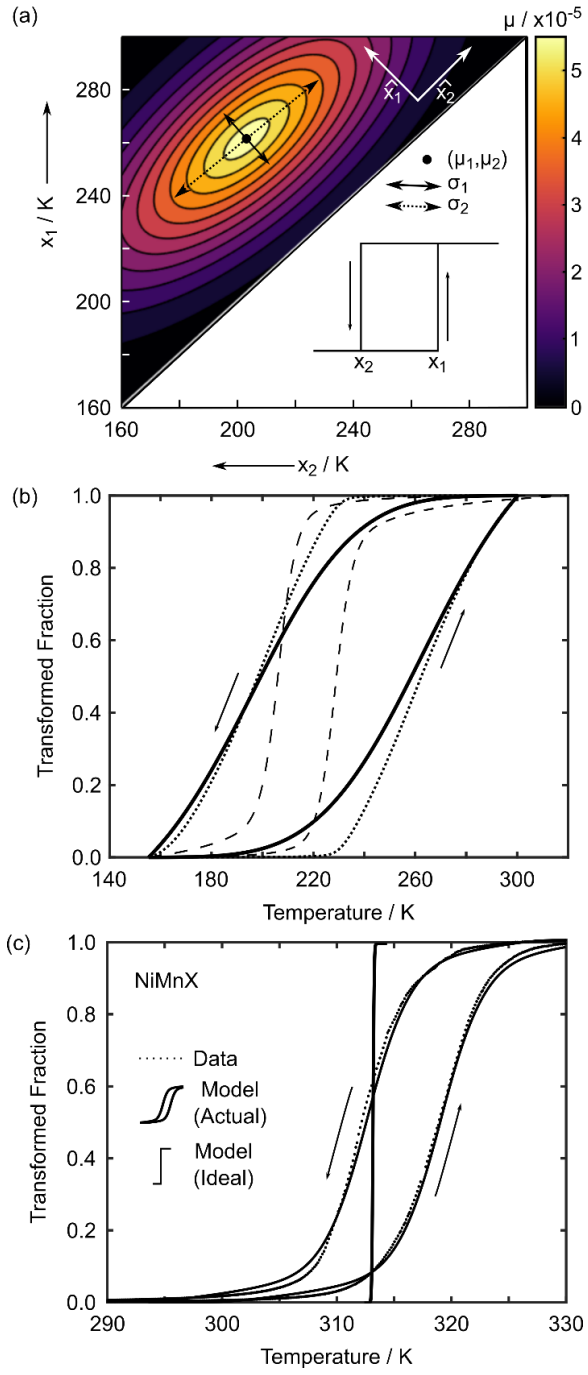

Figure V.3 Preisach hysteresis models. (a) Generalized pseudo-Voight distribution $\boldsymbol{\mu(x_1, x_2)}$ in the Preisach plane. (b) Corresponding hysteresis loop to Preisach model in a) [dark bold], in addition two other hysteresis loops enabled by model Eqn. V.6-V.9 [dashed, dotted]. (c) Fitted Preisach model using NiMnX experimental data, as well as idealized minimal hysteresis loop as discussed in the text.

Although somewhat more abstract, these parameters can be interpreted to describe the curvature and shape of the free-energy scaled hysteresis loops (Fig. V.3b), which again, is a property of the transformation of each alloy, and not of the $T - B$ state it happens to be in at a given point in the cycle. Models were fit using non-linear least-squares regression as implemented in Matlab, and uncertainties are computed using the numerical estimate of the Jacobian of the model. Note that these can be quite large when fitting models to relatively sparse data sets, as here, so we have also included adjusted R^2 values as another measure of goodness-of-fit.

$\phi\{\Delta G\}$: Pseudo-Voight Preisach parameters (Idealized)				
Alloy	**Range / K**	λ	(μ_1, μ_2) / K	(σ_1, σ_2) / K
NiMnX	[312.6, 314.6]	1.00	312.6 + (0.75, 0.75)	(0.1, 0.1)
Fe2P-1	[287.4, 289.4]	1.00	287.4 + (0.75, 0.75)	(0.1, 0.1)
Fe2P-2	[333.8, 335.8]	1.00	333.8 + (0.75, 0.75)	(0.1, 0.1)
LaFeSi	[195.3, 197.3]	1.00	195.3 + (0.75, 0.75)	(0.1, 0.1)
Gd	[400.0, 402.0]	1.00	400.0 + (0.75, 0.75)	(0.1, 0.1)

Table V.5 Summary of Preisach idealized model parameters. Table of model parameters for pseudo-Voight Preisach hysteresis operators used to model the free energy-phase hysteresis loops, $\boldsymbol{\phi}\{\boldsymbol{\Delta G}\}$, for ~0 hysteresis.

Finally, in order to better understand the ways in which hysteresis of the magnetocaloric phase transformation adversely affects the performance of potential magnetic refrigeration cycles, we have also completed the cycle simulation process for a standardized "minimal hysteresis" characteristic, which generates hysteresis loops with ~0.1 K hysteresis width and ~0.1 K coexistence (Fig. V.3c, Table V.5). This represents

the performance of each magnetocaloric alloy if it were possible to reduce the phase transformation hysteresis without affecting any of the alloy's thermomagnetic properties, including the entropy and magnetization changes across the phase transformation. Although this condition is an ideal limit for the actual non-negligible tradeoffs between hysteresis and thermomagnetic properties in these alloy systems, many investigations report techniques for reducing hysteresis while maintaining the majority of the large entropy and magnetization changes across the phase transition. This work emphasizes the need for further investigations in this direction in order to put magnetic refrigeration systems on par with current vapor compression systems, and in the meantime gives some insight into the design constraints between hysteresis and thermomagnetic properties to guide future magnetocaloric materials design.

The most relevant transformation properties for each alloy are the change in magnetization across the transformation ΔM, the isothermal field-induced entropy change across the transformation ΔS_{m}, the heat capacities C_{p} before and after the transformation in the low and high temperature α and β phases, and the hysteresis ΔT_{hyst} and phase coexistence $\Delta T_{\mathrm{elast}}$ observed in the transformation (Table V.6). Compared to the full magnetization, entropy, and hysteresis surfaces throughout the temperature-magnetic field space for each alloy, these parameters are necessarily incomplete. However, it is common for experiments to summarize their investigations within these parameters, and therefore any useful analysis of performance metrics should ultimately be referenced to these parameters, as we will here.

Summary of Transformation Properties						
Alloy	$\Delta \boldsymbol{M}$	$\Delta \boldsymbol{S_m}$	$\boldsymbol{C_p(\alpha)}$	$\boldsymbol{C_p(\beta)}$	$\Delta \boldsymbol{T_{hyst}}$	$\Delta \boldsymbol{T_{elast}}$
NiMnX	88	24.6	410	530	7.1	34.2
Fe2P-1	78	29.6	510	520	4.2	34.2
Fe2P-2	96	29.6	510	520	3.2	51.6
LaFeSi	94	22.5	475	465	4.5	27.1

Table V.6 Summary of transformation properties. Parameters for change in magnetization $\boldsymbol{\Delta M}$, magnetic entropy $\boldsymbol{\Delta S_m}$, heat capacities $\boldsymbol{C_p}$, transformation hysteresis $\boldsymbol{\Delta T_{hyst}}$ and phase coexistence $\boldsymbol{\Delta T_{elast}}$ provide concise, but incomplete summary of relevant material properties.

V.3 Results and Discussion

V.3.1 Effects of Maximum Field Constraints on Cycle Performance

Once the material models have been defined in terms of $M(T,B)$, $S(T,B)$ and $\phi\{\Delta G\}$, it is relatively straightforward to evaluate these models along specific $T-B$ paths corresponding to Brayton cycles of interest. By simulating Brayton cycles across the space of potential magnetic field changes and cooling / heating temperature reservoirs, the cycle metrics Eqn. V.2-V.5 can be computed and collected throughout the cycle space. As a summary, it is especially useful to visualize the cycle efficacy of particular magnetocaloric alloys as the Pareto optimality fronts of cycles with Pareto-optimal heat absorption Q_c for a given temperature span ΔT_{span}, these along with 2nd law efficiency χ being the primary "outputs" of concern for any desired refrigeration system. Such Pareto fronts in $Q_c - \Delta T_{span}$ space for each of the alloy families (with actual and idealized hysteresis characteristics) undergoing magnetic Brayton cycles between 0 T and 5 T and 0 and 1.5 T have been generated (Fig. V.4) to facilitate direct comparisons.

First, we note that the simulated refrigeration metrics for the GMCE alloys are well within feasibility for applications of interest. For the relatively unlikely case of Brayton cycles between 0 and 5 T, the zero-heat load temperature span for alloys modeled with realistic hysteresis (solid lines) varies from about 7-10 K, almost the temperature differential between an air-conditioned interior (23.9 °C) and the outside environment (35 °C) on a warm day. The zero-temperature span cycles' cooling power varies from 4-10 J/g, about enough for a 1 kg MR bed to freeze a 100 g block of water at 0 °C after 6 cycles. Realistic cycles will operate between zero-heat load and zero-temperature span conditions, obtaining 20-60 % of Carnot efficiency while doing so, depending on the alloy system.

Although applied fields of order 5 T are a helpful standpoint from which to begin analyzing potential refrigeration cycles built on GMCE in reported material systems, they can only be generated by magnetic materials supercooled to a superconducting state, a major obstacle to the economics of magnetic refrigeration. The largest magnetic fields capable of being produced by permanent magnetic systems are of order 1.5 T, and these require careful engineering of the permanent magnet array. This change from 5 T to 1.5 T has a profound effect on the Brayton heating load curves (again, for as-modeled hysteresis), decreasing the zero-temperature span cooling powers by 2/3 to 4-5 J/g, and the zero-heat load temperature spans for all materials excepting NiMnX to 2-4 K, meaning that systems-level augmentation through cascading or active regeneration is absolutely required for Brayton cycles between 0 T and 1.5 T. This decrease is a simple consequence of the thermodynamic laws: when changing from 5 T to 1.5 T maximum

fields, only about $\frac{1.5}{5.0} = 0.3$ of the total work is available, and so the available refrigeration work $W_{\text{ref}} = \Delta S \Delta T$ is about 1/3 as much, and so at constant ΔT_{span} the cooling power is reduced by 1/3, and vice-versa. The cycle efficiencies away from these limiting cases are mostly unchanged, these being dependent on hysteresis losses, which scale together with the reduced cooling power and work input.

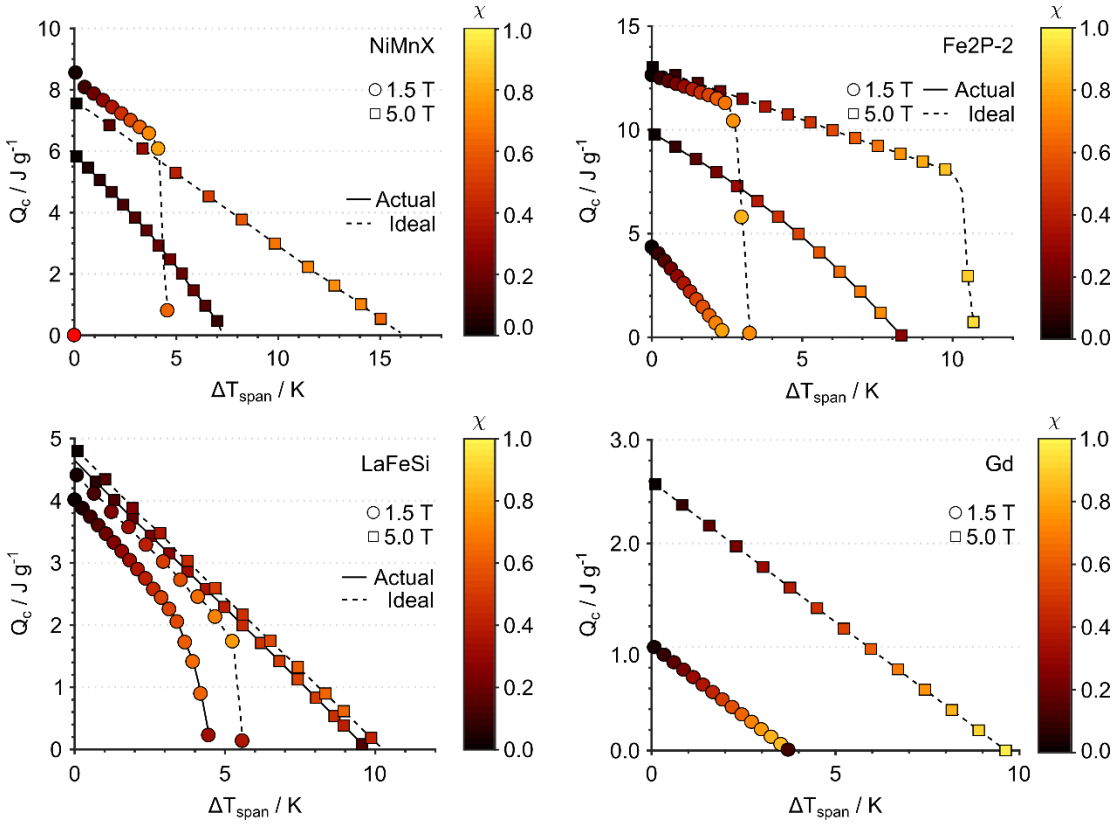

Figure V.4 Brayton heat loading curves.Summary of Pareto-optimal cooling power $\boldsymbol{Q_c}$ vs. temperature span $\boldsymbol{\Delta T_{span}}$ and 2nd Law efficiency $\boldsymbol{\chi}$ for simulated materials with actual modeled hysteresis (solid lines) and idealized ~0 hysteresis (dashed lines) from Brayton cycles between 0 and 1.5 T (circles) and 0 and 5 T (squares).

It should be emphasized that these results are all for alloys of a single composition undergoing "simple" Brayton and Ericsson cycles with the whole

refrigeration bed all at one temperature-magnetic field state. As has been shown, magnetic refrigeration systems can have much extended temperature spans by implementing active regeneration; the metrics presented here should be seen as lower limits for what is achievable through AMRR, and could conceivably be treated as representative volume elements for larger-scale simulations of such systems.

V.3.2 Effects of Hysteresis Losses on Cycle Performance

Although a critical factor in determining refrigeration performance, the maximum applied field is constrained by the permanent magnet array, and there is good reason to believe that ~1.5 T is a fundamental limit to what can be achieved. On the other hand, the transformation hysteresis and phase coexistence can be tuned through materials design, mainly through composition of the transforming phase and eliminating stresses and impurity phases. In many ways, hysteresis has about as large of an impact on refrigeration performance as maximum field constraints, When comparing corresponding heating loads for as-modeled hysteresis and ideal ~0 hysteresis for the alloys in 0 T to 5 T cycles, it is clear that the presence of hysteresis both decreases the zero-temperature span cooling power and zero-heat load temperature span by about 20-25 %, and corresponding efficiencies decrease by 20-30 % (except for LaFeSi which already has a sharp, anhysteretic transformation). This is again a simple result from thermodynamics: hysteresis irreversibilities decrease the available work. Hence given the same amount of potential refrigeration work corresponding to the input magnetic work, greater hysteresis means less available work, and lower cooling power, temperature span, and efficiency, as seen in Eqn. V.10 below:

$$W_{\mathrm{ref}} = W - \oint T\delta S_{\mathrm{irr}}, \quad \oint T\delta S_{\mathrm{irr}} \geq 0. \qquad (V.10)$$

For the 1.5 T cycles, the proportional decrease in refrigeration work W_{ref} is even greater, and so the cooling power, temperature span, and efficiency are decreased even more severely, with differences between corresponding as-modeled hysteresis and ideal hysteresis heat load curves now on the order of 60 % for Fe2P-2. Even more strikingly, the NiMnX alloy with as-modeled hysteresis has essentially no heat load curve; there are no cycles for which it can transport some degree of heat across some temperature span, even in the zero-heat load and zero-temperature span limits. This is due to a secondary effect of hysteresis, which is that it directly reduces the effective temperature span by 1 K for each 1 K increase in hysteresis, as is evident from Eqn. V.11:

$$\Delta T_{\mathrm{span,max}} \approx \left|\frac{\Delta M}{\Delta S}\right| \Delta B - \left(\Delta T_{\mathrm{hyst}} + \Delta T_{\mathrm{elast}}\right). \qquad (V.11)$$

From Table V.6, the NiMnX alloy has such a large hysteresis and coexistence that it completely negates any potential temperature span it could have in 1.5 T Brayton cycles. On the other hand, if materials processing techniques could be developed to reduce the alloy's hysteresis and coexistence without perturbing any of its other magnetothermal properties, it obtains a respectable 8.5 J/g zero-temperature span cooling power and 5 K zero-heat load temperature span within the same cycles, which out-performs the

temperature span of Fe2P-2 and the cooling power of LaFeSi under the same conditions. This demonstrates the critical importance of hysteresis engineering to future MR development: there is great potential in the MC refrigerants we already have, if the transformation hysteresis and coexistence can only be reduced.

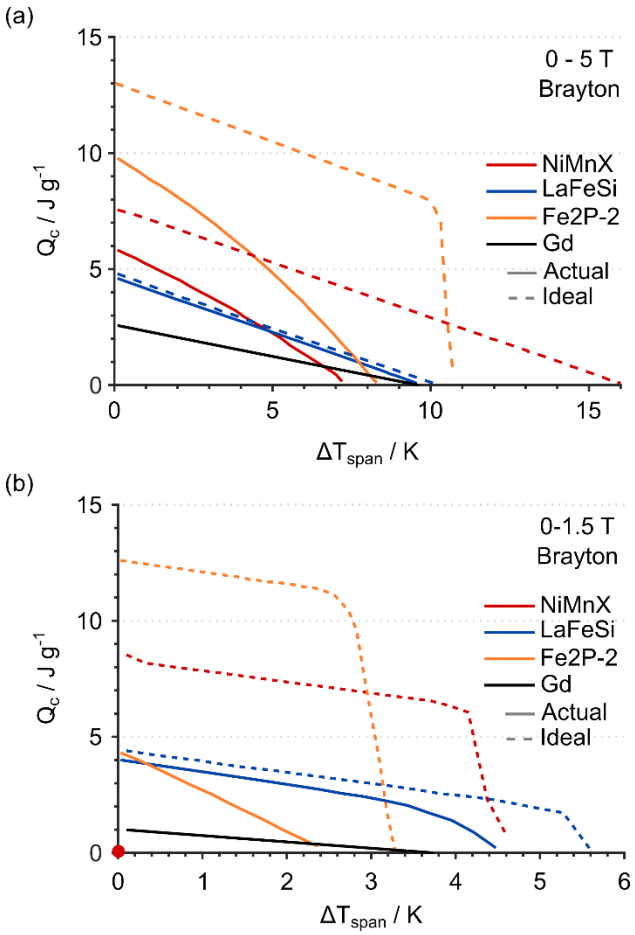

Figure V.5 Summary of Brayton heat load curves for 5 T and 1.5 T cycles.Pareto-optimal cooling power $\boldsymbol{Q_c}$ versus temperature span $\boldsymbol{\Delta T_{span}}$ for cycles between 0 T and (a) 5 T and (b) 1.5 T. Loading curves are created for both actual modeled hysteresis (solid lines) and idealized ~0 hysteresis (dashed lines) Preisach models.

V.3.3 Direct Comparison of Candidate Refrigerant Materials

Comparing the heat load curves for the different materials on the same axes (Fig. V.5) immediately makes several points clear. Gd is among the least effective materials in terms of refrigeration performance, attaining only 2.5 J/g zero-span cooling power at 5 T and 1 J/g at 1.5 T, which is smaller than any GMCE alloy, even for the as-modeled hysteresis. It is long been expected that GMCE alloy's sharp, large transformation entropies compared to Gd's broad, small entropy should make them more effective refrigerants, but there are not many studies that have been able to demonstrate this in cycles. This is especially good news for the MR community, since Gd has long been a benchmark refrigerant used in several proof-of-concept devices, and so presumably, GMCE alloys should also begin to be used in proof-of-concept devices. The real strength of Gd is in its relatively large zero-heat load temperature spans of 10 K for cycles with 5 T maximum field and 3.5 K for cycles with 1.5 T field, which is larger than nearly all the alloys' respective temperature spans with as-modeled hysteresis. However, when replaced with ideal ~0 modeled hysteresis, Gd again is surpassed by every other GMCE alloy, showing that it is hysteresis, and not some intrinsic property of Gd, that causes GMCE alloys with their actual hysteresis to fall behind the Gd benchmark. The other differences between the alloy systems largely follow systematically from their material properties (Table V.6). The Fe_2P alloys have the largest transformation entropy ΔS_{m}, and so they have the largest zero-span heat load, when modeled with ~0 K hysteresis. The LaFeSi alloy has the largest ratio $|\Delta M/\Delta S_{\mathrm{m}}|$ and so it has the largest zero-heat temperature span, again, when modeled with ~0 K hysteresis.

V.5 Conclusion

This investigation has undertaken to explore the interacting effects of magnetothermal properties, cycle constraints, and transformation hysteresis on the relative performance of magnetic Brayton cycles, and to investigate the feasibility of GMCE based on magneto-structural transformations for MR applications. By carefully fitting models to experimental data for leading GMCE classes, the magnetization, entropy, and hysteresis properties of each were decoupled and incorporated into a rational thermodynamic framework enabling simulations of Brayton cycles incorporating hysteresis effects. Simulations were performed throughout the space of relevant cycle parameters, operating between 0 T and 5 T, and 0 T and 1.5 T, and visualized as Pareto optimality fronts of cooling power, temperature span, and efficiency. Through analysis of these optimality fronts, it was found that (1) maximum field constraints are a major limiter of system performance, with cooling powers and temperature spans decreasing due to simple scaling with the total magnetic work input; (2) hysteresis is the critical materials limitation to MR development, with many otherwise compelling GMCE refrigerants becoming greatly limited or even non-useable due solely to hysteresis; (3) the heat load curves of individual alloys reflect their particular characteristics in terms of the magnetization and entropy change across the transformation, but all considered GMCE alloy systems have greater potential performance compared to benchmark Gd, provided their hysteresis and phase coexistence can be minimized. This work lays the foundations for future MR systems

and materials development, based off of rational, thermodynamically based considerations of cycle performance.

V.6 References

[1] J. Liu, T. Gottschall, K. P. Skokov, J. D. Moore, and O. Gutfleisch, Nat Mater **11,** 620 (2012).

[2] F. X. Hu, B. G. Shen, J. R. Sun, Z. H. Cheng, G. H. Rao, and X. X. Zhang, Applied Physics Letters **78,** 3675 (2001).

[3] N. H. Dung, L. Zhang, Z. Q. Ou, and E. Bruck, Scripta Materialia **67,** 975 (2012).

[4] V. K. Pecharsky, A. P. Holm, K. A. Gschneidner, Jr., and R. Rink, Phys Rev Lett **91,** 197204 (2003).

[5] E. Brück, Journal of Physics D: Applied Physics **38,** R381 (2005).

[6] K. A. Gschneidner and V. K. Pecharsky, International Journal of Refrigeration **31,** 945 (2008).

[7] A. Smith, C. R. H. Bahl, R. Bjork, K. Engelbrecht, K. K. Nielsen, and N. Pryds, Advanced Energy Materials **2,** 1288 (2012).

[8] T. D. Brown, N. M. Bruno, J. H. Chen, I. Karaman, J. H. Ross, and P. J. Shamberger, Jom **67,** 2123 (2015).

[9] P. V. Trevizoli, J. A. Lozano, G. F. Peixer, and J. R. Barbosa, Journal of Magnetism and Magnetic Materials **395,** 109 (2015).

[10] E. W. Lemmon, McLinden, Mark O. and Friend, Daniel G. , in *NIST Chemistry WebBook*, edited by P. J. a. M. Linstrom, W. G. (National Institute of Standards and Technology, U.S. Dept. of Commerce, Gaithersburg MD, 20899, 2018).

[11] P. J. Shamberger and F. S. Ohuchi, Physical Review B **79** (2009).

[12] X. F. Miao, H. Sepehri-Amin, and K. Hono, Scripta Materialia **138,** 96 (2017).

[13] T. D. Brown, T. Buffington, and P. J. Shamberger, Journal of Applied Physics **123** (2018).

[14] T. D. Brown, I. Karaman, and P. J. Shamberger, Materials Research Express **3** (2016).

[15] V. Srivastava, X. A. Chen, and R. D. James, Applied Physics Letters **97** (2010).

[16] J. Lyubina, Journal of Applied Physics **109** (2011).

[17] J. Lyubina, O. Gutfleisch, M. D. Kuz'min, and M. Richter, Journal of Magnetism and Magnetic Materials **321,** 3571 (2009).

[18] N. H. Dung, Z. Q. Ou, L. Caron, L. Zhang, D. T. C. Thanh, G. A. de Wijs, R. A. de Groot, K. H. J. Buschow, and E. Brück, Advanced Energy Materials **1,** 1215 (2011).

[19] N. T. Trung, Z. Q. Ou, T. J. Gortenmulder, O. Tegus, K. H. J. Buschow, and E. Brück, Applied Physics Letters **94** (2009).

[20] Y. H. Qu, D. Y. Cong, X. M. Sun, Z. H. Nie, W. Y. Gui, R. G. Li, Y. Ren, and Y. D. Wang, Acta Materialia **134,** 236 (2017).

[21] E. Stern-Taulats, P. O. Castillo-Villa, L. Manosa, C. Frontera, S. Pramanick, S. Majumdar, and A. Planes, Journal of Applied Physics **115** (2014).

[22] H. L. Yan, C. F. Sanchez-Valdes, Y. D. Zhang, J. L. S. Llamazares, Z. B. Li, B. Yang, C. Esling, X. Zhao, and L. Zuo, Journal of Alloys and Compounds **767,** 544 (2018).

[23] D. W. Zhao, J. Liu, X. Chen, W. Sun, Y. Li, M. X. Zhang, Y. Y. Shao, H. Zhang, and A. R. Yan, Acta Materialia **133,** 217 (2017).

[24] V. Franco, J. S. Blázquez, B. Ingale, and A. Conde, Annual Review of Materials Research **42,** 305 (2012).

[25] G. V. Brown, Journal of Applied Physics **47,** 3673 (1976).

[26] C. Zimm, A. Jastrab, A. Sternberg, V. Pecharsky, K. Gschneidner, M. Osborne, and I. Anderson, in *Advances in Cryogenic Engineering, Vol 43 Pts a and B*; *Vol. 43*, edited by P. Kittel (Plenum Press Div Plenum Publishing Corp, New York, 1998), p. 1759.

[27] A. M. Rowe and J. A. Barclay, **613,** 995 (2002).

[28] J. A. Monroe, I. Karaman, B. Basaran, W. Ito, R. Y. Umetsu, R. Kainuma, K. Koyama, and Y. I. Chumlyakov, Acta Materialia **60,** 6883 (2012).

[29] J. H. Chen, N. M. Bruno, I. Karaman, Y. J. Huang, J. G. Li, and J. H. Ross, Acta Materialia **105,** 176 (2016).

[30] H. Yibole, F. Guillou, L. Zhang, N. H. van Dijk, and E. Brück, Journal of Physics D: Applied Physics **47** (2014).

[31] Z. Q. Ou, Thesis, Delft University of Technology, 2013.

[32] A. Fujita, S. Fujieda, Y. Hasegawa, and K. Fukamichi, Physical Review B **67,** 104416 (2003).

[33] S. Y. Dan'kov, A. M. Tishin, V. K. Pecharsky, and K. A. Gschneidner, Physical Review B **57,** 3478 (1998).

[34] I. Mayergoyz, IEEE Transactions on Magnetics **22,** 603 (1986).

CHAPTER VI

EFFECT OF HEAT TREATMENT ON RELAXATION AND RECOVERY OF MULTI-STEP TRANSFORMATIONS IN $(MN,FE)_2(P,SI)$ ALLOYS

VI.1 Introduction

Magnetocaloric materials in which thermal and magnetic properties are highly coupled are of primary interest for novel sensing, switching, and thermal management applications [1-4]. Optimal performance is typically obtained in alloy systems like Ni-Mn-X meta-magnetic shape memory alloys (MSMAs), $La(Fe,Si)_{13}$ and its hydrides, and $(Mn,Fe)_2(P,Si)$, in which a first order change in magnetization couples to a sudden, reversible change in crystal structure near some critical temperature [5-7]. The alloy nature of these systems makes them amenable to compositional tuning [8-13], which is crucial for simultaneous optimization over the transformation's properties, such as the changes in magnetization and entropy it induces, as well as its critical temperature and hysteresis.

However, the transformations in these alloys are also susceptible to modification by heat treatment due to a variety of thermally-activated mechanisms, for example, (1) relaxation of internal stresses and defects; (2) chemical order / disordering; (3) compositional modulation through the presence of other equilibrium impurity phases; (4) transient diffusive chemical redistribution within the transforming phase. Mechanisms (1) and (2) are primarily active in the Ni-Co-Mn-X MSMA systems (X = Sn, In, Sb) [14-16], where increased annealing times relax internal stresses and defects [17,18] but also

affect the $L2_1$-B2 ordering state of the alloy [19,20] depending on the annealing temperature, with chemically ordered Mn atoms developing greater ferromagnetic exchange in the in the high-temperature phase [21]. Together, these mechanisms greatly influence the magneto-structural transformation properties, with increased annealing leading to somewhat decreased transformation hysteresis, increased transformation enthalpy, and substantial increase or decrease in critical temperatures, depending on the alloy system [22,23]. Mechanism (3) dominates in the La-Fe-Si alloy system, where annealing can also lead to increased volumes of non-transforming impurity Fe-rich α-Fe phases [24-26], thereby decreasing the mass-averaged transformation enthalpy and changing the transformation critical temperature and hysteresis through the Fe content of the transforming $La(Fe,Si)_{13}$ phase [27]. Finally, hydrogenated La-Fe-Si-H alloys offer a unique example of mechanism (4), where hydrogen spontaneously segregates [28], creating H-poor and H-rich regions of $La(Fe,Si)_{13}$ phase. This segregation reveals itself macroscopically as a separation of a single well-defined first order transformation into two distinct first order transformations at different temperatures after repeated cycling [29]. However, the original single transformation behavior can be easily recovered by short time annealing around 450 K [30] where the homogenized hydrogen distribution is again recovered.

In the $(Mn,Fe)_2(P,Si)$ alloys, the properties of coupled magneto-structural transformations are linked to order-disorder and phase segregation mechanisms through heat treatment. $(Mn,Fe)_2(P,Si)$ alloys typically possess a strong site preference, with Mn in square pyramidal *3g* sites and Fe in tetrahedral *3f* sites [31] (Fig. VI.1). However,

quenching from high temperature can disorder these sites [32], resulting in an increase in their magnetic moments [33,34] that tunes the critical temperature of the transformation. A similar ordering effect can also be induced just by varying Si content, with Si preference on the *2c* site also decreasing the Mn and Fe magnetic moment [35,36]. At the same time, the alloy system typically manifests a complicated multi-phase equilibrium with a variety of P-depleted cubic $(Mn,Fe)_xSi$ phases coexisting with the transforming phase [37,38]. Just as for the La-Fe-Si system, the presence of these impurities both decreases the evident transformation entropy and magnetization and modifies the composition of the transforming phase, hence the transformation's critical temperature and hysteresis [39].

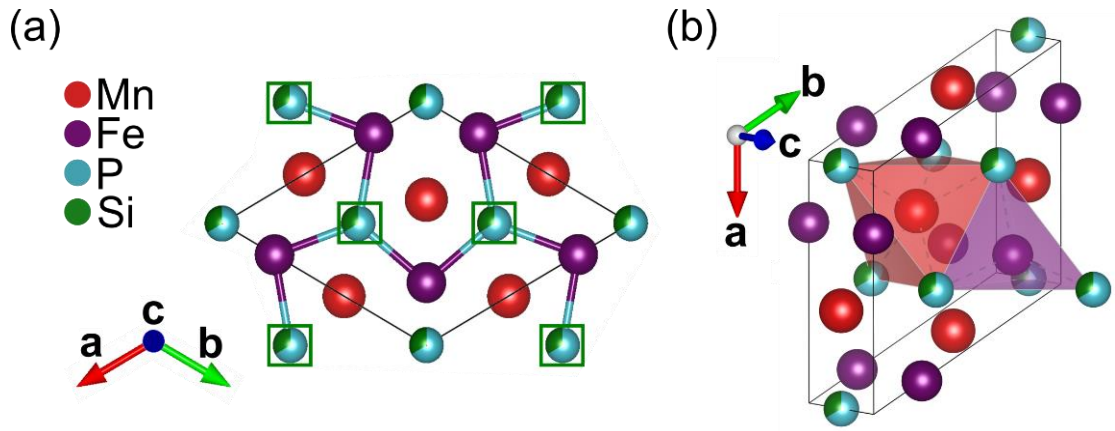

Figure VI.1 Crystal structure of $(Mn_{1.00}Fe_{1.00})(P_{0.67}Si_{0.33})$. As viewed (a) perpendicular to (0001) basal planes and (b) from oblique view emphasizing pyramidal and tetrahedral coordination. Green boxes mark non-metal 2c sites that are increasingly Si-ordered with increasing total Si content.

In this work, we investigate the mechanisms underlying the effects of heat treatment on the magneto-structural transformation in $(Mn,Fe)_2(P,Si)$ alloys. First, we report a two-step heat treatment resulting in split multi-step first-order transformations,

and show that this multi-step splitting corresponds to a relaxation process activated by annealing for intermediate times at 1173 K and 1273 K. The relaxation is reversible, and further annealing for a week at these temperatures recovers the usual single-step transformation. Through diffraction and magnetometry experiments, we confirm the magneto-structural nature of both components of the multi-step transformation, and that the splitting process results from a segregation of the main phase alloy into two distinct populations. Finally, we argue that this segregation corresponds to a compositional dynamic re-equilibration process, as opposed to an order-disorder transition, and we demonstrate a clear correspondence between the existence of a multi-step transformation and bi-modal composition distributions in the alloy samples. Together, these investigations prove the importance of heat treatments and internal compositional gradients to controlling the properties of the first-order magneto-structural transformation in $(Mn,Fe)_2(P,Si)$ alloys.

VI.2 Experimental Methods

$(Mn_xFe_{2-x})(P_{1-y}Si_y)$ alloys of varying composition were synthesized following a powder metallurgy process beginning from mixing 99.9 % purity Mn and 99.99 % Si powders [ESPI Metals, metals basis] as well as 99.5 % Fe_2P and 99.99 % red P powders [Sigma Aldrich], followed by high-energy ball milling in ZrO_2 milling jars with 3 mm ZrO_2 media [Retsch] at 250 rpm for 3 h, then 300 rpm for 5 h. Milled powders were subsequently pressed into 8 mm diameter pellets under 1000 psi uniaxial stress for 120 s. Green pellets were sealed under Ar into fused quartz ampoules, then initially sintered for 6 h at 1373 K followed by annealing for 20 h at 1173 K, then furnace cooled to room

temperature (denoted FC). At all stages O_2 was excluded by processing under Ar glovebox atmosphere (<0.1 ppm O_2, <0.5 ppm H_2O) or by using vacuum grease and parafilm to seal samples within containers under Ar for processing steps occurring outside of the glovebox.

Variable temperature powder X-ray diffraction data were acquired every 5 K from 303 K to 353 K in Bragg-Brentano geometry using a Bruker D8-Vario X-ray powder diffractometer with an MTC oven attachment in an ambient Ar atmosphere. Cu Kα radiation was used with a Lynxeye detector. Specific magnetization measurements were performed using a Quantum Design Magnetic Property Measurement System (MPMS) equipped with the Reciprocating Sample Option tool. The iso-field temperature-dependent magnetization measurements at 0.1 T and 0.5 T were performed between 10 K and 400 k using zero-field cooled warming, field-cooled cooling, and field-cooled warming protocols.

Differential scanning calorimetry (DSC) traces were obtained using a Thermal Analysis QA-20 system equipped with an RCS90 cooling unit at a standard 10 K / min ramp rate except where otherwise noted. Electron imaging and quantitative composition analysis via wavelength dispersive spectroscopy (WDS) were performed using the Cameca SXFive electron microprobe. Spot (point) analyses were conducted using a beam voltage of 15 kV and a beam current of 20 nA with counting times of 20 s on peak and 10 s on each background. Quantitative maps were obtained on several areas using a beam voltage of 15 kV and a beam current of 100 nA with counting times of 250 ms on

peak and 20 ms on each background for every pixel. GaP was used as the P standard, while pure element standards were used for Mn, Fe, and Si.

VI.3 Results

VI.3.1 Observation of Secondary Phases and Multi-step Transformations

After initial synthesis via ball milling and sintering and annealing heat treatments (1373 K / 6 h + 1173 K / 20 h + Furnace Cool, FC), $(Mn,Fe)_2(P,Si)$ alloys generally manifest a single first-order peak in calorimetry experiments, corresponding to the expected first-order coupled magnetic and structural transformation (Fig. VI.2a, "A" traces). High z-contrast BSE imaging and WDS reveals a rich phase microstructure as reported previously [37,40] consisting of the desired quaternary alloy, as well as P-poor ternary cubic phases in various (Mn,Fe):Si ratios (Fig. VI.2b). To ensure equilibrium of solid-state reactions, pieces of alloys having undergone "A" initial heat treatment were subsequently powderized under Ar with agate mortar and pestle, re-pressed into 8 mm pellets and put through identical 1373 K / 1173 K / FC heat treatment a second time.

Surprisingly, a majority of alloys undergoing this second "B" heat treatment now manifest two distinct calorimetry peaks on both heating and cooling, with the first "primary" heating peak ~30 K above the initial "A" alloy's transformation, and a "secondary" heating transformation another 30 K above that (Fig. VI.2a, "B" traces). The peak areas for the two "B" transformations are symmetric on heating and cooling, strongly suggesting the presence of a multi-step first-order transformation. Despite this change, the microstructure of the "B" treated alloys is largely the same as for the "A"

treated alloys; BSE and WDS confirm coexistence of the same P-depleted ternary phases with the hexagonal phase of interest (Fig. VI.2c).

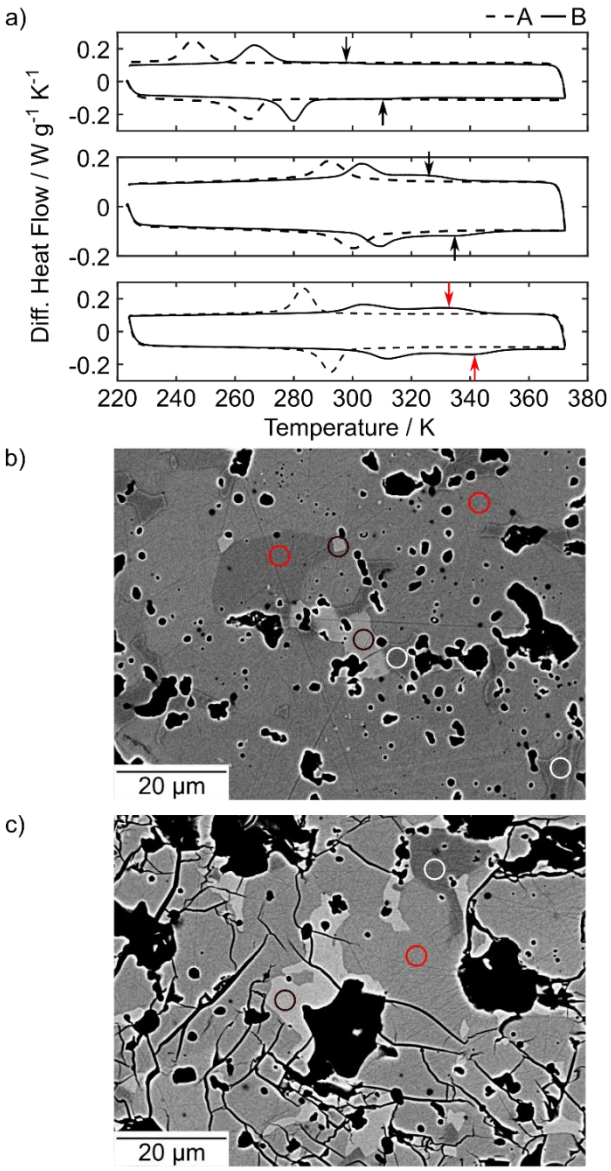

Figure VI.2 Calorimetry and electron micrographs for single and multi-step alloys. (a) Single and multi-step transformations in DSC calorimetry traces for selected $(Mn_xFe_{2-x})(P_{1-y}Si_y)$ alloys (top) (x=1.25, y=0.44); (middle) (x=1.28, y=0.48); (bottom) (x=1.26, y=0.48) before (dashed, A) and after (solid, B) attempted homogenizing re-processing. Compare with phase microstructure in (x=1.26, y=0.48) alloy after (b) "A" and (c) "B" heat treatments consisting of majority (Mn+Fe):(P+Si) = 2:1 phase (red circles) as well as 3:1 (white circles) and 4.5:1 (black circles) P-poor impurity phases.

The multi-step transformation manifests some complicated compositional dependence, with large variations in the relative areas ascribed to the secondary versus primary peaks (0-40 %) and in the difference in critical temperatures between the transformations (23-36 K). The multi-step transformation in the "B" $(Mn_xFe_{2-x})(P_{1-y}Si_y)$ alloy with nominal (x=1.26, y=0.48) composition has one of the more pronounced secondary peaks, and so it has been selected for further investigation of the mechanism behind the observed multi-step first-order transformation.

VI.3.2 Multi-step Transformation Formation Kinetics

To gain additional insight into the nature of the component transformations, we have further probed the kinetics by which a single step transformation becomes multi-step through further heat treatments. Additional pellets of (x=1.26, y=0.48) alloy having undergone "B" processing were re-sealed under Ar in fused quartz ampoules and put through additional "C" heat treatment consisting of annealing at 1373 K, followed by annealing steps at 1173 K or 1273 K for various times (0 h, 20 h, 1 wk) before quenching into water at room temperature (Fig. VI.3a). A summary of heat treatments and sample names used in the text is given (Table VI.1).

Baseline-subtracted cooling calorimetry traces (Fig. VI.3b) reveal that in all cases, the first order transformation is preserved, suggesting that even at 1373 K, the desired transforming hexagonal $(Mn,Fe)_2(P,Si)$ phase remains an equilibrium phase. The sample held at 1373 K for 8 h and then immediately quenched displays only a single step transformation despite being derived from a multi-step "B" sample, showing that the single step transformation is recovered by high temperature annealing. Evidently, it is

the annealing step at 1173 K and 1273 K that drives the system towards multi-step transformation. This observation is borne out by the samples held at 1173 K and 1273 K for 20 h before quenching, in which clearly defined secondary transformations reminiscent of the original "B" multi-step transformation are observed. Further annealing up to one week at 1173 K and 1273 K before quenching actually drives the system in the opposite direction, so that multi-step transformations observed at intermediate annealing times are then again re-converted to single step transformations, although their critical temperatures have somewhat shifted.

The overall picture suggests that a single stable transforming population is obtained even after relatively short times (<10 h) at 1373 K. On cooling to 1273 K and 1173 K, the alloy system relaxes towards a new equilibrium, again with just one transforming population, after long time (>100 h) annealing at these temperatures. However, this relaxation process evidently brings the system through an as-yet unidentified intermediate state, with median annealing times causing decomposition of the initial single step transformation into two component first-order transformations, before these finally re-combine after further annealing. The recombination of the component transformations appears more nearly complete for the "C" alloy annealed at 1273 K for 20 h than for the alloy annealed at 1173 K for 20 h, implying the mechanism underlying the relaxation of the multi-step transformation proceeds faster at higher temperature.

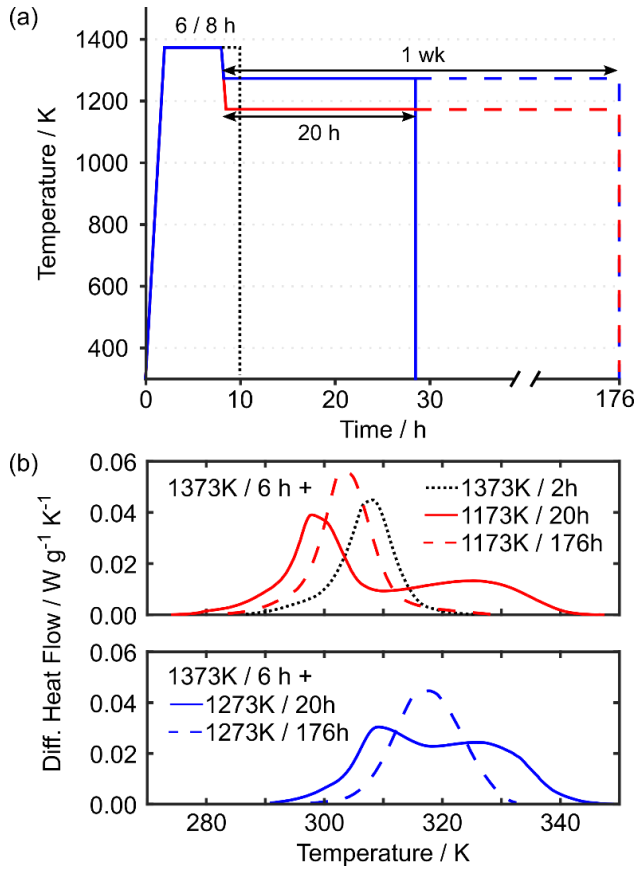

Figure VI.3 Heat treatments and calorimetry for third-heat treated alloys. (a) Heat treatment protocols and (b) resulting baseline subtracted cooling 10 K/min DSC traces for (x=1.26, y=0.48) alloy samples undergoing various third "C" heat treatments.

Sample	Starting Material	1st Heat Treatment	2nd Heat Treatment	Cooling
"A"	Milled Powders	1373 K / 6 h	1173 K / 20 h	FC
"B"	Re-pressed "A"	1373 K / 6 h	1173 K / 20 h	FC
1373Q	Unmodified "B"	1373 K / 6 h	1373 K / 2 h	WQ
1273Q-20h	Unmodified "B"	1373 K / 6 h	1273 K / 20 h	WQ
1273Q-1wk	Unmodified "B"	1373 K / 6 h	1273 K / 168 h	WQ
1173Q-20h	Unmodified "B"	1373 K / 6 h	1173 K / 20 h	WQ
1173Q-1wk	Unmodified "B"	1373 K / 6 h	1173 K / 168 h	WQ

Table VI.1 Summary of sample "C" heat treatments used in the study. Cooling methods are either "Furnace Cooled" (FC) or "Water Quenched" (WQ).

VI.3.3 Magnetostructural Character of Multi-step Transformation

The multi-step transformation is consistent with at least two distinct interpretations: (1) one population which transforms twice, perhaps through an intermediate state, as $\alpha \rightarrow \gamma \rightarrow \beta$ versus (2) two populations which each transform once, as $(\alpha_1 \rightarrow \beta_1)$ at T_1 followed by $(\alpha_2 \rightarrow \beta_2)$ at T_2. In order to distinguish these possibilities, as well as to verify the expected magneto-structural nature of both component first-order transformations we turn to further structural and magnetic characterization.

Powder diffraction (Fig. VI.4a-b) clearly demonstrates the presence at room temperature of the expected hexagonal phase, space group 189, with $a = 6.11$ Å, $c = 3.30$ Å. As the sample is heated, new diffraction peaks associated with a high-temperature hexagonal phase, space group 189, $a = 6.09$ Å, $c = 3.44$ Å, appear, and the volume fraction associated with this phase gradually increases at the expense of the low-temperature phase. Importantly, this shift from low temperature hexagonal phase to high temperature hexagonal phase is continuous throughout the whole temperature range and divides into two steps 303 K < T < 318 K associated with the primary "B" transformation, as well as 323 K < T < 353 K associated with the secondary "B" transformation. At no point throughout either of the transformation ranges is there ever any evidence of a third set of diffraction peaks corresponding with a different structure, excluding the possibility of an intermediate transformation to a third crystal structure, for example, the hexagonal to body-centered orthorhombic to hexagonal multi-step transformation observed in some $(Mn,Fe)_2(P,Ge)$ alloys [41].

Further low-field temperature-dependent magnetization measurements verify large magnetization changes coupled with the crystallographic shifts observed by diffraction (Fig. VI.4c). Importantly, the decrease in specific magnetization from ~55 emu/g to ~0 emu/g in the "B" processed sample also occurs in two steps at 312 K and 338 K, proving that both components of the multi-step transformation are magneto-structural in nature. Therefore, the components of the multi-step transformation are essentially of the same character as the single step transformation from which it derives, and regardless of whether the transformation proceeds in a single or in multiple steps, the general equilibrium between highly-magnetic hexagonal parent phase and weakly-magnetic hexagonal daughter phase is largely preserved. Similarly, for both "A" and "B" processed samples, the cumulative decrease in specific magnetization from ~54-55 emu/g to ~0 emu/g is in very good agreement, suggesting that any other factors affecting specific magnetization, such as the relative proportion of transforming quaternary phase versus non-transforming cubic impurities, appear to be essentially unchanged. Taken together, these investigations imply that all transformations are iso-structural and manifest similar magneto-structural coupling, which appears to support the second mechanism, with ($\alpha_1 \rightarrow \beta_1$) and ($\alpha_2 \rightarrow \beta_2$) at two separate temperatures.

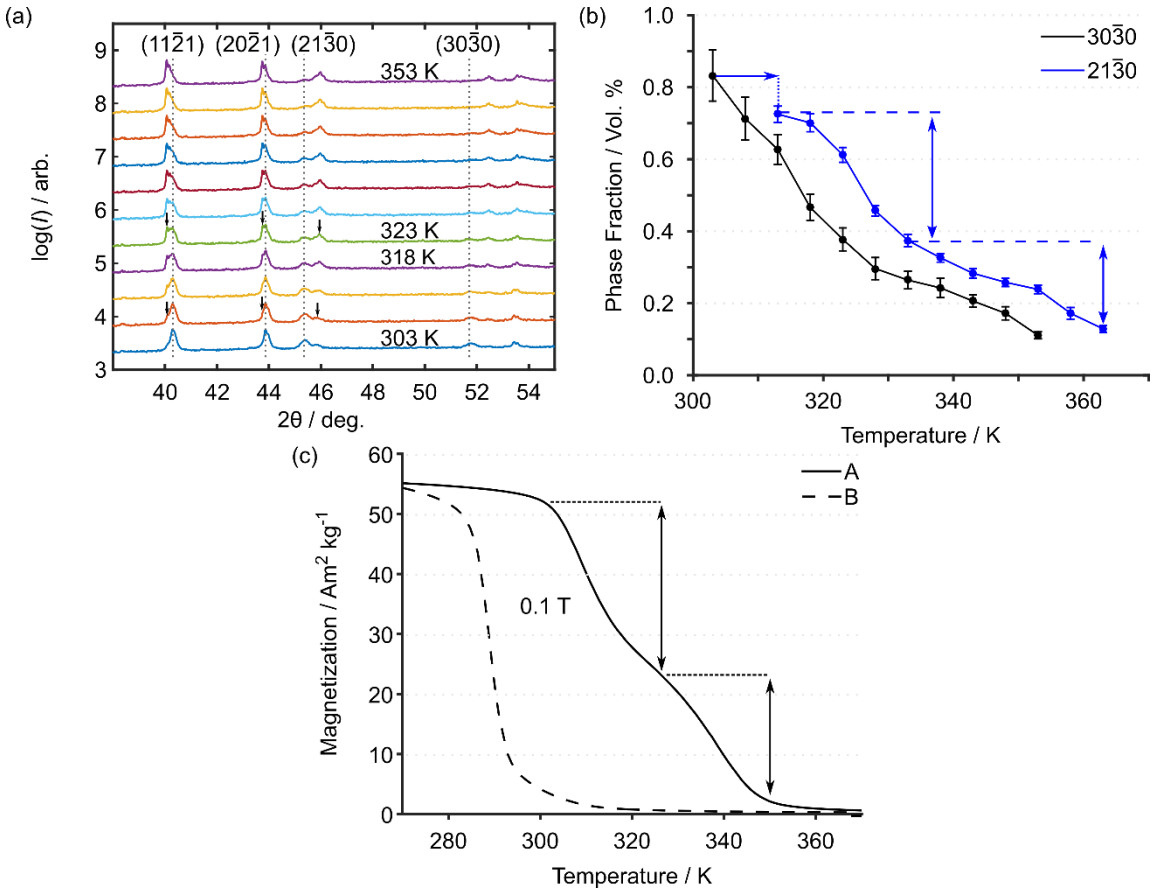

Figure VI.4 Magnetic and structural characterization of transformation. (a) Temperature-resolved powder diffraction two-theta scans and (b) corresponding phase fraction every 5 K on heating from 303 K to 353 K in "B" processed (x=1.26, y=0.48) alloy with grey dashed guidelines marking the centers of selected diffraction peaks for low-T hexagonal phase at room temperature. Black arrows mark the emergence of corresponding high-T hexagonal phase diffraction peaks at the onset of primary (303 K to 308 K) and secondary (318 K to 323 K) heating peaks. (c) Temperature-dependent specific magnetization at 0.1 T applied field of (x=1.26, y=0.48) alloy after "A" and "B" processing showing clear magnetization decrease associated with both "B" transformation peaks

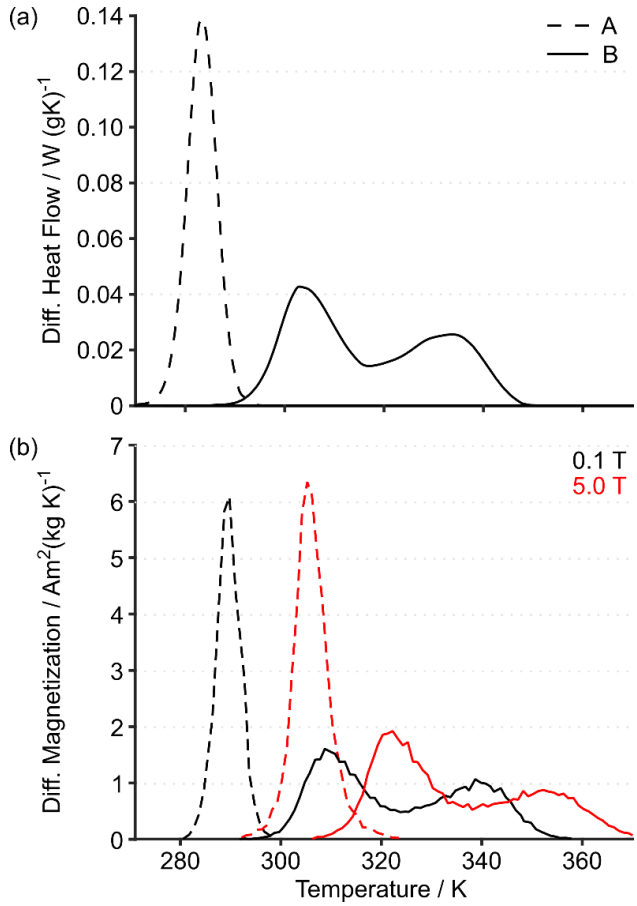

Figure VI.5 Calorimetry for long-time annealed samples. Baseline subtracted cooling differential signal for (a) 2 K / min calorimetry traces and (b) 2 K / min temperature-dependent magnetization measured at 0.1 T and 5.0 T, of (x=1.26, y=0.48) sample measured after initial (A) and post-homogenizing processing (B).

Direct comparison of the differential calorimetry (Fig. VI.5a) and magnetization (Fig. VI.5b) signals for the alloy following "A" and "B" processing further points towards the two-population model for the multi-step transformation. First, the shifts in transformation critical temperatures T_C with applied magnetic field B are related to the changes in specific magnetization Δm and entropy Δs induced by the magneto-structural transformation through the magnetic Clausius-Clapeyron equation, as below:

$$-\frac{\mathrm{d}T_C}{\mathrm{d}B} = \frac{\Delta m}{\Delta s}. \qquad (VI.1)$$

The fact that the critical temperature shifts from 0.1 T to 5.0 T for the primary (+12 K) and secondary (+13 K) components of the multi-step transformation are in agreement (Fig. VI.5b) alludes to the similar mechanism behind the primary and secondary transformations, but also implies through the C-C relation the following relation:

$$\frac{\Delta m_1}{\Delta s_1} = \frac{\Delta m_2}{\Delta s_2} \Rightarrow \frac{\Delta m_1}{\Delta m_2} = \frac{\Delta s_1}{\Delta s_2}. \qquad (VI.2)$$

With the subscripts 1 and 2 referring to changes in specific magnetization Δm and entropy Δs developed during the primary and secondary components of the multi-step transformation, respectively.

If the two-population model is correct and there are two separate transforming populations in proportions ϕ and $1-\phi$, then the total observed steps in magnetization ΔM and entropy ΔS must both be due to the same two populations transforming, *i.e.*, $\Delta M_1 = \phi \Delta m_1$, $\Delta M_2 = (1-\phi)\Delta m_2$, $\Delta S_1 = \phi \Delta s_1$, and $\Delta S_2 = (1-\phi)\Delta s_2$, with ϕ being the same constant fraction across all four equations. Combining these with the Clausius-Clapeyron shift constraint yields the final equation:

$$\frac{\Delta M_1}{\Delta M_2} = \frac{\Delta S_1}{\Delta S_2} \approx \frac{\Delta H_1}{\Delta H_2}. \qquad (VI.3)$$

Therefore, the fractional integrated area below the differential signals corresponding to the primary and secondary multi-step components must be the same in each case. In fact,

the area fractions of the "B" enthalpy steps computed from DSC traces is (52.6 % / 47.3 %); for the magnetization steps at 0.1 T and 5.0 T the area fractions are (51.0 % / 49.0 %) and (51.7 % / 48.3 %), respectively, which is an excellent agreement. This agreement of C-C slopes and area fractions is a necessary consequence of the two-population model.

If, on the other hand, the observed multi-step transformation was due to one population transforming twice, the $\alpha \rightarrow \gamma$ and $\gamma \rightarrow \beta$ steps would correspond to genuinely different transformations. In this case we should not expect the specific entropy and magnetization steps across each component transformation to be the same, nor to stand in the same ratio, so constraint relations like Eqn. VI.2 and Eqn. VI.3 would be purely incidental and surprising. Furthermore, the Clausius-Clapeyron shift for the single-step transformation (+15 K) agrees fairly well with those of the multi-step components (+12 K / +13 K), and the cumulative areas under the differential signals also agree within 25%, which again suggests the splitting of one transforming population into two individual transforming populations.

VI.4 Discussion

VI.4.1 Potential Multi-step Transformation Mechanisms

Overall, the experimental results suggest that a single magneto-structurally transforming population decomposes into two individual magneto-structurally transforming populations on annealing for median times below 1373 K. After further annealing below 1373 K, the two populations recombine again into a single transforming population, which is similar to the original single population despite a slight shift in

critical temperature. Furthermore, the properties of the two distinct populations are similar to each other and to the single populations obtained before and after annealing below 1373 K, with good agreement between transformation hystereses and cumulative changes in entropy and magnetization induced by the transformation. The crystal structures of the two multi-step transformation populations must also be similar enough that their respective diffraction peaks are unresolvable, suggesting the lattice parameters of the populations differ by less than $|\Delta a| < 0.12$ Å and $|\Delta c| < 0.01$ Å. All of these point towards the two transforming populations being essentially the same phase, with some small modification between the two, such as (1) a difference in site ordering, (2) a difference in phase composition.

Previous investigations have shown how $(Mn,Fe)_2(P,Si)$ alloys can disorder at high temperature [33,36], and although most work has focused on how this impacts magnetic moments on the atomic sites, this could also affect the thermodynamics of the system, and thus, the critical temperatures and hysteresis of the transformation. Furthermore, ordering is a time-dependent process whose progress can be frozen in by quenching after prescribed times, as we have done here. The ordering process is expected to leave the lattice parameters relatively unchanged, but also would be practically insensitive to XRD intensities due to the extremely similar scattering factors between Mn and Fe and between P and Si [42]. However, ordering is a second-order transformation process in which initially small order parameter fluctuations grow exponentially, and so a single broad peak representing the two near-disordered phases would increasingly split into further distinct peaks representing oppositely-ordered anti-

phases. In fact, the opposite is observed, with two distinct peaks merging after long annealing times into one broad peak, which is strongly against chemical ordering as the mechanism leading to multi-step transformation.

On the other hand, the alloy system clearly exhibits a multitude of phases regardless of heat treatment. If ternary $(Mn,Fe)_xSi$ phases are always observed in the microstructure, it may not be surprising that the transforming quaternary $(Mn,Fe)_2(P,Si)$ phase may itself also temporarily segregate into at least two distinct compositions distinguished by slightly different Mn:Fe and P:Si ratios. In this case, it is supposed that the equilibrium composition of the quaternary phase depends on temperature, so that one composition stable at 1373 K slowly converts to a different equilibrium composition at 1273 K and 1173 K. However, this process is diffusion-limited with slow kinetics, leading to a non-uniform dynamic re-equilibration process; after just 20 h annealing time this process is incomplete and two transient composition populations are observed. This interpretation is potentially consistent with other observations, as it is well-known that crystal structure, magnetothermal properties, critical temperatures, and hystereses of the alloy system are all sensitive to composition. Previous investigations into compositional dependence of these properties suggest the observed deviation in a and c lattice parameters could be consistent with at most a 2-4 at. % increase in Si content [36,43,44]; the shift in critical temperatures corresponds to a 1 % increase in Si or a 4 % decrease in Mn content [12,13]. Hence if two distinct compositional populations are present, their Mn and Si contents are expected to differ by at least 1 at. % and at most 4 at. %.

V1.4.2 Investigation of Compositional Dynamic Re-equilibration

The suggested dynamic re-equilibration mechanism requires that the equilibrium composition of the transforming hexagonal phase changes from 1373 K to 1273 K and 1173 K, and together with slow long-range diffusion kinetics, this driving force results in the observed two transforming phases. Initial compositional analysis *via* spot averaged WDS measurements found no evidence for the temperature dependence of equilibrium compositions (Table VI.2). For all analyzed samples, the variation in average composition is small, within experimental uncertainties.

Sample	Mn / at. %	Fe / at. %	P / at. %	Si / at. %	O / wt. %
"A"	41.9 ± 0.1	24.9 ± 0.1	17.2 ± 0.3	15.9 ± 0.4	0.6 ± 0.3
"B"	41.1 ± 0.3	25.8 ± 0.2	16.9 ± 0.4	16.2 ± 0.5	0.7 ± 0.3
1373Q	41.9 ± 0.3	25.5 ± 0.3	16.9 ± 0.4	15.7 ± 0.4	0.9 ± 0.3
1273Q-20h	41.7 ± 0.2	25.7 ± 0.2	16.5 ± 0.6	16.0 ± 0.6	1.1 ± 0.3
1273Q-1wk	41.7 ± 0.2	25.8 ± 0.2	16.7 ± 0.4	15.9 ± 0.4	0.8 ± 0.3

Table VI.2 Variations in composition of transforming hexagonal phase over heat treatment cycles. Median compositions are taken from 12-16 5 μm WDS spots each encapsulated in a different grain of the hexagonal phase; uncertainty taken as 95% CI for each element; oxygen content measured from oxygen-by-difference of weight percent totals.

However, further investigation of spatial elemental distributions *via* quantitative WDS mapping does support the potential for bimodal segregation in multi-step transforming samples (Fig. VI.6). For the multi-step sample after "B" processing, the distribution in elemental P is highly bimodal, with sharp compositional gradients between ~11 wt. % and ~10 wt. %. This bimodality may also be seen in the Fe spatial distribution, with sharp gradients between ~31.5 wt. % and ~29.5 wt. %. This contrasts sharply with the elemental P and Fe distributions for the single-step transforming sample taken after the long 1 week anneal at 1273 K. For this sample, the P distribution is less

bimodal, with long-range gradients over many tens of microns. The Fe distribution for this sample is even more homogeneous, with a nearly complete absence of both short and long range composition gradients. The comparison of composition bimodality can be seen even more clearly from histograms over the entire selected areas (Fig. VI.7).

Despite these differences, long range P gradients still exist to a lesser extent in the single-step transforming sample even after the 1 week long anneal, suggesting that the kinetics of P diffusion are particularly slow in this system. Comparison of the WDS maps to the corresponding BSE images (supplementary) reveals that the P-poor regions in the main quaternary phase are adjacent to the P-depleted cubic 3:1 and 5:1 phases, suggesting that these impurity phases may play a role in assisting the dynamic re-equilibration process.

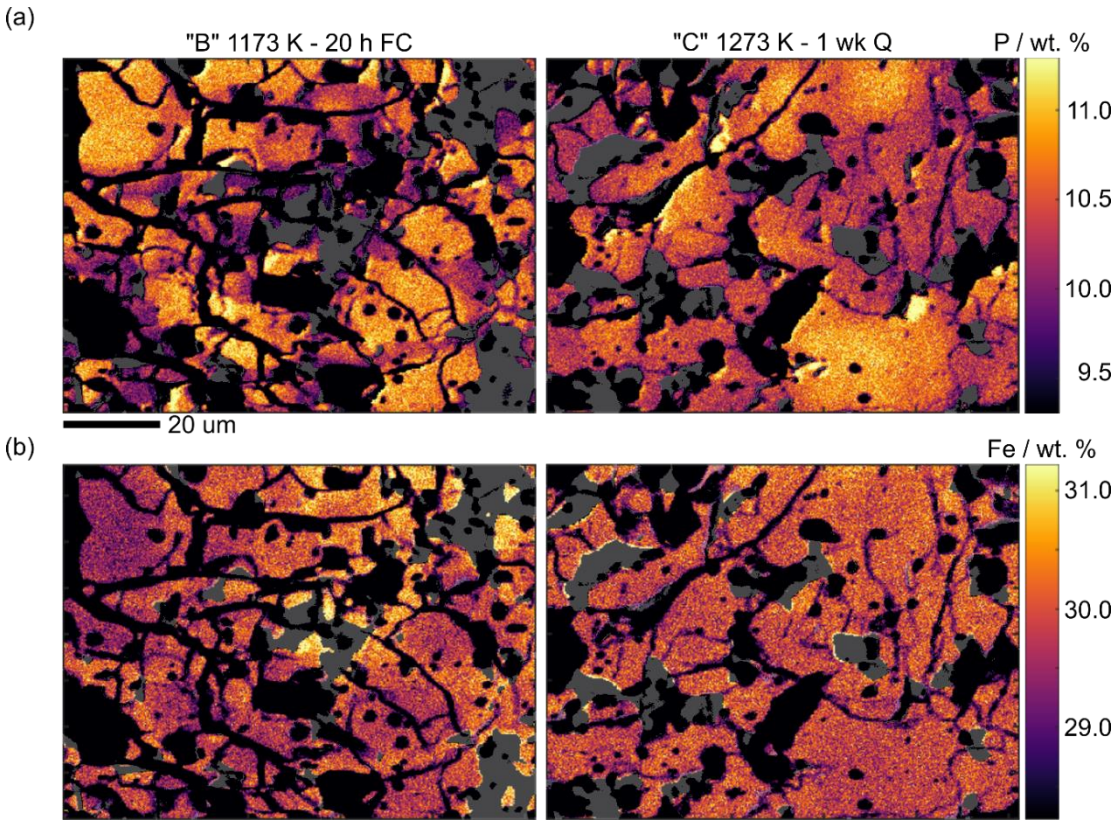

Figure VI.6 Comparison of elemental distributions for P (a) and Fe (b) for two selected samples. Multi-step transforming sample (left) is obtained after "B" processing, furnace cooling from 1173 K, and has many short-range compositional gradients. Single-step transforming sample (right) is obtained after "C" processing, quenched after 1 week anneal at 1273 K. Impurity cubic phases (grey) have been excluded to emphasize gradients within only the phase of interest.

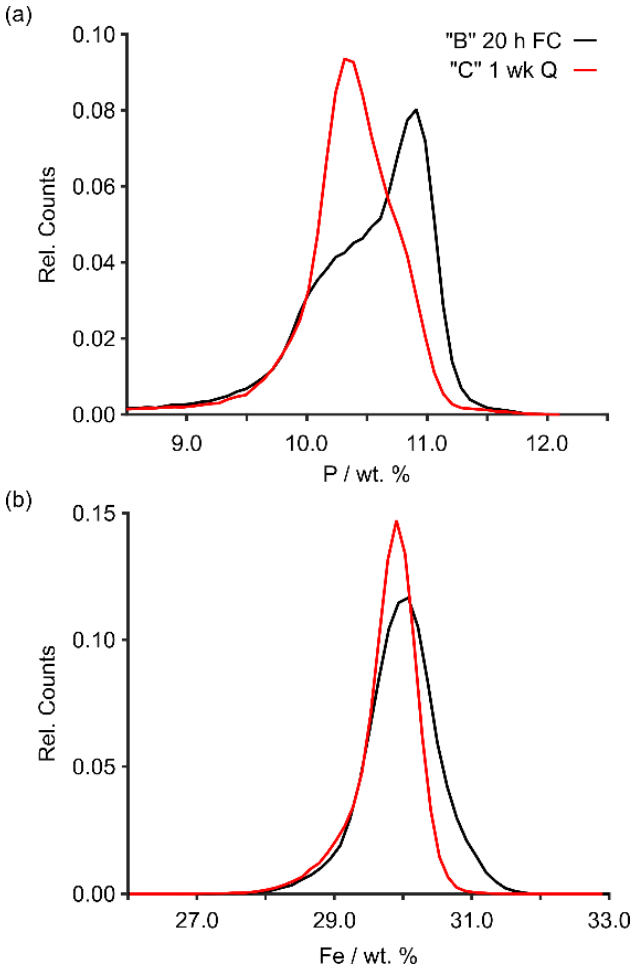

Figure VI.7 Comparison of elemental composition histograms. Histograms of elemental compositions for (a) P and (b) Fe corresponding to the WDS maps in Figure VI.6.

VI.5 Conclusion

We have shown that multi-step first-order phase transformations in $(Mn,Fe)_2(P,Si)$ magnetocaloric alloys derive from a segregation phenomenon in which two distinct compositions of the transforming quaternary hexagonal phase coexist, yet transform separately. These compositional populations are a result of a dynamic re-equilibration process active between 1173 K and 1373 K, where slow diffusion kinetics govern the rate at which the composition of the transforming alloy approaches its

equilibrium value at each temperature. The gradients resulting from this diffusional process suggest that the coexistence of P-depleted cubic impurity phases play an important role in re-equilibration, and more work is needed to establish if, for example, diffusion across the impurity interface, as opposed to through the transforming phase, is a limiting factor.

The dynamic re-equilibration process also explains the observed dependence of transformation behavior on heat treatment, where multi-step transformations are observed after intermediate annealing times, and then relax back into single-step transformations after much longer annealing. Evidently, the diffusional processes responsible for re-equilibration are so slow that intermediate annealing times result in well-defined bimodal composition distributions that are observed both in composition maps and calorimetry experiments. It is only after long annealing times on the order of one week that the alloy more nearly re-homogenizes, although even after this time, substantial unimodal P inhomogeneities are observed. Multi-step transformation behavior undesirable for applications, and can be avoided through short annealing times at 1373 K, although this must be weighed against disorder-induced decreases in the entropy and enthalpy of transformation.

VI.6 References

[1] E. Brück, Journal of Physics D: Applied Physics **38,** R381 (2005).

[2] A. Smith, C. R. H. Bahl, R. Bjork, K. Engelbrecht, K. K. Nielsen, and N. Pryds, Advanced Energy Materials **2,** 1288 (2012).

[3] X. Moya, S. Kar-Narayan, and N. D. Mathur, Nature Materials **13,** 439 (2014).

[4] V. Franco, J. S. Blázquez, B. Ingale, and A. Conde, Annual Review of Materials Research **42,** 305 (2012).

[5] J. Liu, T. Gottschall, K. P. Skokov, J. D. Moore, and O. Gutfleisch, Nat Mater **11,** 620 (2012).

[6] A. Planes, L. Manosa, and M. Acet, Journal of Physics-Condensed Matter **21** (2009).

[7] F. X. Hu, B. G. Shen, J. R. Sun, Z. H. Cheng, G. H. Rao, and X. X. Zhang, Applied Physics Letters **78,** 3675 (2001).

[8] M. Khan, N. Ali, and S. Stadler, Journal of Applied Physics **101** (2007).

[9] T. Krenke, E. Duman, M. Acet, E. F. Wassermann, X. Moya, L. Manosa, and A. Planes, Nat Mater **4,** 450 (2005).

[10] J. C. Debnath, R. Zeng, J. H. Kim, P. Shamba, and S. X. Dou, Applied Physics A **106,** 245 (2011).

[11] S. Fujieda, A. Fujita, and K. Fukamichi, Science and Technology of Advanced Materials **4,** 339 (2016).

[12] N. H. Dung, Z. Q. Ou, L. Caron, L. Zhang, D. T. C. Thanh, G. A. de Wijs, R. A. de Groot, K. H. J. Buschow, and E. Brück, Advanced Energy Materials **1,** 1215 (2011).

[13] N. T. Trung, Z. Q. Ou, T. J. Gortenmulder, O. Tegus, K. H. J. Buschow, and E. Brück, Applied Physics Letters **94** (2009).

[14] Y. Zhang, L. L. Zhang, Q. Zheng, X. Q. Zheng, M. Li, J. Du, and A. Yan, Scientific Reports **5,** 11 (2015).

[15] R. Sahoo, D. M. R. Kumar, D. A. Babu, K. G. Suresh, A. K. Nigam, and M. M. Raja, Journal of Magnetism and Magnetic Materials **347,** 95 (2013).

[16] R. Caballero-Flores, T. Sanchez, W. O. Rosa, J. Garcia, L. Gonzalez-Legarreta, D. Serantes, V. M. Prida, L. Escoda, J. J. Sunol, and B. Hernando, Journal of Alloys and Compounds **545,** 216 (2012).

[17] H. C. Xuan, K. X. Xie, D. H. Wang, Z. D. Han, C. L. Zhang, B. X. Gu, and Y. W. Du, Applied Physics Letters **92,** 3 (2008).

[18] S. C. Ma, Q. Q. Cao, H. C. Xuan, C. L. Zhang, L. J. Shen, D. H. Wang, and Y. W. Du, Journal of Alloys and Compounds **509,** 1111 (2011).

[19] N. M. Bruno, D. Salas, S. Wang, I. V. Roshchin, R. Santaniarta, R. Arroyave, T. Duong, Y. I. Chumlyakov, and I. Karaman, Acta Materialia **142,** 95 (2018).

[20] N. M. Bruno, C. Yegin, I. Karaman, J.-H. Chen, J. H. Ross, J. Liu, and J. Li, Acta Materialia **74,** 66 (2014).

[21] A. Ghosh and K. Mandal, Applied Physics Letters **104,** 4 (2014).

[22] L. Chen, F. X. Hu, J. Wang, J. Shen, J. R. Sun, B. G. Shen, J. H. Yin, L. Q. Pan, and Q. Z. Huang, Journal of Applied Physics **109,** 3 (2011).

[23] J. Liu, T. G. Woodcock, N. Scheerbaum, and O. Gutfleisch, Acta Materialia **57,** 4911 (2009).

[24] T. Liu, Y. G. Chen, Y. B. Tang, S. F. Xiao, E. Y. Zhang, and J. W. Wang, Journal of Alloys and Compounds **475,** 672 (2009).

[25] C. Xiang, Y. G. Chen, and Y. B. Tang, Journal of Magnetism and Magnetic Materials **323,** 3177 (2011).

[26] P. Gebara, P. Pawlik, and M. Hasiak, Journal of Magnetism and Magnetic Materials **422,** 61 (2017).

[27] J. Liu, M. Krautz, K. Skokov, T. G. Woodcock, and O. Gutfleisch, Acta Materialia **59,** 3602 (2011).

[28] M. Krautz, J. D. Moore, K. P. Skokov, J. Liu, C. S. Teixeira, R. Schafer, L. Schultz, and O. Gutfleisch, Journal of Applied Physics **112,** 6 (2012).

[29] C. B. Zimm and S. A. Jacobs, Journal of Applied Physics **113,** 3 (2013).

[30] H. Y. Zheng, Y. B. Tang, Y. G. Chen, J. H. Wu, H. S. Wang, X. Z. Xue, J. Wang, and W. K. Pang, Journal of Alloys and Compounds **646,** 124 (2015).

[31] V. Hoglin, M. Hudl, M. Sahlberg, P. Nordblad, P. Beran, and Y. Andersson, Journal of Solid State Chemistry **184,** 2434 (2011).

[32] M. J. Neish, M. P. Oxley, J. Guo, B. C. Sales, L. J. Allen, and M. F. Chisholm, Physical Review Letters **114,** 5 (2015).

[33] M. Hudl, P. Nordblad, T. Bjorkman, O. Eriksson, L. Haggstrom, M. Sahlberg, Y. Andersson, E. K. Delczeg-Czirjak, and L. Vitos, Physical Review B **83,** 7 (2011).

[34] G. J. Li, O. Eriksson, B. Johansson, and L. Vitos, Journal of Applied Physics **118,** 7 (2015).

[35] X. F. Miao, N. V. Thang, L. Caron, H. Yibole, R. I. Smith, N. H. van Dijk, and E. Brück, Scripta Materialia **124,** 129 (2016).

[36] Z. Q. Ou, L. Zhang, N. H. Dung, L. van Eijck, A. M. Mulders, M. Avdeev, N. H. van Dijk, and E. Bruck, Journal of Magnetism and Magnetic Materials **340,** 80 (2013).

[37] M. Fries, L. Pfeuffer, E. Bruder, T. Gottschall, S. Ener, L. V. B. Diop, T. Gröb, K. P. Skokov, and O. Gutfleisch, Acta Materialia **132,** 222 (2017).

[38] J. W. Lai, Z. G. Zheng, B. W. Huang, H. Y. Yu, Z. G. Qiu, Y. L. Mao, S. Zhang, F. M. Xiao, D. C. Zeng, K. Goubitz, and E. Brück, Journal of Alloys and Compounds **735,** 2567 (2018).

[39] J. H. Grebenkemper, J. D. Bocarsly, E. E. Levin, G. Seward, C. Heikes, C. Brown, S. Misra, F. Seeler, K. Schierle-Arndt, S. D. Wilson, and R. Seshadri, Acs Applied Materials & Interfaces **10,** 7208 (2018).

[40] Y. X. Geng, Z. J. Zhang, O. Tegus, C. Dong, and Y. X. Wang, Science China-Materials **59,** 1062 (2016).

[41] N. H. Dung, L. Zhang, Z. Q. Ou, and E. Bruck, Applied Physics Letters **99** (2011).

[42] C. T. O. Chantler, K.; Dragoset R. A.; Chang, J.; Kishore, A. R.; Kotochigova, S. A.; and Zucker, D. S., in *NIST Standard Reference Database 66*, edited by P. M. L. NIST (United States Secretary of Commerce, 2001).

[43] N. H. Dung, L. Zhang, Z. Q. Ou, and E. Bruck, Scripta Materialia **67,** 975 (2012).

[44] Z. Q. Ou, Thesis, Delft University of Technology, 2013.

CHAPTER VII

OXYGEN-MEDIATED COMPOSITION MODULATION OF MAGNETO-STRUCTURAL TRANSFORMATIONS IN MAGNETOCALORIC $(MN,FE)_2(P,SI)$ ALLOYS

VII.1 Introduction

Magnetocaloric alloy systems like $La(Fe,Si)_{13}$, Ni-Mn-X metamagnetic shape memory alloys (MSMAs), and $(Mn,Fe)_2(P,Si)$ manifest coupled magneto-structural transformations (MSTs) [1-4], making them of primary interest for solid-state magnetic refrigeration [5,6] and thermomagnetic generation applications [7,8]. In order to most efficiently interconvert thermal and magnetic energy in these applications, systems must be designed with large heat absorption and minimal losses distributed across large temperature ranges, for example, with graded regenerator beds [9]. At the materials level, this translates directly into designing families of magnetocaloric alloys whose MSTs all generate maximum entropy of transformation and minimal hysteresis loss, each with some different critical temperature near room temperature. Fortunately, the MST transformation entropy, hysteresis, and critical temperature can all be tuned sensitively by alloy composition [10-12]; however, it is very difficult to affect one parameter without also changing the others, and so simultaneous optimization over the three together is highly constrained. Hence, the ability to design the composition of magnetocaloric alloys within narrow tolerances is absolutely critical to further development for refrigeration and generation applications.

At the same time, magnetocaloric alloys are multicomponent systems that can often spontaneously phase segregate, which by definition, causes the composition of the phase of interest to deviate from the designed nominal composition. This challenge is well recognized in La-Fe-Si, where the desired $La(Fe,Si)_{13}$ phase is nearly always accompanied by Fe-rich α–(Fe,Si) and La-rich $La_1Fe_1Si_1$ phase, with the resulting excess Si content in the 1:13 phase causing steadily decreased MST critical temperature [13-16]. Stability of the α phase has proven particularly tenacious, with conventional arc-melting syntheses [17,18] requiring homogenization heat treatments for several hours at temperatures above 1550 K [19,20] or 7-50 day heat treatments around 1353 K [21,22] to form >50 vol. % of 1:13 phase. Since then, the underlying formation mechanism of 1:13 phase through the peritectic / peritectoid $\alpha + La_1Fe_1Si_1 \rightarrow La(Fe,Si)_{13}$ reaction [23-27] has been understood, so that α phase suppression [28,29] / formation [30] in hyper- / hypo-peritectic La-Fe-Si [31] has been clarified. This has led directly to the development of new rapid quench and ball milling [32] processes that effectively seed the as-cast alloys with many small $La(Fe,Si)_{13}$ nuclei that rapidly grow after just minute-long anneals [33,34], greatly reducing the volume of impurity phases, and thus the deviation of the transforming 1:13 phase from its designed nominal value. Similarly, a Co-rich γ disordered FCC phase observed in NiCoMnIn [35,36] alloys is responsible for increasing the critical temperature [37] and broadening the transformation [38,39] in the In-poor transforming Heusler phase. The formation of the γ phase is evidently governed by the $L \longrightarrow \gamma + L2_1$ eutectic reaction [40,41], so rapidly-quenched melt-spun NiCoMnIn alloys

can suppress the γ phase [42], again mitigating the composition modulation of the transformation caused by phase segregation.

Phase segregation plays an equally important role in Mn-Fe-P-Si alloys, where coexistence of P-depleted ternary $(Mn,Fe)_3Si$ and $(Mn,Fe)_5(P,Si)_3$ phases creates a P excess in the transforming hexagonal $(Mn,Fe)_2(P,Si)$ phase [43], thereby lowering its critical temperature and increasing its hysteresis [44]. Although it is suggested that higher Fe content can suppress the $(Mn,Fe)_3Si$ phase [45] and element additions like B can help stabilize the $(Mn,Fe)_2(P,Si)$ phase [46], the quantitative equilibria of these phases is not well known. In any case, substantial $(Mn,Fe)_2(P,Si)$ content is formed even directly after casting, and later annealing heat treatments continuously grow the 2:1 phase [47] without evidencing any competition between the hexagonal and impurity phases that would be characteristic of a diffusion-limited peritectic reaction. Characteristic microstructures for a variety of cooling treatments show the impurities segregated at $(Mn,Fe)_2(P,Si)$ grain boundaries [48], with no fine lamellae characteristic of a eutectic reaction. Although a partial phase diagram for Mn-Fe-P-Si has been developed [49], it does not yet suggest a similar method for reducing impurity phases and composition deviations in these alloys.

In this work, we further investigate the mechanisms behind the phase segregation leading to compositional modulation in $(Mn_xFe_{2-x})(P_{1-y}Si_y)$ alloys, and their impact on the resulting magneto-structural transformation properties. Through quantitative compositional analyses of transforming hexagonal and non-transforming ternary phases in alloys throughout the composition space, we establish that (1) deviations of up to 4 at. % Si and 2 at. % Mn from desired nominal compositions are due entirely to the presence

of P-depleted ternary and SiO_2 impurity phases and (2) the relative amount of at least one of these ternary phases is greatly affected by oxidation, increasing steadily from 1 vol. % to 7 vol. % after repeated oxidizing processing cycles. Finally, we quantify the underlying sensitivity of transformation critical temperature, hysteresis, and enthalpy on composition of the transforming $(Mn,Fe)_2(P,Si)$ phase, showing for example that a deviation of 1 at. % Si can modulate transformation critical temperatures and hysteresis by as much as 26 K and 3 K, respectively. Together, these results suggest the importance of oxygen-free processing to controllable synthesis of $(Mn_xFe_{2-x})(P_{1-y}Si_y)$ alloys for refrigeration applications, since relatively minor amounts of ~5 vol. % impurity phase with only ~4 wt. % oxygen content can cause transformation critical temperatures and hystereses to deviate by more than 100 K and 15 K from desired design values.

VII.2 Experimental Methods

$(Mn_xFe_{2-x})(P_{1-y}Si_y)$ alloys with nominal compositions ($1.18 \leq x \leq 1.28$) and ($0.53 \leq y \leq 0.61$) were synthesized by powder metallurgy starting from mixing 99.9 % purity Mn and 99.99 % Si powders [ESPI Metals, metals basis] with 99.5 % Fe_2P and 99.99 % red P powders [Sigma Aldrich] and high-energy milling in ZrO_2 milling jars with 3 mm ZrO_2 media [Retsch] at 250-300 rpm for 8 h. Milled powders were pressed under 1000 psi uniaxial stress into 8 mm diameter pellets and sintered in Ar-filled quartz ampoules at 1373 K for 6 h followed by annealing at 1173 K for 20 h and furnace cooling. Annealed pellets were re-ground and pressed into new pellets under Ar and put through the identical 1373 K / 6 h + 1173 K / 20 h heat treatment, with the first press / anneal cycle designated “A” processing, the second designated “B”, etc., as in the

remainder of the text. Except where otherwise specified, oxygen was excluded during all processing steps, including milling under Ar in vacuum grease- and parafilm- sealed ZrO_2 jars, storing raw powders and pressing pellets under glovebox Ar (<0.1 ppm O_2, <0.5 ppm H_2O), and melt sealing quartz ampoules within 3-5 minutes of backfilling with Ar in a glovebox.

Electron micrographs and quantitative composition analyses via energy and wavelength dispersive spectroscopy (EDS and WDS) were taken using the Cameca SXFive electron microprobe. Phase compositions were measured by average spot (point) analyses using a beam voltage of 15 kV and a beam current of 20 nA with counting times of 20 s on peak and 10 s on each background. GaP was used as the P standard, while pure element standards were used for Mn, Fe, and Si. Mean compositions and standard deviations were taken from 12 5 μm spots in the majority $(Mn,Fe)_2(P,Si)$ phase and 2-3 1 μm spots in all other phases. Phase transformation properties of the processed alloys were characterized via differential scanning calorimetry (DSC) with a QA-20 system equipped with an RCS90 cooling unit [Thermal Analysis] at a standard 10 K / min ramp rate. Transformation critical temperatures and hystereses have been computed from DSC traces as the average and difference, respectively, of the peak temperatures on heating and cooling. Transformation enthalpies have been computed as the area between each heating / cooling peak and a sigmoidal baseline defined at four points where the derivative heat flow signal is approximately constant.

VII.3 Results

VII.3.1 Multiphase Microstructure and Measured Compositions

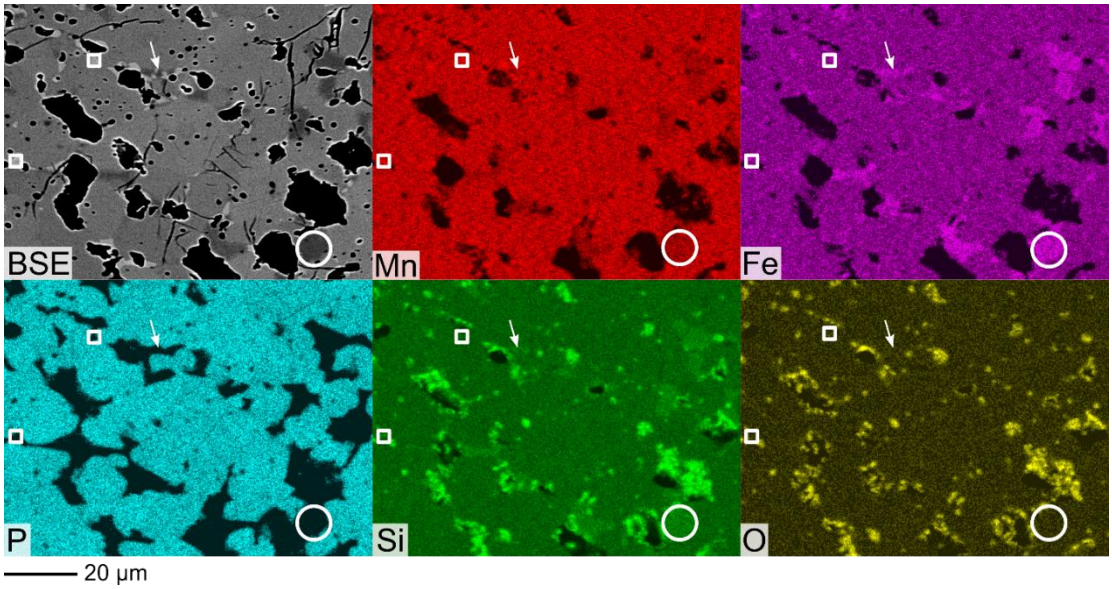

Figure VII.1 Phase microstructure of typical alloy. Backscatter electron (BSE) image and corresponding Energy Dispersive Spectroscopy (EDS) elemental Mn, Fe, P, Si composition maps for $(Mn_xFe_{2-x})(P_{1-y}Si_y)$ alloy with nominal (x = 1.239, y = 0.559) composition. Presence of P-depleted ternary phases (white squares, circles) and SiO_2 (white diamond) modulates composition of majority $(Mn,Fe)_2(P,Si)$ phase.

After heat treatment, alloys throughout the composition space manifest a typical multiphase microstructure consisting of majority hexagonal $(Mn,Fe)_2(P,Si)$ phase with minor impurities (boxes, circles) on the order of 5-20 μm. Qualitative composition mapping via Energy Dispersive Spectroscopy (EDS) confirms that the impurity phases are not merely P-poor, but essentially P-depleted (0.5-2.0 at. %), consistent with previous observations (Fig. VII.1). The impurity with darker Z-contrast is evidently rich in Fe and Si and poor in Mn with respect to the hexagonal phase; whereas the brighter phase is somewhat rich in Mn but has an otherwise similar composition to the matrix. The two impurity phases are most commonly observed as separate islands, but also

occasionally directly paired up within the same island (white arrow), which may suggest a mechanism by which one phase transforms into the other. The SiO_2 content at first appears large, but much of it is layered within voids and is probably introduced after processing during early polishing steps. The volume of SiO_2 inclusions in the matrix that likely contributes to composition modulation is far smaller.

Phase	Mn / at. %	Fe / at. %	P / at. %	Si / at. %	Me : NM
Nominal	41.3 ± ---	25.4 ± ---	14.7 ± ---	18.6 ± ---	2.00 : 1
Matrix	42.3 ± 0.1	25.1 ± 0.1	16.5 ± 0.4	16.2 ± 0.4	2.06 : 1
Squares	53.9 ± 0.7	28.3 ± 0.7	0.4 ± 0.7	17.4 ± 0.7	4.62 : 1
Circles	39.4 ± 0.1	32.4 ± 0.1	1.7 ± 0.9	26.0 ± 0.9	2.59 : 1

Table VII.1 Summary of compositions of matrix and impurity phases. Summary of compositions and Metal to Non Metal ratio (Me : NM) of phases in Fig. VII.1 measured from spot-averaged Wavelength Dispersive Spectroscopy (WDS) across the alloy surface. Means and standard deviations taken from 12 5μm spots in the majority $(Mn,Fe)_2(P,Si)$ phase and 2-3 1 μm spots in the impurity phases.

Further quantitative composition analysis via Wavelength Dispersive Spectroscopy (WDS) confirms these initial observations (Table VII.1), and demonstrates substantial deviation in P and Si content in the $(Mn,Fe)_2(P,Si)$ phase. The measured Metal-to-Non Metal (Me : NM) stoichiometries of the impurity phases deviate substantially from the $(Mn,Fe)_3Si$ and $(Mn,Fe)_5Si_3$ phases normally reported, being more similar to $(Mn,Fe)_5Si_2$ and $(Mn,Fe)_9Si_2$. In order to better clarify the relationship between the impurity phases and the observed deviation of the $(Mn,Fe)_2(P,Si)$ phase composition, we have collected these composition data (Fig. VII.2) for $(Mn_xFe_{2-x})(P_{1-y}Si_y)$ alloys throughout the nominal composition space ($1.18 \leq x \leq 1.28$) and ($0.53 \leq$

$y \leq 0.61$). Viewed in this manner, it is clear that the $(Mn,Fe)_5Si_2$ and $(Mn,Fe)_9Si_2$ phases are neither outliers nor mis-characterizations of the expected $(Mn,Fe)_3Si$ and $(Mn,Fe)_5Si_3$ phases. Instead, all four impurities are expected from the Mn-Si binary phase diagram and so clearly distinguished by their Me : NM ratio (Fig. VII.2a), and only these four impurities are observed repeatedly throughout the alloy space. Typically only two or at most three of the impurities are observed in any given sample, but there do not appear to be any trends governing which pairs or triplets appear together, nor any clear dependence on the nominal or actual $(Mn,Fe)_2(P,Si)$ phase composition. However, it is clear that the $(Mn,Fe)_9Si_2$ phase alone is distinguished by its high oxygen content (Fig. VII.2b). This shows that despite the presence of oxygen within SiO_2 or $(Mn,Fe)_9Si_2$ in the system, the $(Mn,Fe)_2(P,Si)$ phase of interest remains largely unaffected, and also suggests that oxygen may be playing some role in controlling the observed phase microstructure.

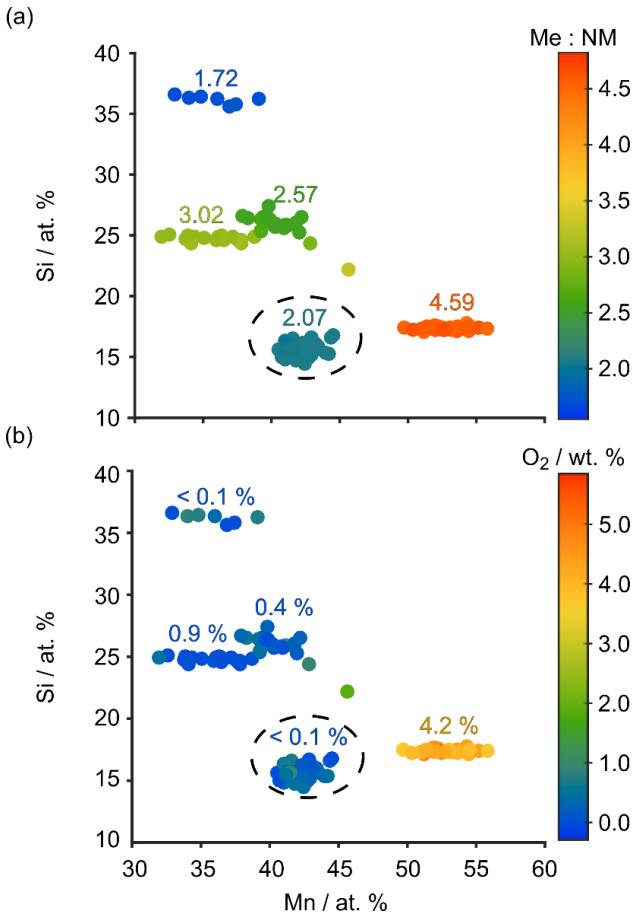

Figure VII.2 Scatter plots of compositions for matrix and impurity phases in all samples. Measured compositions of multi-phase assemblages taken from spot-averaged Wavelength Dispersive Spectroscopy (WDS) in terms of Mn and Si contents, as well as (a) Metal-to-Non Metal ratio, Me : NM, and (b) O_2 content.

VII.3.2 Phase Evolution During Repeated Processing

In order to improve homogenization of the alloys, samples were re-ground and pressed into new pellets under Ar before re-sintering and annealing in quartz ampoules under the same 1373 K / 6 h + 1173 K / 20 h heat treatment. The alloys after the first and second rounds of annealing were designated “A” and “B” processed, respectively. In fact, no homogenization effects on repeated processing were observed, and instead all “A” and “B” samples manifested one or more of the P-depleted impurity phases. In

many cases, the same impurities in an "A" sample persisted into its corresponding "B" sample, although occasionally one phase was observed to replace another in the "B" sample, strongly suggesting a conversion of one impurity into another. The composition deviations of the $(Mn,Fe)_2(P,Si)$ phase also showed a strong dependence on "A" versus "B" processing (Fig. VII.3), with substantial deviation before and after "A" processing compared to much smaller deviation before and after "B" processing (Table VII.2). The deviation before and after "A" processing is quite large, with a mean value of $(\Delta Mn, \Delta Fe, \Delta P, \Delta Si) = (+1.55, -0.83, +2.40, -3.12)$ at. % especially considering, for example, the change in critical temperature with Mn in $(Mn_xFe_{2-x})(P_{0.4}Si_{0.6})$ is reported at -7.2 K / at. % [45].

In these samples, great care was taken to exclude oxygen during all processing steps, with all grinding and processing taking place under Ar, and even by using a temporary mechanical seal to backfill the quartz ampoule within glovebox atmosphere before melt sealing within 3-5 minutes. Despite this, it is likely that some small random amount of oxygen was added, causing the zero-centered random scatter of the composition deviations before and after "B" processing. Together, these results suggest that large composition deviations due to phase segregation in the "A" processing cycle quickly converge, so that the average deviation induced during the "B" processing is already zero. At the same time, additional processing does introduce small amounts of oxidation and random composition deviation.

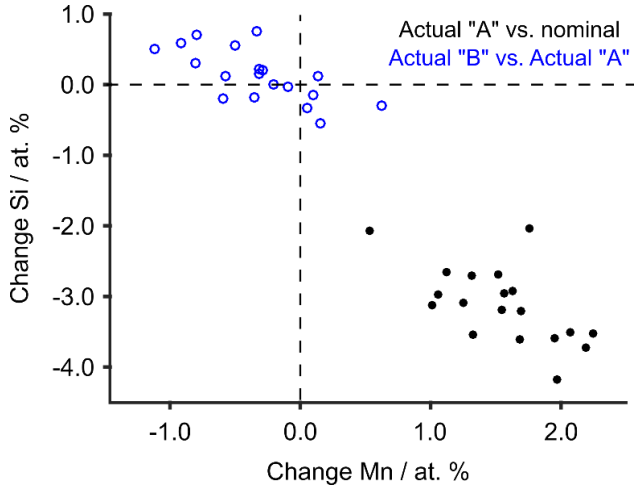

Figure VII.3 Deviations in composition during processing. Measured composition deviations of transforming hexagonal phase for all alloys between "A" processing cycle with respect to nominal (black, filled) and second "B" processing cycle with respect to initial "A" processing.

Processing Cycle	ΔMn / at. %	ΔFe / at. %	ΔP / at. %	ΔSi / at. %	L_2 Dev.
"A" vs. nom.	+1.55 ± 0.44	-0.83 ± 0.47	+2.40 ± 0.50	-3.12 ± 0.55	4.31 ± 0.52
"B" vs. "A"	-0.32 ± 0.43	+0.37 ± 0.40	-0.13 ± 0.36	+0.13 ± 0.37	0.52 ± 0.41

Table VII.2 Summary of hexagonal phase composition deviations described in Fig. VII.3. The L_2 norm of the deviation vector, $\sqrt{(\Delta\mathrm{Mn})^2 + (\Delta\mathrm{Fe})^2 + (\Delta\mathrm{P})^2 + (\Delta\mathrm{Si})^2}$ decreases greatly from the "A" to "B" processing cycle.

In order to further investigate this competition between homogenization and oxidation induced by additional processing, we have selected an alloy with nominal composition ($x = 1.250$, $y = 0.640$) for further processing. By again performing all grinding, pressing, and temporary sealing steps under glovebox Ar atmosphere, but this time waiting 35-40 minutes before melt sealing, we have been able to introduce a larger somewhat controlled oxygen content in the alloy throughout "A"-"D" processing steps. Although the resulting micrographs (Fig. VII.4) do not initially show much visible change in the microstructure throughout "A"-"D" processing, the BSE Z-contrast

intensities for each of the $(Mn,Fe)_5Si_2$, $(Mn,Fe)_9Si_2$, and $(Mn,Fe)_2(P,Si)$ phases are all distinct enough to be discriminated by a thresholding procedure (Fig. VII.4, orange, blue, and yellow, respectively), for further quantitative analysis in the Sec. VII.4.2.

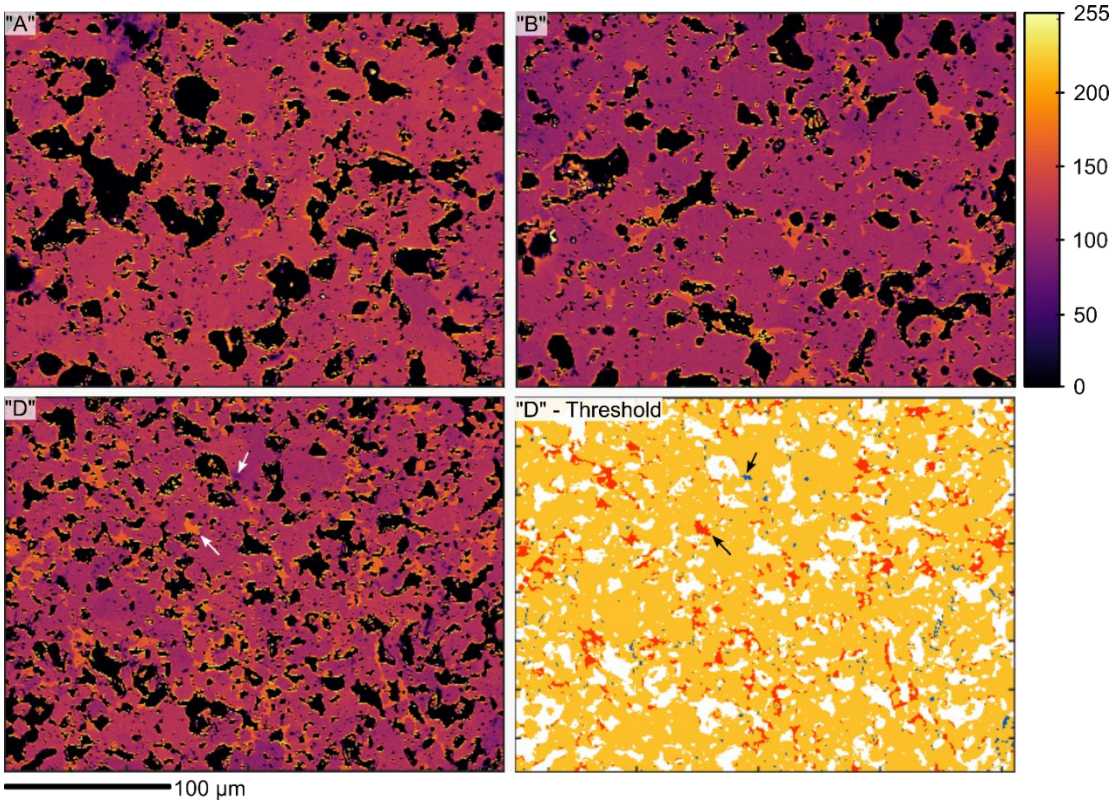

Figure VII.4 Electron micrographs after repeated oxidizing processing. Phase microstructure development of $(Mn_xFe_{2-x})(P_{1-y}Si_y)$ alloy with nominal ($x = 1.250$, $y = 0.540$) composition after repeated processing cycles "A"-"D" intended to promote oxidation. BSE intensity thresholding for "D" micrograph emphasizes volume fractions of minority phases.

VII.4 Discussion

VII.4.1 Phase Segregation Controlled Composition Modulation

Although composition modification of the transforming $(Mn,Fe)_2(P,Si)$ phase through the presence of the P-depleted impurities and SiO_2 appears most likely, other mechanisms, for example, imperfect 2:1 stoichiometry in the starting Fe_2P powder or

evaporation of P due to thermal gradients within the furnace, are also possible. In order to indirectly investigate the feasibility of these other mechanisms, we consider a simple phase mixture model, as:

$$C[\text{nom}] = b_1\,\bar{C}[\text{ternaries}] + b_2\,C[\text{SiO}_2] + (1 - b_1 - b_2)\,C[\text{hex}], \qquad (VII.1)$$

where b_1, b_2, and $1 - b_1 - b_2$ are the mole fractions of P-depleted impurity, SiO_2, and $(Mn,Fe)_2(P,Si)$ hexagonal phases, respectively, and the C's are their respective compositions. Eqn. VII.1 actually represents four equations for each alloy composition, bearing in mind the Mn, Fe, P, and Si contents are all required to balance on both sides of the equation. After some algebra and rearrangement we obtain:

$$(C[\text{nom}] - C[\text{hex}]) = b_1(\bar{C}[\text{ternaries}] - C[\text{hex}]) + b_2\,(C[\text{SiO}_2] - C[\text{hex}]), \qquad (VII.2)$$

$$\Delta C[\text{nom}] = b_1\,\Delta\bar{C}[\text{ternaries}] + b_2\,\Delta C[\text{SiO}_2], \qquad (VII.3)$$

which is the mathematical expression of the constraint that, if the phase mixture model Eqn. VII.1 holds, then the deviation of the hexagonal phase from nominal $\Delta C[\text{nom}]$ should also just be the weighted sum of the deviations of the hexagonal phase from the ternary phases and SiO_2 together.

With measured values for all of the compositions $C[\text{nom}]$, $C[\text{hex}]$, $\bar{C}[\text{ternaries}]$, $C[\text{SiO}_2]$, Eqn. (VII.3) defines a simple multiple linear regression for the mole fractions b_i of the phases in terms of the composition deviations $X_i = \Delta C_i$, given by:

$$\hat{Y} = b_1 X_1 + b_2 X_2. \qquad (VII.4)$$

Although perhaps at first unfamiliar, Fig. VII.5 presents a convenient way of visualizing the model Eqn. VII.4 and its fit to the composition data; instead of indirectly comparing plots of the data $Y(X_1, X_2)$ and model $\hat{Y}(X_1, X_2)$ together as functions of input, it is often more convenient to directly compare the data Y versus the model on a scatter-plot $\hat{Y}$.

If the model is perfect, the scatter plot lies perfectly on the diagonal line $Y = \hat{Y}$ through the origin (Fig. VII.5, dashed line). Fig. VII.5 clearly shows good agreement between the actual deviations and phase mixture model for all elements and samples, yielding an adjusted coefficient of determination $R^2 = 0.91$ for a total ternary impurity mole fraction of $b_1 = 0.120 \pm 005$ and SiO_2 mole fraction of $b_2 = 0.030 \pm 001$. The good fit of the model is further shown by the nearly linear normal quantile-quantile (Q-Q) plot (Fig. VII.5, inset) which shows the model residuals $Y - \hat{Y}$ are indeed normally distributed about zero, as required in linear regression. Furthermore, the correlation between the data and the model residuals $\rho(Y, Y - \hat{Y}) = 0.30$ is relatively small, and the standard error of estimation $S = 0.6$ at. % implies a precision of better than 1 at. % in composition deviations predicted by the model (Table VII.3).

Finally, the fitted model becomes much worse for regressions excluding either the P-depleted impurities or SiO_2 inclusions from the phase mixture, with R^2 dropping more than a third and the data-residual correlation and standard error both doubling, indicating a much lower degree of explained variance in either model. The remaining $100\%\ (1 - R^2) = 9\%$ of the observed data variance is far more likely due to random error than to unaccounted mechanisms like additional phases, P-evaporation, or non-stoichiometry of the starting powders. Together, the regression analyses present strong

indirect evidence that the compositions of the P-depleted and SiO_2 phases, and only those phases, are responsible for the systematic deviation of the $(Mn,Fe)_2(P,Si)$ phase from its designed nominal composition.

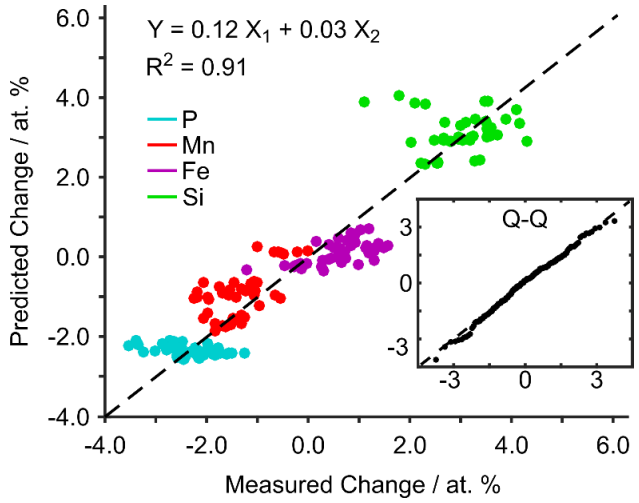

Figure VII.5 Comparison of data with phase mixing model. Hexagonal phase composition deviations (measured with respect to nominal) versus predictions from multilinear regression model assuming deviations due only to P-deleted ternary phases and SiO_2 phases. High goodness-of-fit indicated by coefficient of determination $R^2 \sim 1$ and nearly-linear normal quantile-quantile (Q-Q) plot (inset).

VII.4.2 Effect of Oxidation on Phase Microstructure

In order to further investigate the competing effects of homogenization and oxidation on the phase microstructure during intentional oxidizing steps, multiple thresholded BSE images like in Fig. VII.4 have been collected for each "A"-"D" sample beginning from the nominal ($x = 1.250$, $y = 0.540$) composition. Volume fractions for each of the $(Mn,Fe)_2(P,Si)$ phase and the two $(Mn,Fe)_5Si_2$ and $(Mn,Fe)_9Si_2$ impurities have been collected as thresholded area fractions for 5 300 μm BSE micrographs for each "A"-"D" sample, providing an estimate of uncertainties. Calculated volume

fractions have been normalized with respect to the total non-void volume by subtracting out the observed 21 ± 3 vol. % of voids. The computed volume fractions (Fig. VII.6a) of the oxidized $(Mn,Fe)_9Si_2$ phase clearly increase throughout the "A"-"D" oxidizing processing. The volume fraction of the non-oxidized $(Mn,Fe)_5Si_2$ phase behaves much less systematically, but the uncertainties are also much larger, mainly due to the difficulty of distinguishing the $(Mn,Fe)_2(P,Si)$ and $(Mn,Fe)_5Si_2$ BSE intensities during thresholding. Given this fact, it seems most likely that the content of $(Mn,Fe)_5Si_2$ phase mostly stays about the same throughout.

Segregation Model	$b_1 \pm se(b_1)$	$b_2 \pm se(b_2)$	R^2	$\rho(Y, Y-\hat{Y})$	S / at. %
Hex + Ternaries + SiO_2	0.120 ± 0.005	0.030 ± 0.001	0.91	0.30	0.6 %
Hex + Ternaries	0.160 ± 0.010	- -	0.56	0.66	1.4 %
Hex + SiO_2	- -	0.030 ± 0.002	0.61	0.62	1.3 %

Table VII.3 Goodness-of-fit for selected models. Comparison of mixture models $Y = b_1X_1 + b_2X_2$, (X_1: mean composition of P-depleted ternary phases; X_2: composition of SiO_2) describing hexagonal phase composition modulation. Goodness-of-fit indicated by the fitted volume fraction standard errors $se(b_i)$, adjusted coefficient of determination R^2, data-residual correlations $\rho(Y, Y-\hat{Y})$, and standard error of the regression S.

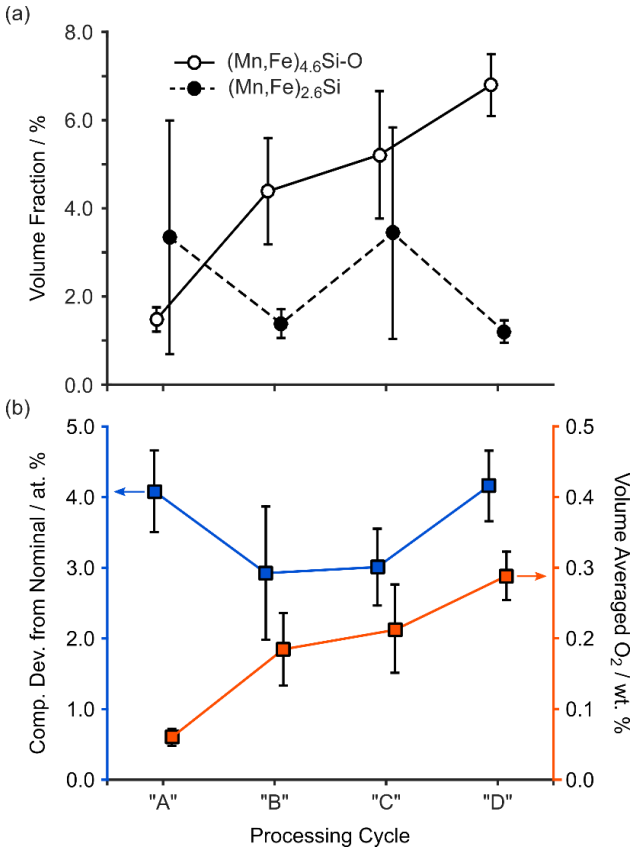

Figure VII.6 Impact of oxidation on phase microstructure. Effect of repeated "A"-"D" processing cycles intended to promote oxidation on (a) volume fractions of minority P-depleted impurity phases and (b) volume averaged O_2 content and hexagonal phase composition deviation, taken as the L_2 norm of the deviation vector (ΔMn, ΔFe, ΔP, ΔSi). Means and standard deviations calculated from sample of 5 BSE images for each "A"-"D" cycle.

Processing Cycle	ΔMn / at. %	ΔFe / at. %	ΔP / at. %	ΔSi / at. %	L_2 Dev.
"A" vs. nom.	1.0 ± 0.2	-0.3 ± 0.1	2.4 ± 0.3	-3.1 ± 0.4	4.1 ± 0.6
"B" vs. nom	0.7 ± 0.2	0.1 ± 0.2	1.6 ± 0.6	-2.4 ± 0.6	2.9 ± 0.9
"C" vs. nom	0.2 ± 0.2	0.5 ± 0.2	1.7 ± 0.3	-2.4 ± 0.3	3.0 ± 0.5
"D" vs. nom	0.5 ± 0.2	0.2 ± 0.1	2.6 ± 0.3	-3.2 ± 0.3	4.2 ± 0.5

Table VII.4 Elemental composition deviations from nominal in oxidizing processed alloys. The L_2 norm of the deviation vector, $\sqrt{(\Delta Mn)^2 + (\Delta Fe)^2 + (\Delta P)^2 + (\Delta Si)^2}$ is plotted in Fig. VII.6b.

By assuming only the $(Mn,Fe)_9Si_2$ phase has non-zero oxygen content, the volume-averaged oxidation of the alloys can be obtained (Fig. VII.6b, orange), and since the oxygen content of $(Mn,Fe)_9Si_2$ is 4.1 ± 0.1 wt. % throughout, the total oxygen content increases similarly to the volume fraction. Finally, this increase can be compared with deviation of the $(Mn,Fe)_2(P,Si)$ phase from the designed nominal composition (Fig. VII.6b, blue), plotted here as the L_2 norm, $(\sum(v_i)^2)^{0.5}$, of the deviation vector $\vec{\boldsymbol{v}} = (\Delta Mn, \Delta Fe, \Delta P, \Delta Si)$. The composition deviation in cycles "B"-"D" follows the shape of the total oxygen content reasonably closely, as expected for the proposed oxygen-mediated $(Mn,Fe)_9Si_2$ phase segregation mechanism. However, the L_2 deviation actually decreases between the "A" and "B" cycles, which is surprising. Additional insight can be gleaned by comparing the deviations of the individual elements (Table VII.4), which shows that between post-"A" and post-"B" processing, the $(Mn,Fe)_2(P,Si)$ phase's Si and Fe contents increase and its Mn content decreases. This is consistent with replacement of a Mn-poor, Fe and Si rich impurity, *e.g.* $(Mn,Fe)_5Si_2$, by one with richer Mn content and poorer Fe and Si content, *e.g.* $(Mn,Fe)_9Si_2$ (Table VII.1, Fig. VII.2). From cycle "B" onward, the compositional changes cannot be explained so simply, and it seems likely that potential SiO_2 growth in later cycles may also be playing a role. In any case, it is clear that compositional deviation in the $(Mn,Fe)_2(P,Si)$ phase is dominated by P and Si, and is correlated with the amount of oxygen in the system. Mechanisms that mitigate the initial large composition deviation after the first processing cycle, like the potential transformation of non-oxidized impurities into oxidized impurities with more favorable composition should be subject to further investigation.

VII.4.3 Effect of Hexagonal Phase Composition on Transformation Properties

Transformation critical temperatures, hystereses, and enthalpies have all been computed from DSC traces taken at 10 K /min for each "A" and "B" processed (Mn_xFe_{2-x})($P_{1-y}Si_y$) alloy throughout the nominal ($x = 1.239$, $y = 0.559$) composition space. Each transformation property has been fit against the measured $(Mn,Fe)_2(P,Si)$ phase composition with a 2-D model of the form:

$$\hat{Y} = b_0 + b_1 X_1 + b_2 X_2, \qquad (VII.5)$$

with $\hat{Y}$ the predicted critical temperatures, and X_1 and X_2 the Mn and Si contents of the $(Mn,Fe)_2(P,Si)$ phase measured from WDS. The 4-D (Mn, Fe, P, Si) model is simplified to a 2-D (Mn, Si) one to avoid over-fitting with excess parameters, and since, to a good approximation, Fe and P contents are entirely determined by Mn and Si contents, respectively.

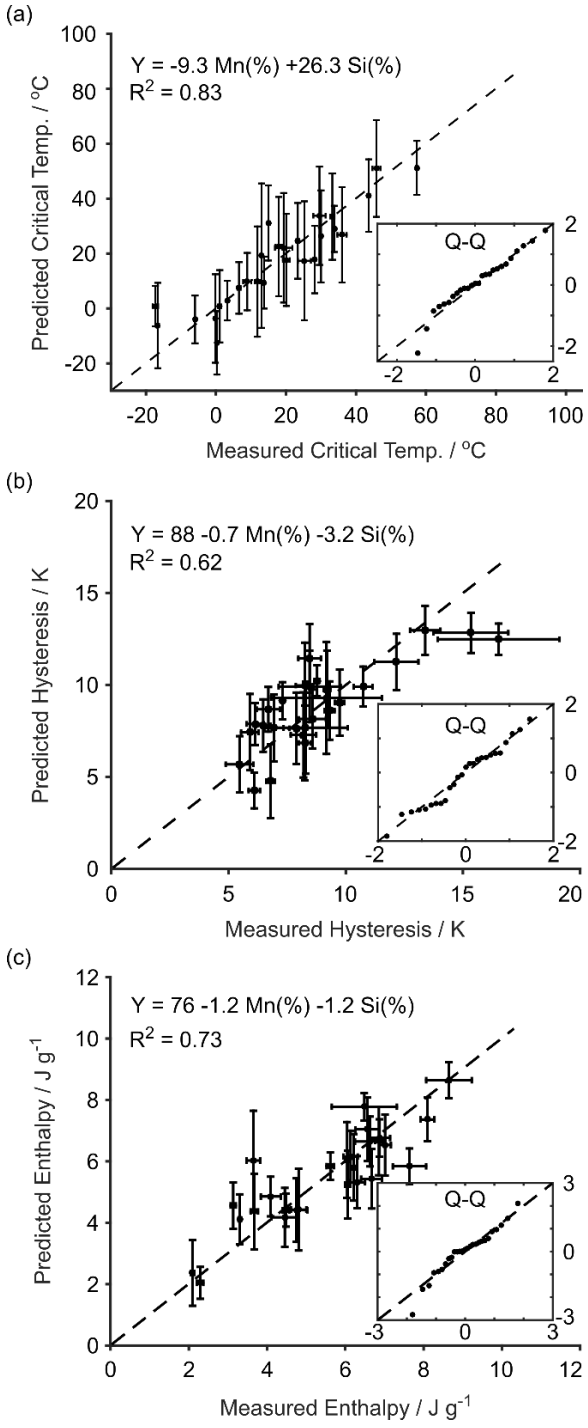

Figure VII.7 Composition dependence of transformation properties. Multilinear regressions for dependence of transformation (a) critical temperatures, (b) hystereses, (c) enthalpies measured from DSC on hexagonal phase Mn and Si content. Goodness-of-fit is indicated by adjusted coefficients of determination R^2 and somewhat linear normal quantile-quantile (Q-Q) plots (insets).

Predicted Var.	$b_0 \pm \mathrm{se}(b_0)$	$b_1 \pm \mathrm{se}(b_1)$	$b_2 \pm \mathrm{se}(b_2)$	R^2	$\rho(Y, Y-\hat{Y})$	S
Critical Temperature	- -	-9.3 ± 0.8	26.3 ± 2.3	0.83	0.40	7.1
Therm. Hysteresis	88 ± 16	-0.7 ± 0.4	-3.2 ± 0.5	0.62	0.59	1.6
Trans. Enthalpy	76 ± 10	-1.2 ± 0.2	-1.2 ± 0.3	0.73	0.49	0.8

Table VII.5 Goodness-of-fit for composition dependence regressions. Summary of fitting parameters and goodness-of-fit parameters for multilinear regressions $Y = b_0 + b_1(\mathrm{Mn}) + b_2(\mathrm{Si})$. Adjusted coefficients of determination R^2 and target-residual correlations $\rho(Y, Y-\hat{Y})$ are unitless; standard error of the regression S has same units U as data Y; slopes b_i and standard errors $\mathrm{se}(b_i)$ have units of either U or U / at. %.

The corresponding multilinear regressions (Fig. VII.7) show fairly good agreement between the model and predictions, with reasonably high R^2 values and generally linear Q-Q plots. Comparison of the goodness-of-fit parameters (Table VII.5) suggests that the regression models for critical temperature and enthalpy of transformation are relatively well fit, with relative errors in the fitting parameters b_i of 10-25 %, $R^2 > \rho(Y, Y-\hat{Y})$, and S only about 12-15 % of the total data range, suggesting a precision in model predictions on the order of 12-15 %. A closer glance at the Q-Q plots reveals that model over-predictions of the order of 2-3 σ are larger than expected for the normal distribution, which can be suggestive of an outlier. In fact, the worst over-estimations in both critical temperature and enthalpy are for the same ($x = 1.280$, $y = 0.540$) nominal composition with actual critical temperature and enthalpy of -16.6 °C and 4.5 J / kg, respectively. However, neither the DSC nor WDS data suggests any reason to exclude this point. The regression analysis for the hysteresis model reveals a somewhat worse fit, with larger 15-50 % relative error in fitting parameters, $R^2 \sim \rho(Y, Y-\hat{Y})$, and S on the order of 15 %. The Q-Q plot also deviates substantially

from straight-line behavior even around the middle -1 to 1 σ range, which should not happen for a well-fit model. This worse fit may be expected since hysteresis can depend on extrinsic factors like defect structures in addition to intrinsic compositional effects, and these can be difficult to control from sample to sample despite identical heat treatments.

Overall, there can be reasonably good confidence in the regression coefficients for the critical temperatures and enthalpies, with critical temperatures increasing by about 26 K / at. % Si and decreasing by about -9 K / at. % Mn, and enthalpies decreasing by about -1 (J / g) / at . % Mn or Si. Hysteresis probably decreases by about 1-4 K / at. % Mn and Si, with Si having a larger effect. It is instructive to compare these models with previously reported trends in the data for similarly prepared alloys [12] that we have computed from published plots (Table VII.6). The regression slopes b_1 and b_2 for the critical temperatures at -8 K / at. % Mn and + 24 K / at. % Si are in good agreement with those developed here, and also with the – 7 K / at. % Mn reported in $(Mn_xFe_{2-x})(P_{0.4}Si_{0.6})$ [45]. Although the slopes for the hystereses at -3 K / at. % Mn and -5 K / at. % do not agree quite as well, they are of the same magnitude. At first, the model intercepts b_0 appear to be completely different. But if we assume that the published data are based off of nominal compositions with similar phase segregation composition deviations of +1.6 at. % Mn and -3.1 at. % Si (Table VII.2) as observed here, the agreement improves. That is, with the formal substitutions written as:

$$\mathrm{Si} = \mathrm{Si}' - 3.1, \qquad (VII.5)$$

$$\mathrm{Mn} = \mathrm{Mn}' + 1.6, \qquad (VII.6)$$

our regression models Eqn. VII.4 become:

$$\hat{Y} = b_0' + b_1' X_1' + b_2' X_2', \qquad (VII.7)$$

with the new regression parameters summarized in Table VII.7. Under these corrections, our models and the published critical temperature data agree extremely well, and it is evident that potentially neglecting the effect of phase segregation modulation of the $(Mn,Fe)_2(P,Si)$ phase's composition can create prediction errors of as much as 100 K. Despite significant improvement, there is still substantial disagreement between the hysteresis models, which may be due to slight differences in the processing methods.

Predicted Var.	b_0	b_1	b_2
Critical Temperature	-90	-7.57	23.7
Therm. Hysteresis	190	-2.65	-4.54

Table VII.6 Computed composition dependence regressions from literature. Computed linear regression fits to the composition maps of critical temperature and hysteresis reported in [12].

Predicted Var.	$b_0' \pm \mathrm{se}(b_0')$	$b_1' \pm \mathrm{se}(b_1')$	$b_2' \pm \mathrm{se}(b_2')$	R^2	$\rho(Y, Y-\hat{Y})$	S
Critical Temperature	-96 ± 2	-9.3 ± 0.8	26.3 ± 2.3	0.83	0.40	7.1
Therm. Hysteresis	97 ± 1	-0.7 ± 0.4	-3.2 ± 0.5	0.62	0.59	1.6

Table VII.7 Transformed composition dependence regressions. Transformed linear regression fits to composition maps of critical temperature and hysteresis reported here (Table VII.5), assuming a simple constant deviation from nominal composition.

VII.5 Conclusion

Through comprehensive characterization of the compositions of main and impurity phases observed throughout the $(Mn_xFe_{2-x})(P_{1-y}Si_y)$ alloy system, we have shown that phase segregation of a variety of impurity P-depleted phases, some reported for the first time here, is responsible for large 1-4 at. % deviations of the transforming $(Mn,Fe)_2(P,Si)$ phase from its desired nominal composition. Oxidation plays an important role in mediating at least one of these segregating phases, so even relatively small volume fractions of oxygen content added through repeated processing can greatly affect the transforming phase's composition deviation. The extreme compositional sensitivity of the transformation critical temperature to Si becomes a major challenge here, since alloy deviations of 4 at. Si can easily lead to critical temperature deviations of 100 K, making quantitative comparisons between different investigations, as well as targeted regenerator bed design, difficult. Together, these results suggest oxygen control may be one way to indirectly control the composition and MST transformation properties of $(Mn,Fe)_2(P,Si)$ alloys, thereby enabling desired refrigeration and generation applications.

VII.6 References

[1] A. Fujita, S. Fujieda, Y. Hasegawa, and K. Fukamichi, Physical Review B **67,** 104416 (2003).

[2] F. X. Hu, B. G. Shen, J. R. Sun, Z. H. Cheng, G. H. Rao, and X. X. Zhang, Applied Physics Letters **78,** 3675 (2001).

[3] J. Liu, T. Gottschall, K. P. Skokov, J. D. Moore, and O. Gutfleisch, Nat Mater **11,** 620 (2012).

[4] N. H. Dung, L. Zhang, Z. Q. Ou, and E. Bruck, Scripta Materialia **67,** 975 (2012).

[5] K. A. Gschneidner and V. K. Pecharsky, International Journal of Refrigeration **31,** 945 (2008).

[6] E. Brück, Journal of Physics D: Applied Physics **38,** R381 (2005).

[7] A. Post, C. Knight, and E. Kisi, Journal of Applied Physics **114** (2013).

[8] A. Waske, D. Dzekan, K. Sellschopp, D. Berger, A. Stork, K. Nielsch, and S. Fahler, Nature Energy **4,** 68 (2019).

[9] S. Jeong, Cryogenics **62,** 193 (2014).

[10] J. C. Debnath, R. Zeng, J. H. Kim, P. Shamba, and S. X. Dou, Applied Physics A **106,** 245 (2011).

[11] M. Khan, N. Ali, and S. Stadler, Journal of Applied Physics **101** (2007).

[12] N. H. Dung, Z. Q. Ou, L. Caron, L. Zhang, D. T. C. Thanh, G. A. de Wijs, R. A. de Groot, K. H. J. Buschow, and E. Brück, Advanced Energy Materials **1,** 1215 (2011).

[13] Y. F. Chen, F. Wang, B. G. Shen, J. R. Sun, G. J. Wang, F. X. Hu, Z. H. Cheng, and T. Zhu, Journal of Applied Physics **93,** 6981 (2003).

[14] S. Fu, Y. Long, W. Sun, X. P. Yi, Y. Q. Chang, R. C. Ye, and K. Yang, Journal of Rare Earths **30,** 1225 (2012).

[15] P. Gebara, P. Pawlik, and M. Hasiak, Journal of Magnetism and Magnetic Materials **422,** 61 (2017).

[16] H. Zhang, Y. Long, Q. Cao, Y. Mudryk, M. Zou, K. A. Gschneidner, and V. K. Pecharsky, Journal of Magnetism and Magnetic Materials **322,** 1710 (2010).

[17] X. Chen, Y. G. Chen, Y. B. Tang, and D. Q. Xiao, Phase Transitions **88,** 1045 (2015).

[18] P. Gebara, P. Pawlik, E. Kulej, J. J. Wyslocki, K. Pawlik, and A. Przybyl, Optica Applicata **39,** 761 (2009).

[19] X. Chen, Y. G. Chen, and Y. B. Tang, Phase Transitions **85,** 27 (2012).

[20] X. Chen, Y. G. Chen, D. Q. Xiao, and Y. B. Tang, Journal of Rare Earths **33,** 182 (2015).

[21] S. Fujieda, K. Fukamichi, and S. Suzuki, Journal of Alloys and Compounds **566,** 196 (2013).

[22] J. Liu, M. Krautz, K. Skokov, T. G. Woodcock, and O. Gutfleisch, Acta Materialia **59,** 3602 (2011).

[23] X. L. Hou, Y. Xue, C. Y. Liu, H. Xu, N. Han, C. W. Ma, and M. H. Phan, Nanoscale Research Letters **10,** 1 (2015).

[24] X. D. Liu, X. B. Liu, Z. Altounian, and G. H. Tu, Applied Physics a-Materials Science & Processing **82,** 339 (2006).

[25] H. Zhang, B. Bao, P. J. Shi, B. Fu, Y. Long, Y. Q. Chang, and F. R. Wan, Journal of Rare Earths **26,** 727 (2008).

[26] S. Fu, Y. Long, C. L. Wang, M. Zhang, O. Soumei, and F. X. Hu, Ieee Transactions on Magnetics **48,** 3757 (2012).

[27] L. Yang, Z. N. Zhou, J. R. Qian, X. Ge, J. Li, Q. D. Hu, and J. G. Li, Metallurgical and Materials Transactions a-Physical Metallurgy and Materials Science **48a,** 4229 (2017).

[28] L. H. Bao, W. Wei, W. D. Fan, and O. Tegus, Journal of Alloys and Compounds **589,** 416 (2014).

[29] Z. T. Zhang, C. He, M. X. Zhang, and J. Liu, Physica B-Condensed Matter **476,** 167 (2015).

[30] X. Chen, Y. G. Chen, Y. B. Tang, and D. Q. Xiao, Journal of Rare Earths **33,** 1293 (2015).

[31] K. Niitsu and R. Kainuma, Intermetallics **20,** 160 (2012).

[32] M. Phejar, V. Paul-Boncour, and L. Bessais, Intermetallics **18,** 2301 (2010).

[33] X. B. Liu, Z. Altounian, and G. H. Tu, Journal of Physics-Condensed Matter **16,** 8043 (2004).

[34] X. B. Liu, X. D. Liu, Z. Altounian, and G. H. Tu, Journal of Alloys and Compounds **397,** 120 (2005).

[35] S. Y. Yang, Y. Su, C. P. Wang, J. H. Zhu, and X. J. Liu, Materials Letters **108,** 215 (2013).

[36] S. Y. Yang, C. P. Wang, Z. Shi, J. M. Wang, J. B. Zhang, Y. X. Huang, and X. J. Liu, Materials Science and Engineering a-Structural Materials Properties Microstructure and Processing **655,** 204 (2016).

[37] Y. Feng, J. H. Sui, Z. Y. Gao, G. F. Dong, and W. Cai, Journal of Alloys and Compounds **476,** 935 (2009).

[38] F. Chen, W. L. Liu, Y. G. Shi, and P. Mullner, Journal of Magnetism and Magnetic Materials **377,** 137 (2015).

[39] J. Liu, T. G. Woodcock, N. Scheerbaum, and O. Gutfleisch, Acta Materialia **57,** 4911 (2009).

[40] A. M. Perez-Sierra, J. Pons, R. Santamarta, P. Vermaut, and P. Ochin, Acta Materialia **93,** 164 (2015).

[41] J. K. Yu, H. W. Li, Q. J. Zhai, J. X. Fu, Z. P. Luo, and H. X. Zheng, Advances in Manufacturing **2,** 353 (2014).

[42] F. Chen, Y. X. Tong, Y. J. Huang, B. Tian, L. Li, and Y. F. Zheng, Intermetallics **36,** 81 (2013).

[43] Z. G. Zheng, Z. R. Zhu, H. Y. Yu, D. C. Zeng, Y. H. Li, A. He, and Y. Mozharivskyj, Journal of Alloys and Compounds **725,** 1069 (2017).

[44] J. H. Grebenkemper, J. D. Bocarsly, E. E. Levin, G. Seward, C. Heikes, C. Brown, S. Misra, F. Seeler, K. Schierle-Arndt, S. D. Wilson, and R. Seshadri, Acs Applied Materials & Interfaces **10,** 7208 (2018).

[45] Y. X. Geng, Z. J. Zhang, O. Tegus, C. Dong, and Y. X. Wang, Science China-Materials **59,** 1062 (2016).

[46] Z. G. Zheng, W. H. Wang, Q. Zhou, L. Lei, Y. Hong, D. C. Zeng, and Y. Mozharivskyj, Journal of Magnetism and Magnetic Materials **477,** 203 (2019).

[47] J. W. Lai, Z. G. Zheng, B. W. Huang, H. Y. Yu, Z. G. Qiu, Y. L. Mao, S. Zhang, F. M. Xiao, D. C. Zeng, K. Goubitz, and E. Bruck, Journal of Alloys and Compounds **735,** 2567 (2018).

[48] M. Fries, L. Pfeuffer, E. Bruder, T. Gottschall, S. Ener, L. V. S. Diop, T. Grob, K. P. Skokov, and O. Gutfleisch, Acta Materialia **132,** 222 (2017).

[49] V. Hoglin, J. Cedervall, M. S. Andersson, T. Sarkar, M. Hudl, P. Nordblad, Y. Andersson, and M. Sahlberg, Rsc Advances **5,** 8278 (2015).

CHAPTER VIII

THERMOELASTIC PHASE BOUNDARY GROWTH IMAGED BY IN-SITU MAGNETIC FORCE MICROSCOPY IN MAGNETOCALORIC $(MN_{1.23}Fe_{0.79})(P_{0.48}Si_{0.49})$ ALLOY

VIII.1 Introduction

Magneto-structural transformations (MSTs) in materials effectively couple magnetic field-induced changes in crystal structure [1-3] to first-order discontinuities in material properties, thus giving rise to phenomena like magneto-volume [4,5], magnetic field-induced strain (MFIS) [6-9], and magneto-caloric [10-15] effects. The non-diffusive and reversible nature of the MSTs underlying these phenomena make them attractive for fast switches and actuators, and especially, novel forms of efficient refrigeration and thermomagnetic generation [16-18]. However, MSTs also proceed by nucleation and growth, potentially requiring over-driving forces to overcome energy barriers along the way that lead to hysteresis loss and critically limit the efficacy of desired applications [19-24]. Engineering materials to reduce these adverse effects requires more sophisticated understanding of the energy barriers opposing transformations, and although these barriers cannot be observed directly, their effects on the progression of the phase transformation can. In this way, *in situ* local observations of MST transformation phenomena and their interaction with microstructural features are critical to further materials development by providing crucial evidence for the hysteretic mechanisms and barriers active throughout the MST.

The MST phenomena in magnetic shape memory alloy (MSMA) systems, especially MFIS, result in macro-scale twinning that can be directly observed through optical surface deformation [25-30], but more detailed understanding of transformation mechanisms is illuminated by *in-situ* magnetic characterization across a variety of length and time scales. Magneto-optical Kerr Effect (MOKE) microscopy studies [31,32] are diffraction-limited to 200-500 nm resolution but most nearly approach real-time characterization [33]. This has allowed, for example, for observations of magnetic-field induced preferential growth of twins in Ni_2MnGa single crystals, based off of the orientation of their magnetic domains' easy axis with respect to the applied field [34]. Similarly, magneto-optical studies using indicator films and colloids [35,36] have worse 1000 nm resolution but amplify weak, sensitive magnetic signals, and have observed domain wall pinning from adjacent twins with domains oriented orthogonal to the applied field in Co-Mn-Ga [37], as well as domain conversion from maze-like to rake-like morphologies after stress-induced twin motion in Ni_2MnGa [38]. Also at the scale of 1000 nm resolution are Scanning Hall Probe Microscopy (SHPM) studies [39,40] that have the added benefit of quantitative stray field measurement, but require slower scans for worse time resolution [41]. SHPM has been used, for example, to demonstrate step-wise growth behavior in Ni-Mn-In, with large regions of austenite-martensite phase coexistence from quenched-in chemical disorder [42]. At much better 1-50 nm resolution, Lorentz Transmission Electron Microscopy (LTEM) studies [43-49] provide a great deal of coupled topographic, crystallographic, and magnetic domain information in thin films [50], showing, for example, that $L2_1$ anti-phase boundaries in Ni_2MnGa act as domain

wall pinning sites, enabling the martensitic domain and twin morphology to carry-over between cycles [51]. Finally, for bulk studies, Magnetic Force Microscopy (MFM) studies [52-57] provide similar 50-100 nm resolution with some quantitative information on coupled topography and stray field, but require much longer time scales [58]. MFM studies in MSMAs have shown a pronounced magneto-elastic interaction in Co-Ni-Ga, with the magnetic domain structure coarsening from nano- to micro-scale domains after repeated stress training [59].

In $La(Fe,Si)_{13}$ and $(Mn,Fe)_2(P,Si)$ magnetocaloric alloys surface deformation beyond cracking [60] is totally absent, and so *in situ* investigations of MST progression rely with few exceptions [61] entirely on the magnetic signal between ferromagnetic (FM) and paramagnetic (PM) phases. The MST in $La(Fe,Si)_{13}$ and related alloys has again been studied across length scales, with magneto-optical imaging suggesting magnetic impurity α-Fe phases [62] as well as microcracks act as defect sites that pin the ferromagnetic-paramagetic phase boundary in La-Fe-Co-Si [63]. At the micro-scale, LTEM studies have given further clues for the high reversibility in these alloys, demonstrating that phase boundaries pass quickly ($t < 33$ ms) through defect- and stress-free ribbons of La-Fe-Si alloys, and the magnetic domain structure is highly repeatable from cycle-to-cycle [64-66]. These kinds of magnetic observations are also beginning to illuminate the MST in $(Mn,Fe)_2(P,Si)$ alloys, with SHPM suggesting the role of magnetoelastic strain induced cracking in the virgin cycle effect [67], and magneto-optical microscopy demonstrating statistical spread in transformation hysteresis and critical temperature for distributions of particles likely due to local variations in

composition or stress [68]. Despite these recent investigations, fundamental questions about the MST in $(Mn,Fe)_2(P,Si)$ remain unresolved, especially regarding the nature of nucleation and growth in the transformation, and how they may be affected by defects at the microscale, like voids and grain boundaries.

To further investigate these questions, we probed the coupled magneto-structural transformation in an $(Mn,Fe)_2(P,Si)$ alloy at the scale of individual grains using magnetic force microscopy (MFM). By observing magnetic phase contrast images throughout the transformation and correlating with topographic features like voids and grain boundaries, we (1) establish the morphology of magnetic domain structures within the ferromagnetic phase of $(Mn,Fe)_2(P,Si)$; (2) demonstrate the utility of temperature-dependent MFM for observing the evolving phase microstructure in the transforming phase; (3) report multi-step and reversible phase boundary movement within a single grain consistent with thermoelastic growth behavior. Finally, we correlate the thermoelastic phase evolution with the underlying topography, suggesting that ferromagnetic phase retained at grain boundaries even well above the transformation provides energetically favorable initiation of the reverse transformation consistent with more growth-dominated behavior. Together these results begin to illuminate the transformation mechanisms and microstructural factors controlling hysteresis in this alloy system, providing a basis for future magnetic studies of MST in $(Mn,Fe)_2(P,Si)$ alloys.

VIII.2 Experimental Methods

An alloy of $(Mn_xFe_{2-x})(P_{1-y}Si_y)$ with $(x = 1.23, y = 0.52)$ was synthesized according to a powder metallurgy route beginning from high purity powders (99.9 % Mn

and 99.99 % Si, ESPI Metals; 99.5 % Fe_2P and 99.99 % red P; Sigma Aldrich), followed by high-energy ball milling for 3 h at 250 rpm then 5 h at 300 rpm. Green pellets pressed uniaxially at 1000 psi were subsequently sealed in quartz ampoules under Ar and sintered for 6 h at 1373 K, annealed for 20 h at 1173 K, and furnace cooled to room temperature. Annealed pellets were additionally homogenized by re-grinding by hand and re-pressing pellets under Ar, then sintering and annealing under the same 1373 K / 6 h + 1173 K / 20 h heat treatment. Homogenized pellets were mounted in Buehler Kunductomet conductive polishing mount, polished, and etched for 20 min at 333 K with a solution of 2.4 mL HCl + 8.00 g $FeCl_3 \cdot 6\ H_2O$ + 19.2 mL EtOH, in order to remove non-transforming ternary phases and emphasize grain boundaries within the transforming $(Mn,Fe)_2(P,Si)$ phase. The polished and etched sample was thermally cycled several times prior to AFM analysis to eliminate virgin transformation effects.

Coupled surface topography and magnetic phase contrast images were obtained using a Nanosurf Flex-Axiom Atomic Force Microscope (AFM) system equipped with a C-3000 controller and isolation stage together with AppNano Low-Moment (LM) CrCo-coated Si probes with lateral resolution better than 60 nm. Temperature control was obtained to better than 0.1 K at setpoint using a Nanosurf resistive heater with Omega CN9600 temperature controller. Magnetic noise from transient currents inside the resistive heater was shielded using a thin sheet of YShield MCF5 magnetic shielding foil sandwiched between two layers of double-sided copper tape. Magnetic phase images were taken during the AFM second scan in contouring mode with 0.7 V free vibration amplitude at lift heights between 150-200 nm above the sample surface. Slight filtering

of AFM images has been performed using a 2x3 pixel Weiner filter. Differential Scanning Calorimetry (DSC) traces were obtained at 10 K / min ramp rate using a Thermal Analysis QA-20 system equipped with an RCS90 cooling unit. Compositional analyses *via* Wavelength Dispersive Spectroscopy (WDS) and backscatter electron (BSE) imaging were performed using the Cameca SXFive electron microprobe.

VIII.3 Results & Discussion

VIII.3.1 Phase Microstructure and Calorimetry

Backscatter electron images show clear majority $(Mn,Fe)_2(P,Si)$ phase with small regions of impurity P-depleted $(Mn,Fe)_3Si$ and $(Mn,Fe)_5Si$ cubic phases (Fig. VIII.1a, BSE). Mean composition of the majority $(Mn_xFe_y)(P_zSi_w)$ phase taken from an average of 12 5-um spot analyses gives ($x = 1.23$, $y = 0.79$, $z = 0.48$ $w = 0.49$), in relatively good agreement with the nominal composition ($x' = 1.21$, $y' = 0.79$, $z' = 0.46$, $w' = 0.54$) calculated from mixing the stock powders. Deviations from nominal composition are consistent with the presence of Mn poor, P depleted impurities forcing an excess of Mn and P into the $(Mn,Fe)_2(P,Si)$ phase. Presence of the first-order magneto-structural transformation is confirmed by calorimetry traces, displaying an endothermic peak on heating around 333.5 K and an exothermic peak on cooling around 327.3 K (Fig. VIII.1b). Although bulk magnetometry has not been used here to explicitly confirm the coupled magnetization change in this particular alloy, an alloy of similar composition ($x = 1.26$, $y = 0.75$, $z = 0.52$ $w = 0.48$) undergoing identical heat treatment was previously reported (Chapter VI) to undergo a magnetization change from ~55 emu / g to

~3 emu / g at 0.1 T applied field. Additional evidence of the first-order magnetization change through magnetic force microscopy will be given presently.

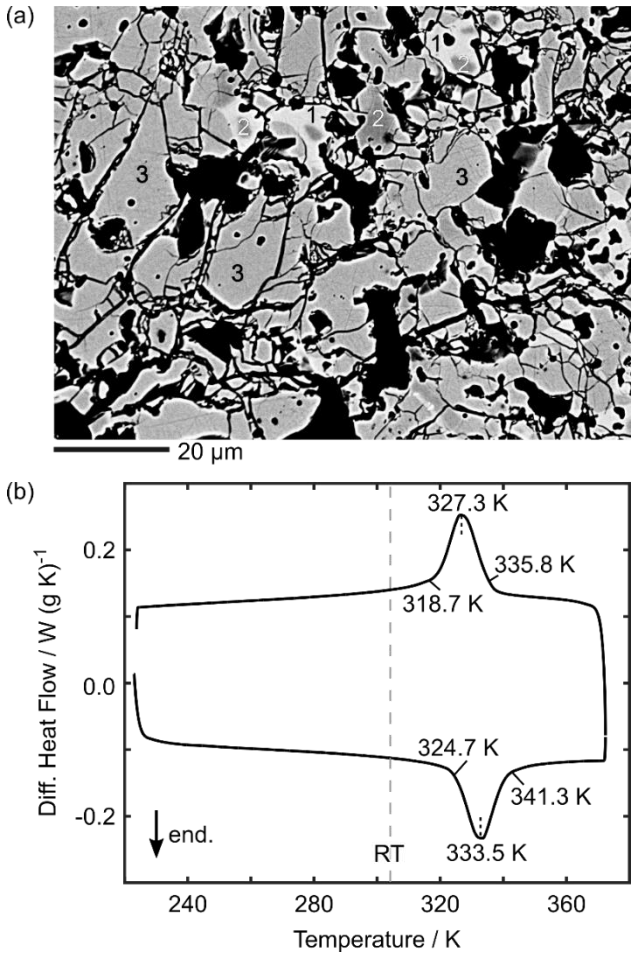

Figure VIII.1 Characterization of magneto-structurally transforming phase. Magneto-structurally transforming hexagonal $(Mn,Fe)_2(P,Si)$ phase as evidenced by (a) BSE imaging and WDS and (b) calorimetry traces. Impurity phases $(Mn,Fe)_{4.6}Si$ (1) and $(Mn,Fe)_5Si_3$ (2) along with majority $(Mn,Fe)_2(P,Si)$ phase (3) are confirmed from WDS. The sample is maximally in its low-temperature ferromagnetic phase at room temperature.

VIII.3.2 Magnetic Domain Structure Below and Above MST

At room temperature, the alloy is well below its cooling transformation and is therefore expected to be almost completely in its low-temperature, ferromagnetic state.

Competition between ferromagnetic exchange energy and magneto-static self-energy leads to the formation of magnetic domains [69] whose stray fields interact with the magnetized AFM probe (Fig. VIII.2), creating a phase shift in the probe's second scan oscillation governed by Eqn. VIII.1:

$$\Delta\phi \propto \frac{\partial^2 B_z}{\partial z^2}, \qquad (VIII.1)$$

with z the height above the sample surface and B_z the component of the net stray magnetic field in this direction.

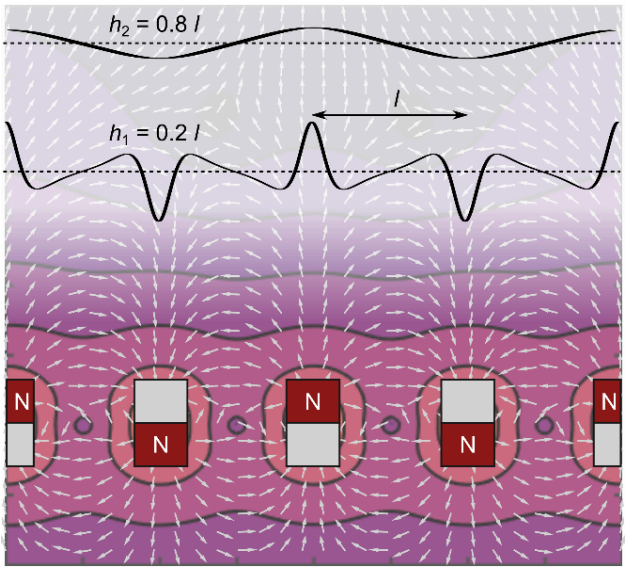

Figure VIII.2 Mechanics of magnetic force microscopy. [bottom] Schematic net stray field magnitude (colors) and direction (arrows) from 1-D array of ideal alternating magnetic domains together with [top] resulting phase shift signals relatively close to the sample surface ($h_1 = 0.2l$) and relatively far from the sample surface ($h_2 = 0.8l$). Distances not to scale.

AFM topography (Fig. VIII.3a) generally reveals a multi-grained structure with grains on the order of 5-8 μm with a relatively smooth surface of 74 nm RMS roughness across the entire area. The corresponding room temperature magnetic phase contrast image (Fig. VIII.3b) consists mainly of irregularly shaped regions of large positive phase (red) directly adjacent to regions of negative phase (blue), as would be expected for adjacent oppositely polarized domain regions. Although there is some correlation between the top-left and top-middle grains (G1 and G2) and the uniform red and blue domain regions near the top of the image, the domain structure is generally uncorrelated with topographical features like voids and grain boundaries. In particular, the magnetic domain regions appear to be continuous across the grain boundaries, demonstrating that the second scan magnetic phase contrast image has been sufficiently decoupled from the first scan topography to avoid serious image artifacts.

Although the observed domain structure bears little resemblance to the repetitive and geometric features of typical maze, mosaic, or ribbon morphologies, similar reversal domains with irregular boundaries have been observed in Co thin films under zero applied field [70] and under stress [71]. In fact, the room temperature magneto-crystalline anisotropy of Co of $K_1 \sim 0.40$ MJ / m^3 [72] is in fairly good agreement with single crystal magnetization experiments in Fe-rich (Mn,Fe)$_2$(P,Si) alloys that determined $K_1 = 0.28$ MJ / m^3 at 5 K [73]. Assuming this anisotropy does not change much for the present Mn-rich alloy, it is suggested that the irregular domain structure observed here is a result of the weak but non-negligible anisotropy in these alloys, potentially in combination with magnetoelastic interactions between neighboring grains. In any case, the domain

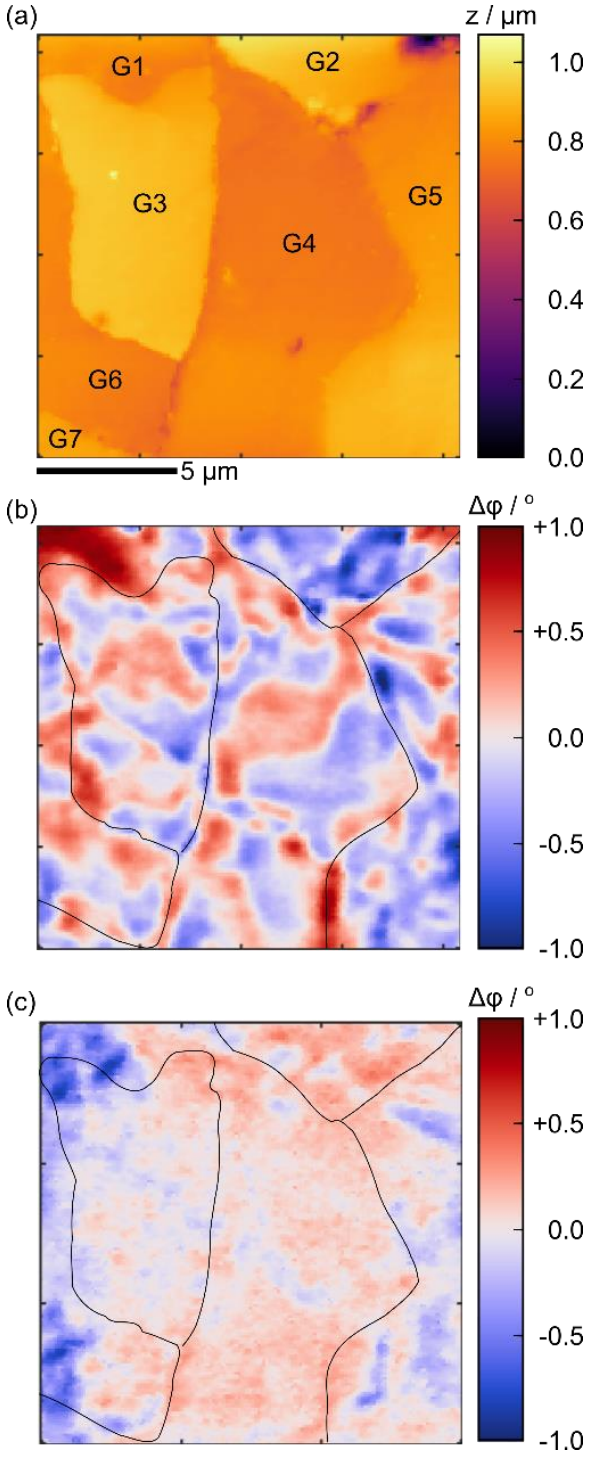

Figure VIII.3 Topography and magnetic phase contrast of multiple-grain region. Room temperature AFM (a) topography and (b) magnetic phase contrast images of a multi-grained region in $(Mn_{1.23}Fe_{0.79})(P_{0.48}Si_{0.49})$ alloy, as compared to (c) magnetic phase contrast above the MST at . Grains are numbered as in the text.

structure is seen to change dramatically from below the MST where FM phase dominates (Fig. VIII.3b) to above the MST where PM phase dominates (Fig. VIII.3c), and acts as an adequate signal for movement of the MST phase boundary.

VIII.3.3 Heating Transformation in Multiple Grains

In order to further probe the progression of the phase boundary throughout the entire progress of the phase transformation, we perform *in situ* characterization of the magnetic phase contrast every 1-2 K degrees on heating (Fig. VIII.4a) and subsequent cooling (Fig. VIII.4b). In most cases on heating we observe a sudden switch from mottled phase contrasts manifesting short-range large-amplitude oscillations, to more uniform phase contrasts, and the reverse on heating. Taking mottled MFM signals as evidence of domain structures in the FM phase and uniform signals as evidence of PM phase, the observations suggest the rapid switching of individual grains from FM to PM phase, *e.g.* grain G3 on heating between 327 and 328 K. In what follows, it is important to distinguish between these fundamental changes in mottled / uniform phase contrast morphology from a simple signal fade-out at high temperature which we attribute to 2^{nd} order Curie demagnetization, *i.e.* from 331 K to 330 K on cooling the G3 signal increases in intensity, but does not actually undergo first-order transformation until the 327 K to 325 K step. Given this caveat, within this region only single-step transformation behavior is observed within each grain on both heating and cooling.

Furthermore, the grain switching sequence on heating {G3, G2, G4/G5/G6} exactly mirrors the sequence on cooling {G4/G5/G6, G2, G3}, with similar values for hysteresis of the within-grain transformations (Table VIII.1), although these are

somewhat lower than the bulk DSC measurement of ~6 K. Most of this discrepancy is presumably due to rate-dependent effects since DSC traces were taken at a rate of 10 K /min whereas MFM traces are taken at a rate of about 1 K / hr, although grain-to-grain variation likely also plays some role. Overall, observations over this region are consistent with a population of transforming grains manifesting single-step transformations with essentially the same hysteresis, with slight differences in critical temperatures likely due to minute composition variations (Chapter VI).

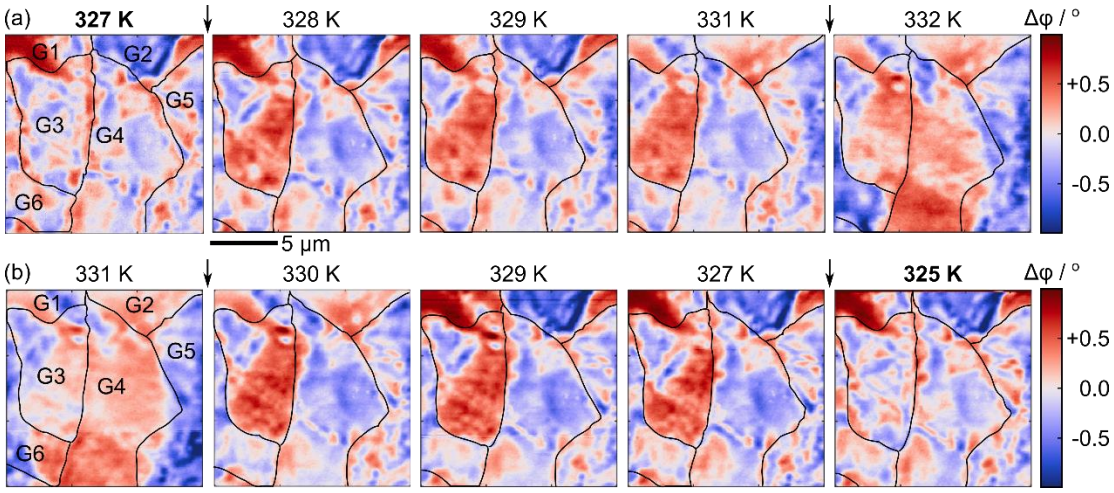

Figure VIII.4 Magneto-structural transformations observed in individual grains. Snap transformations observed on (a) heating and (b) cooling by magnetic phase contrast. Individual grains are numbered [left] as in the text.

Grain	Heating T_c / K	Cooling T_c / K	Hysteresis / K
G2	328	325	3
G3	331	329	2
G4	332	330	2
G5	332	330	2
G6	332	330	2

Table VIII.1Magneto-structural transformations observed in individual grains. Distribution of individual grains' heating and cooling transformation critical temperatures T_c suggest overall similar transformation behavior.

VIII.3.4 Thermoelastic Boundary Growth

The grains in the investigated region (Fig. VIII.4) are all uniformly small on the order of 5 μm. Further insight into the transformation mechanisms, *e.g.*, whether it is nucleation- or growth-dominated, can be gained by observing the transformation ideally across a large range of crystallite sizes so that excluded-volume nucleation or multiple-step growth behavior can be discerned. For this region, the *in-situ* MFM experiment has been performed again over a region with somewhat larger grains ~15 μm (Fig. VIII.5). Once again, the transformation from mottled-contrast FM phase to uniform-contrast PM phase on heating and back again on cooling is observed over a similar temperature range 325 K-334 K. Grain H5 displays a sudden single-step transformation at 331 K and 328 K on heating and cooling, and non-transforming signal fade-out is observed in H1, H2, H4, and H6. However, grain H5 displays an altogether different transformation behavior which appears to occur over several steps, with first its bottom-left corner alone transforming on heating at 328 K, and then marginal phase boundary steps from left to

right at 330 K, 331 K, and 332 K. On cooling, the exact opposite is observed, with the phase boundary back-propagating in steps from 332 K to 328 K. In general, it is difficult to distinguish between phase boundary incremental growth and multiple nucleation at several regions in a single grain. However, the fact that the transformation proceeds precisely from left to right, then right to left only along adjacent regions is strongly suggestive. Assuming independent nucleation events, the stochastic nature of nucleation suggests that a four-step nucleation process would happen to result in the observed transformation behavior $(1/24)(1/24) = 0.2$ % of the time whereas it is almost a certainty under a growth interpretation. Overall, it seems likely that at least in this one grain, the transformation manifests reversible thermoelastic growth behavior, in which the phase boundary moves incrementally between sequential chemical / elastic energy equilibria.

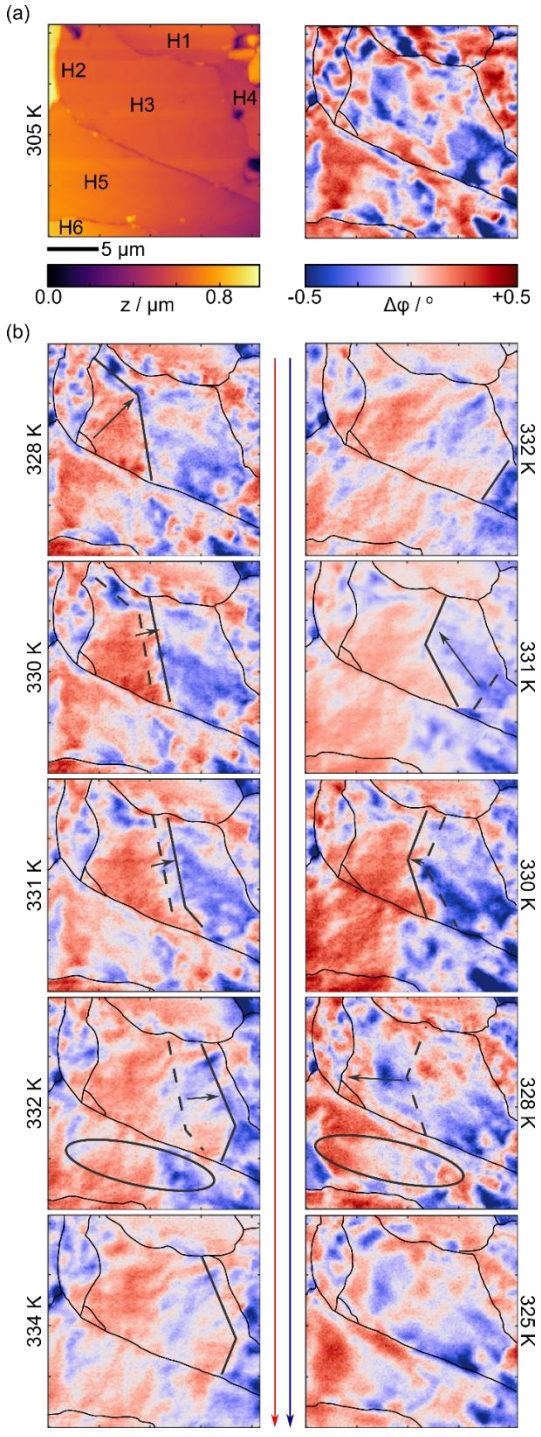

Figure VIII.5 Transformation in a region with larger grains displaying multi-step, thermoelastic behavior. (a) Room temperature topography and magnetic phase contrast and (b) corresponding magnetic phase contrast images on heating [left] and cooling [right].

VIII.3.5 Thermoelastic Growth from Retained Martensite

Given the importance of observed nucleation or growth-dominated transformation to understanding the underlying factors causing hysteresis in these alloys, it is crucial to both establish the validity of these thermoelastic growth observations, as well as try to determine their underlying cause. The *in-situ* MFM experiments have again been repeated on a third independent area consisting of three large grains meeting in a pronounced triple point (Fig. VIII.6). Once again, sudden single step transformations are observed in grains J2 and J1 on heating at 329 K and 333 K, respectively, and on cooling at 330 K and presumably below 328 K. However, grain J3 also clearly manifests reversible thermoelastic growth behavior, with a well-defined boundary between FM and PM phase moving incrementally from left to right from 330 K-333 K and back again from right to left from 331 K – 328 K. The same statistical argument against nucleation applies again here, and strongly suggests that the reversible thermoelastic phase boundary growth is a real repeatable phenomenon occurring in at least some fraction of the grains.

This third region also clearly shows a feature not as easily discerned in the other images: there is a clear remanent FM-type mottled signal still present at the main grain boundary and triple point even at 333 K, well after all of the other areas have transformed into PM phase. Further experiments (not shown here) demonstrate that this retained FM signal remains even after heating to as high as 353 K, more than 20 K above the DSC heating peak. Furthermore, the thermoelastic boundary in grain J2 appears to be influenced by this retained FM phase, first forming near it and growing

away on cooling, although it is harder to see a similar influence on heating. Taken together, this evidence suggests that the retained FM phase acts as a seed for growth of the forward PM→FM phase transformation boundary, potentially circumventing the nucleation process entirely and giving rise to growth-dominated behavior.

VIII.3.6 Stress-Induced Mechanism of Phase Retention at Defects

Given the potential of retained low-temperature FM phase and the important role it could play in obviating nucleation barriers, further investigation of the means by which phase retention is induced is necessary. Closer examination of the previous temperature-dependent magnetic phase contrast images shows other potential regions of retained FM phase at the triple point between grains {G2,G4,G5} (Fig. VIII.4a) and at the triple point between {H1 H3 H4} (Fig. VIII.5b), but certainly not every triple point or grain boundary displays retained FM signal. Evidently, defects where individual grains are all meeting together play some role in FM phase retention, but there is also some other factor at play. One clue to this factor is obtained from the changes in topography observed in the third region investigated (Fig. VIII.7), from which it is clearly seen that the sudden change from FM to PM contrast in grain J2 at 329 K is also accompanied by a large topographic expansion perpendicular to the sample plane. Crystallographic observations show that the unit cell volume in these alloys increases by ~1 % during the magneto-structural transformation, and although this is relatively small, it is still enough to create substantial stress on adjacent grains. This would be a compressive stress that tends to stabilize the lower volume FM phase, and if the stress

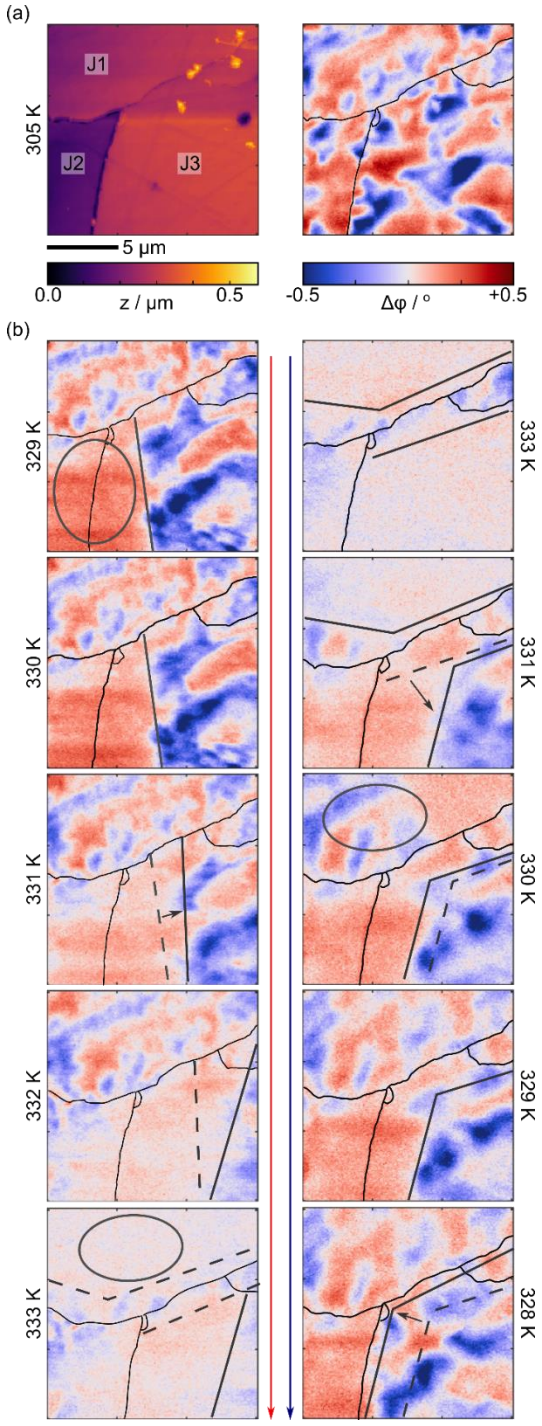

Figure VIII.6 Transformation in a region that appears to grow outwards from retained FM phase. (a) Room temperature topography and magnetic phase contrast and (b) corresponding magnetic phase contrast images on heating [left] and cooling [right]

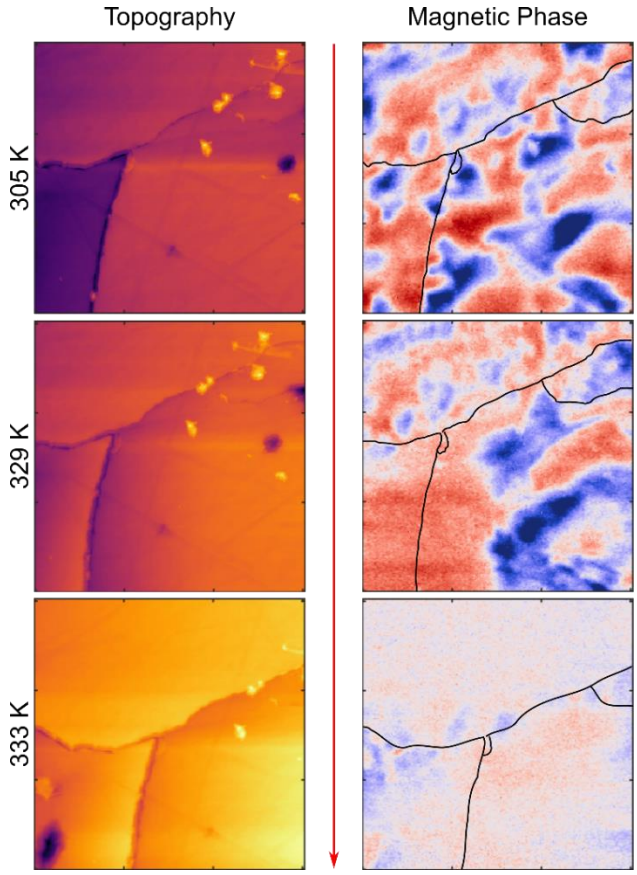

Figure VIII.7 Evidence for stress-based mechanism of un-transformed phase retention. Topography images [left] and corresponding magnetic phase contrast images [right] show clear expansion of first-transforming grain that creates stress at grain boundary favorable for retention of FM phase.

were confined mainly to the grain boundaries, this could result in retained FM phase at the grain boundaries, as reported here.

VIII.4 Conclusions

Reduction of hysteresis in $(Mn,Fe)_2(P,Si)$ alloys' magneto-structural transformations requires understanding the nature of the energy barriers that oppose it, but detailed investigations of these energy barriers are relatively rare. In this work we have begun to explore these questions, using *in-situ* temperature-dependent magnetic force microscopy to track the evolution of the magneto-structural transformation

boundary in individual grains, thereby inferring the nature of some of these hysteretic energy barriers. Although we mainly observe sudden single-step transformations at a well-defined critical temperature, we also find a couple of grains that manifest repeatable reversible incremental growth most likely associated with thermoelastic phenomena. When thermoelastic growth occurs, it appears to be definitely related to the presence of retained ferromagnetic phase at defect structures, which may play a role in circumventing traditional nucleation and implying growth-dominated transformation behavior in these grains. Finally, we correlate the regions containing retained untransformed phase to topography of the sample, which point towards magneto-elastic interactions between neighboring grains as a potential stabilizing mechanism. This work lays the foundations for more detailed studies of transformation mechanisms in $(Mn,Fe)_2(P,Si)$ alloys, thereby enabling hysteresis reduction principles for designing improved magnetocaloric materials.

VIII.5 References

[1] F. X. Hu, B. G. Shen, J. R. Sun, Z. H. Cheng, G. H. Rao, and X. X. Zhang, Applied Physics Letters **78,** 3675 (2001).

[2] J. Liu, T. Gottschall, K. P. Skokov, J. D. Moore, and O. Gutfleisch, Nat Mater **11,** 620 (2012).

[3] N. H. Dung, L. Zhang, Z. Q. Ou, and E. Bruck, Scripta Materialia **67,** 975 (2012).

[4] A. Waske, L. Giebeler, B. Weise, A. Funk, M. Hinterstein, M. Herklotz, K. Skokov, S. Fahler, O. Gutfleisch, and J. Eckert, Physica Status Solidi-Rapid Research Letters **9,** 136 (2015).

[5] H. Yamada, Physica B-Condensed Matter **391,** 42 (2007).

[6] R. Kainuma, Y. Imano, W. Ito, Y. Sutou, H. Morito, S. Okamoto, O. Kitakami, K. Oikawa, A. Fujita, T. Kanomata, and K. Ishida, Nature **439,** 957 (2006).

[7] J. Liu, T. G. Woodcock, N. Scheerbaum, and O. Gutfleisch, Acta Materialia **57,** 4911 (2009).

[8] H. E. Karaca, I. Karaman, B. Basaran, D. C. Lagoudas, Y. I. Chumlyakov, and H. J. Maier, Acta Materialia **55,** 4253 (2007).

[9] H. E. Karaca, I. Karaman, B. Basaran, Y. Ren, Y. I. Chumlyakov, and H. J. Maier, Advanced Functional Materials **19,** 983 (2009).

[10] S. Fujieda, A. Fujita, and K. Fukamichi, Science and Technology of Advanced Materials **4,** 339 (2016).

[11] A. Fujita, S. Fujieda, Y. Hasegawa, and K. Fukamichi, Physical Review B **67,** 104416 (2003).

[12] M. Khan, N. Ali, and S. Stadler, Journal of Applied Physics **101** (2007).

[13] T. Krenke, E. Duman, M. Acet, E. F. Wassermann, X. Moya, L. Manosa, and A. Planes, Nat Mater **4,** 450 (2005).

[14] D. T. Cam Thanh, E. Brück, O. Tegus, J. C. P. Klaasse, T. J. Gortenmulder, and K. H. J. Buschow, Journal of Applied Physics **99** (2006).

[15] N. V. Thang, X. F. Miao, N. H. van Dijk, and E. Bruck, Journal of Alloys and Compounds **670,** 123 (2016).

[16] E. Brück, Journal of Physics D: Applied Physics **38,** R381 (2005).

[17] V. Franco, J. S. Blázquez, B. Ingale, and A. Conde, Annual Review of Materials Research **42,** 305 (2012).

[18] A. Post, C. Knight, and E. Kisi, Journal of Applied Physics **114** (2013).

[19] J. C. Debnath, R. Zeng, J. H. Kim, P. Shamba, and S. X. Dou, Applied Physics A **106,** 245 (2011).

[20] J. Lyubina, O. Gutfleisch, M. D. Kuz'min, and M. Richter, Journal of Magnetism and Magnetic Materials **321,** 3571 (2009).

[21] N. M. Bruno, C. Yegin, I. Karaman, J.-H. Chen, J. H. Ross, J. Liu, and J. Li, Acta Materialia **74,** 66 (2014).

[22] P. J. Shamberger and F. S. Ohuchi, Physical Review B **79** (2009).

[23] N. T. Trung, Z. Q. Ou, T. J. Gortenmulder, O. Tegus, K. H. J. Buschow, and E. Brück, Applied Physics Letters **94** (2009).

[24] N. H. Dung, Z. Q. Ou, L. Caron, L. Zhang, D. T. C. Thanh, G. A. de Wijs, R. A. de Groot, K. H. J. Buschow, and E. Brück, Advanced Energy Materials **1,** 1215 (2011).

[25] F. Cugini, G. Porcari, T. Rimoldi, D. Orsi, S. Fabbrici, F. Albertini, and M. Solzi, Jom **69,** 1422 (2017).

[26] H. Cheng, Z. C. Xia, R. L. Wang, M. Wei, Z. Jin, S. Huang, C. Shang, H. Wu, X. X. Zhang, G. L. Xiao, and Z. W. Ouyang, Journal of Physics D-Applied Physics **50** (2017).

[27] T. Gottschall, K. P. Skokov, B. Frincu, and O. Gutfleisch, Applied Physics Letters **106** (2015).

[28] T. Kihara, I. Katakura, M. Tokunaga, A. Matsuo, K. Kawaguchi, A. Kondo, K. Kindo, W. Ito, X. Xu, and R. Kainuma, Journal of Alloys and Compounds **577,** S722 (2013).

[29] X. Xu, W. Ito, I. Katakura, M. Tokunaga, and R. Kainuma, Scripta Materialia **65,** 946 (2011).

[30] Y. N. Shen, R. L. Wang, Z. G. Sun, G. Cheng, Z. C. Xia, and L. Li, Journal of Materials Science-Materials in Electronics **25,** 2030 (2014).

[31] J. Fikacek, O. Heczko, V. Kopecky, J. Kastil, and J. Honolka, Journal of Magnetism and Magnetic Materials **452,** 373 (2018).

[32] O. Heczko, O. Perevertov, D. Kral, M. Veis, I. V. Soldatov, and R. Schafer, Ieee Transactions on Magnetics **53** (2017).

[33] J. McCord, Journal of Physics D-Applied Physics **48** (2015).

[34] N. Glavatska, Ferroelectrics **292,** 93 (2003).

[35] H. D. Chopra, C. H. Ji, and V. V. Kokorin, Physical Review B **61,** 14913 (2000).

[36] M. R. Sullivan and H. D. Chopra, Physical Review B **70** (2004).

[37] J. N. Armstrong, M. R. Sullivan, M. Le Romancer, V. A. Chernenko, and H. D. Chopra, Journal of Applied Physics **103** (2008).

[38] A. Neudert, Y. W. Lai, R. Schafer, M. Kustov, L. Schultz, and J. McCord, Advanced Engineering Materials **14,** 601 (2012).

[39] K. Morrison, A. Barcza, J. D. Moore, K. G. Sandeman, M. K. Chattopadhyay, S. B. Roy, A. D. Caplin, and L. F. Cohen, Journal of Physics D-Applied Physics **43** (2010).

[40] K. Morrison, J. D. Moore, K. G. Sandeman, A. D. Caplin, and L. F. Cohen, Physical Review B **79** (2009).

[41] G. Boero, M. Demierre, P. A. Besse, and R. S. Popovic, Sensors and Actuators a-Physical **106,** 314 (2003).

[42] V. K. Sharma, J. D. Moore, M. K. Chattopadhyay, K. Morrison, L. F. Cohen, and S. B. Roy, Journal of Physics-Condensed Matter **22** (2010).

[43] H. S. Park, Y. Murakami, D. Shindo, V. A. Chernenko, and T. Kanomata, Applied Physics Letters **83,** 3752 (2003).

[44] A. Budruk, C. Phatak, A. K. Petford-Long, and M. De Graef, Acta Materialia **59,** 6646 (2011).

[45] A. Budruk, C. Phatak, A. K. Petford-Long, and M. De Graef, Acta Materialia **59,** 4895 (2011).

[46] H. Y. Wang, X. F. Dai, Y. G. Wang, X. F. Duan, and G. H. Wu, Materials Transactions **48,** 2255 (2007).

[47] Y. Murakami, D. Shindo, R. Kainuma, K. Oikawa, and K. Ishida, Applied Physics Letters **92** (2008).

[48] Y. Murakami, D. Shindo, K. Oikawa, R. Kainuma, and K. Ishida, Acta Materialia **50,** 2173 (2002).

[49] Y. Murakami, T. Yano, D. Shindo, R. Kainuma, K. Oikawa, and K. Ishida, Scripta Materialia **55,** 683 (2006).

[50] C. Phatak, A. K. Petford-Long, and M. De Graef, Current Opinion in Solid State & Materials Science **20,** 107 (2016).

[51] S. P. Venkateswaran, N. T. Nuhfer, and M. De Graef, Acta Materialia **55,** 5419 (2007).

[52] K. Gross, K. Westerholt, and H. Zabel, New Journal of Physics **18** (2016).

[53] H. C. Xuan, T. Zhang, Y. F. Wu, S. Agarwal, H. L. Yang, X. C. Wen, J. F. Wei, P. D. Han, and Y. W. Du, Physica Status Solidi a-Applications and Materials Science **215** (2018).

[54] D. Niklasch, H. J. Maier, and I. Karaman, Review of Scientific Instruments **79** (2008).

[55] P. Mullner, Z. Clark, L. Kenoyer, W. B. Knowlton, and G. Kostorz, Materials Science and Engineering a-Structural Materials Properties Microstructure and Processing **481,** 66 (2008).

[56] Q. Pan and R. D. James, Journal of Applied Physics **87,** 4702 (2000).

[57] V. Kopecky, L. Fekete, O. Perevertov, and O. Heczko, Aip Advances **6** (2016).

[58] D. Rugar, H. J. Mamin, P. Guethner, S. E. Lambert, J. E. Stern, I. Mcfadyen, and T. Yogi, Journal of Applied Physics **68,** 1169 (1990).

[59] D. Niklasch, J. Dadda, H. J. Maier, and I. Karaman, Journal of Materials Science **43,** 6890 (2008).

[60] M. Fries, L. Pfeuffer, E. Bruder, T. Gottschall, S. Ener, L. V. S. Diop, T. Grob, K. P. Skokov, and O. Gutfleisch, Acta Materialia **132,** 222 (2017).

[61] A. Waske, E. Lovell, A. Funk, K. Sellschopp, A. Rack, L. Giebeler, P. F. Gostin, S. Fahler, and L. F. Cohen, Apl Materials **4** (2016).

[62] C. Bennati, F. Laviano, G. Durin, E. S. Olivetti, V. Basso, G. Ghigo, and M. Kuepferling, Journal of Magnetism and Magnetic Materials **400,** 339 (2016).

[63] M. Kuepferling, C. Bennati, F. Laviano, G. Ghigo, and V. Basso, Journal of Applied Physics **115** (2014).

[64] N. Kawamoto, Y. Murakami, D. Shindo, S. Fujieda, A. Fujita, and K. Fukamichi, Materials Transactions **46,** 1764 (2005).

[65] N. Kawamoto, Y. Murakami, D. Shindo, K. Fukamichi, S. Fujieda, and A. Fujita, Journal of Applied Physics **100** (2006).

[66] N. Kawamoto, Y. Murakami, D. Shindo, K. Fukamichi, S. Fujieda, and A. Fujita, Journal of Magnetism and Magnetic Materials **310,** 2815 (2007).

[67] M. Fries, L. Pfeuffer, E. Bruder, T. Gottschall, S. Ener, L. V. B. Diop, T. Gröb, K. P. Skokov, and O. Gutfleisch, Acta Materialia **132,** 222 (2017).

[68] A. Funk, M. Zeilinger, F. Dotz, I. Soldatov, R. Schafer, and A. Waske, Physica Status Solidi B-Basic Solid State Physics **255** (2018).

[69] C. Kittel, Reviews of Modern Physics **21,** 541 (1949).

[70] J. B. Wedding, M. Li, and G. C. Wang, Journal of Magnetism and Magnetic Materials **204,** 79 (1999).

[71] D. Kumar, S. Singh, P. Vishawakarma, A. S. Dev, V. R. Reddy, and A. Gupta, Journal of Magnetism and Magnetic Materials **418,** 99 (2016).

[72] D. M. Paige, B. Szpunar, and B. K. Tanner, Journal of Magnetism and Magnetic Materials **44,** 239 (1984).

[73] H. Yibole, F. Guillou, L. Zhang, N. H. van Dijk, and E. Brück, Journal of Physics D: Applied Physics **47** (2014).

CHAPTER IX

CONCLUSION AND FUTURE DIRECTIONS

IX.1 Summary

This dissertation presents an investigation into how non-diffusive transformations in one class of magnetocaloric materials, $(Mn,Fe)_2(P,Si)$ alloys, can be engineered to obtain optimal performance when used as a working material in magnetic refrigeration (MR) systems, with a particular focus on the sources of hysteresis in the transformation and its impact on potential performance. The main objectives of the investigation are to answer the two complementary questions (1) *how should magnetocaloric materials and transformations be designed so as to take best advantage of their magnetic entropy change within refrigeration applications?* and (2) *using $(Mn,Fe)_2(P,Si)$ alloys as a model case, what are the mechanisms controlling the magneto-structural transformation and its hysteresis, and how can they be tuned to meet the design constraints?* The dissertation is subdivided into two main sections addressing each objective.

For the first objective, Chapters II-V focus specifically on the challenge of developing a rational thermodynamic modeling framework within which the interacting effects of magnetocaloric properties, transformation hysteresis and phase coexistence, and refrigeration cycle on the overall system level refrigeration performance can be decoupled and studied individually. In Chapter II, the skeleton of the modeling framework is developed, showing how caloric properties, hysteresis effects, and cycle

dependence can all be enfolded within a single thermodynamic treatment coupling mean-field and Preisach hysteresis models with experimental data using the new conceptual framework of free energy-equivalent temperature-field paths. Having constructed and thoroughly validated this new conceptual framework, it is then put to work in simulating the hysteretic, cycle-dependent response of macroscopic magnetothermal properties in a $(Ni,Co)_2(Mn,In)_2$ alloy for Ericsson (Chapter III) and Brayton (Chapter IV) type cycles of interest. Major results include the existence of efficiency-optimal cycles whenever transformation temperatures are matched with cycle temperature reservoirs and the benchmark of 1-2 K maximum allowable hysteresis to obtain 70-90 % efficiency in cycles operating between 0 T and 1.5 T. Finally, the simulation framework is applied to each of four leading caloric material alloys (Chapter V), enabling direct comparisons of cycle performance. Major findings include the improved performance of each of the major GMCE alloys relative to benchmark Gd, which has no non-diffusive transformation but smaller transformation entropy, and the potential for GMCE-based MR systems to drastically expand their effective cooling power and temperature span solely through processing to reduce transformation hysteresis.

For the second objective, Chapters VI-VIII explore the factors tuning transformation properties and hysteresis in $(Mn,Fe)_2(P,Si)$ magneto-structural transformations (MST) at both the macro- and micro-scale. In Chapter VI, the effect of overall homogeneity in the quaternary alloy on its corresponding transformation is investigated in detail through a variety of heat treatments. It is shown that chemical

inhomogeneity on the order of 1-2 at. % is sufficient to create undesired multi-step transformations due to splitting of an initial unimodal quaternary composition distribution into a bimodal distribution, each corresponding to a different component MST. A dynamic re-equilibration mechanism is suggested, and it is shown that homogenizing heat treatments can recover the initial unimodal population and its corresponding single step MST. In Chapter VII, characterization of alloys throughout the composition space is used to determine the precise dependence of transformation hysteresis, critical temperature, and enthalpy on quaternary alloy content, and also to investigate the role of processing and impurity phases in deviations in composition from designed values. An oxygen-driven phase segregation mechanism is suggested, showing how relatively small oxygen contents can drive the formation of impurity phases that substantially modify the quaternary alloy composition and can ultimately create very large deviations in transformation properties from desired values. Finally, microscale mechanisms affecting the transformation are investigated through *in-situ* observations of phase boundary growth in individual grains (Chapter VIII). It is shown that the transformation behavior is consistent with growth from retained seeds of already-transformed phase retained at grain boundaries, with growth being opposed by phase boundary motion through defected volumes. Processing conditions intended to capitalize on these transformation mechanisms in $(Mn,Fe)_2(P,Si)$ alloys are suggested, enabling further hysteresis reductions in these materials.

We conclude by presenting some initial results on three promising directions for future research: (1) synthesis of compositionally-homogenous single crystals of

$(Mn,Fe)_2(P,Si)$ alloys for direct verification of lattice correspondences and other experiments; (2) oxygen pure processing to further explore static and rate-dependent hysteresis composition mapping; (3) a detailed experimental study into order-disorder transformations in $(Mn.Fe)_2(P,Si)$ alloys, and its effect on MST transformation properties.

IX.2 Future Directions for Engineering Transformations and Hysteresis

IX.2.1 Grain Refinement for Verification of Lattice Correspondences and Other Single Crystal Experiments

The James lattice matching theory is a general mathematical theory that develops precise constraints for which a given martensitic transformation may develop (1) an exact geometrically compatible habit plane between austenite and un-twinned martensite or (2) a near-exact compatible habit plane between austenite and twinned martensite [1-3]. Satisfaction of these lattice matching constraints implies the existence of un-strained invariant planes that maintain continuity between the austenite lattice on the one side of interface, and the martensite lattice on the other. These un-strained invariant planes are expected to form and propagate with minimal energy penalty, thus reducing the hysteresis of the transformation. Indeed, in both shape memory alloy systems [4-7] and metamagnetic shape memory alloy systems [8-12], extraordinary consequences of the lattice matching theory have been verified, including observation of atomically exact compatible interfaces between austenite and un-twinned martensite [13], and a rapid decrease in hysteresis to the order of 1-5 K with the compatibility parameter λ_2 [14,15].

Observed hystereses in $(Mn,Fe)_2(P,Si)$ are relatively small (2-20 K) [16] compared especially to the MSMA magnetocaloric alloys (generally >20 K) [17,18], particularly when considering that the change of lattice parameters in Mn-rich alloys is not negligible ($\frac{\Delta a}{a} \approx 0.5-1.5\%; \frac{\Delta c}{c} \approx 1-3\%; \frac{\Delta V}{V} \approx 0.5-1.5\%$) [Chapter VI, 19,20]. Hence, it bears investigating what role lattice matching may play in tuning the observed hysteresis in these alloys.

One important but under-appreciated aspect of the lattice matching theory is that the compatibility parameter λ_2 depends not only on the measured lattice parameters of the austenitic and martensitic lattices but also on their relative orientations, *i.e.* the precise mapping of crystallographic planes and directions in the austenite onto the corresponding planes and directions in the martensite. The importance of this point can be seen directly by comparing two proposed lattice correspondences (LCs, Eq. IX.1-2) for a particular volume-doubling tetragonal-to-martensite transformation (Fig. IX.1),

$$[002]_A \leftrightarrow [001]_M;\ [010]_A \leftrightarrow [010]_M;\ [10\bar{1}]_A \leftrightarrow [100]_M, \qquad (IX.1)$$

$$[\bar{1}0\bar{1}]_A \leftrightarrow [100]_M;\ [010]_A \leftrightarrow [010]_M;\ [10\bar{1}]_A \leftrightarrow [001]_M. \qquad (IX.2)$$

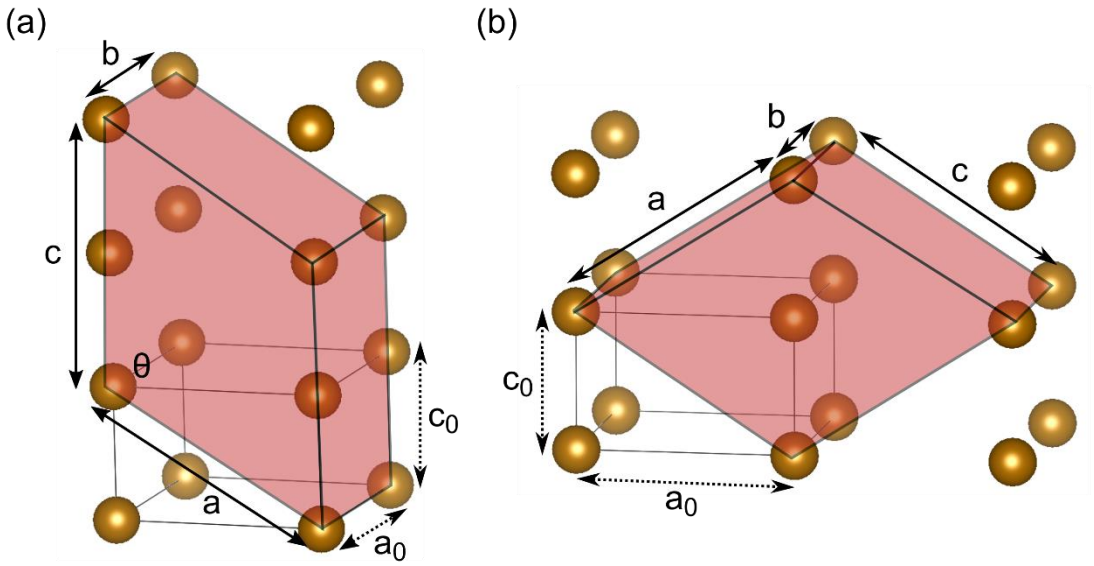

Figure IX.1 Two potential lattice correspondences for model tetragonal-to-monoclinic transformation.

After referencing both lattices to the Cartesian orthonormal basis shown, the calculated Bain transformation matrices are

$$B_1 = \begin{pmatrix} \alpha S & 0 & 0 \\ 0 & \beta & 0 \\ \alpha C + \dfrac{\delta}{2} & 0 & \dfrac{\gamma}{2} \end{pmatrix}, \qquad (IX.1)$$

$$B_2 = \begin{pmatrix} (\alpha+\delta)S'/2 & 0 & (\varepsilon-\gamma)S'/2 \\ 0 & \beta & 0 \\ (\alpha-\delta)C'/2 & 0 & (\epsilon+\gamma)C'/2 \end{pmatrix}, \qquad (IX.2)$$

where $S \equiv \sin\theta$, $C \equiv \cos\theta$, $\alpha \equiv a/a_0$, $\beta \equiv b/a_0$, $\gamma \equiv c/c_0$, $\delta \equiv c/a_0$, $\varepsilon \equiv a/c_0$, $S' \equiv \sin(\theta/2)$, $C' \equiv \cos(\theta/2)$. If these matrices left-multiply some real space vector in the austenite, they yield the corresponding real space vector in the martensite after transformation.

These transformation matrices differ substantially, and so do the calculated invariant plane strains, related to the second ordered eigenvalue, λ_2, of each matrix. For definiteness, suppose initially $a_0 = 4.6$ Å and $c_0 = 2.9$ Å, and $\beta = 0.9$ (10% compression along the b axis). Then the compatibility parameter λ_2 for each proposed LC can be computed as a function of the other two axis stretches, α and γ (Fig. IX.2). The dependence of the compatibility parameter on the transformation stretches is clearly different for the two LCs, with optimal $\lambda_2 \sim 1$ occurring for larger transformation stretches in LC2, and also dropping off less quickly for small deviations from this optimum. Furthermore, the first LC has both $[001]_A$ and $[100]_A$ twinning systems, whereas the second LC only has the former. The point is that the same measured lattice parameters $\{a_0, c_0, a, b, c, \theta\}$ can lead to very different compatibility relationships, depending on the supposed LCs.

Hence, a thorough investigation of lattice matching as a hysteresis tuning mechanism in $(Mn,Fe)_2(P,Si)$ alloys requires an experimental measurement of the proper LCs in the transformation.

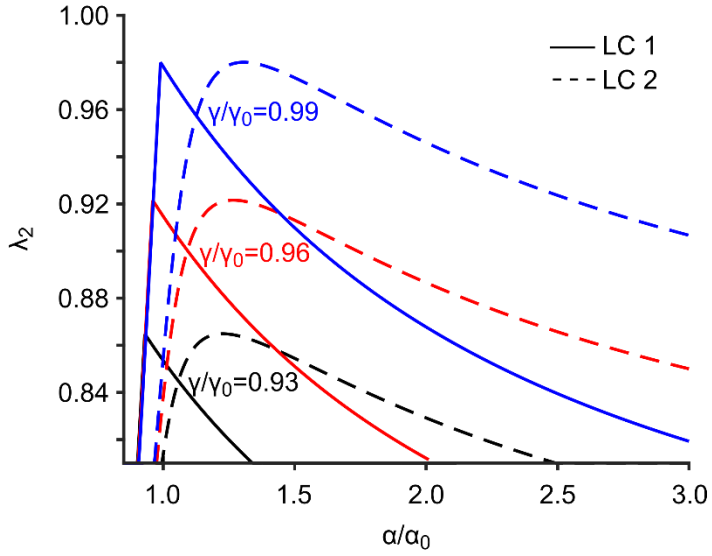

Figure IX.2 Computed dependence of compatibility parameter on transformation stretches. Compatibility relations are compared for two potential lattice correspondences in Fig. IX.1, demonstrating that compatibilities for the same lattice stretches differ substantially between the LCs.

Experimentally, these lattice correspondences may be measured by observing the movement of poles corresponding to certain planes throughout the transformation. For example, if on heating, (0002) poles in the high-temperature phase are observed to appear very near where the (0002) poles in the low-temperature phase were, then $[0002]_A \leftrightarrow [0002]_M$ seems plausible. X-Ray diffraction experiments comparing pole figures for relatively small (10-50) numbers of crystallites before and after the transformation were successfully carried out. However, the results are inconclusive; there are too many crystallites present to reliably track poles *for the same crystallite* across the transformation, and the possibility of additional reorientation due to accommodating transformation in neighboring grains cannot be excluded.

For this reason, we propose to attempt the pole tracking experiment within single crystals of $(Mn,Fe)_2(P,Si)$ alloys. We should note that there are some recent diffraction

studies in single crystals in these alloys. One investigation [21] grew single crystals from Sn flux and performed diffraction both below and above the transformation to confirm the structure; however, the focus of the study was on single crystal magnetization experiments to determine the magnetocrystalline anisotropy, and since only the low-temperature patterns are reported, it is unknown whether reorientation occurred. A second study [19] used *in-situ* Transmission Electron Microscopy (TEM) to observe the transformation in B-doped $(Mn,Fe)_2(P,Si)$ and reported two sets of diffraction patterns with a relative rotation of only 2° within the phase coexistence region. This is strong evidence for complete orientation conservation $[0001]_A \leftrightarrow [0001]_M$, $[10\bar{1}0]_A \leftrightarrow [10\bar{1}0]_M$, $[01\bar{1}0]_A \leftrightarrow [01\bar{1}0]_M$. However, the experiments were carried out on a B-doped polycrystal with much larger 35 K hysteresis, and it is unclear what role this doping and large hysteresis may have played in the observed lattice correspondence. Single crystal x-ray experiments in undoped $(Mn,Fe)_2(P,Si)$ may help to clarify these results, since the much smaller Ewald sphere creates more restrictive diffraction conditions, meaning reorientation of individual poles, as opposed to an entire zone axis pattern, may be observed.

It was found that polycrystals of $(Mn,Fe)_2(P,Si)$ prepared by powder metallurgy could be fractured along grain boundaries through repeated thermal decrepitation (the alloys are quite brittle), *i.e.* repeatedly ($N \sim 200$) heating and cooling through the transformation. Unfortunately, the small size of the crystallites again posed a problem, since after decrepitation samples were either single crystal but too small to align in the diffractometer, or polycrystalline with ~10 distinct domains. Further investigations were

made into the effect of additional heat treatments on crystallite size and on the transformation (Fig. IX.3). Single-step heat treatments showed that either the transformation could be retained with annealing for up to 1 week at 1373 K, or the grains could be made to grow by annealing for as short as 3 h at 1473 K, but not both. (Fig. IX.3c) Most recently, the combined effect of grain growth and transformation retention has been obtained in two-step 1473 K / 1 h + 1273 K / 20 h heat treatments (not shown), and although the transformation is broad, it seems likely that the broadness is due to compositional inhomogeneity that can be homogenized by longer annealing at 1273 K (Chapter VI).

The outlook looks positive for fabricating single crystals in this manner, and due to the relative ease and speed of powder metallurgy compared to flux-growth or TEM sample preparation, free-standing, compositionally homogeneous single crystals could be synthesized throughout the alloy space. Such samples could be used to probe not only potential variation in lattice correspondences across the alloy space, but also for measurements of magnetocrystalline anisotropy and anisotropic mechanical properties, perhaps under nano-indentation. MFM experiments (Chapter VIII) have also suggested retained untransformed phase at grain boundaries may play some role in facilitating the transformation, and controlled grain growth could be used to decouple this as yet unstudied factor from the other hysteresis mechanisms.

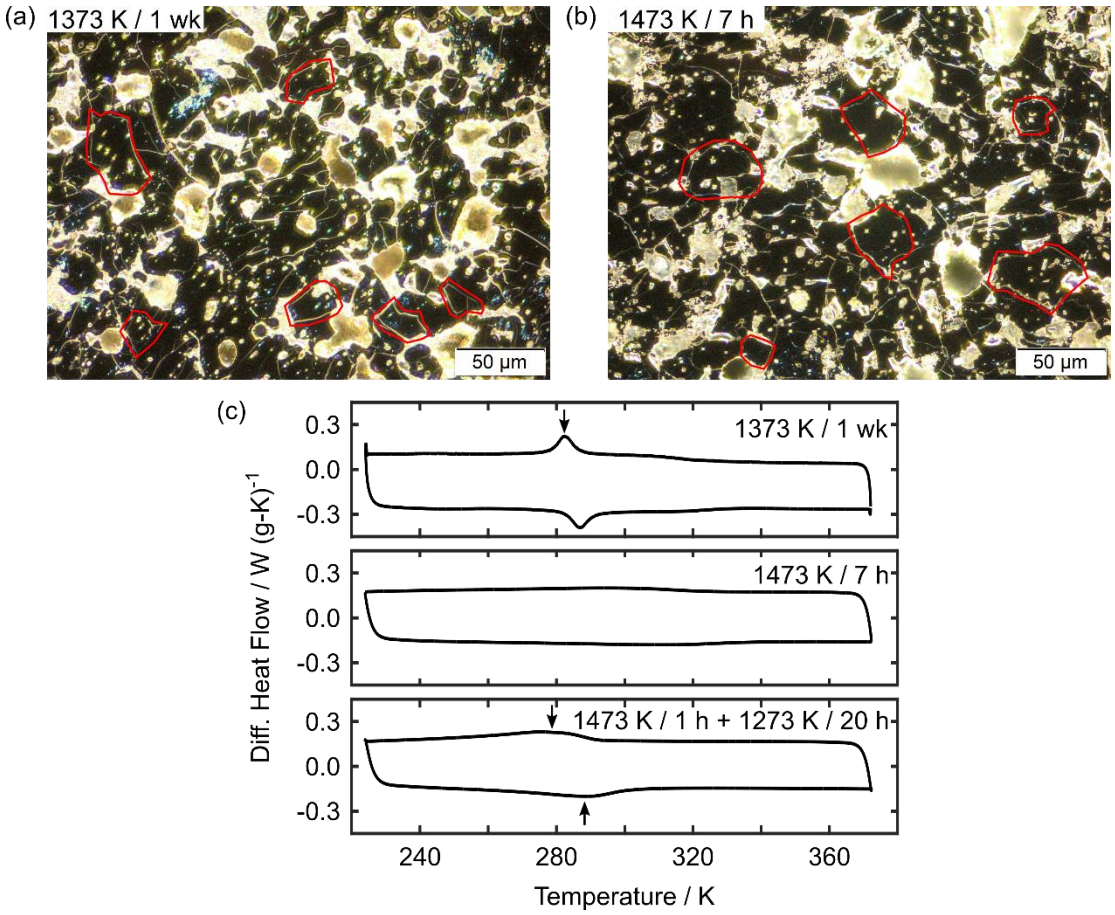

Figure IX.3 Grain growth and transformations in decrepitated $(Mn,Fe)_2(P,Si)$ polycrystals. (a) and (b) grain microstructure under dark field polarized light of one-shot heat-treated polycrystals. (c) Corresponding calorimetry traces for grain-growth heat-treated samples.

IX.2.2 Expanding Composition Maps of Intrinsic and Rate-Dependent Hysteresis

In the initial composition mapping presented in this work (Chapter VII), precedence was given to critical temperatures over hysteresis, so that transformations could be tuned to slightly below or above room temperature, where *in situ* XRD and AFM experiments could be performed. However, as shown in those previous mappings, critical temperatures are about 20x more sensitive to changes in Si than are thermal hystereses. As a result, although a fairly large space of critical temperatures from 250 K

to 330 K was explored, this corresponded to only a relatively narrow range of middling hystereses from mainly 5 K to 15 K (Fig. IX.4). Further development of $(Mn,Fe)_2(P,Si)$ alloys for refrigeration requires minimal hysteresis < 1 K, and deeper understanding of the mechanisms contributing hysteretic energy barriers requires comparative experiments on alloys with both very large and very small hysteresis. For example, additional MFM on large-hysteresis alloys may reveal multiple nucleation points within single grains, further consistent with growth-limited behavior, or altogether different transformation mechanisms in this regime.

These further investigations would require a greater degree of composition control in order to independently tune hysteresis and transformation critical temperature, and in addition to the composition maps already presented, the oxygen-mediated phase segregation mechanisms analyzed here may be some guide. For example, although processing steps have excluded oxygen about as well as feasible, we begin to suspect some of the purchased stock powders (especially Mn and Si) may already have some oxygen contamination on arrival. Some studies in the literature have instead used larger Mn and Si pieces pre-treated with nitric acid to remove surface oxides before processing, and this is one extra precaution that should be taken in future work to further exclude oxygen. In this way, further oxygen exclusion should limit the segregation of (at least one) impurity phases, and improve the overall control over the designed composition of the $(Mn,Fe)_2(P,Si)$ phase.

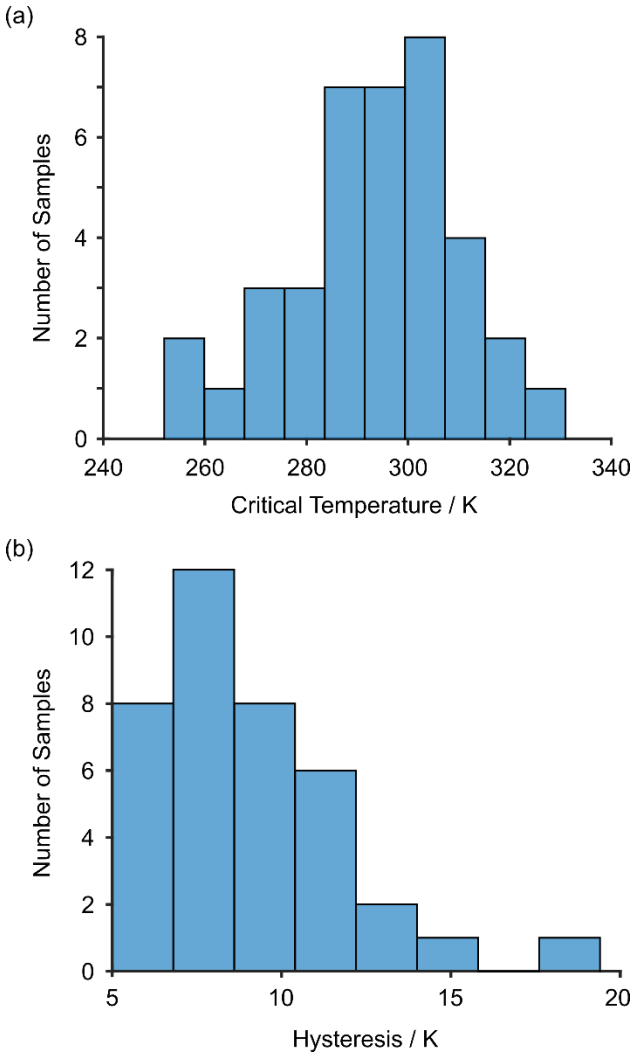

Figure IX.4 Summary of critical temperatures and hystereses for fabricated alloys. The explored space of critical temperatures is considerably larger, due to its substantially greater composition sensitivity.

Like many non-diffusive transformations, the magneto-structural transformation in $(Mn,Fe)_2(P,Si)$ alloys also manifests a degree of rate dependence. In depth studies of rate dependence provide both (1) a pseudo-calibration to scale observed hystereses at 10 K /min to the "intrinsic" hysteresis that would be observed in the limit of infinitesimally slow ramp rates, and (2) indirect information about the magnitudes of hysteretic energy barriers through Arrhenian models of the form

$$R = A \exp \frac{-\Delta G^*}{k_B\left(\left|T - T_{\mathrm{eq}}\right|\right)} \qquad (IX.1)$$

With R the crossing rate over an energy barrier of magnitude ΔG^* at temperature T. Assume the rate of transformation between the start and finish times

$$r \sim \frac{\phi_{\mathrm{f}} - \phi_{\mathrm{i}}}{t_{\mathrm{f}} - t_{\mathrm{i}}} = (\mathrm{ramp}) \frac{1}{|T_{\mathrm{f}} - T_{\mathrm{i}}|} \qquad (IX.2)$$

is approximately equal to R only within some narrow neighborhood around the peak heating / cooling temperature T_{p} ($R = r = 0$ at equilibrium, $T_{\mathrm{eq}} = \frac{T_{p,\mathrm{heat}} + T_{p,\mathrm{cool}}}{2}$). Then these models can be fit to calorimetry traces to estimate the magnitude of the energy barrier (Fig. IX.5).

$$-k_{\mathrm{B}} \ln\left(\frac{\mathrm{ramp}}{|T_{\mathrm{f}} - T_{\mathrm{i}}|}\right) = \left(\frac{1}{|T_{\mathrm{p}} - T_{\mathrm{eq}}|}\right) \Delta G^* - \ln A \qquad (IX.3)$$

The energy barrier from this simple estimate ($N = 6$) comes out to 0.40 ± 0.05 meV or 36.0 ± 4.5 kJ / mol, which is of the same order of magnitude as another calculation for an elastic energy barrier of 13.6 kJ / mol using measured principal strains and elastic constants [19].

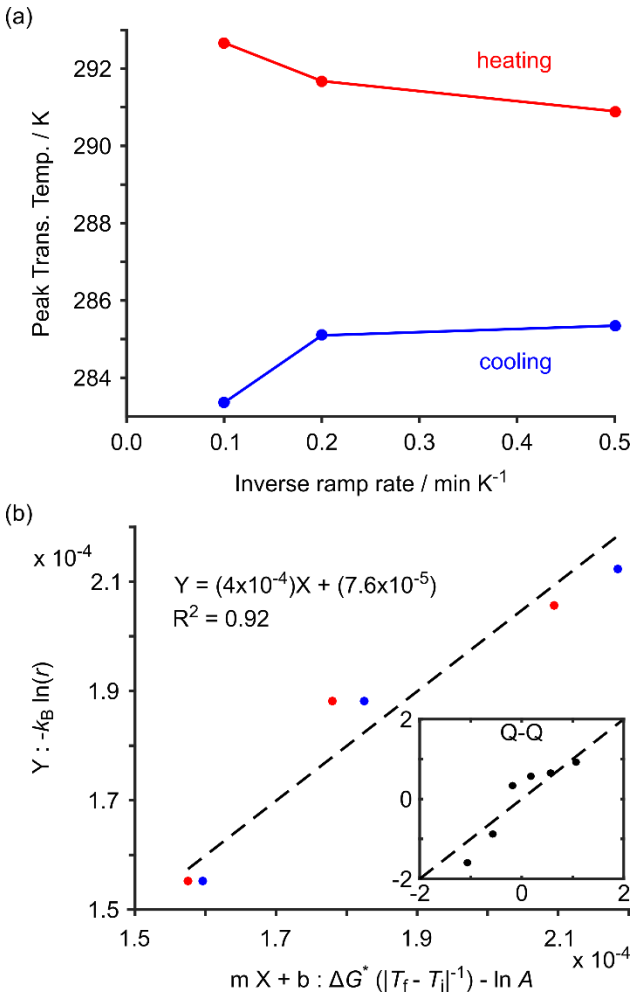

Figure IX.5 Rate dependent transformations in $(Mn,Fe)_2(P,Si)$ alloys. (a) Measured peak heating and cooling transformation temperatures at 10 K /min, 5 K /min, and 2 K / min; (b) Linear regression for model Eqn. IX.3.

These kinds of rate-dependent calorimetry experiments have only been completed for a small fraction of the synthesized alloys, but could easily be performed for the rest of the set and any future alloys. Results for calculated energy barriers for just three alloys (Table IX.1) already show a strong correlation with hysteresis at the slowest ramp rates (Fig. IX.6), and it would be interesting to explore whether this relationship continues to hold for extremely small or large hystereses.

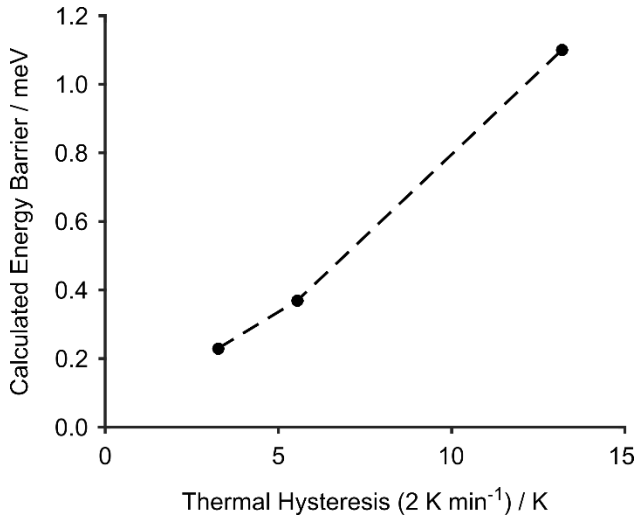

Figure IX.6 Comparison of calculated energy barriers and measured hystereses.Energy barriers calculated as above from regression to Eqn. IX.3, and thermal hysteresis measured as peak-to-peak differences at 2 K / min ramp rate.

ID	Hysteresis / K	$m \pm \mathrm{se}(m)$	$b \pm \mathrm{se}(b)$	R^2	$\rho(Y, Y-\hat{Y})$	S / eV K^{-1}
1247-394A	3.3	(2.3 ± 0.6) E-4	(8 ± 1) E-5	0.98	0.11	2.6 E-6
1205-461A	5.6	(4.0 ± 0.5) E-4	(8 ± 1) E-5	0.92	0.26	5.9 E-6
1207-469A	13.2	(11.0 ± 0.9) E-4	(5 ± 1) E-5	0.97	0.16	3.5 E-6

Table IX.1 Goodness-of-fit summary for calculated energy barriers. Regression parameters summarized as $Y = mX + b$. Other GOF metrics as in Chapter VII.

IX.2.3 Detailed Study of Order-Disorder Transformations

Previous investigations have demonstrated a strong preference for Mn in pyramidal and Fe in tetrahedral sites in slow-cooled samples [22,23]. First principles calculations [24,25] further show that the magnetic moments on these sites are sensitive to the chemical disorder on the sites, with chemical disorder tending to promote about 10 % larger (4.2 vs. 3.8 μ_B) net magnetic moment per unit cell due to an enlarged c/a ratio.

This tuning of magnetic moments and exchange energy is expected to play a critical role in the system's thermodynamics, particularly in the transformation critical temperature and enthalpy, as is observed with B2-$L2_1$ ordering in Ni-Mn MSMAs [26-28]. In our investigation, alloys were mainly slow-cooled from 1173 K to room temperature, but there was one specialized study in which samples were instead water quenched (Chapter VI), and it is instructive to compare the resultant transformation enthalpies and critical temperatures with the predictions from the composition maps (Table IX.2) developed for the slow-cooled alloys (Chapter VII).

Sample	T_c	Q	ΔT	$\widehat{T_c}$	$\widehat{Q}$	$\widehat{\Delta T}$	$\varepsilon(T_c)$	$\varepsilon(Q)$	$\varepsilon(\Delta T)$
1373Q	311	2.8	5.4	295	6.9	8.6	+2.3σ	-5.1σ	-3.6σ
1173Q-20h	301	4.9	6.8	307	6.7	7.5	-0.8σ	-2.3σ	-1.6σ
1173Q-1wk	306	3.7	5.5	304	6.9	7.9	+0.3σ	-4.0σ	-2.6σ
1273Q-20h	313	5.1	7.9	302	6.6	7.7	+1.5σ	-1.9σ	-1.6σ
1273Q-1wk	321	4.0	7.3	318	7.2	7.3	+0.4σ	-4.0σ	-2.0σ

Table IX.2 Comparison of quenched sample transformation properties to composition maps. Composition maps derived in Chapter VII are created from data for slow-cooled samples under heat treatment. Large prediction discrepancies for sample quenched directly from 1373 K may suggest ODO transformation above 1273 K.

All of the quenched samples' enthalpies deviate significantly from the slow-cooled model predictions, potentially due to an excess of oxidized impurity phases, since the previously treated alloys that were used as the starting point for these quenched samples had not been stored under Ar. However, only the sample directly quenched after being held at 1373 K for 8 h has significant deviations from predictions for all three of critical temperature, enthalpy, and hysteresis. This may be a clue that the transformation

properties of this sample quenched directly from 1373 K have been fundamentally changed, perhaps due to a disordering process between 1273 K and 1373 K.

A thorough study of the order-disorder transformation in $(Mn,Fe)_2(P,Si)$ alloys should be completed with a series of heat treatments on a known alloy composition, probably something around $(Mn_{1.25}Fe_{0.75})(P_{0.46}Si_{0.54})$ nominal, since this region of alloy space has already been thoroughly characterized. In order to exclude inhomogenization effects, samples should first undergo identical homogenization heat treatments, 1373 K / 6 h + 1273 / 7 d. The very first experiments (i) should focus on characterizing the state of order within the homogenized alloy under the standard heat treatment, ideally using Mossbauer spectroscopy to observe effects on both Mn/Fe and P/Si ordering through local bonding, but at the very least using neutron diffraction to distinguish Mn/Fe occupancy, since XRD scattering factors are insufficient to distinguish Mn and Fe (Fig. IX.8).

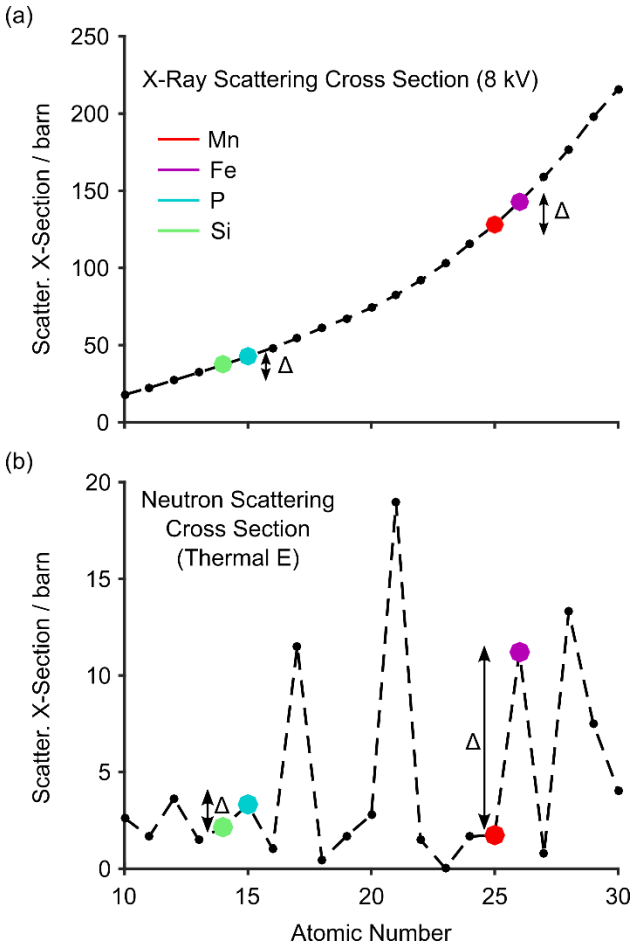

Figure IX.7 X-ray and neutron diffraction scattering cross sections. (a) X-ray cross-sections increase systematically with atomic number, making adjacent elements Mn/Fe and P/Si difficult to distinguish. (b) Neutron cross-sections exhibit a more chaotic dependence on atomic number, making Mn/Fe easy to distinguish in ODO experiments. P/Si are still probably better distinguished by Mossbauer spectroscopy.

With such long annealing times, the homogenized alloy should be in either a totally ordered or disordered state. From this point, the investigation can proceed forward through adding a third set of heat treatments to identically prepared 1373 K / 6 h + 1273 K / 7 d alloys, as (ii) a set of varied annealing temperatures 1073 K-1473 K at fixed time to determine the order-disorder temperature, T_{DO}, then (iii) a set of varied time anneals around T_{DO} to determine the kinetics of ordering / disordering. Finally, the effect of

ordering and disordering on the magnetic properties could be measured directly *via* bulk magnetometry to compare with the first-principles calculations.

IX.3 References

[1] J. M. Ball and R. D. James, Philosophical Transactions of the Royal Society of London A. **338,** 389 (1992).

[2] R. D. James, Nature **521,** 298 (2015).

[3] K. Bhattacharya, S. Conti, G. Zanzotto, and J. Zimmer, Nature **428,** 55 (2004).

[4] C. Chluba, W. W. Ge, R. L. de Miranda, J. Strobel, L. Kienle, E. Quandt, and M. Wuttig, Science **348,** 1004 (2015).

[5] Y. Song, X. Chen, V. Dabade, T. W. Shield, and R. D. James, Nature **502,** 85 (2013).

[6] K. C. Atli, B. E. Franco, I. Karaman, D. Gaydosh, and R. D. Noebe, Materials Science and Engineering: A **574,** 9 (2013).

[7] Z. Zhang, R. D. James, and S. Müller, Acta Materialia **57,** 4332 (2009).

[8] V. Srivastava, X. Chen, and R. D. James, Applied Physics Letters **97** (2010).

[9] E. Stern-Taulats, P. O. Castillo-Villa, L. Manosa, C. Frontera, S. Pramanick, S. Majumdar, and A. Planes, Journal of Applied Physics **115** (2014).

[10] D. W. Zhao, J. Liu, X. Chen, W. Sun, Y. Li, M. X. Zhang, Y. Y. Shao, H. Zhang, and A. R. Yan, Acta Materialia **133,** 217 (2017).

[11] Y. H. Qu, D. Y. Cong, X. M. Sun, Z. H. Nie, W. Y. Gui, R. G. Li, Y. Ren, and Y. D. Wang, Acta Materialia **134,** 236 (2017).

[12] H. L. Yan, C. F. Sanchez-Valdes, Y. D. Zhang, J. L. S. Llamazares, Z. B. Li, B. Yang, C. Esling, X. Zhao, and L. Zuo, Journal of Alloys and Compounds **767,** 544 (2018).

[13] R. Delville, D. Schryvers, Z. Zhang, and R. James, Scripta Materialia **60,** 293 (2009).

[14] R. Zarnetta, R. Takahashi, M. L. Young, A. Savan, Y. Furuya, S. Thienhaus, B. Maaß, M. Rahim, J. Frenzel, H. Brunken, Y. S. Chu, V. Srivastava, R. D. James, I. Takeuchi, G. Eggeler, and A. Ludwig, Advanced Functional Materials **20,** 1917 (2010).

[15] J. Cui, Y. S. Chu, O. O. Famodu, Y. Furuya, J. Hattrick-Simpers, R. D. James, A. Ludwig, S. Thienhaus, M. Wuttig, Z. Zhang, and I. Takeuchi, Nat Mater **5,** 286 (2006).

[16] N. H. Dung, Z. Q. Ou, L. Caron, L. Zhang, D. T. C. Thanh, G. A. de Wijs, R. A. de Groot, K. H. J. Buschow, and E. Brück, Advanced Energy Materials **1,** 1215 (2011).

[17] J. H. Chen, N. M. Bruno, I. Karaman, Y. J. Huang, J. G. Li, and J. H. Ross, Acta Materialia **105,** 176 (2016).

[18] J. A. Monroe, I. Karaman, B. Basaran, W. Ito, R. Y. Umetsu, R. Kainuma, K. Koyama, and Y. I. Chumlyakov, Acta Materialia **60,** 6883 (2012).

[19] X. F. Miao, H. Sepehri-Amin, and K. Hono, Scripta Materialia **138,** 96 (2017).

[20] N. H. Dung, L. Zhang, Z. Q. Ou, and E. Bruck, Scripta Materialia **67,** 975 (2012).

[21] H. Yibole, F. Guillou, Y. K. Huang, G. R. Blake, A. J. E. Lefering, N. H. van Dijk, and E. Bruck, Applied Physics Letters **107** (2015).

[22] V. Hoglin, J. Cedervall, M. S. Andersson, T. Sarkar, M. Hudl, P. Nordblad, Y. Andersson, and M. Sahlberg, Rsc Advances **5,** 8278 (2015).

[23] M. J. Neish, M. P. Oxley, J. Guo, B. C. Sales, L. J. Allen, and M. F. Chisholm, Physical Review Letters **114,** 5 (2015).

[24] G. J. Li, O. Eriksson, B. Johansson, and L. Vitos, Journal of Applied Physics **118,** 7 (2015).

[25] M. Hudl, P. Nordblad, T. Björkman, O. Eriksson, L. Häggström, M. Sahlberg, Y. Andersson, E.-K. Delczeg-Czirjak, and L. Vitos, Physical Review B **83,** 134420 (2011).

[26] A. Ghosh and K. Mandal, Applied Physics Letters **104,** 4 (2014).

[27] N. M. Bruno, C. Yegin, I. Karaman, J.-H. Chen, J. H. Ross, J. Liu, and J. Li, Acta Materialia **74,** 66 (2014).

[28] R. Sahoo, D. M. R. Kumar, D. A. Babu, K. G. Suresh, A. K. Nigam, and M. M. Raja, Journal of Magnetism and Magnetic Materials **347,** 95 (2013).